KAUNAS UNIVERSITY OF TECHNOLOGY

DOMANTĖ DAVIDOVIČIENĖ

ADSORPTION PROPERTIES, THERMAL STABILITY, AND APPLICATION OF DIFFERENTLY STRUCTURED SYNTHETIC DIBASIC CALCIUM SILICATE HYDRATES

Doctoral dissertation
Technological Sciences, Chemical Engineering (T 005)

Kaunas, 2022

This doctoral dissertation was prepared at Kaunas University of Technology, Faculty of Chemical Technology, Department of Silicate Technology during the period of 2018–2022. The studies were supported by the Research Council of Lithuania.

Scientific Supervisor
Prof. Dr. Kęstutis BALTAKYS (Kaunas University of Technology, Technological Sciences, Chemical Engineering, T 005).

Edited by: English language editor Brigita Brasienė (Publishing House "Technologija"), Lithuanian language editor Rozita Znamenskaitė (Publishing House "Technologija").

The official defence of the dissertation will be held at 10 a.m. on 16 September, 2022 at the public meeting of Dissertation Defence Board of Chemical Engineering Science Field in M7 Hall at The Campus Library of Kaunas University of Technology.

Address: Studentu 48-M7, 51367 Kaunas, Lithuania.
Tel. no. (+370) 37 300 042; fax. (+370) 37 324 144; e-mail doktorantura@ktu.lt

Doctoral dissertation was sent out on 16 August, 2022.
The doctoral dissertation is available on the internet http://ktu.edu and at the library of Kaunas University of Technology (K. Donelaičio St. 20, 44239 Kaunas, Lithuania).

KAUNO TECHNOLOGIJOS UNIVERSITETAS

DOMANTĖ DAVIDOVIČIENĖ

SKIRTINGOS STRUKTŪROS SINTETINIŲ DVIBAZIŲ KALCIO HIDROSILIKATŲ ADSORBCINĖS SAVYBĖS, TERMINIS STABILUMAS IR JŲ TAIKYMAS

Daktaro disertacija
Technologiniai mokslai, chemijos inžinerija (T 005)

Kaunas, 2022

Disertacija rengta 2018–2022 metais Kauno technologijos universiteto Cheminės technologijos fakultete, Silikatų technologijos katedroje. Mokslinius tyrimus rėmė Lietuvos mokslo taryba.

Mokslinis vadovas:
Prof. dr. Kęstutis BALTAKYS (Kauno technologijos universitetas, technologiniai mokslai, chemijos inžinerija, T 005).

Redagavo: anglų kalbos redaktorė Brigita Brasienė (leidykla „Technologija“), lietuvių kalbos redaktorė Rozita Znamenskaitė (leidykla „Technologija“)

Chemijos inžinerijos mokslo krypties disertacijos gynimo taryba:
Prof. dr. Raimundas ŠIAUČIŪNAS (Kauno technologijos universitetas, technologiniai mokslai, chemijos inžinerija, T 005) – **pirmininkas**;
Prof. dr. Rimvydas KAMINSKAS (Kauno technologijos universitetas, technologiniai mokslai, chemijos inžinerija, T 005);
Prof. habil. dr. Aivaras KAREIVA (Vilniaus universitetas, gamtos mokslai, chemija, N 003);
Doc. dr. Jolanta ROUSSEAU (Artua universitetas, Prancūzija, gamtos mokslai, chemija, N 003);
Prof. dr. Eugenijus VALATKA (Kauno technologijos universitetas, technologiniai mokslai, chemijos inžinerija, T 005).

Disertacija bus ginama viešame Chemijos inžinerijos mokslo krypties disertacijos gynimo tarybos posėdyje 2022 m. rugsėjo 16 d. 10 val. Kauno technologijos universiteto studentų miestelio bibliotekoje, salėje M7.

Adresas: Studentų g. 48-M7, 51367 Kaunas, Lietuva.
Tel. (+370) 37 300 042; faks. (+370) 37 324 144; el. paštas doktorantura@ktu.lt

Disertacija išsiųsta 2022 m. rugpjūčio 16 d.
Su disertacija galima susipažinti interneto svetainėje http://ktu.edu ir Kauno technologijos universiteto bibliotekoje (K. Donelaičio g. 20, 44239 Kaunas).

TABLE OF CONTENTS

LIST OF ABBREVIATIONS 7
INTRODUCTION 8
1. LITERATURE REVIEW 12
1.1.Sources of heavy metals and their environmental impact..... 12
1.2.Classification, formation, and synthesis properties of different crystallinity calcium silicate hydrates compounds..... 14
1.2.1. Calcium silicate hydrates classification 14
1.2.2. Dicalcium silicate hydrates compounds formation and their synthesis properties 18
1.2.3. The influence of additives on the different crystal order of calcium silicate hydrates compounds formation 19
1.3.Adsorption..... 21
2. MATERIALS AND METHODS 27
2.1. Materials 27
2.2. Methods 28
3. RESULTS AND DISCUSSION 37
3.1. The adsorption peculiarities of heavy metals and the structure properties of A1 adsorbent 37
3.1.1. The adsorption capacity of A1 adsorbent for the Co^{2+} ions..... 37
3.1.2. The adsorption capacity of A1 adsorbent for the Cu^{2+} and Cr^{3+} ions.... 45
3.2. The adsorption peculiarities for heavy metals, the structure properties and microstructure parameters of A2 adsorbent 52
3.2.1. The adsorption peculiarities for heavy metals of A2 adsorbent 52
3.2.2. The structure properties and porosity of A2 adsorbent..... 57
3.2.3. Texture and microstructure parameters of A2 adsorbent substituted with Cu^{2+} ions 63
3.2.4. Texture and microstructure parameters of A2 adsorbent substituted with Co^{2+} ions 69
3.2.5. Texture and microstructure parameters of A2 adsorbent substituted with Cr^{3+} ions 75
3.3. Intercalation of Cu^{2+}, Co^{2+}, Cr^{3+} ions into the synthetic compounds under hydrothermal synthesis conditions..... 83
3.3.1. The synthesis of calcium silicate hydrates with incorporated Cr^{3+} ions 83
3.3.2. H-Cr sample texture and microstructure parameters in the temperature range 25–550 °C 88
3.3.3. The synthesis of calcium silicate hydrates with incorporated Cu^{2+} ions 91
3.3.4. H-Cu sample texture and microstructure parameters in the temperature range 25–600 °C 94
3.3.5. The synthesis of calcium silicate hydrates with incorporated Co^{2+} ions 97

3.3.6. H-Co sample texture and microstructure parameters in 25–550 °C temperature range 100
3.4. Application of poorly-ordered and well-ordered structure synthesized calcium silicate hydrates compounds in propanol oxidation reactions 103
3.5. Technological recommendations for the poorly-ordered and well-ordered structure calcium silicate hydrates compounds synthesis, adsorption, or thermal activation 108
4. CONCLUSIONS 111
5. SANTRAUKA 113
REFERENCES 137
CURRICULUM VITAE 149
LIST OF SCIENTIFIC PUBLICATIONS 150
ACKNOWLEDGMENTS 152
Appendix 1. Adsorbent A2 texture and specific surface area 153
Appendix 2. A2-750 texture and specific surface area 155
Appendix 3. H-Cr texture and specific surface area 158
Appendix 4. H-Cr550 texture and specific surface area 161

LIST OF ABBREVIATIONS

A1 adsorbent – well-ordered crystalline dibasic calcium silicate hydrates samples
A2 adsorbent – poorly-ordered amorphous/crystalline dibasic calcium silicate hydrates samples
A2-750 – A2 adsorbent calcinated at 750 °C temperature
A2-Co sample – A2 adsorbent with incorporated Co^{2+} ions during the adsorption
A2-Co750 sample – A2-Co sample calcinated at 750 °C temperature
A2-Cr sample – A2 adsorbent with incorporated Cr^{3+} ions during the adsorption
A2-Cr550 sample – A2-Cr sample calcinated at 550 °C temperature
A2-Cu sample – A2 adsorbent with incorporated Cu^{2+} ions during the adsorption
A2-Cu600 sample – A2-Cu sample calcinated at 600 °C temperature
AAS – atomic absorption spectrometry
CS – calcium silicate
C/S – the molar ratio of CaO and SiO_2
CSH – calcium silicate hydrate
C-S-H – semi-crystalline type compounds C-S-H(I) and/or C-S-H(II)
DSC – differential scanning calorimetry
EDX – energy dispersive X-ray spectrometry
FT-IR – Fourier-transform infrared spectroscopy
H-Co sample – sample with incorporated Co^{2+} ions during hydrothermal synthesis
H-Co550 sample – H-Co sample calcinated at 550 °C temperature
H-Cr sample – sample with incorporated Cr^{3+} ions during hydrothermal synthesis
H-Cr550 sample – H-Cr sample calcinated at 550 °C temperature
H-Cu sample – sample with incorporated Cu^{2+} ions during hydrothermal synthesis
H-Cu600 sample – H-Cu sample calcinated at 600 °C temperature
PFO – pseudo-first-order kinetic model
PSO – pseudo-second-order kinetic model
S_a – surface area
S_{BET} – the specific surface area of sample calculated by the BET equation
SEM – scanning electron microscopy
STA – simultaneous thermal analysis
TEM – transmission electron microscopy
TG – thermogravimetry
VOC – volatile organic compounds
w/s –ratio of liquid media (ml) and solid state material (g)
XRD – X-ray diffraction analysis
α-C_2SH – α-dicalcium silicate hydrate ($2CaO \cdot SiO_2 \cdot H_2O$)

INTRODUCTION

According to various sources, humanity is facing more than 15 environmental concerns, such as air, water, and soil pollution, global warming, health issues, and others. One of the major contributors to the global air pollution (denoted by the contribution to ozone and chemical smog) and human health is volatile organic compounds (VOCs, alkenes, alkanes, esters, alcohols, etc.). The main sources of these compounds are chemical and petroleum industry, pharmaceutical plants, etc. In addition, a large variety of VOCs are generated from the household products. There are many technologies for VOC neutralization: biological degradation, adsorption, ozonation, thermal treatment, and oxidation. Catalytic oxidation is one of the most common attractive ways to eliminate these compounds by converting them to CO_2 and H_2O at low temperature (200–500 °C). The conventional catalysts require precious metals (Pt, Pd, Au), which are expensive; therefore, the scientists are looking for new catalysts based on the transitional metals.

Calcium silicate hydrates (CSH) have been industrially produced as the main constituents for the heat insulating materials, building materials and artificial wood due to its high stability at high temperatures and fibrous crystal form. Moreover, due to the high adsorption capacity, CSH play important roles in many areas: in drug delivery, bone tissue engineering, adsorption of heavy metal ions, etc. It is known that dibasic calcium silicate hydrates have good adsorption properties for some metal ions. For this reason, the attention has been given to the mesoporous calcium silicate hydrates ($xCaO{\cdot}ySiO_2{\cdot}zH_2O$) or calcium silicates ($xCaO{\cdot}ySiO_2$) (these compounds can be synthesized by calcining calcium silicate hydrates or liquid and solid sintering of calcium- and silicon-containing material), which are adsorbents with high adsorption capacity and promising catalyst support. These compounds have the aforementioned properties and are chemically stable and able to disperse metal particles on the surface. In addition, calcium silicates and calcium silicate hydrates allow retaining the unique properties of metal ions and promoting catalytic activity.

Calcium silicate hydrates exist in nature, can be formed as the hydration product of Portland cement, or can be synthesized in $CaO\text{-}SiO_2\text{-}H_2O$ mixtures under hydrothermal conditions within the 100–350 °C temperature range. Usually, the preparation of catalysts supported with calcium silicates or calcium silicate hydrates involves three steps: (1) synthesis of calcium silicates or calcium silicate hydrates, (2) adsorption of metal ions, (3) calcination at a selected temperature (in order to achieve active metal oxides). In addition, it is possible to incorporate metal ions into the structure of calcium silicates and their hydrates during their synthesis. Such compounds with incorporated metal ions can be used as catalysts for ethanol conversion to butadiene, the synthesis of bisphenol F, and the oxidation of ketones and aldehydes. Unfortunately, there is a lack of information about the influence of metals on the formation, thermal stability, microstructure, and other properties of calcium silicates and their hydrates.

According to the literature data, some metal ions, such as sodium or potassium, have a positive effect on the reactivity of crystalline silicon-containing compounds by eroding their surface and promote the formation of calcium silicate hydrates. Different

results were obtained using aluminum oxide for the synthesis of dibasic calcium silicate hydrate at 200 °C, because this additive retarded the dissolution of portlandite and the formation of calcium silicate hydrates but stimulated the crystallization of calcium silicate. Cations, such as Al^{3+}, B^{3+}, and Be^{2+}, can change silicon in the silicon-oxygen tetrahedron, while others (Na^{+}, K^{+}, Fe^{2+}, Mn^{2+}, Ti^{2+}, Zr^{2+}, etc.) intercalate outside it. The later cations connect silicon-oxygen tetrahedrons to each other. Thus, the cations change the formation, thermal stability, microstructure, and other properties of calcium silicate hydrates and calcium silicates.

For these reasons, copper, cobalt, and chromium metal ions incorporation into the structure of calcium silicate hydrate by the adsorption or hydrothermal synthesis and their stability (or changes) of mineral composition was examined in detail. Meanwhile, after the investigation of CSH adsorption capacity for heavy metal ions, the microstructure and catalytic activity of synthetic and calcined products were determined.

The aim of the dissertation is to is to determine the adsorption kinetic parameters of synthesized poorly-ordered and well-ordered structure calcium silicate hydrates (CaO/SiO_2 = 1.5) samples for Cu^{2+}, Co^{2+}, and Cr^{3+} ions and evaluate their thermal stability as well as catalytic activity.

The objectives of the dissertation

1. to determine the adsorption capacity of poorly-ordered and well-ordered structure calcium silicate hydrates (CaO/SiO_2 = 1.5) samples for Cu^{2+}, Co^{2+}, and Cr^{3+} ions and describe these reactions using adsorption kinetic models;
2. to investigate the stability of adsorbents samples, substituted with Cu^{2+}, Co^{2+}, and Cr^{3+} ions, at 25–1000 °C temperature in the air environment;
3. to evaluate the effect of Cu^{2+}, Co^{2+}, and Cr^{3+} ions under hydrothermal conditions on the mineral composition and structure stability of calcium silicate hydrate (CaO/SiO_2 = 1.5) sample;
4. to investigate the possibilities of the best synthetic and calcined calcium silicate hydrates adsorbents samples application for the adsorbents-catalysts production and prepare technological recommendations for the production.

Statements presented for the defense

1. Synthesized poorly-ordered and well-ordered structure calcium silicate hydrates (CaO/SiO_2 = 1.5) samples have a high adsorption capacity (25–100 mg/g) of heavy metal ions;
2. Pure and substitute with Cu^{2+}, Co^{2+}, and Cr^{3+} ions calcium silicate hydrate (CaO/SiO_2 = 1.5) samples are mesoporous materials and have a large specific surface area (> 68 m^2/g).

Scientific novelty of the research

1. It has been proved that different quantity (25–100 mg/g) of Cu^{2+}, Co^{2+}, and Cr^{3+} ions can be incorporated into the structure of poorly-ordered phases of calcium silicate hydrates (CaO/SiO_2 = 1.5) samples under hydrothermal treatment conditions.

2. Synthesized, controlled specific surface area chemisorbents samples substituted with Cu^{2+}, Co^{2+}, and Cr^{3+} ions are stable till 550–750 °C, while at higher temperature, the formation of CuO, Co_3O_4, and Cr_2O_3 proceeded.

Practical significance of the scientific research

Synthesized poorly-ordered and well-ordered phases of calcium silicate hydrates (CaO/SiO_2 = 1.5) samples can be used as chemisorbents for Cu^{2+}, Co^{2+} and Cr^{3+} ions removal in the adsorption processes. It has been proved that the mentioned metal ions from the liquid solution can be incorporated into the calcium silicate hydrates samples under hydrothermal treatment conditions. Synthesized and calcined samples substituted with Cu^{2+}, Co^{2+}, and Cr^{3+} metal ions can be used as materials for the catalytic applications for propanol oxidation reactions, because at temperatures lower than 175 °C, the compounds act as adsorbents, while at higher temperatures, the catalytic oxidation proceeds.

Approval and publication of the research results

The results of the research were presented in 4 scientific publications in journals indexed in the Web of Science with Impact Factor (JCR SCIE): 1 of them published in *Buildings*, 1 in *Journal of Thermal Analysis and Calorimetry*, 1 in *Desalination and Water Treatment*, and 1 in *Nanomaterials*. The results of the dissertation have been reported in 5 international conference proceedings or abstracts: "5th Central and Eastern European conference on thermal analysis and calorimetry (CEEC-TAC5) and 14th Mediterranean conference on calorimetry and thermal analysis (Medicta 2019)" (2019, Italy), "Open readings 2019: 62nd international conference for students of physics and natural sciences" (2019, Lithuania), "Advanced materials and technologies" (2019, Lithuania), "6th Central and Eastern European conference on thermal analysis and calorimetry (CEEC-TAC6) and 15th Mediterranean conference on calorimetry and thermal analysis (Medicta2021)", and in one national conference "Technorama" (2019, Lithuania).

Contribution of the author and co-authors

The author synthesized and described all calcium silicate hydrates mentioned samples in the thesis, examined the adsorption, calcination, and catalytic properties of the synthesized compounds, and performed kinetic research and BET calculations. Kęstutis Baltakys advised on the possibilities of calcium silicates formation during the hydrothermal synthesis and the progress of the experiment and preparation of the manuscripts. Tadas Dambrauskas consulted on the thermal activation properties of compounds and calculation of adsorption kinetics. Anatolijus Eisinas together with Kęstutis Baltakys advised on the technological recommendations. Andrius Jaskūnas consulted about the adsorption and catalytic processes.

Structure and contents of the dissertation

The dissertation consists of an introduction, literature review, experimental part, results and discussion, conclusions, a list of references, a list of publications on the

topic of the dissertation, and appendices. The list of references includes 192 bibliographic sources. The main results are discussed in 164 pages and illustrated in 20 tables and 72 figures.

1. LITERATURE REVIEW

1.1. Sources of heavy metals and their environmental impact

The fast economic growth, increasing human population, and industrial development generate high waste globally [1, 2]. According to various sources, the total wastewater amount generated in the World is equal to 390–500 km^3 per year [3]. Most of it is produced by agriculture and industry. These usually toxic wastes may include various industrial pollutants, such as organic and inorganic compounds, heavy metals, or petroleum products [4, 5]. The pollution of surface and groundwater with heavy metals is recognized as an important environmental problem, causing danger to life and health. According to the Korte aggregate index, which shows danger to life, health, and heredity, heavy metals are among the first ecological problems, because of exposure to chemical fertilizers, consequences of oil spills, pesticides, acid rain [6]. Heavy metals are persistent pollutants: they do not decompose, but only travel from one ecological niche to another, threatening poorly defined consequences. The individual dangerous chemical pollutants as well as their combined synergistic effect are dangerous [7, 8]. The sources of pollution of toxic chemical elements and other compounds that are entering the environment with them are the most diverse and are presented in Table 1.1.

Table 1.1. Anthropogenic sources of heavy metals [9]

Sources of pollution	Detected heavy metals
Metal processing (manufacture of machine tools, machines, tools, auxiliary repair shops, and bars for cars and other devices)	Virtually, all elements are detected, but mainly: molybdenum (Mo), cobalt (Co), nickel (Ni), vanadium (V), chromium (Cr), tungsten (W), barium (Ba), manganese (Mn), boron (B), niobium (Nb), titanium (Ti), arsenic (As), yttrium (Y), ytterbium (Yb), scandium (Sc), gallium (Ga)
Electric, radio, telephone, household appliances manufacturing and repair companies	Copper (Cu), zinc (Zn), lead (Pb), silver (Ag), cadmium (Cd), mercury (Hg), tin (Sn)
Galvanic	Nickel (Ni), zinc (Zn), copper (Cu), cadmium (Cd), chromium (Cr), cobalt (Co) vapor
Coal-fired stoves	Arsenic (As), boron (B), molybdenum (Mo), nickel (Ni), silver (Ag), gallium (Ga), barium (Ba), scandium (Sc)
Printing houses	Zinc (Zn), lead (Pb), tin (Sn), cadmium (Cd), copper (Cu)

For example, copper (Cu) is widely used in various industries, such as fertilizers, plant protection, electronics, pharmaceuticals, textiles, or paints [10]. However, this metal is as well a naturally occurring trace element in many organisms, both plant and animal, and is a component of essential processes, such as photosynthesis and respiration. Excessive accumulation of copper in the soil, and later in the roots and

leaves, causes various metabolic disorders in plants, restricts growth and development by damaging DNA and reducing the processes involved in photosynthesis. Cu compounds cause nasal congestion, gastritis, diarrhea, and toxic symptoms, such as chronic lung injury [11, 12].

Cobalt (Co) is used in a variety of industries, such as mining, electronics, catalysts, alloys, planting, pigments, and steel, and is essential for the synthesis of vitamin B12 in biological systems [13]. Due to the widespread use, Co can be found in water bodies and sediments that usually are released from the manufacturing prices with little or no raw treatment and in high concentrations. Cobalt industrial waste that is removed without pretreatment causes physical and chemical interactions with organic (humic and fulvic acids) and inorganic soil constituents (minerals) [14, 15].

Chromium (Cr) is one of the most common heavy metals on earth. It is known as the fourth major toxic metal after mercury, lead, and cadmium. Exposure to chromium can lead to serious illness, such as vomiting, stomach ulcers, diarrhea, liver congestion, and kidney failure [16]. In addition, it is a strong carcinogenic agent that alters the process of DNA transcription and causes important chromosomal aberrations. In general, Cr is widespread in wastewater, resulting from chromium plating, pigment production, skin tanning, corrosion control, and stainless steel production [17].

The maximum level of heavy metal in soils has to be not harmful to the human health by indefinite or even lifetime exposure to plants, water, air and does not directly or indirectly affect heredity. Based on the Lithuanian hygiene norm, the maximum allowable heavy metals concentrations are defined in Table 1.2 [18]. According to this order, the users of soil resources must not pollute soil with household, production, construction and other waste chemicals that are hazardous to the human health and environment, preserve, and increase the soil fertility. Illegal activities that have polluted or otherwise caused damage to the soil must compensate it, clean up the contaminated soil, and restore soil fertility in accordance with the procedure established by the legal acts [18].

Table 1.2. Maximum levels of dangerous substances [18]

Name of the substance	Maximum allowable concentration, mg/kg
Chrome (Cr)	100
Zinc (Zn)	300
Mercury (Hg)	1.5
Cadmium (Cd)	3
Cobalt (Co)	30
Manganese (Mn)	1500
Nickel (Ni)	75
Lead (Pb)	100
Copper (Cu)	100
Potassium chloride	500

It is worth mentioning that the listed pollutants are highly soluble in aquatic environments; thus, it can be absorbed by the living organisms and may accumulate in the human body [8, 19]. For this reason, heavy metals should be prevented from

reaching the natural environment. In order to remove pollutants from the water systems, the conventional technologies, such as chemical precipitation, ion exchange, electrochemical treatment, coagulation, foam flotation, filtration, aerobic and anaerobic treatment, solvent extraction, activated sludge, adsorption, etc., are used [20, 21]. Among these techniques, adsorption offers flexibility in design and operation, and in many cases, it generates high quality treated effluents. In addition, mineral, organic, or biological origin zeolites and others materials with high surface area can be used as adsorbents [22, 23]. However, these adsorbents often have low adsorption capacity, poor regeneration (metal ion removal), and short lifetime. Due to the poor adsorbent properties, adsorption becomes expensive and economically useless. Therefore, the researchers are investigating new, promising adsorbents [24, 25]. For this reason, the attention has been paid to the mesoporous calcium silicates or calcium silicate hydrates, which are promising adsorbents. These compounds can be easily synthesized from inexpensive starting materials, are chemically stable, and have a high adsorption capacity.

1.2. Classification, formation, and synthesis properties of different crystallinity calcium silicate hydrates compounds

1.2.1. Calcium silicate hydrates classification

Compound formed under hydrothermal conditions, i.e., calcium silicate hydrate (CSH), is a salt of silicic acid. The relationship between their constituent components can be expressed with the general formula of CSH:

$$xCaO \cdot ySiO_2 \cdot pH_2O;$$

where x, y, p are the number of moles [26, 27].

CSH is an important group of silicate minerals, ranging from amorphous to crystalline compounds with various compositions in a wide range of C/S ratios between 0.44–3.0 [27]. Both indicators have a decisive influence on the strength and durability of articles. More than forty CSH are known, some of which are found in nature, mostly in combination with volcanic calcium rocks [28]. Mainly calcium silicates are formed during the autoclaving of products or in the production of thermal insulation materials. Various parameters influence the synthesis of calcium silicates: reaction time, temperature, composition of the mixture, dispersity, and nature of raw materials, mixing intensity, water to solids ratio in the suspension. It should be noted that the above-mentioned parameters affect the synthesis process and the microstructure of products [29, 30].

The symmetric properties of the structural elements (atoms, molecules) of CSH crystals have been explained by using Order–Disorder theory. It has been claimed that it is possible to determine the accurate structures of tobermorite, reyerite, gyrolite, truscottite, and other group minerals [31, 32]. The structures of these CSH were found to consist of similar main layers with calcium and silicon components. It should be noted that not all CSH structures have been studied; thus, there is no perfect CSH classification [33, 34]. Currently, the most widely accepted is the classification proposed by H. F. W. Taylor and R. M. Roy, which is supplemented by new data of

I. G. Richardson [27]. According to this classification, CSH is distributed into wollastonite, tobermorite, jennite, gyrolite, γ-Ca_2SiO_4, and other CSH grope.

The wollastonite group includes nekoite, okenite, xonotlite, foshagite, hillebrandite, wollastonite 1A, pectolite [27]. The most important and most practical compound in this group is xonotlite. This compound is formed under natural conditions and hydrothermally cured silicate articles and influences their strength properties [35, 36]. Due to its unique porous structure and low density, heat-insulating panels, ceramics, or sorption processes are produced from xonotlite [37]. Their linear shrinkage at 1000 °C temperature does not exceed 2%. Wollastonite group minerals have lengths of approximately 2 μm and widths between 100 and 500 nm. This group of particles reminds a lath-shape [22, 23, 38] and needle-like micro-fibers (Fig. 1.4) [39].

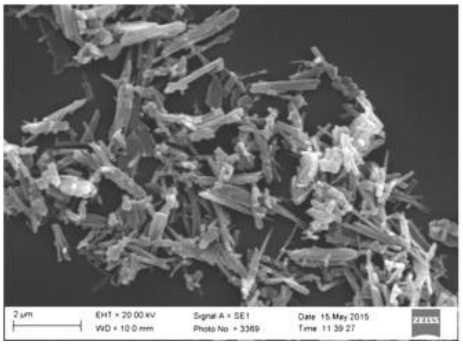

Fig. 1.4. SEM images of xonotlite [39]

Xonotlite can be synthesized under hydrothermal conditions at 190–400 °C temperature, when the molar ratio of the initial mixture is C/S = 1. Increasing the synthesis temperature significantly shortens the crystallization time of xonotlite. Using a mixture of tetraethyl orthosilicate and $Ca(OH)_2$, xonotlite can be synthesized at 180 °C in a saturated water vapor environment. This compound remains stable up to 710 °C temperature, and at 750–800 °C temperature, it recrystallizes to β wollastonite [27, 40]. Under the same conditions, xonotlite can be synthesized by using carbide slurry at 800–1000 °C temperature before the synthesis. It has been found that the temperature and duration of hydrothermal treatment that is required for the synthesis of this compound can be significantly reduced when $Na_2SiO_3 \cdot 9H_2O$ and $Ca(NO_3)_2 \cdot 4H_2O$ are used for the synthesis, and the conventional autoclaving is replaced by microwave synthesis. In this case, pure xonotlite is obtained after 90 min. at 180 °C temperature [41].

The tobermorite group includes 1.4 nm tobermorite, 1.1 nm tobermorite, 1.13 nm tobermorite, 0.93 nm tobermorite, clinobermorite, 0.9 nm clinobermorite, Oyelite, C-S-H (I) (when C/S ≤ 1.5) [27].

Tobermorite compounds are the main minerals formed in industrial silicate products, and 1.13 nm tobermorite is an important component of various construction products. Tobermorite gel and semi-crystalline tobermorite are formed under natural conditions by the hardening of Portland cement and determine the strength, durability, and other key performance characteristics of the cement stone. In addition, these

calcium silicate hydrates can be used as fillers, pigments, adsorbents in rubber, paper, and other industries [42, 43]. Tobermorite group compounds could be synthesized in the range of 0.1–100 μm, and the shape of products could remind typical needle-like fibers (Fig. 1.5) [44].

Fig. 1.5. SEM images of tobermorite [44]

The chemical composition, conditions of formation, and stability of 1.13 nm tobermorite have been studied in detail and confirmed by thermodynamic calculations [40, 45]. When the molar ratio of the starting mixture is C/S = 0.73 and 0.83, 1.13 nm tobermorite dominated in the synthesis products. At 175 °C temperature, 1.13 nm tobermorite recrystallizes to xonotlite.

The jennite group includes jennite, metajennite, C-S-H (II) [27]. The first two structures are close to the poorly crystallized calcium silicate hydrate formed during the hardening of Portland cement. C-S-H (II) is formed during the hydration of tricalcium silicate in a cement stone and has a nanostructure characteristic of jennite. These compounds have different diameters giving a wide range between 10 and 300 μm. The structure of jennite compounds usually resembles a honeycomb structure [46, 47].

The gyrolite group includes gyrolite, truscottite, reyerite, Z-phase, fedorite, K-phase [27, 48]. In recent years, there has been a growing interest in gyrolite as a new field of application has been found, i.e., chromatography, it can be used as an adsorbent. Gyrolite absorbs heavy metals well, and the used adsorbent can be disposed of as an additive to the ordinary Portland cement. Heavy metals do not leach or promote ordinary Portland cement hydration [49, 50]. The particles of gyrolite mainly consist of a plate shape structure (Fig. 1.6) [27, 51].

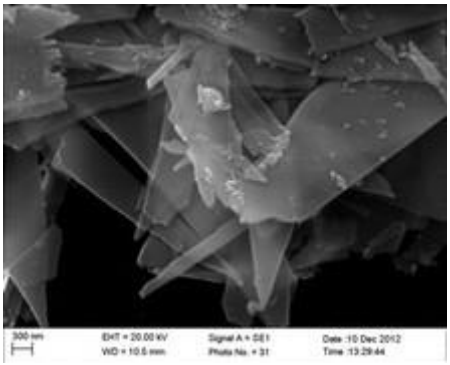

Fig. 1.6. SEM images of pure gyrolite [51]

It has been thought that gyrolite forms only at temperatures above 120 °C, because at lower temperatures, a semi-crystalline C-S-H gel without a clear crystal structure is obtained. The studies have shown that this compound is stable in the presence of saturated water vapor at temperatures from 120 °C to 200 °C and the formation of truscottite at temperatures above 200 °C. Several literature sources suggest that gyrolite can be synthesized as well at 270 °C temperature [27, 40].

The group of γ-Ca_2SiO_4 includes γ-C_2S hydrate, kilchoanite, calcium chondrodite [27]. γ-Ca_2SiO_4 is one of the five strains of dicalcium silicate. This compound is undesirable in Portland cement clinker, because it is almost hydraulically nonreactive [52]. CSH of this group is formed only under hydrothermal synthesis conditions [53].

The research has shown that the addition of Na_2O and very intensive milling (2000 rpm) can significantly increase the hydraulic activity of γ-Ca_2SiO_4 [52]. It has been found that γ-Ca_2SiO_4 can be synthesized under hydrothermal conditions using intensive heating [53]. In this case, the reaction capsules are isolated from the water vapor during the rising period. The required product is obtained from the initial mixtures with a C/S ratio in the range 1.5–3 by hydrothermal treatment at 220 °C temperature. According to the other authors, γ-Ca_2SiO_4 can be obtained by hydrothermal treatment of a stoichiometric reagent mixture (C/S = 2) at 100 °C for 8 h and calcinating the resulting product at 1450 °C for 2 h [54].

Other CSH includes 0.315 nm phase, suolunite, rosenhahnite, killalaite, afwillite, α-C_2S hydrate, dellaite, Y-phase, C_3S hydrate, cuspidine, jaffeite, poldervaartite, tilleyite. Many of these compounds are less significant in the chemistry of cement and binders. In industrial products, they form only α-C_2S hydrate that is used in the production of silicate cement [27]. This compound is not found as a natural mineral. α-C_2S hydrate has the lowest degree of polymerization, i. e., the structure is dominated by insulated silicate tetrahedra. α-C_2S hydrate crystals are orthorhombic, which crystallize in the form of rectangular plates (200 × 50 × 10 μm) (Fig. 1.7) [55].

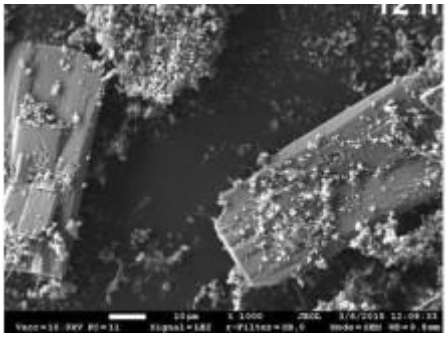

Fig. 1.7. SEM images of α-C_2S hydrate [55]

Other minerals that are formed under hydrothermal conditions include scawtite, fukalite, rustumite, bicchulite, katoite hydrogarnet [27].

CSH has a wide range of uses due to its very high water absorption capacity, fine particle size, and low bulk density, large specific surface. It could be used as alternative cementation material or a carrying agent for pesticides and similar powdered materials. It can be used as an anti-caking and free-flow agent in chemicals, adhesives, battery separators, brake linings, paint primers, paper, plasticized PVC, plastisols, polishes, printing inks, sealants and mastics, tableting and pelletizing, textiles, and thermal insulation [56–59].

1.2.2. Dicalcium silicate hydrates compounds formation and their synthesis properties

Dicalcium silicate hydrates are important in binder chemistry, adsorption, i.e., hillebrandite, α-C_2S hydrate, and γ-C_2S hydrate [60].

α-C_2S hydrate is not found as a natural mineral, and in a saturated water vapor environment, in the $CaO\text{-}SiO_2\cdot nH_2O\text{-}H_2O$ system [61]. The latter dibasic CSH is known to form via the intermediate C-S-H (II), and it remains stable in the system even in small amounts of unreacted parent compound, containing a CaO component. In the presence of excess SiO_2, the α-C_2S hydrate recrystallizes to the lower base CSH.

α-C_2S hydrate is formed under hydrothermal synthesis conditions at 95–200 °C temperature. In addition, this dibasic CSH is formed during hydrothermal treatment (150–200 °C) in dense autoclaved and silicate articles with a molar C/S ratio of close to 2.0 [62]. It has been found that the synthesis of α-C_2S hydrate at 150 °C is inefficient because even after 16 hours of hydrothermal treatment, a large amount of unreacted portlandite remains. In addition, it was determined that the temperature of the hydrothermal treatment influences the mineral composition of the synthesis products, because at 175 °C temperature, after 16 h, the synthesis products are dominated by α-C_2S hydrate with portlandite. At 200 °C temperature, the hilebrandite and portlandite were identified in the synthesis product. The research shows that the starting materials react faster when the suspension is mixed [63, 64].

The other research investigated Lithuanian rocks for the CSH synthesis. It has been found that α-C_2S hydrate can be synthesized from natural rock mixtures with a molar C/S ratio of 2 [63, 65]. The investigation stated that the hydrothermal synthesis

of α-C_2S hydrate at 175 °C and 200 °C temperatures in opoka and chalk pure mixtures is economically inefficient, because the starting raw materials react slowly, and the amount of α-C_2S hydrate that is formed increases slowly. Meanwhile, in the stirred suspensions at 200 ºC temperature, α-C_2S hydrate was identified after 2 hours of hydrothermal treatment, and after 4–8 h, the unreacted portlandite remains ~2%. It should be noted that the researchers mentioned above as well studied the formation of α-C_2S hydrate during the hydrothermal synthesis in stirred suspensions at 200 °C temperature in a mixture of limestone and quartz sand. The starting materials were found to react slowly; thus, the Na_2O additive was used, which accelerated the dissolution of quartz, and α-C_2S hydrate became the predominant compound in the synthesis products only after 8 hours of hydrothermal treatment.

α-C_2S hydrate does not have cementitious properties, but it increases the durability and frost resistance of the products. This CSH is slowly carbonized, and the strength of the samples increases during the carbonization. During the carbonization, α-C_2S hydrate crystals do not decompose, only their volume increases [40]. It has been found that calcinated α-C_2SH recrystallizes to anhydrous calcium silicates (CS), which may have hydraulic activity. Five varieties of Ca_2SiO_4 or C_2S are known to exist: α, $\acute{\alpha}_H$, $\acute{\alpha}_L$, β, and γ. The scheme of its polymorphism is as follows [66, 67]:

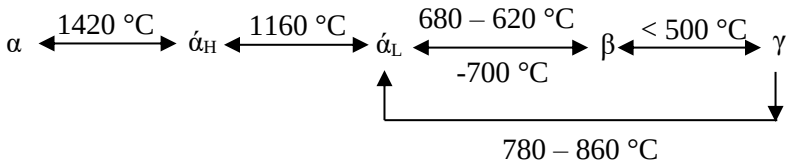

The γ variety is stable under normal conditions but has no hydraulic activity. However, β variety is unstable at room temperature but is hydraulically active. From the α varieties, $\acute{\alpha}_L$-C_2S is the most hydraulically active. These three varieties differ in the heat value of formation. Unlike β-C_2S and $\acute{\alpha}_L$-C_2S crystals, γ-C_2S crystals have calcium atoms that are arranged neatly in the crystal planes, and most of their orbitals are filled, resulting in much more excellent stability [67, 68].

1.2.3. The influence of additives on the different crystal order of calcium silicate hydrates compounds formation

The ions of many chemical elements can intervene in the crystal structure of calcium silicate hydrate. The effectiveness of each additive may vary depending on the properties of raw materials that are used, the synthesis process regime, and other factors. It has been noted that additives that are containing sodium [69, 70] or aluminum [71, 72] ions have a more profound effect on the CSH formation. The influence of other elements on the synthesis and properties of CSH is less significant [69, 73, 74].

The effect of additives is most extensively studied in low base CSH. For example, it has been found that the influence of SO_4^{2-} at 200 °C temperature with a C/(Si + S) ratio of 0.66 (corresponding to gyrolite) at the beginning of the synthesis initiates the formation of poorly crystalline Assarsson's Z-phase. Prolonging the hydrothermal synthesis, the formed compound recrystallizes into well-ordered

gyrolite and anhydrite [75, 76]. It should be noted that the recrystallization from C-S-H (primary C/S ratio 0.83) into tobermorite is accelerated by the SO_4^{2-} at 175 °C when S/(Si + S) ration is 0.02 and at 200 °C when S/(Si + S) ration is 0.0125 [77]. It has been determined that sulphate can stabilize tobermorite at 100 °C, which is much lower than the temperature that is generally used to synthesize tobermorite [76].

In another study, the CdO and CuO additive influence on the CSH formation and structure was investigated [78]. The CdO and CuO was incorporated in the crystalline structure of the CSH during the hydrothermal treatment at 200 °C, when the C/S ration was equal to 0.55, and the concentration of metal oxide was 2.27% of the mixture. It has been revealed that CdO became unstable and intercalated into the structure of the gyrolite gel and Z phase after 24 h of hydrothermal synthesis. It should be noted that in the same thermal treatment condition, the CuO did not interact into the structure of products. It has been determined that CdO incorporation in CHS increased its specific surface area SBET from 28.11 m^2/g to 39.91 m^2/g [78].

Meanwhile, there are some different effects of K^+ and Na^+ ions influence on the CSH structure stability. There are literature data [79] that state: when using Na_2SiO_3 as siliceous materials (Na/Si ration = 2) to synthesize xonotlite at 225 °C (CaO/SiO_2 ration = 1), only pectolite is observed in the samples. It should be noted that in the same conditions, only using K_2SiO_3 xonotlite is formed as the main crystalline phase. Furthermore, when Na_2O is added to the system with K_2SiO_3, xonotlite persists up to 5 wt% of Na_2O, while at high Na_2O contents, xonotlite is gradually replaced by pectolite [80]. Na^+ easily incorporated into the structure of low basicity, poorly crystalline C-S-H, and tobermorite [81]. When the Al^{3+} ions are incorporated, the bridging sites of SiO_4 chain can increase the content of bound Na^+, as the charge deficit due to the replacement of Si^{4+} with Al^{3+} that can be balanced by binding monovalent Na^+ or K^+ ions [76, 81]. The intercalation of Al^{3+} ions could increase the formations of tobermotite at 190 °C, when the duration of synthesis is 12 h [82]. In addition, Al as well influences the morphology of tobermorite. CSH that was formed before tobermorite formation could become destabilized by Al^{3+} ions. This means that the barrier to tobermorite crystallization could be diminished by Al [76].

The influence of Fe incorporation in CSH is not widely investigated, because Portland cement usually contains 2–5 wt% of iron. There are literature data that reported that added Fe in the primary CSH synthesis products could form a small amount of tobermorite at 175 °C after 4 h of autoclaving. Prolonging synthesis duration to 16h, tobermorite crystallinity could be increased, characterized by improved silicate chain polymerization and chain cross-linkage. For this reason, the morphology of tobermorite conversion would change from a typical platy shape to a fiber shape [83]. According to the researcher, during hydrothermal synthesis at 345 °C temperature and using steel slag, Fe hydrogarnet was formed as the main product in the C/S system. When the SiO_2 was added to the system to reach a molar rate of 0.8, the main synthesis product was observed, i.e., Fe-substituted tobermorite with an incorporated amount of Fe around 10–15 wt% [84]. It has been determined that Fe^{3+} ions occupied the tobermorite microstructure and took the position of the interlayer Ca^{2+} without losing CHS characteristic crystallinity [85]. Depending on the chosen

method of product synthesis, these compounds can be used in adsorption processes. Currently, the most relevant studies of CSH adsorption capacity are investigated.

α-C_2SH has been identified by several different authors as the major product of C_3S hydration in the 130–200 °C temperature range [86]. Interesting results have been obtained using the addition of fly ash, which differed in the C/S ratio to the cement. With a ratio of 0.3 to 0.7, α-C_2SH was the predominant product in all samples after 1 day of hydrothermal treatment at 180 °C temperature. It should be noted as well that after the addition of 35% finely divided SiO_2 to the cement, this compound only begins to dominate after 25 days of hydrothermal treatment at 180 °C. Other authors have shown that α-C_2SH is formed after 2 h hydration of cement dough at 130 °C [87]. The addition of calcium gluconate or sodium phosphonate (0.1%) promotes the formation of the α-C_2SH compound. α-C_2SH is relatively easily formed under hydrothermal conditions from CaO and silicic acid as the starting materials at 150–200 °C temperature [88]. The authors as well note that the addition of Al^{3+} in mixtures with amorphous SiO_2 promotes the formation of α-C_2SH and inhibits its recrystallization to hilebrandite. However, the literature concerning the influence of additives on the hydrothermal synthesis of CSH, which CaO/SiO_2 ratio = 1.5–2, is scarce.

1.3. Adsorption

Adsorption and desorption of reactants are very important phenomena and are found in most catalytic processes. Due to the higher concentration of substances (or partial pressure p) in the medium, the adsorbate concentrates at the surface of the adsorbent–adsorption takes place. According to the physicochemical classification, adsorption processes are classified as the distribution of the components between the volume phase and the surface layer. This process can be initiated by physical forces or a chemical reaction between the adsorbent and the adsorbate [89–91]. The chemical reaction can occur in the same way as the chemical bonding of atoms or molecules or ion exchange. According to the nature of the interaction between the adsorbent and the adsorbate, the adsorption is divided into [92]:

1. Physisorption (physical adsorption),
2. Chemisorption (chemical adsorption).

The simplest form of adsorption is physical adsorption or molecular adsorption. Physical adsorption is caused by Van der Waals forces between the adsorbent and the adsorbate. It is characterized by reversibility: the adsorbed molecules detach from the surface of the adsorbent and return to the surrounding space, i.e., desorption occurs. At the beginning of the process, the adsorption rate is higher than that of the desorption, but gradually, the adsorption slows down, and the desorption accelerates. At some point, the velocities of both processes equalize, and the adsorption equilibrium is reached. A high rate characterizes the physical adsorption. As the temperature (or the pressure) increases, the adsorption decreases as the increased thermal motion accelerates the desorption [93].

Chemical adsorption is based on the chemical interactions, is irreversible, and the adsorbed material may differ from the desorbed in the presence of strong chemosorption [94]. In addition, this method is used to select compounds for some

classes. During chemosorption, the structure of the starting materials usually changes. Chemosorption increases with increasing temperature. Chemical adsorption, like chemical reactions, requires some activation energy, which is called activated adsorption.

It is sometimes challenging to distinguish chemosorption from the physical adsorption. These difficulties can be absorbed when chemosorption is weak and between the physical and chemical interactions. The interaction forces in physical and chemical adsorption are different, which is evident when comparing the thermal effects of these processes (heat of adsorption). In physical adsorption, this effect does not exceed 100 kJ/mol and is close to the heat of gas condensation and chemical adsorption: the heat of chemical compound formation reaches more than 100 kJ/mol. Chemical adsorption occurs at a low rate, which increases at higher temperatures. It can as well occur at high temperatures where physical adsorption is very low. It should be noted that there are cases when activated adsorption is reversible. Such issues are significant for heterogeneous catalytic reactions.

Table 1.3. Comparison of physical and chemical adsorption [93]

Physical adsorption	**Chemical adsorption**
Thermal effect (heat of adsorption) is no more than 100 kJ/mol	The high heat of adsorption is more than 100 kJ/mol
Van der Waals forces dictate	Chemical forces cause
Reversible process	Irreversible process
No activation energy required	Activation energy required
High pressure is a positive factor that reduces desorption	High pressure is a positive factor, but desorption does not occur when reduced
It takes place in the polymolecular layer	It takes place in the monomolecular layer
It occurs at low temperatures and decreases with increasing temperature	It takes place at high temperatures
Limited specific process	Specific process
Adsorption energy 8–34 kJ/mol	Adsorption energy up to 840 kJ/mol

The type of adsorption depends on the following factors:

- Adsorbent activity;
- The nature of the adsorbate and adsorbent;
- Adsorbent surface area;
- Experimental conditions (temperature, pressure, etc.).

The potential energy curves (Fig. 1.1) for physical adsorption and chemosorption are presented below [95]. The energy minimum (A) of physical adsorption is higher than for the chemosorption (B), and the equilibrium of physical adsorption (r1) will always be higher than for the chemosorption (r2). Curves 1 and 2 are separated by an energy barrier, the activation of which requires activation energy. In most cases, chemosorption is an exothermic process (although sometimes, when forming adsorbent surfaces for complex intermediates, the overall thermal effect of the process may appear before).

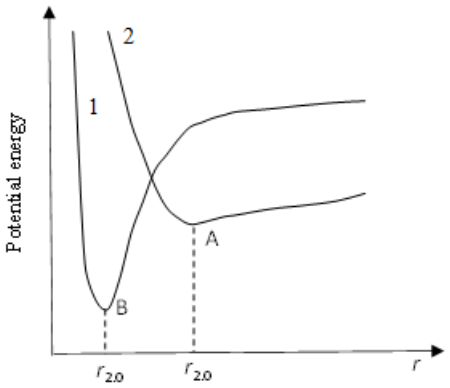

Fig. 1.1. Potential energy curves for physical (1) and chemical (2) adsorptions [95]

It is very important to distinguish chemosorption from a physical adsorption by experimental data, and this can be done, according to the following process features [95]:

1. According to the thermal effect of the process. Physical adsorption is characterized by low (2–6 kcal/mol for molecules and 10–20 kcal/mol for complex) thermal effect and chemical adsorption by high (20–100 kcal/mol) thermal effect. In both cases, the heat of adsorption depends on the degree of filling the adsorbent with the adsorbate.

2. According to the adsorption rate. Physical adsorption occurs rapidly with virtually no activation energy, whereas chemosorption is characterized by the activation energy that is close to the reaction and is slow.

3. According to the temperature range. Physical adsorption takes place close to the boiling point of the adsorbate, while chemical adsorption takes place at much higher temperatures.

4. According to the reversibility of the process. Physical adsorption is an equilibrium process that equilibrates very quickly and is a reversible process. Chemosorption can be both equilibrium and irreversible. At very high temperatures, reversible chemosorption processes can occur.

5. According to the process selectivity. Physical adsorption is nonspecific: vapors and gases are adsorbed on various adsorbents, although the adsorption capacity depends on the nature of the adsorbent and the adsorbent. In contrast, chemosorption is specific: it occurs only when the adsorbate and the adsorbent can form a chemical bond.

There are other criteria to distinguish physical adsorption from chemosorption. One of the most important is the charge formed on the surface during the year of chemosorption.

The dependence of the amount of adsorbed substance on its partial pressure is shown by the adsorption isotherms [96, 97]. The form of the isotherms depends on the adsorbent and the adsorbate parameters (specific surface structure, chemical

nature). The IUPAC guidelines divided the adsorption isotherms into six types [98] (Fig. 1.2).

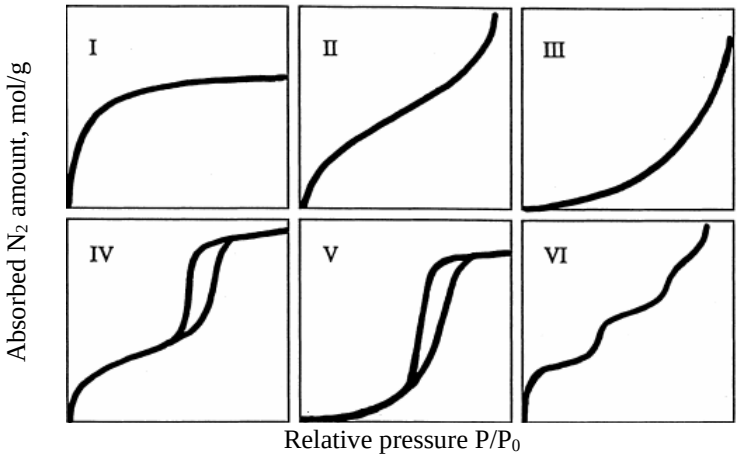

Fig. 1.2. Classification of adsorption isotherms [99]

This classification was proposed by Brunauer, Emmet, and Teller and named BET Theory [97, 100]. Type I isotherms are characteristic of microporous materials with relatively small external surface area values (e.g., activated carbon, molecular zeolite sieves, porous oxides). The compounds with this type of isotherms have predominantly narrow micropores, wider pore size over a range of 1–2.5 nm [101]. Type II and Type III isotherms are characteristic of non-porous and macroporous materials and solids [101]. Type IV isotherms are mesoporous adsorbents, such as many oxide gels, industrial adsorbents, and molecular sieves [99, 101]. The interaction between adsorbent and adsorbate determines the adsorption process in mesoporous materials, thus the interaction between the condensed molecules. In this case, after single-molecular and multi-molecular, the formation of layers on the walls of mesopores (having the same curve as the corresponding part of the type II isotherm) is followed by gas condensation in the pores. Type V isotherms are observed when the water is adsorbed on hydrophobic micro- and mesoporous adsorbents [102]. The reversible gradual type VI isotherm is characterized by adsorption layer by layer on a very smooth, non-porous surface [100]. In this case, the height of the step indicates the capacity of each adsorbed layer, and the sharpness of the angle depends on the system and temperature [101].

Origin and classification of hysteresis loops

Hysteresis loops are formed in the multimolecular layer and are usually associated with adsorbate condensation in pores and adsorption metastability. Based on the IUPAC classification, six main types of hysteresis loops are distinguished (Fig. 1.3).

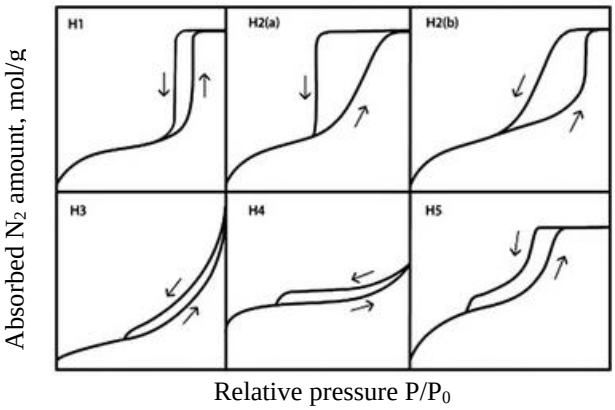

Fig. 1.3. Classification of hysteresis loops [99]

The H1-type hysteresis loop is characteristic of materials with cylindrical pores or spherical particles of similar size. In this case, the effect of the pore network is minimal, and the upright, narrow loops are a clear sign of delayed condensation in the adsorption portion. In addition, H1-type hysteresis loops can be in the bottle neck-shaped pore networks where the diameters of the channel (neck) and the pores are similar. This type of hysteresis loops is characteristic of structured silicas, controlled-pore glasses, and neatly arranged mesoporous carbons [103].

The H2 (a) hysteresis loop is triangular with a straight desorption branch. The loops of this type are typical of materials with a predominance of disordered bottle neck-shaped pores (i.e., different size and distribution); thus, the effect of the pore network is vital for type H2 (a) hysteresis. The very steep part of the desorption can be attributed to the pore blocking in a narrow range of pore necks or cavitation-induced evaporation. H2 (a) type hysteresis loops feature many silica gels, some porous glasses. There, the H2 (b) type loop is as well associated with pore blocking, but the distribution range of the pair neck widths is much more extensive. Hysteresis loops of this type are typical of silica foam, silica gel that is hydrothermally treated, etc. [99, 104].

H3 type hysteresis loops have two distinctive features: 1) narrow hysteresis loop, 2) adsorption and desorption branches coincide at P/P0 > 0.3 (the lower limit of the desorption curve is usually in the cavitation-induced P/P0 range). Hysteresis loops of this type are typical of materials in which sli-shaped pairs predominate between the parallel crystalline plates [99, 103].

The H4-type hysteresis loop has almost parallel and horizontal adsorption and desorption branches. H4 hysteresis loops are characteristic of zeolites or carbons with narrow crack-shaped pores. It should be noted that in the substances with H4 type hysteresis loop, there are micro- and meso-pores [103, 104].

The H5-type hysteresis loop is unusual. It has a peculiar shape associated with pore structures that contain both open and partially closed mesopores. A feature of the H5 hysteresis loops is the sudden drop in the desorption fraction.

It should be noted that in practice, materials are characterized by pairs of different sizes and shapes; thus, the combinations of hysteresis loops, which are

interpreted by mathematical calculations and other instrumental analysis studies (e.g., scanning electron microscopy), are most common [99, 103, 104].

A highly important issue related to the adsorption process is the utilization (stabilization/solidification (S/S)) of adsorbents that are contaminated with metal ions. The regeneration of adsorbents is a complex and expensive process or even impossible; thus, the adsorbents after the process are stored in landfills, which cause secondary pollution of the environment. A more acceptable way is to utilize adsorbents that are contaminated with metal ions in the production of concrete or reuse them as catalysts.

According to literature, calcium silicate hydrates with intercalated metal ions can be utilized as additives in Ordinary Portland cement (OPC). The utilization of such adsorbents would allow to solve the problems of secondary pollution, and such additives would improve the properties of cement and concrete. Thus, the immobilization of inorganic adsorbents contaminated with metal ions in mortars and concretes (produced using OPC) is one of the effective ways.

The direct utilization of adsorbents with intercalated metal ions is economically useless, because adsorbents bound metal ions, which can be firstly used as cheap catalysts.

Heavy metals are significant environmental pollutants, and their toxicity is a reason for increasing ecological, evolutionary, nutritional, and environmental problems. These metals are mainly discharged in industrial wastewater due to the mining operations, battery manufacturing processes, production of paints and pigments. For this reason, heavy metals should be prevented from reaching the natural environment. In order to remove pollutants from the water systems, the adsorption process is most commonly used. Different crystallinity calcium silicate hydrates compounds are one of the promising adsorbents. The ion exchange properties of calcium silicate hydrates depend on their chemical composition and the structure of crystalline lattice. Intercalated heavy metal ions change CSH compounds structure due to the different properties of cations and anions, such as valence, atom charge, or molecular size. Such compounds, after thermal treatment, form a stable catalyst support and metal oxide, a complex that can be widely used.

CSH compounds substituted with heavy metal ions can have a large surface area, high thermal stability, which expands the use of these compounds in perspective area. The promising basis for adsorbent-catalysts is functional calcium silicate hydrates and calcium silicates. However, there is a lack of comprehensive studies on the CSH adsorption capacity to heavy metals, their specific surface parameters, mineral composition, and thermal stability.

2. MATERIALS AND METHODS

2.1. Materials

The following reagents were used

Calcium oxide has been produced from $Ca(OH)_2$ (“Reaktiv”, Russia), additionally burned at 550 °C temperature for 1 h, ground for 30 s in a vibrating cup “Pulverisette 9” mill (speed: 600 rpm), and passed through a sieve with a mesh size of 80 μm. Surface area S_a = 2071 m^2/kg by CILAS LD 1090 granulometry, and the quantity of free CaO is equal to 98.7 mass %. Based on the particle size distribution of calcium oxide given in Fig. 2.1, it has been found that the predominance of particles with a range of diameters varies between 0.8–5.5 μm.

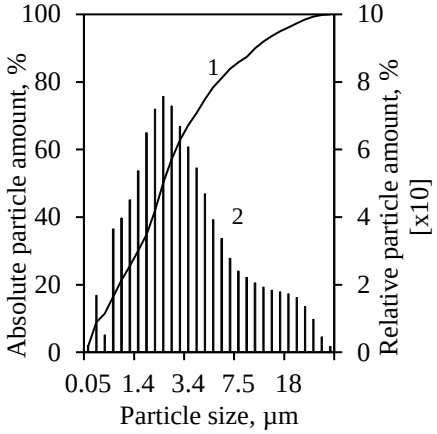

Fig. 2.1. Granulometric composition of calcium oxide; indexes: 1 is the absolute amount of particles, 2 is the relative amount of particles

Amorphous silicon dioxide (“Reaktiv”, Russia) was ground for 2.5 min in a vibrating cup “Pulverisette 9” mill (speed: 850 rpm) and passed through a sieve with a mesh size of 80 μm. S_a = 1291 m^2/kg; the loss of ignition is 5.19%. Based on the particle size distribution of silicon dioxide given in Fig. 1.2, it has been found that the predominance of particles with a range of diameters varies between 0.8–50 μm.

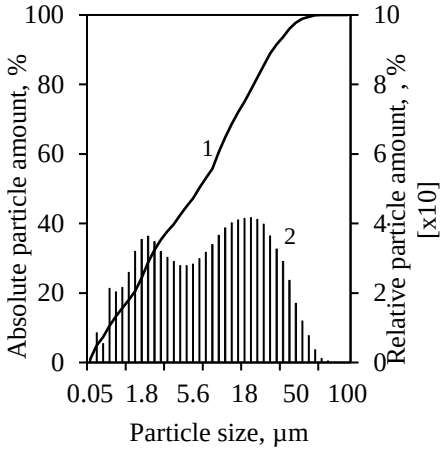

Fig. 2.2. Granulometric composition of SiO_2; indexes: 1 is the absolute amount of particles, 2 is the relative amount of particles

Copper nitrate solution (c = 0.25, 1, 10, g Cu^{2+}/L) was prepared by dissolving $Cu(NO_3)_2 \cdot 3H_2O$ granules ("Penta", The Czech Republic, purity 99%) in distilled water.

Cobalt nitrate solution (c = 0.25, 1, 10, g Co^{2+}/L) was prepared by dissolving $Co(NO_3)_2 \cdot 6H_2O$ ("Reachem Slovakia s.r.o.", Slovakia, purity 99%) in distilled water.

Chromium nitrate solution (c = 0.25, 1, 10, g Cr^{3+}/L) was prepared by dissolving $Cr(NO_3)_3 \cdot 9H_2O$ ("Sigma–Aldrich", UAS, purity 99%) in distilled water.

Calcium nitrate solution (c = 1 g Ca^{2+}/L) was prepared by dissolving $Ca(NO_3)_2 \cdot 4H_2O$ ("Penta", The Czech Republic, purity 99%) in distilled water.

Other pure chemical reagents include acetone, HCl.

2.2. Methods

Hydrothermal synthesis of A1 and A2 adsorbents

Fine ground $SiO_2 \cdot nH_2O$ and CaO were used as starting materials. The hydrothermal synthesis of calcium silicate hydrate has been carried out in unstirred suspensions in 25 mL volume PTFE cells, which were placed in a stainless steel autoclave ("Parr instruments", Germany) under saturated steam pressure in 175 °C, when the duration of isothermal curing was 16 (A2 adsorbent) and 24 h (A1 adsorbent), applying extra argon gas (7 bar). The molar ratio of the primary mixture (C/S) was equal to 1.5, while the w/s ratio was 10. The temperature was reached within 2 h. After hydrothermal treatments, the autoclave was quenched to room temperature. After synthesis, the suspensions were filtered, the products rinsed with acetone to prevent carbonization of materials, dried at 50 °C ± 5 for 24 h, and sieved (< 80 μm).

Hydrothermal synthesis of A1 adsorbent was synthesized under hydrothermal conditions at 175 °C temperature when the duration of isothermal curing was 24 h, and the molar ratio of the primary mixture C/S was equal to 1.5. It has been determined that the dibasic calcium silicate α-C_2SH (PDF No. 04-009-6343) and semi-crystalline C-S-H type compounds C-S-H(I) and/or C-S-H(II) (PDF No. 00-033-0306 and No.

PDF00-034-0002) were formed in the synthesis products (Fig. 2.3 a). In addition, small intensity diffraction peaks of calcium carbonate (PDF No. 04-012-0489) were identified as well. X-ray diffraction analysis (XRD) data were proved by the results of the simultaneous thermal analysis (STA) (Fig. 2.3 b). In the DSC curve, the first endothermic effect (50–200 °C) can be assigned to the loss of adsorption/crystallization water in calcium silicate hydrates. Meanwhile, the endothermic effect in a 400–500 °C temperature range describes the decompositions of α-C_2SH [125].

$$2CaO{\cdot}SiO_2{\cdot}H_2O \rightarrow 2CaO{\cdot}SiO_2 + H_2O$$

It has been determined that ~5.26% of the synthesis product mass was lost (Fig. 2.3 b, curve 1). According to this data, it was calculated that ~55.5% of α-C_2SH was formed. In addition, two exothermic effects at ~852 and ~872 °C, which are characteristic of the recrystallization of C-S-H(I) and C-S-H(II) to wollastonite, were identified (Fig. 2.3 b, curve 2). Meanwhile, an endothermic effect at ~679 °C was assigned to the decomposition of calcium carbonate.

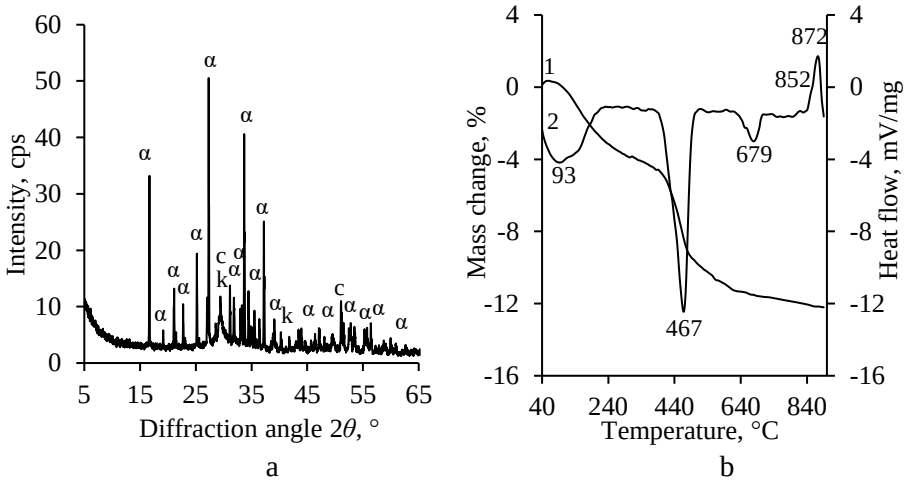

Fig. 2.3. XRD pattern (a) and STA curves (curve 1—TG; curve 2—DSC), (b) of A1 adsorbent; indexes: α – α-C_2SH, k – $CaCO_3$, c – C-S-H(I) and C-S-H(II)

Hydrothermal synthesis of A2 adsorbent was carried out in unstirred suspensions when C/S molar ratio of the primary mixture was equal to 1.5, and the duration of isothermal curing at 175 °C temperature was 16 h. It has been determined that after the hydrothermal treatment, the semi-crystalline C-S-H(I) and/or C-S-H(II) dominated in the synthesis product (Fig. 2.4 a). Moreover, the traces of dibasic calcium silicate α-C_2SH was identified in the XRD curve (Fig. 2.4 a). In the DSC curve, the endothermic effect at 116 °C temperature reflected the removal of adsorption/crystallization water in semi-crystalline C-S-H type compounds (Fig. 2.4 b, curve 2). Meanwhile, at the higher temperature (400–500 °C), the dehydration of α-C_2SH was observed (Fig. 2.4 b, curve 2). In addition, two exothermic effects at ~804 and ~868 °C temperatures, reflecting the recrystallization of C-S-H(I) and C-S-H(II) to calcium silicates were noticed (Fig. 2.4 b, curve 2). It is worth mentioning that the

endothermic effect of calcium carbonate decomposition was observed at 666 °C temperature. According to the TGA data, less than 3% of the mentioned compound was formed (Fig. 2.4 b, curve 1).

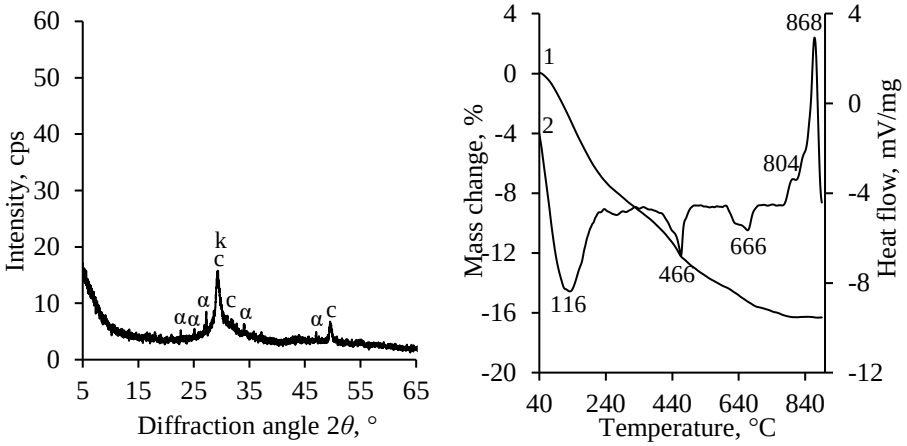

a b

Fig. 2.4. XRD pattern (a) STA curves (curve 1 – TG, curve 2 – DSC), (b) of A2 adsorbent; indexes: α – α-C_2SH, c – C-S-H(I) and/or C-S-H(II), k – $CaCO_3$

Adsorption experiments were conducted at 25 °C in the thermostatic adsorber Grant Sub14 by stirring 5 g of synthetic crystalline and amorphous structure adsorbents in 500 mL of $Co(NO_3)_2 \cdot 6H_2O$, $Cu(NO_3)_2 \cdot 3H_2O$, and $Cr(NO_3)_3 \cdot 9H_2O$ solutions, which contained 0.25, 1, and 10 g Me^{x+}/L (where Me^{x+} is Co^{2+}, Cu^{2+}, and Cr^{3+} ions, respectively), while the duration of adsorption varied in a 0.5–30 min range. The pH values of primary solutions are given in Table 1. The concentrations of heavy metal ions were determined using a Perkin–Elmer Analyst 4000 spectrometer (Perkin Elmer, Waltham, MA, USA) and calculated as the arithmetic mean of 3 individual results. The measurement deviations were below 3%. The values of pH were measured with a Hanna instrument (Hi 9321, microprocessor pH meter, Hanna Instruments, Woonsocket, RI, USA). After adsorption experiment, the products were dried at 50 °C ± 5 °C temperature for 24 h.

Desorption experiments for heavy metals (Cu^{2+}, Co^{2+}, Cr^{3+}) were carried out in 500 ml of distilled water by adding 5.0 g of adsorbent (A1 or A2) with incorporated heavy metals, while the desorption duration at 25 °C was 30 min. The amount of desorbed ions was determined by examining the concentration of desorbed ions in the liquid medium. After leaching, the suspensions were filtered off; the products were dried at 50 °C ± 5 °C temperature for 24 h.

Table 2.1. The pH values of initial solutions

Solution	Solution concentration, g/L	Initial pH value
$Co(NO_3)_2 \cdot 6H_2O$	0.25	6.07
	1	4.91
	10	2.99
$Cu(NO_3)_2 \cdot 3H_2O$	0.25	6.07
	1	4.72
	10	4.08
$Cr(NO_3)_3 \cdot 9H_2O$	0.25	3.57
	1	2.99
	10	2.25

Atomic Absorption Spectrometry (AAS)

The concentration of Cu^{2+}, Co^{2+}, Cr^{3+}, and Ca^{2+} ions was determined by using a Perkin Elmer Analyst 400 atomic absorption spectrometer with the following parameters: Cu^{2+} wavelength = 324.75 nm; Co^{2+} wavelength = 240.73 nm; Cr^{3+} wavelength = 357.87 nm; Ca^{2+} wavelength = 422.67 nm; hollow cathode lamp current (I) = 30 mA; the type of flame was C_2H_2-air; oxidant air = 10 l/min; acetylene = 2.5 l/min. All tests were repeated three times. The calibration curves are given in the Fig. 2.5.

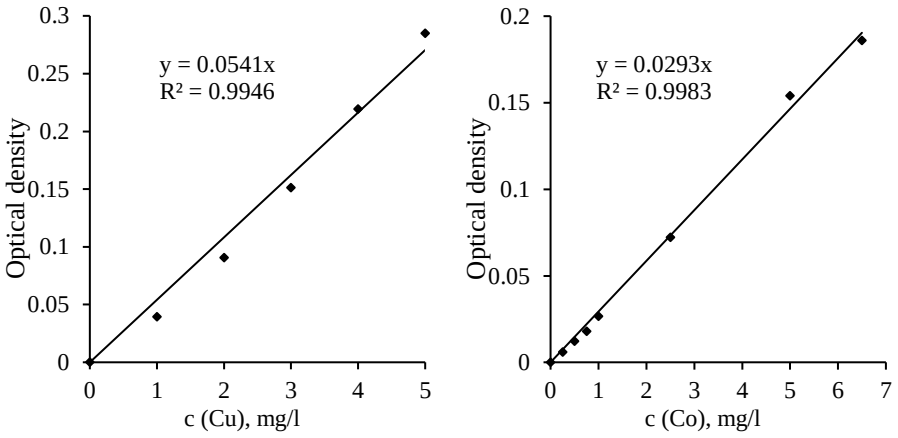

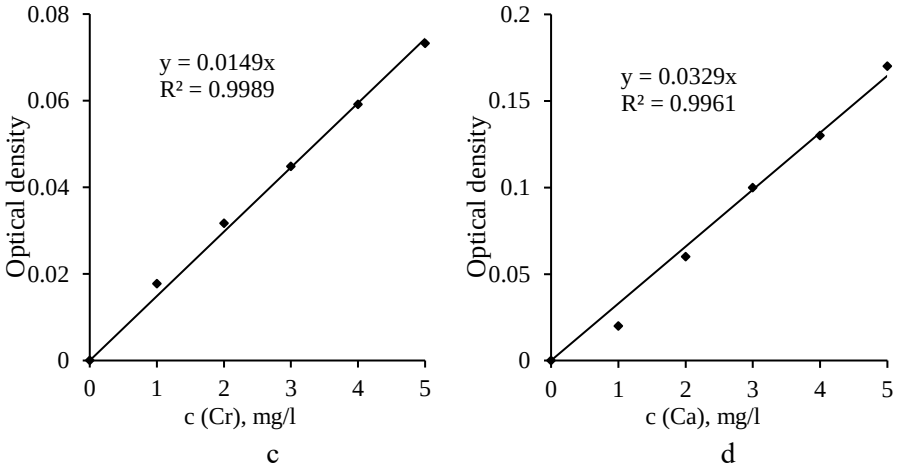

Fig. 2.5. Calibration curves for the calculation of Cu^{2+} (a), Co^{3+} (b), Cr^{3+} (c), and Ca^{2+} (d) ions concentration in nitrate solutions

The concentration of nitrate anions was determined by using a Flow Injection Analyst FIAlyzer-100 (FIA, FIAlab Instruments, Seattle, WA, USA); FIAlyzer-100 system: FIAlyzer-100, integrated FIA LOB manifold, USB4000 UV/VIS spectrometer, HL2000-LL visible tungsten lamp.

Adsorption kinetic models

In order to determine the kinetic parameters of adsorption reactions, the kinetic models have been developed and fitted for the adsorption process. The first-order adsorption kinetics model was chosen analogous to the Largergren model [105–107], which can be represented by the following equation:

$$\frac{dq_t}{dt} = k_1 \cdot (q_e - q_t); \tag{2.1}$$

where q_e and q_t are the amount of adsorbed ions at equilibrium and at time t_e, respectively (mg/g), k_1 is the rate constant of pseudo-first-order adsorption. After integration and applying boundary conditions $t = 0$ *to* $t = t_e$ and $q_t = 0$ *to* $q_t = q_e$, the integrated form becomes:

$$\log(q_e - q_t) = \log q_e - \frac{k_1}{2.303} \cdot t. \tag{2.2}$$

The pseudo-second-order adsorption kinetic model was chosen analogous to these models [106, 108, 109] and can be expressed as follows:

$$\frac{dq_t}{dt} = k_2 \cdot (q_e - q_t)^2; \tag{2.3}$$

where k_2 is the rate constant of the pseudo-second-order adsorption (g/mg·min). For the boundary conditions $t = 0$ *to* $t = t_e$ and $q_t = 0$ *to* $q_t = q_e$, the integrated form of the equation becomes (the integrated rate law for the pseudo-second-order reaction):

$$\frac{t}{q_t} = \frac{1}{kq_e^2} + \frac{1}{q_e} \cdot t. \quad (2.4)$$

The X-ray diffraction analysis

The X-ray diffraction (XRD) powder analysis of the samples was performed on the D8 Advance diffractometer (Bruker AXS, Karlsruhe, Germany) operating at the tube voltage of 40 kV and tube current of 40 mA. The X-ray beam was filtered with Ni 0.02 mm filter to select the CuKα wavelength. The diffraction patterns were recorded in a Bragg–Brentano geometry, using a fast counting detector Bruker LynxEye based on the silicon strip technology. The specimens were scanned over the range of 3–70 ° (2 θ) at a scanning speed of 6 °/min, using a coupled two theta/theta scan type. An XRD software "Diffrac.Eva" was used to calculate the crystallite size (D_{hkl}) and intensities of synthesis products using Scherrer's equation:

$$D_{hkl} = \frac{k \cdot \lambda}{B_{hkl} \cdot \cos\Theta}; \quad (2.5)$$

where λ is the wavelength of the CuKα radiation, Θ is Bragg's diffraction angle, B_{hkl} is the full width at half maximum intensity, and k is a constant (the value used in this study was 0.94).

In Situ XRD analysis was made with a high-temperature camera MTC-hightemp (Bruker AXS, Germany). The measurements were carried out with a step width of 0.02 2θ and 0.6 s/step at the heating rate of 50 °C/min after the equilibration for 5 min at the desired temperature.

Simultaneous thermal analysis (STA)

STA (differential scanning calorimetry (DSC) and thermogravimetry (TG)) was employed for measuring the thermal stability and phase transformation of samples. The tests were carried out by using two different apparatuses:

1) Netzsch instrument STA 409 PC Luxx. Parameters: a heating rate of 15 °C/min and the temperature range from 30 °C up to 1000 °C under air atmosphere. The ceramic sample handlers and crucibles of Pt-Rh were used as well.

2) Linseis PT10 instrument. Parameters: a heating rate of 15 °C/min and the temperature range from 30 °C up to 575 °C under air atmosphere. Ceramic sample handlers and Al crucibles were used as well.

Thermal stability of synthesis products

The thermal stability of synthesis products was estimated in a high-temperature furnace Nabertherm LH 15/13 at 550, 600, 750 °C temperatures for 24 h. The calcination temperature was reached within 48 h.

The specific surface area was determined by Brunauer, Emmet, and Taller (BET) method. The measurements were performed on a KELVIN 1042 Sorptometer (Costech Instruments, USA) using a nitrogen adsorption isotherm 77 K. The specific surface area was calculated according to the BET equation, using N_2 adsorption isotherm data in the range of $0.05 < P/P_0 < 0.35$:

$$\frac{1}{X \cdot \left(\frac{p_0}{p} - 1\right)} = \frac{C-1}{X_m \cdot C} \cdot \frac{p}{p_0} + \frac{1}{X_m \cdot C}; \quad (2.6)$$

where X is the mass of adsorbate adsorbed on the sample at relative pressure P/P_0 (p is the partial pressure of the adsorbate, and p_0 is the saturated vapor pressure of adsorbate); X_m is the mass of adsorbate adsorbed at a coverage of one monolayer; C is a constant, which is a function of the heat of the adsorbate condensation and the heat of adsorption (C_{BET}).

The BET equation yields a straight line when $\frac{1}{X\cdot\left(\frac{p_0}{p}-1\right)}$ is plotted versus $\frac{p}{p_0}$. The slope of $\frac{C-1}{X_m\cdot C}$ and the intercept of $\frac{1}{X_m\cdot C}$ was used to determine X_m and C: $S = slope = \frac{C-1}{X_m\cdot C}$ and $I = intercept = \frac{1}{X_m\cdot C}$. In order to calculate these parameters, the equations were rewritten as follows: $X_m = \frac{1}{S+I}$ and $C = \frac{1}{1+X_m}$. The BET equation plot provides a linear change in the range of P/P_0 = 0.05–0.35. The total surface area St of the sample is calculated from the equation:

$$S_t = \frac{X_m\cdot N\cdot A_{cs}}{M}; \quad (2.7)$$

where A_{cs} is the cross-sectional area of the adsorbate molecule ($A_{ad} = 16.2\cdot10^{-20}$ m^2), M is the molecular weight of adsorbate, N is Avogadro constant ($6.023\cdot10^{23}$).The specific surface area is calculated from the equation:

$$S_{BET} = \frac{S_t}{m}. \quad (2.8)$$

The total pore volume and the pore size distribution were calculated according to the corrected Kelvin equation and Orr et al. scheme [98, 110, 111] using the entire N_2 desorption isotherm at 77 K. The Kelvin equation relates the adsorbate vapor pressure depression to the radius of a capillary, which was filled with adsorbate:

$$ln\frac{p}{p_0} = -2\cdot\frac{\gamma\cdot V_m\cdot\cos\theta}{R\cdot T\cdot r_k}; \quad (2.9)$$

where p is the saturated vapor pressure in equilibrium with the adsorbate condensed in a capillary or pore, p_0 is the normal adsorbate saturated vapor pressure, γ is the surface tension of nitrogen at its boiling point (γ = 8.85 ergs/cm^2 at –195.8 °C), V_m is the molar volume of liquid nitrogen (V_m = 34.7 cm^3), θ is the wetting angle (usually taken 0° and cos θ = 1), the gas constant R is $R = 8.134\cdot10^7$ ergs/deg mol, the absolute temperature T is T = 77 K, and r_K is the Kelvin radius of a pore.

The thickness t of the adsorbed layer is calculated according to the following equation:

$$t = \frac{V_a}{V_m}\cdot\tau; \quad (2.10)$$

where V_m is the volume of absorbed gas, mm^3/g, and τ is the thickness of monomolecular adsorbent, mm.

As the cylindrical pore model $r_p = r_k + t$ is used, the following equation is obtained:

$$V_p = \left(\frac{\overline{r}_p}{\overline{r}_k}\right)^2 \cdot (V_L - \Delta t \cdot \Sigma A); \quad (2.11)$$

where $\overline{r}_p$ is the actual average of pore radius in the range of r_2–r_1, Å.

The volume of desorbed liquid in any desorption isotherm range is related to the volume of gas evolved $\Delta Vp = \Delta Vd$ ($1.54 \cdot 10^{-3}$). The cylindrical pores are calculated by the following equation:

$$A = \frac{2 \cdot \Delta V_P}{\bar{r}_p} \cdot 10^4; \quad (2.12)$$

where ΔV_p is the volume of emitted gas, cm^3.

Parallel plate type pairs are calculated using the following equation:

$$\overline{d_p} = r_k + 2t; \quad (2.13)$$

where r_k is the measured distance between two plates, Å; $\overline{d_p}$ is the actual distance between the two plates, Å.

The average pore distance between two plates $\overline{d}_p$volume V_p is equal:

$$V_p = \frac{\overline{d}_p}{\overline{r}_k}(\Delta V_L - 2\Delta t \Sigma A). \quad (2.14)$$

The theoretical surface area A of the pore walls is calculated by the following equation:

$$A = \frac{2V_p}{d_p}. \quad (2.15)$$

The calculations are completed using any model when $\Delta t \cdot \Sigma A$ exceeds ΔV_L value.

The catalyst activity in oxidation reactions was determined as follows. Propanol was used as a volatile organic compound for catalytic oxidation experiments. In addition, 0.945–1.009 g of the analyzed sample was placed inside a fixed-bed quartz reactor, equipped with a coil preheater. A quartz reactor was mounted inside a Nabertherm LH 15/13 furnace for maintaining the constant temperature, while K-type thermocouple inside the reactor was used for accurate temperature monitoring. The inlet and the outlet of the reactor are equipped with special analysis points for the collection of gaseous flow samples and CO and CO_2 concentration measurement probes that are connected directly to a TESTO 445 unit. Catalytic oxidation was performed with a constant 370 mL/min flow of air, which was saturated with 475–640 ppm of volatile organic compounds (VOC). The concentrations of propanol in the gas stream were determined with a Perkin Elmer Clarus 500 GC/MS system equipped with a COL-ELITE 5MS universal capillary column, which is 30 m long and has a 0.25 mm internal diameter.

Scanning electron microscopy (SEM)

SEM (JEOL JSM-7600F, Japan) coupled with energy dispersive X-ray spectrometry (EDX) (Inca Energy 350, Oxford Instruments), Silicon Drift type detector X-Max20) was performed by using the accelerating voltage of 10 kV, the

working distance of 8.6 and 8.7 mm for the SEM observation, and 200 s accumulation time for EDX analysis.

Transmission electron microscope (TEM)

Transmission electron microscope (TEM) was performed by using Tecnai G2 F20 X-TWIN instrument (FEI, Netherlands) with a Schottky type field emission electron source. The accelerating voltage was 200 kV. In order to take TEM images, a high angle annular dark field detector (HAADFD) was used.

Fourier transform infrared spectroscopy (FT-IR)

The FT-IR spectra of samples were recorded with the help of spectrometer Perkin Elmer FT-IR system Spectrum X. The specimens were prepared by mixing 1 mg of the sample in 200 mg of KBr. The spectral analysis was performed in the range of 4000–400 cm^{-1} with a spectral resolution of 1 cm^{-1}.

The determination of free CaO

In fact, 1 g of the sample was weighed and placed into a 250 cm^3 conical flask, poured with 150 cm^3 of distilled water, and 5–10 pieces of glass beads were added. The slurry was heated for 5 minutes. After that, the suspension was cooled down, the inner wall of the flask was sprayed with distilled water, and 2–3 drops of phenolphthalein indicator were added. Finally, the suspension was titrated with 1N HCl, until the pink color disappeared. The amount of free CaO (X) in the sample was calculated by using the following equation:

$$X = \frac{V \cdot N \cdot 28.04 \cdot 100}{G \cdot 1000}; \quad (2.16)$$

where N is the normality of HCl; V is the volume of titrated HCl, cm^3; 28.04 is CaO equivalent, g; G is the initial mass of the sample, g.

Ignition of losses

Furthermore, 1 g of amorphous silicon dioxide was weighed with the analytical balance and placed into an annealed crucible. The material was calcinated to constant weight at 1000 °C for 90 minutes. The cooled crucible was weighed, and the heaters were calculated according to the formula:

$$K = \frac{(m - m_1)}{m} \cdot 100\%; \quad (2.17)$$

where m is the initial mass of the sample, g; m_1 is the mass of the sample after calcination, g.

3. RESULTS AND DISCUSSION

3.1. The adsorption peculiarities of heavy metals and the structure properties of A1 adsorbent

It is known that the calcium silicate hydrates are stable in the liquid medium, which pH values are equal to 7–12 [112, 113]. Unlike calcium silicate hydrates, metal ions (Mn^{2+}, Fe^{2+}, Co^{2+}, Ni^{2+}, Cu^{2+}, Zn^{2+}, Pb^{2+}, Cd^{2+}, or Hg^{2+}) exist only in acid media, because the formation of complex compounds or metal hydroxides proceed in the alkaline solutions [114]. Several studies suggest that it is not expedient to alkaline the nitrate solutions for the following reasons:

1) practical aspects: the wastewater having acidic properties cannot exist in alkaline media because it forms complex compounds [115–117]. For example, when ammonia water is added to the solution (to increase pH value), the metal ions form complex compounds, such as $[Cu(NH_3)_4](OH)_2$, the adsorption process is following a much more complicated mechanism [118, 119];
2) due to different properties (valence, atom charge) of cations and anions (ammonium, nitrate, etc.);
3) alkaline ions (sodium, etc.) usually block adsorbent active centers, which negatively impact the adsorption process [120].

3.1.1. The adsorption capacity of A1 adsorbent for the Co^{2+} ions

Firstly, the adsorption experiment was carried out in a $Co(NO_3)_2 \cdot 6H_2O$ solution, containing 0.25 g Co^{2+}/L. It has been determined that the latter process proceeds intensively at the beginning, because after 30 s of reaction, about 50% of cobalt ions were incorporated into the structure A1 adsorbent (Fig. 3.1). Moreover, the adsorbed amount of these ions increased, and after 5 min, it was equal to 24.68 mg Co^{2+}/g. However, the further increment in experiment duration did not affect the uptake of Co^{2+} ions, because after 30 min of reaction, the amount of absorbed ions remained almost the same and was equal to 24.73 mg Co^{2+}/g (Fig. 3.1).

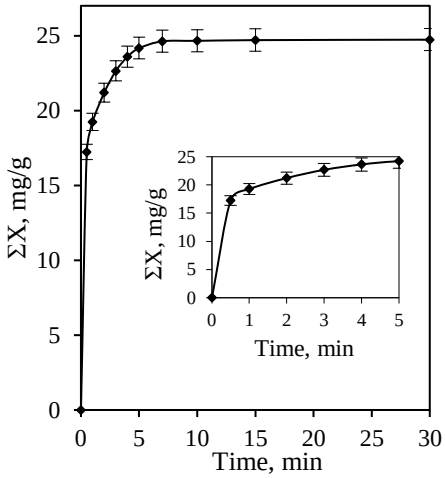

Fig. 3.1. The integral kinetic curve of Co^{2+} ion adsorption by A1 adsorbent when the initial concentration of Co^{2+} was equal to 0.25 g/L

It is worth noting that at the beginning of the experiment, about 7.2% (30 mg) of Ca^{2+} ions were released from the structure of the adsorbent, showing that the ion exchange reaction takes place between the A1 adsorbent and the $Co(NO_3)_2 \cdot 6H_2O$ solution (Fig. 3.2). These data can be explained by evaluating the crystal structure of the latter compound. It is well known that α-C_2SH with isolated silicate tetrahedrons possess the lowest degree of polymerization, and its crystal structure consists of isolated acidic $SiO_3(OH)$ tetrahedra, which share edges with alkaline $Ca(O,OH)_6$ and $Ca(O,OH)_7$ polyhedra [121, 122]. Presumably, for this reason, both Ca^{2+} cations and OH^- anions are released when the structure of this compound is destroyed in an acidic environment. These data are in good agreement with the value of pH of liquid medium, which increased from 4.91 (before adsorption) to 6.07 (after 30 min of adsorption). As expected, due to the excellent adsorption properties of calcium silicate hydrates for metal ions, the concertation of Ca^{2+} ions in the liquid medium decreased to 4.56% (18.6 mg) by prolonging the adsorption to 15–30 min.

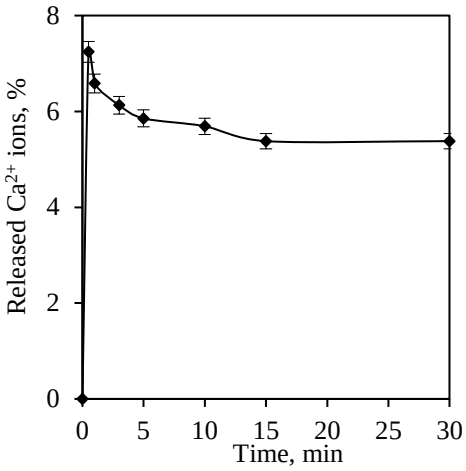

Fig. 3.2 Differential kinetic curve of released Ca^{2+} ions amount from the adsorbent when the initial concentration of Co^{2+} was equal to 0.25 g/L

Thus, it can be seen that almost all Co^{2+} ions that had been present in the liquid medium were adsorbed by the A1 adsorbent when a lower concentration of $Co(NO_3)_2 \cdot 6H_2O$ solution (0.25 g/L) was used. For this reason, in the next stage of this work, it was raised to 1 g of Co^{2+}/L.

It has been determined that a higher metal ions concentration has a positive effect on the incorporation of Co^{2+} ions (Fig. 3.3 a). After 30 s of adsorption, A1 adsorbent adsorbed 90% of initial Co^{2+} ions (90.01 mg Co^{2+}/1 A1 adsorbent) (Fig. 3.3 a) and released 22.1% (89.84 mg) of Ca^{2+} ions (Fig. 3.3 b). When the duration of the experiment was extended to 10 min, the equilibrium was attained, and the amount of adsorbed ions reached 99.61 mg Co^{2+}/1 g A1 adsorbent (Fig. 3.3 a). Additionally, as in the previous case, a decrease in the concentration of desorbed OH^- anions was observed. It is worth mentioning that due to the higher destruction of adsorbents, the pH value of the liquid medium increased from 4.91 to 10.97. In order to confirm the intercalation of Co^{2+} ions, XRF analysis was performed after 30 min, and it has been found that A1 adsorbent contained 14.6% of Co^{2+} ions.

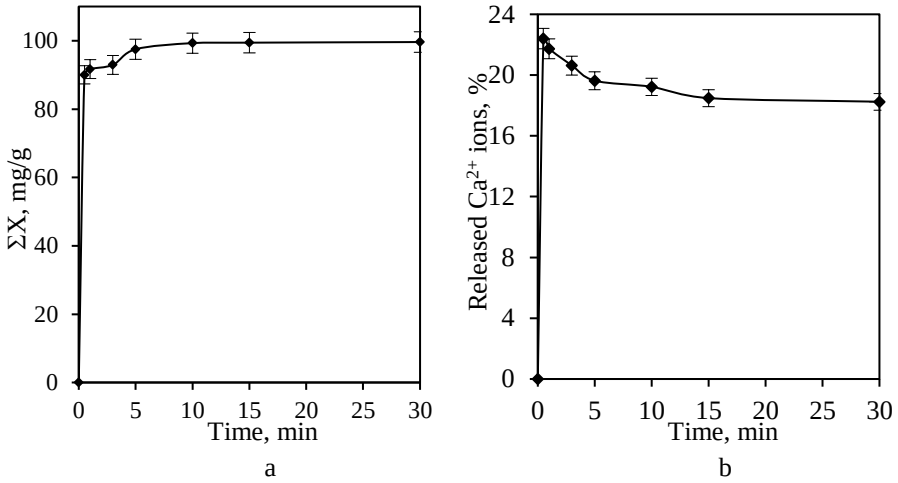

Fig. 3.3 Integral kinetic curve of Co^{2+} ion adsorption by A1 adsorbent (a) and differential kinetic curve of released Ca^{2+} ions amount from the A1 adsorbent (b) when the initial concentration of Co^{2+} was equal to 1 g/L

Thus, the previous results indicated that the interaction between the adsorbent and the adsorptive is followed by the following reaction:

$$\text{A1 adsorbent} + Co^{2+} \rightarrow \text{A1 adsorbent}{-}\text{Co sample} + Ca^{2+}.$$

In order to determine the maximum adsorption capacity of the A1 adsorbent for Co^{2+} ions, the concentration of $Co(NO_3)_2 \cdot 6H_2O$ solution was increased to 10 g/L.

It has been found that the adsorption capacity was equal to 288 mg Co^{2+}/g after 30 min of adsorption (Fig. 3.4), but ~50% of Ca^{2+} ions were released to a liquid medium within the same duration.

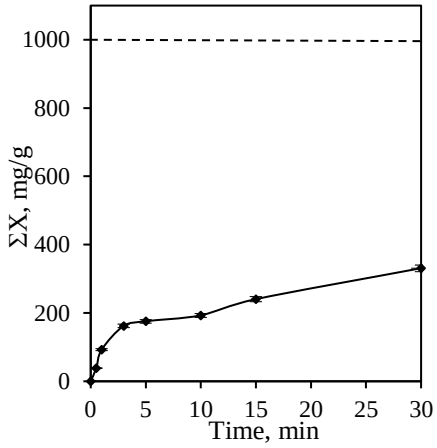

Fig. 3.4 Integral kinetic curve of Co^{2+} ion adsorption by A1 adsorbent when the initial concentration of Co^{2+} was equal to 10 g/L

According to the literature, the adsorption capacity of lower basicity calcium silicate hydrates (gyrolite, xonotlite, and tobermorite) depends on the nature of the adsorptive. Kasperaviciute et al. [123] determined that the maximum amount of adsorbed Cu^{2+} ions by gyrolite is equal to 1480 mg Cu^{2+}/g. Meanwhile, Bankauskaite et al. [124] showed that the adsorption capacity of this compound for Co^{2+} ions is equal only to 14 mg Co^{2+}/g.

In order to determine if adsorption is a reversible process or not in a neutral liquid medium, A1 adsorbent sample with intercalated Co^{2+} ions (1 g Co^{2+}/L) was dried up and immersed in the distilled water. It was measured that after 60 min at 25 °C, Co^{2+} ion concentrations in the solution did not exceed ~0.008%. It is worth mentioning that after the desorption process, Co^{2+} ions were detected in the A1 adsorbent structure via XRF analysis.

Furthermore, in the next stage of this research, the kinetic adsorption parameters were determined by applying pseudo-first-order and pseudo-second-order equations (Table 3.1). In order to obtain the experimental data, the cobalt nitrate solutions containing 0.25 g and 1 g Co^{2+}/L concentration were used. The mentioned equation suitability for the adsorption reaction was verified by comparing the calculated equilibrium concentrations ($q_{e(cal)}$) of Co^{2+} ions to the experimental concentrations ($q_{e(exp)}$). In addition, the equation is suitable only if the errors between $q_{e(cal)}$ and $q_{e(exp)}$ do not exceed 5%.

Using the pseudo-first-order equation was found that the values of R^2 were lower (0.84, 0.85) and the values of $q_{e(cal)}$ disagreed with the experimental $q_{e(exp)}$ ones (Table 3.1). Thus, the pseudo-first-order equation did not fit well with the Co^{2+} ions adsorption mechanism description.

Table 3.1. A1 adsorbent with incorporated Co^{2+} ions kinetic parameters of the pseudo-first-order and pseudo-second-order kinetic models

Concentration (g Co^{2+}/L)	R^2	$q_{e(exp)}$ (mg/g)	$q_{e(cal)}$ (mg/g)	k_1 (g/(mg·min))	k_2 (g/(mg·min))
Pseudo-First-Order Kinetic Models					
0.25	0.84	24.73	8.39	0.450	-
1.00	0.85	99.62	16.93	0.356	-
Pseudo-Second-Order Kinetic Models					
0.25	0.99	24.73	25.08	-	0.139
1.00	1.00	99.62	100.00	-	0.091

Different results were obtained by using the pseudo-second-order kinetics equation: the values of R^2 were near 1 and equal to 0.99 (0.25 g Co^{2+}/L) and 1.00 (1 g Co^{2+}/L) (Fig. 3.5). In addition, the calculated $q_{e(cal)}$ values were close to the experimental $q_{e(exp)}$ ones (Table 3.1). Thus, it can be stated that the pseudo-second-order kinetics model adequately describes the Co^{2+} ion adsorption mechanism of the A1 adsorbent. Moreover, it was calculated that the Co^{2+} ion adsorption rate (k_2 = 0.139 g/(mg·min)) is higher in the solution containing 0.25 g Co^{2+}/L than in the solution containing 1 g Co^{2+}/L (k_2 = 0.091 g/(mg·min)) (Table 3.1). It should be noted that these data agree with the experimental results and confirm that Co^{2+} ions are

chemisorbed by A1 adsorbent. The same phenomenon can be found in the literature [123–128].

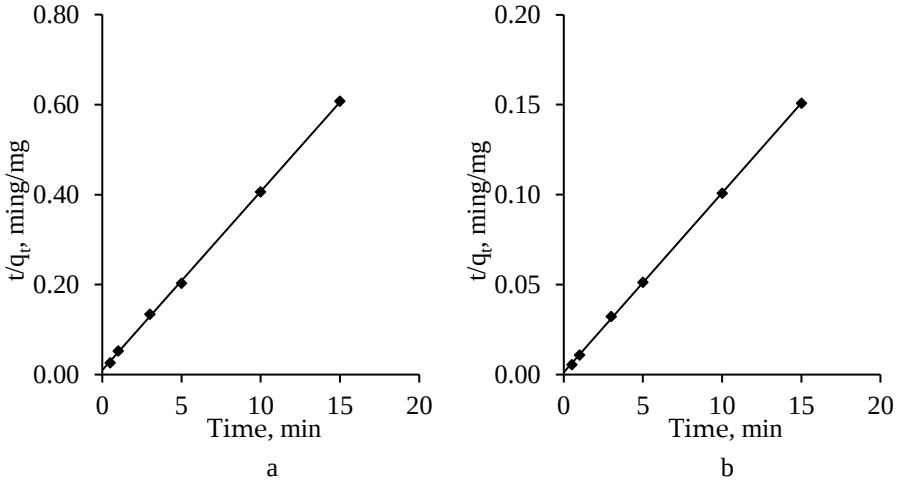

Fig. 3.5. Pseudo-second-order kinetic plots when the initial concentration of Co^{2+} was equal to 0.25 g/L (a) and 1 g/L (b)

In order to evaluate the stability of the adsorbent, A1 adsorbent was described by XRD and STA. It was determined that 89.84 mg of Ca^{2+} ions were desorbed from the crystal structure of the A1 adsorbent. However, the structure of the latter compound remained stable. In addition, the adsorption process in the solution containing 0.25 and 1 g Co^{2+}/L, the intensity of the main diffraction peaks (*d*-spacing: 0.422, 0.326 nm) α-C_2SH decreased by 1.77 and 2.53 times, respectively (Fig. 3.6 b, c). However, the opposite tendency has been observed with the calcite compound, as its content increased in both samples (Fig. 3.6 b, c). Meanwhile, after adsorption in the solution containing 10 g Co^{2+}/L, A1 adsorbent fully decomposed, because the diffraction peaks that are typical to this compound are not detected in the XRD patterns (Fig. 3.6 d). It is worth mentioning that one diffraction peak (*d*-spacing 0.91 nm) that is characteristic of a new compound was observed, but no standards in the database that match or describe the resulting compound were found (Fig. 3.6 d).

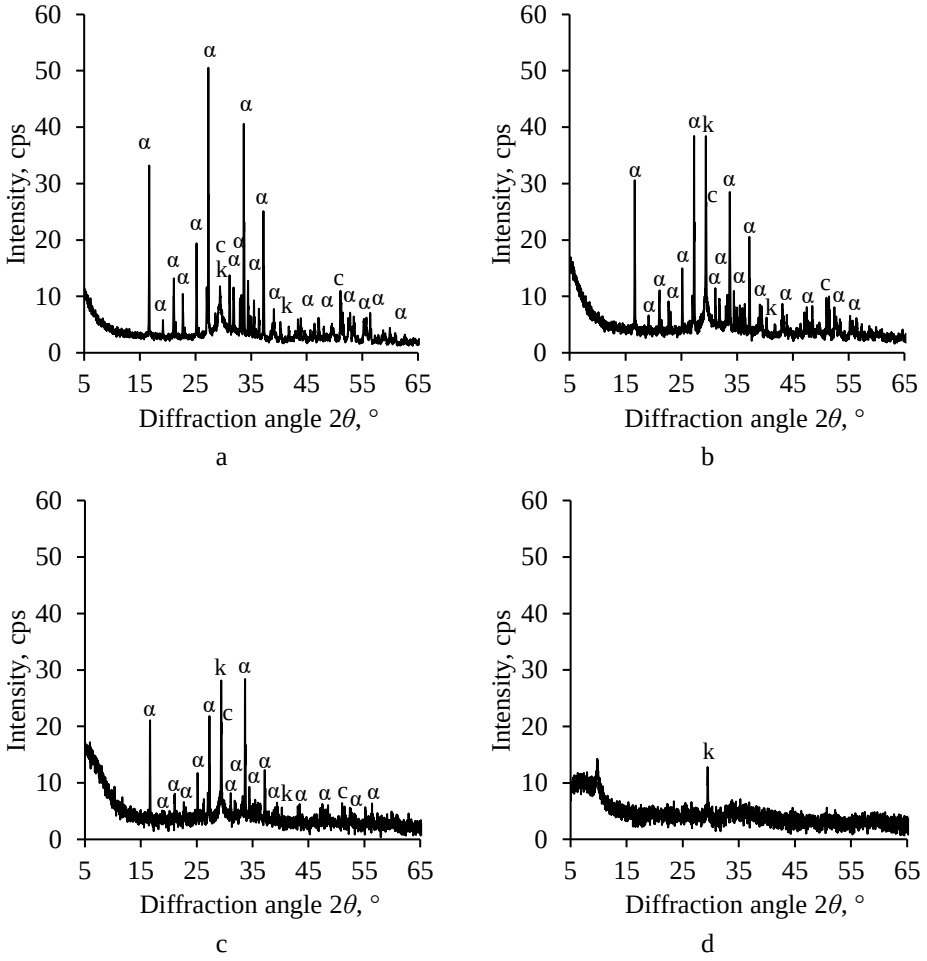

Fig. 3.6. XRD curves of A1 adsorbent after synthesis (a) and the adsorption process when the initial concentration of Co^{2+} was equal to 0.25 g/L (b), 1 g/L (c), and 10 g/L (d); indexes: α – α-C_2SH, k – $CaCO_3$, c – C-S-H(I), and/or C-S-H(II)

The XRD results were supported by the STA analysis data. It has been found that the absorbed heat of the first endothermic effect increased from 84.26 J/g (pure A1 adsorbent) (Fig. 3.7 a) to 175.78 J/g (A1 adsorbent after adsorption in a solution containing 10 g Co^{2+}/L) (Fig. 3.7 d). These data can be associated with the amorphization of the synthesis product. Meanwhile, the values of the heat characteristic to α-C_2SH decreased by 1.8 times after the adsorption in the solutions with lower Co^{2+} ion concentrations. It has been observed as well that the endothermic effect that is typical to this compound was not identified in the DSC curves of a sample, in which 10 g/L $Co(NO_3)_2 \cdot 6H_2O$ solution was used (Fig. 3.7 c). These results clearly show that the A1 adsorbent is fully decomposed in such acidic environment, and the thermal effects that are typical to the cobalt salts and/or oxides were identified (Fig. 3.7 d) [129, 130]. It has been found that semi-crystalline calcium silicate

hydrates C-S-H(I) and/or C-S-H(II) decomposed after the adsorption in a solution containing 1 g Co^{2+}/L (Fig. 3.7 c). It is worth mentioning that during the adsorption process, the carbonization appeared, and according to the TG results, the quantity of calcium carbonate increased to 6.75–9% (Fig. 3.7 c).

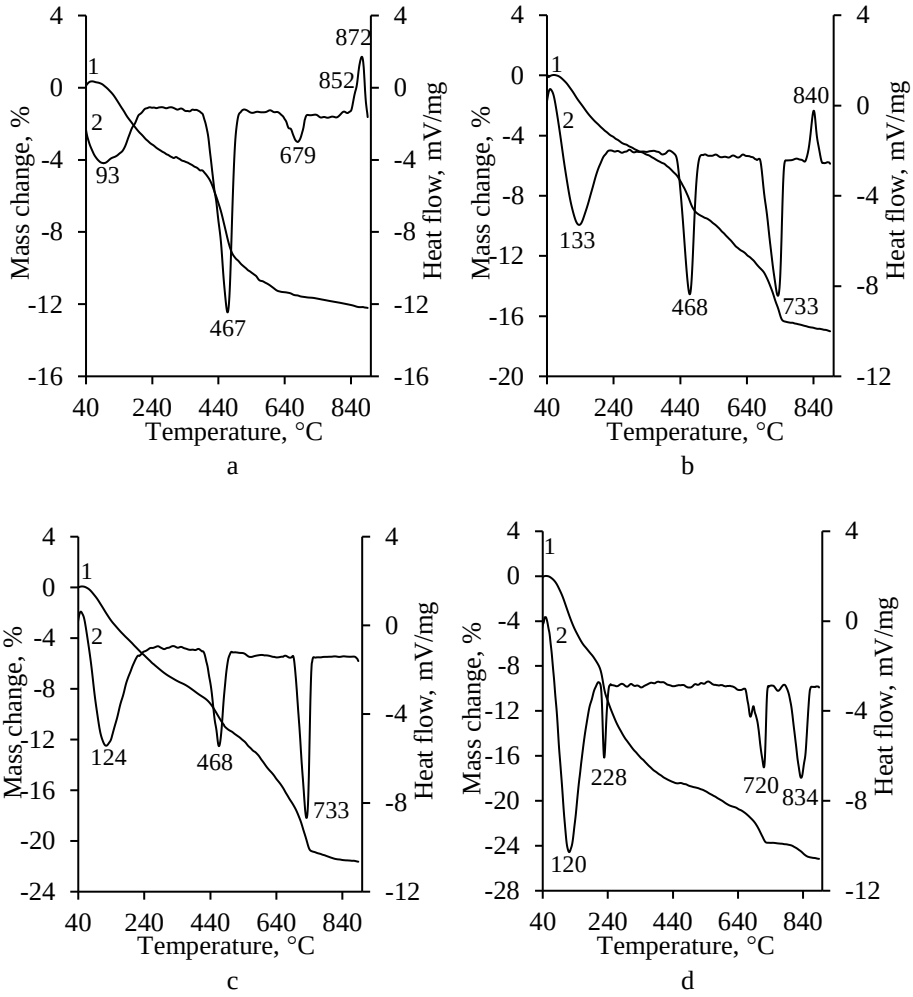

Fig. 3.7. STA curves (curve 1 – TG, curve 2 – DSC) of A1 adsorbent after the synthesis (a) and the adsorption process when the initial concentration of Co^{2+} was equal to 0.25 g/L (b), 1 g/L (c), and 10 g/L (d)

Thus, when evaluating the pH values of solutions in different concentrations, literature data, and obtained results, it is not recommended that more than 1 g Co^{2+}/L of $Co(NO_3)_2 \cdot 6H_2O$ solution would be used for the adsorption experiments with A1 adsorbent. Since the synthetic adsorbent remains stable at low Co^{2+} ions concentration (0.25 and 1 g/L), more heavy metals, usually found in the wastewater, were investigated. Accordingly, the Cu^{2+} and Cr^{3+} ions intercalation into the A1 adsorbent structure were determined.

3.1.2. The adsorption capacity of A1 adsorbent for the Cu^{2+} and Cr^{3+} ions

As expected, in the lower concentration metal ions solutions (0.25 g/L), the adsorption process proceeded intensively at the beginning, because after 30 s, all Cu^{2+} (25 mg Cu^{2+}/g) (Fig. 3.8 a) and Cr^{3+} (Fig. 3.8 b) ions (25 mg Cr^{3+}/g) from the primary solution were incorporated into the structure of A1 adsorbent. Due to the fast adsorption of the Cu^{2+} and Cr^{3+} ions by the adsorbent, the PFO and PSO equation cannot be used for the description of the process.

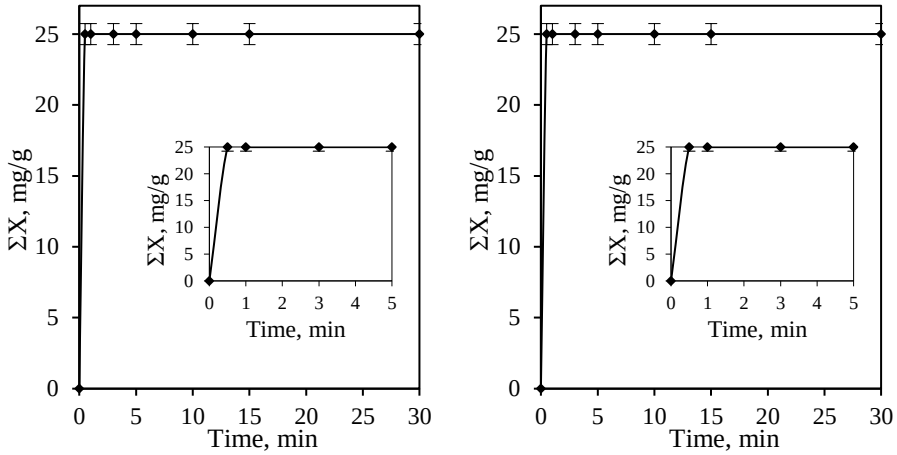

Fig. 3.8. Integral kinetic curves of Cu^{2+} (a) and Cr^{3+} (b) ions adsorption by A1 adsorbent when the initial concentration of ions was equal to 0.25 g/L

In order to determine whether the adsorption reactions are reversible or irreversible, the saturated adsorbents were dried up and immersed in the distilled water (water to solid ratio is 10). The results revealed that after 30 min, the concentration of metal ions in the liquid medium does not exceed the atomic absorption spectrometer detection limit. Moreover, during the adsorption, the structure of the A1 adsorbent remained stable as the intensity of the main diffraction peaks (*d*-spacing: 0.422, 0.327 nm) of this compound decreased (Fig. 3.9). It should be noted that calcite main diffraction peaks (*d*-spacing: 0.304, 0.187 nm) decreased as well (Fig. 3.9).

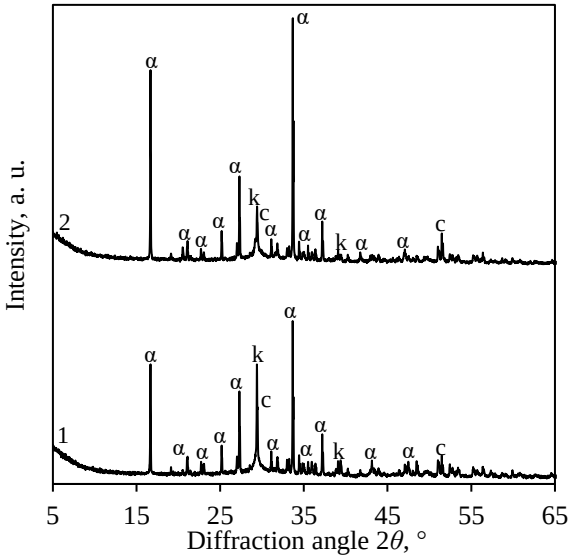

Fig. 3.9. XRD patterns of A1 adsorbent after the adsorption in copper (curve 1) and chrome (curve 2) nitrate solutions when the initial concentration was equal to 0.25 g Cu^{2+} or Cr^{3+}/L; indexes: α – α-C_2SH, k – $CaCO_3$, c – C-S-H(I), and/or C-S-H(II)

In brief, the A1 adsorbent showed good adsorption properties in 0.25 g Cu^{2+} or Cr^{3+}/L solutions in comparison with other adsorbents [131]. Thus, in the next stage of this work, the adsorption experiment was performed in higher concentration solutions (1 g/L).

When the concentration of heavy metal ions in the solution was equal to 1.00 g Me^{x+}/L, the uptake of these ions by the adsorbent proceeded slower (Fig. 3.10). Within 30 s of Cu^{2+} ions adsorption, the removal efficiency of A1 adsorbent reaches ~73% (72.91 mg/g) (Fig. 3.10 a). Meanwhile, the quantity of adsorbed Cr^{3+} ions (Fig. 3.10 b) by the latter compound was higher and equal to 86% (86.14 mg/g). By prolonging the duration of the experiment to 3 min, the adsorbed amount of Cu^{2+} ions slightly increased. However, the removal of these ions was completed only after 30 min (Fig. 3.10 a). In the meantime, the uptake of Cr^{3+} ions reached 100% already after 3 min (Fig. 3.10 b). As in the previous case (0.25 g Me^{x+}/L), it has been found that the adsorption process is irreversible because the concentration of heavy metal ions in the liquid medium did not exceed ~0.01%. The obtained results were confirmed by the XRF analysis: 16.1% of Cu^{2+} and 16.4% of Cr^{3+} ions were detected in the adsorbent.

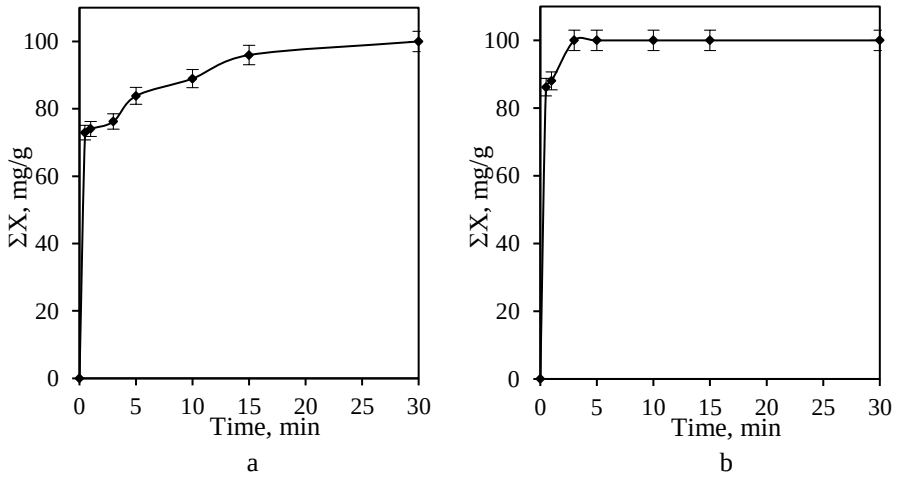

Fig. 3.10. The integral kinetic curve of Cu^{2+} (a) and Cr^{3+} (b) ions adsorption by A1 adsorbent when the initial concentration of ions was equal to 1 g/L

Meanwhile, the measurements of calcium ions concentration have shown that after 30 s of adsorption in 1 g/L heavy metal solution, 88.0 mg (20.9%) of mentioned ions were released from the structure of the adsorbent in $Cu(NO_3)_2 \cdot 3H_2O$ solution (Fig. 3.11 a). Moreover, unexpected results were obtained: after 1 min of adsorption, the amount of released Ca^{2+} ions decreased, while after 5 min, the equilibrium was attained, and the amount of released ions was equal to 115.6 mg (27.4%) (Fig. 3.11 a). The same tendency was observed in $Cr(NO_3)_3 \cdot 9H_2O$ solution, although the amount of released Ca^{2+} ions was 1.31 times higher after 30 min of the experiment (Fig. 3.11 b). It is worth mentioning that the amount of released Ca^{2+} ions tends to increase by increasing the duration of experiments when the lower basicity calcium silicate hydrates are used for Me^{x+} ions adsorption [20].

The results have shown that after 30 min of Cu^{2+} adsorption, the exchange of $Cu^{2+} \leftrightarrow Ca^{2+}$ proceeded stoichiometric, while $Cr^{3+} \leftrightarrow Ca^{2+}$, in a non-stoichiometric way. Presumably, it can be explained by the different valence or atomic radius between Ca^{2+} and adsorbed ions (Cr^{3+}, Cu^{2+}). According to literature [132, 133], the crystal structure of A1 adsorbent consists of isolated $SiO_3(OH)$ tetrahedra, which share edges with $Ca(O,OH)_6$ and $Ca(O,OH)_7$ polyhedra. Thus, during the desorption of Ca^{2+} cations, OH^- anions are released as well into the liquid medium. This fact was confirmed by the value of pH of liquid medium, which increased from 2.99 (0 min) to 10.15 (30 min) in $Cr(NO_3)_3 \cdot 9H_2O$ solution and from 4.72 (0 min) to 9.17 (30 min) in $Cu(NO_3)_2 \cdot 3H_2O$ solution.

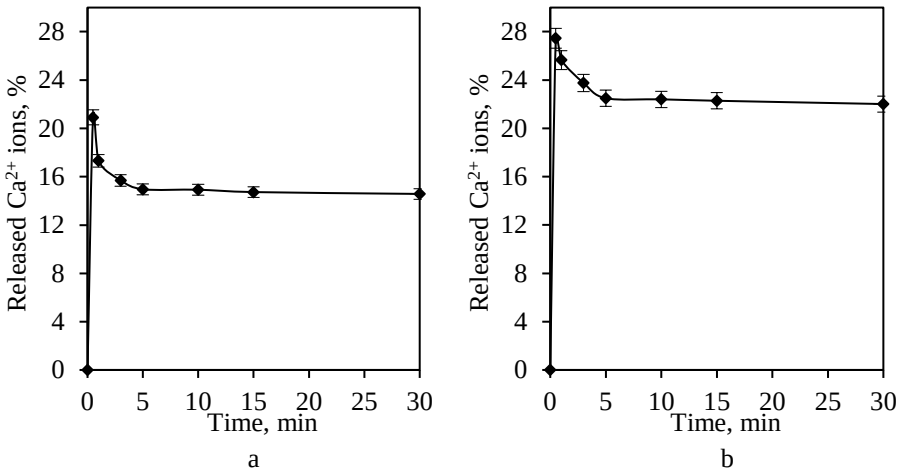

Fig. 3.11. The differential kinetic curves of released Ca^{2+} ions amount from the adsorbent when the initial concentration of Cu^{2+} (a) and Cr^{3+} (b) was equal to 1 g/L

In order to determine the kinetic parameters, the adsorption process was described by PFO and PSO equations. It was determined that the PFO equation (Eq. 2) did not fit the adsorption mechanism of Cu^{2+} and Cr^{3+} ions by the synthetic adsorbent because the error between the adsorbed ($q_{e(exp)}$) and calculated ($q_{e(cal)}$) amount of Me^{x+} was higher than 5–10% [107]. In addition to this, the values of correlation coefficients (R^2) were low (Table 3.2). However, different results were obtained when using PSO equation (Eq. 4): the values of R^2 were equal to 0.99 (Table 3.2), and the relation between $q_{e(exp)}$ and $q_{e(cal)}$ values was observed. It was calculated that the adsorption rate of Cr^{3+} ions (k_2 = 0.065 g/(mg·min)) was approximately 3 times higher than Cu^{2+} (k_2 = 0.020 g/(mg·min)). These results correspond to the experimental data because the adsorption process of Cr^{3+} ions ended after 3 min, while in the case of Cu^{2+} ions, after 30 min (Fig. 3.10 b). The same results can be found in literature [123, 125].

Table 3.2. A1 adsorbent with incorporated Cu^{2+} or Cr^{3+} ions kinetic parameters of the pseudo-first-order and pseudo-second-order kinetic models

Metal ions	R^2	$q_{e(exp)}$, mg/g	$q_{e(cal)}$, mg/g	k_1, g/(mg·min)	k_2, g/(mg·min)
Pseudo-First-Order Kinetic Models					
Cu^{2+}	0.813	100.00	42.89	0.813	-
Cr^{3+}	0.492	100.00	12.56	0.492	-
Pseudo-Second-Order Kinetic Models					
Cu^{2+}	0.999	100.00	100.00	-	0.020
Cr^{3+}	0.999	100.00	101.01	-	0.065

X-ray diffraction analysis data have shown that A1 adsorbent became metastable, since after the adsorption in $Cu(NO_3)_2 \cdot 3H_2O$ and $Cr(NO_3)_3 \cdot 9H_2O$ solutions, the intensity of α-C_2SH compound (*d*-spacing: 0.422, 0.327 nm) diffraction

peaks decreased by 1.1 and 2.3 times, respectively (Fig. 3.12). In the case of Cr^{3+} ions, the lower intensity of the aforementioned peaks can be explained by a higher amount of released Ca^{2+} ions from the adsorbent structure (Fig. 3.11). These results confirmed that heavy metal ions were adsorbed by A1 adsorbent, as there is no evidence of new compound formation (metal hydroxides, metal oxides).

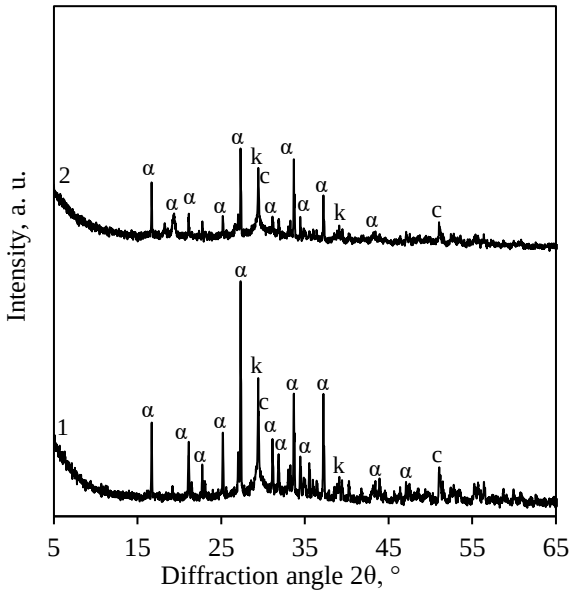

Fig. 3.12. XRD patterns of A1 adsorbent after the adsorption in copper (curve 1) and chrome (curve 2) nitrate solutions when the initial concentration was equal to 1.00 g Cu^{2+} or Cr^{3+}/L; indexes: α – α-C_2SH, k – $CaCO_3$, c – C-S-H(I), and/or C-S-H(II)

The previous results were confirmed by the data of STA analysis. According to literature [134], the first endothermic effect can be assigned to the dehydration of amorphous structure calcium silicate hydrates and/or removal of the adsorption water. It was calculated that after the adsorption, the mass loss and the heat of the mentioned thermal conversion increased two times (Fig. 3.13, Table 3.3).

According to the TGA data, the adsorbent lost 5.25% of the mass during the decomposition of A1 adsorbent (Table 3.3), which is equivalent to 55.42% of A1 adsorbent. It was determined that after the adsorption, the amount of the mentioned compound decreased to 33.99% in $Cu(NO_3)_2 \cdot 3H_2O$ and 21.01% in $Cr(NO_3)_3 \cdot 9H_2O$ solutions (Fig. 3.13). These data were in good agreement with the results of Ca^{2+} desorption and XRD (Fig. 3.11, Fig. 3.12). Meanwhile, in the case of Cu^{2+} ions, the increment in the intensity of the third endothermic effect confirmed that during the adsorption experiments, the carbonization proceeded (Fig. 3.13). Additionally, an exothermic effect, which can be assigned to the recrystallization of semi-crystalline C-S-H, was shifted towards the lower temperature (Fig. 3.13 a, b). It can be explained by the intercalation of Cu^{2+} ions or the decrement in crystallinity [135]. In order to avoid the interaction between Cr^{3+} ions and platinum crucibles, which were used for the STA analysis, the experiment was carried out only at 540 °C.

Table 3.3. The mass loss and heat of A1 adsorbent after the synthesis and adsorption process

	Mass loss, %							
	90–140 °C		460–470 °C		625–705 °C		700–710 °C	
	Δm, %	Q, J/g	Δm, %	Q, J/g	Δm, %	Q, J/g	Δm, %	Q, J/g
A1 adsorbent	2.77	84	5.25	189	0.32	22	-	-
A1-Cu sample	5.43	153	3.22	145	-	-	2.33	61
A1-Cr sample	4.83	381	1.99	34	-	-	-	-

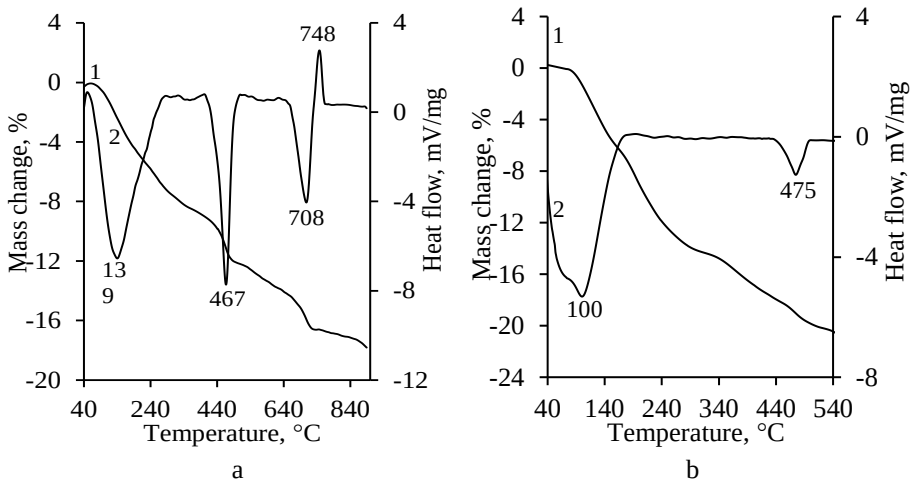

Fig. 3.13. STA curves (curve 1 – TG, curve 2 – DSC) of A1 adsorbent after the adsorption in $Cu(NO_3)_2 \cdot 3H_2O$ (a) and $Cr(NO_3)_3 \cdot 9H_2O$ (b) solutions when the initial concentration of Cu^{2+} or Cr^{3+} was equal to 1 g/L

In order to determine the maximum adsorption capacity of A1 adsorbent for Cu^{2+} and Cr^{3+}ions, the concentration of these ions was increased to 10 g/L. It has been found that at the beginning of Cu^{2+} ions adsorption (30 s), the adsorbed amount of the mentioned ions increased rapidly to 228.2 mg/g, and after 30 min, it was equal to 615.54 mg/g (Fig. 3.14 a). Meanwhile, in the case of Cr^{3+}ions adsorption, the removal efficiency was ~2.5 times lower, and the amount of incorporated ions was equal to 241.42 mg Cr^{3+}/g (Fig. 3.14 b). During the adsorption, more than 50% of Ca^{2+} ions were released from the adsorbent into the liquid medium in both cases.

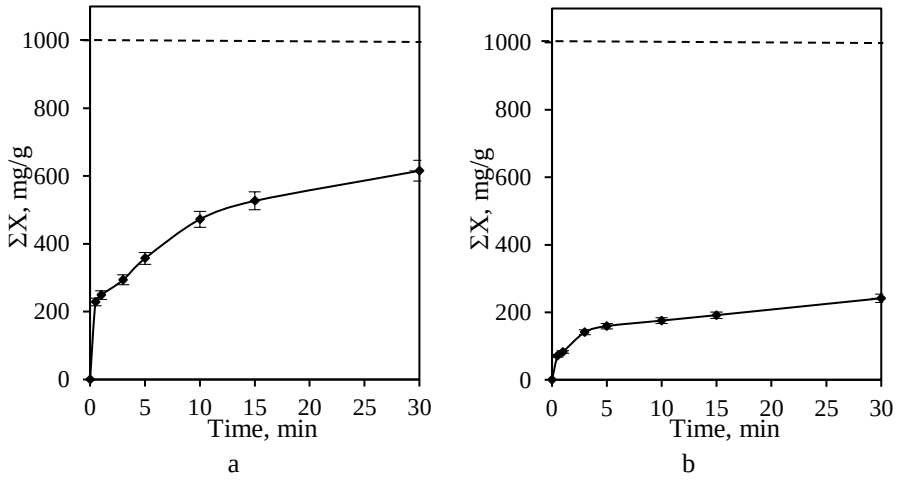

Fig. 3.14. The integral kinetic curve of Cu^{2+} (a) and Cr^{3+} (b) ions adsorption by A1 adsorbent when the initial concentration of ions was equal to 10 g/L

It was estimated that after the adsorption experiments, A1 adsorbent was fully decomposed because the diffraction peaks that are typical to this compound were not detected in the XRD patterns (Fig. 3.15 a). It is worth mentioning that in the copper nitrate solution, the precipitation of gerhardtite $Cu_2(NO_3)(OH)_3$ (PDF No. 04-011-9699) proceeded. The formation of this compound can be explained by a high concentration of OH^- anions, which were released with Ca^{2+} cations, and the low stability of metal ions in the alkaline medium. The formation of the mentioned compound was confirmed by the STA data (Fig. 3.15 b): at 237 °C temperature, the decomposition of gerhardtite proceeded [136].

$$4Cu_2(OH)_3NO_3 \rightarrow 8CuO + 4NO_2 + O_2 + 6H_2O$$

The endothermic effect at 400–500 °C temperature, a characteristic of α-C_2SH, was not observed (Fig. 3.15 b).

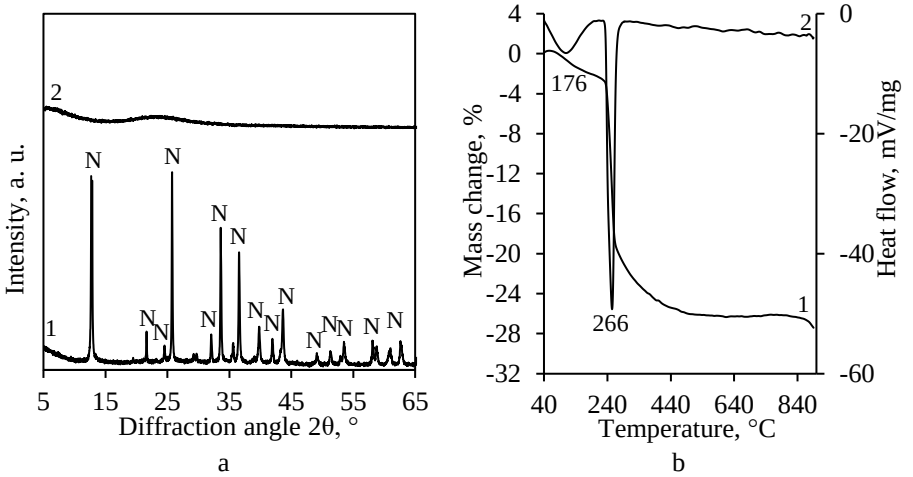

Fig. 3.15. XRD patterns (a) of A1 adsorbent after the adsorption in Cu^{2+} (curve 1) and Cr^{3+} (curve 2) ions solutions and STA curves (curve 1 – TG, curve 2 – DSC) (b) after the adsorption in Cu^{2+} solution when the initial concentration was equal to 10.00 g Cu^{2+} or Cr^{3+}/L; indexes: N – $Cu_2(NO_3)(OH)_3$

Therefore, it can be stated that a pseudo-second-order kinetics model adequately describes the Cu^{2+}, Co^{2+}, and Cr^{3+} ions adsorption mechanism by A1 adsorbent. It should be noted that a pseudo-second-order kinetics model describes chemisorption; thus, the A1 adsorbent acts more as a chemisorbent [137].

Thus, synthetic A1 adsorbent is a promising chemosorbent for the removal of heavy metal ions from the liquid medium, since its adsorption capacity for Cu^{2+}, Co^{2+}, and Cr^{3+} ions are 2–10 times higher than other adsorbents (hydrotalcite, C-S-H (I), zeolites) [138–140]. It should be noted that the adsorption process with the mentioned adsorbents proceeds 2–3 times slower in comparison with synthetic A1 adsorbents [141].

3.2. The adsorption peculiarities for heavy metals, the structure properties and microstructure parameters of A2 adsorbent

3.2.1. The adsorption peculiarities for heavy metals of A2 adsorbent

As the structure of the A1 adsorbent becomes unstable at high concentration heavy metals solution, the adsorption properties of the synthetic amorphous structure A2 adsorbent were investigated, i.e., $Co(NO_3)_2 \cdot 6H_2O$, $Cu(NO_3)_2 \cdot 3H_2O$, and $Cr(NO_3)_3 \cdot 9H_2O$ solutions, which contained 0.25, 1, and 10 g Me^{x+}/L (where Me^{x+} is Co^{2+}, Cu^{2+}, and Cr^{3+} ions, respectively). It has been determined that in $Cr(NO_3)_2 \cdot 6H_2O$ solution containing 1 g Cr^{3+} ions, the adsorption process proceeded intensively at the beginning, because already after 0.5 min of adsorption, the amount of intercalated Cr^{3+} ions reached 100% (100.00 mg Cr^{3+}/g A2 adsorbent) (Table 3.4). Almost the same tendency was observed in the case of Cu^{2+} ions. After 0.5 min of interaction, the amount of adsorbed ions was equal to 92.00 mg Cu^{2+}/g A2 adsorbent, and after 1 min, the process was completed (Table 3.4). Meanwhile, the uptake of Co^{2+} ions by A2 adsorbent was slower, because after 30 s of the process, only 62% (62.50 mg Co^{2+}/g

A2 adsorbent) of mentioned ions were intercalated into the adsorbent (Table 3.4). It was established that the adsorption of Co^{2+} ions was completed only after 15 min.

Table 3.4. The amount of adsorbed metal ions by A2 adsorbent in 1 g/L solution

Metal ions	Time, min/The amount of adsorbed Me^{x+} ions, mg/g						
	0.5	1	3	5	10	15	30
Cr^{3+}	100	100	100	100	100	100	100
Cu^{2+}	92.00	100	100	100	100	100	100
Co^{2+}	62.50	74.55	79.90	85.46	99.69	100	100

In order to determine the adsorption kinetic parameters, the pseudo-first-order and pseudo-second-order equations were applied [142]. Due to the fast penetration of Cu^{2+} and Cr^{3+} ions into the A2 adsorbent, the adsorption data could not be used to calculate the mentioned parameters. For this reason, these calculations were only applied for the adsorption of Co^{2+} ions. The data of the pseudo-first-order equation showed that this equation is not suitable for Co^{2+} ions adsorption mechanism description, because the value of correlation coefficient R^2 was equal to 0.8, and the calculated $q_{e(cal)}$ (50.11 mg/g) value disagreed with the experimental $q_{e(exp)}$ (99.30 mg/g) one (Table 3.5). According to the literature, the equation is suitable only if the errors between the mentioned values do not exceed 5% [143, 144].

The obtained results of pseudo-second-order equation showed that the correlation coefficient was equal to 0.99, and the agreement between calculated $q_{e(cal)}$ (98.23 mg/g) and the experimental $q_{e(exp)}$ (99.30 mg/g) values were observed. Thus, it can be stated that the pseudo-second-order equation adequately described the adsorption process of Co^{2+} ions by A2 adsorbent. It is worth mentioning that these experimental results were in good agreement with the data in literature, and they confirmed that in this case, A2 adsorbent acts as a chemisorbent [145–147].

Table 3.5. Co^{2+} ions adsorption kinetic parameters of the pseudo-first- and pseudo-second-order kinetic models

Kinetic parameters of the pseudo-first-order kinetic models			
R^2	$q_{e(exp)}$, mg/g	$q_{e(cal)}$, mg/g	k_1, g/(mg·min)
0.80	99.30	50.11	0.331
Kinetic parameters of the pseudo-second-order kinetic model			
R^2	$q_{e(exp)}$, mg/g	$q_{e(cal)}$, mg/g	k_2, g/(mg·min)
0.99	99.30	98.23	0.015

After the adsorption process, the A2 adsorbent was characterized by XRD. X-ray diffraction analysis data showed that during and after the adsorption experiments, the carbonization of A2 adsorbent proceeded, because the intensive diffraction peaks, characteristic of calcium carbonate, were identified (Fig. 3.16). It is worth mentioning that the intensity of the mentioned peaks was ~2 times higher in the A2-Co sample and A2-Cu sample, comparing them to the A2-Cr sample. It should be indicated that the diffraction peaks, characteristic of α-C_2SH, were not observed in XRD patterns.

In the A2-Cr sample, a low intensity diffraction peaks of chromium hydroxide hydrate ($Cr(OH)_3 \cdot 3H_2O$, (PDF No. 00-016-0817)) were identified (Fig. 3.16, curve 3).

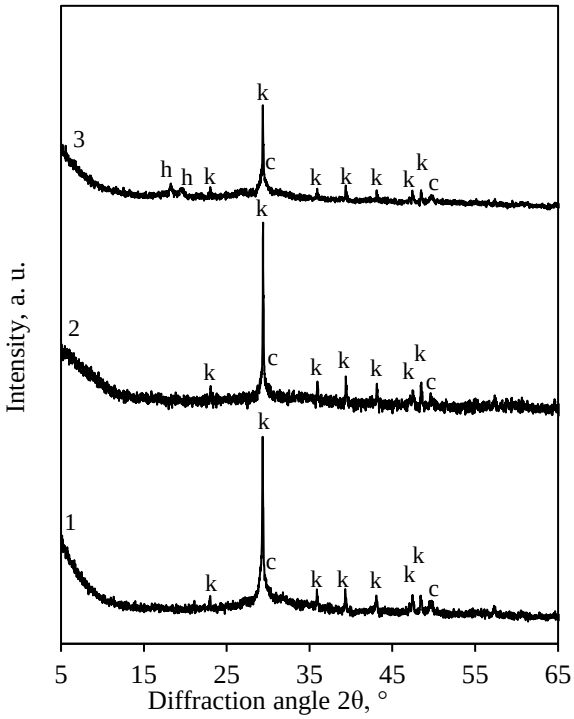

Fig. 3.16. XRD patterns of A2-Cu sample (curve 1), A2-Co sample (curve 2), and A2-Cr sample (curve 3); indexes: k – $CaCO_3$, h – $Cr(OH)_3 \cdot 3H_2O$, c – C-S-H(I), and/or C-S-H(II)

The previous results were confirmed by the data of STA. The DSC curves of A2 adsorbent samples showed two endothermal effects, where the first one is related to the removal of adsorption/crystallization water and the second one, to the decomposition of $CaCO_3$ (Fig. 3.17). Moreover, it was estimated that during the decomposition of the latter compound, the mass loss was equal to 4.45% in a case of A2-Cu sample, 5.12% in a case of A2-Co sample, and 2.65% in a case of A2-Cr sample, which was equivalent to 10.11%, 11.64%, and 6.03% of calcium carbonate, respectively (Table 3.6). Presumably, the exothermic effects at 730 °C (A2-Cu sample) and 779 °C (A2-Co sample) are related to the formation of metal oxides (Fig. 3.17 a, b). Meanwhile, at ~830 °C temperature, the exothermic effects occur due to the recrystallization of semicrystalline compounds to wollastonite in the A2-Co sample and A2-Cr sample (Fig. 3.17 b, c). It is worth mentioning that during Cu^{2+} ions adsorption, C-S-H(I) and/or C-S-H(II) were decomposed, because the exothermic effect at 830–850 °C temperature was not observed in the DSC curve (Fig. 3.17 a).

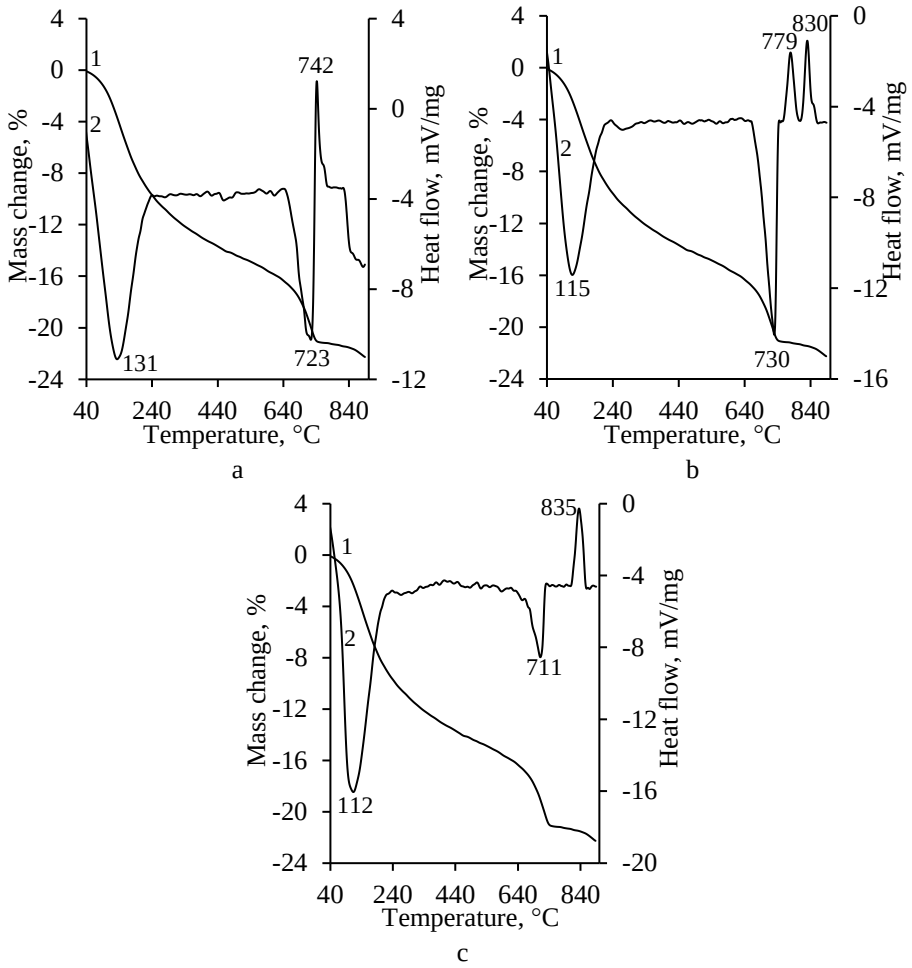

Fig. 3.17. STA curves (curve 1 – TG, curve 2 – DSC) of A2-Cu sample (a), A2-Co sample (a), and A2-Cr sample (a)

Table 3.6. The loss on ignition of A2 adsorbent substituted with metal ions

Sample	Loss on ignition, %		
	50–240 °C	650–770 °C	Total
A2-Cu sample	9.85	4.45	22.45
A2-Co sample	10.33	5.12	22.88
A2-Cr sample	15.50	2.65	26.05

It was observed that the FT-IR spectrum of A2 adsorbent substituted with the metal ions was significantly changed in the region of silicate vibrations (Fig. 3.18) in comparison to the pure system [148]. The intensity of the adsorption band of δ(O–Si–

O) vibration (~465 cm^{-1}) decreased more than 2.5 and 9 times in the A2-Co sample and A2-Cu sample, respectively (Fig. 3.18). Moreover, in the A2-Cr sample and A2-Cu sample, the stretching signals of ν_s(Si–O–Si) almost disappeared. It should be noted that in the A2-Cr sample, the $\nu(-CO_3^{2-})$ vibrations were determinate at 1489, 1413 cm^{-1}, and 873 cm^{-1} (Fig. 3.18, curve 3), while in the A2-Cu and A2-Co samples, the higher wavenumber disappeared, and respectively, 1454 cm^{-1}, 873 cm^{-1}, and 1424 cm^{-1}, 874 $cm^{-1}\nu(-CO_3^{2-})$ stretching signals were investigated (Fig. 3.18, curve 1, 2). The changes of FT-IR spectrum in the 800–2000 cm^{-1} range can be associated with the intercalation of metal ions into the crystal structure of the adsorbent.

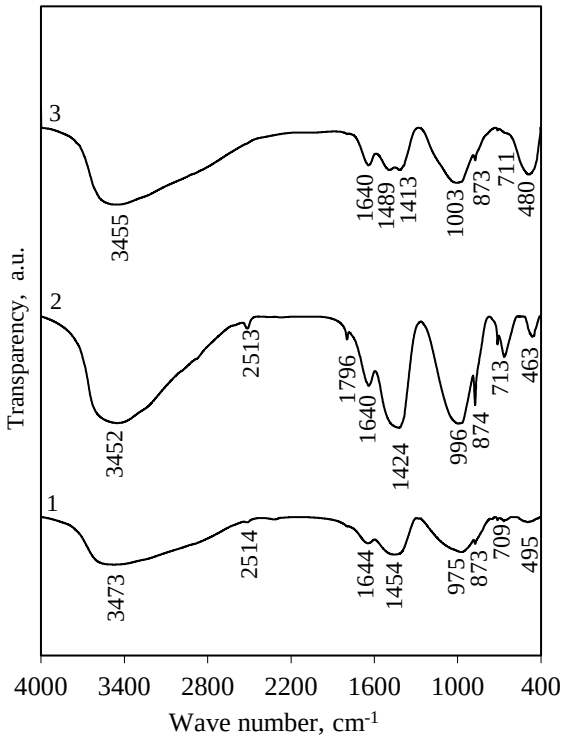

Fig. 3.18. FT-IR spectrum of A2-Cu sample (curve 1), A2-Co sample (curve 2), and A2-Cr (curve 3) sample

The previous results were in good agreement with the data of SEM analysis (Fig. 3.19). The SEM micrograph of the A2 adsorbent was packed and interspersed with thin crystals (called foils or honeycomb) [149, 150]. It has been determined that after the adsorption process, the mentioned structure was partially destroyed. The metal ions incorporation was as well proven by the SEM/EDX analysis: in all samples, ~30% of metal ions were observed (Fig. 3.19). It is worth mentioning that SEM/EDX analysis has shown that the round crystals in the A2-Cr sample consist of mainly Cr^{3+} ions. Thus, these crystals can be attributed to the compounds, which contain chromium. These data agree with the XRD results, where $Cr(OH)_3 \cdot 3H_2O$ was identified (Fig. 3.16).

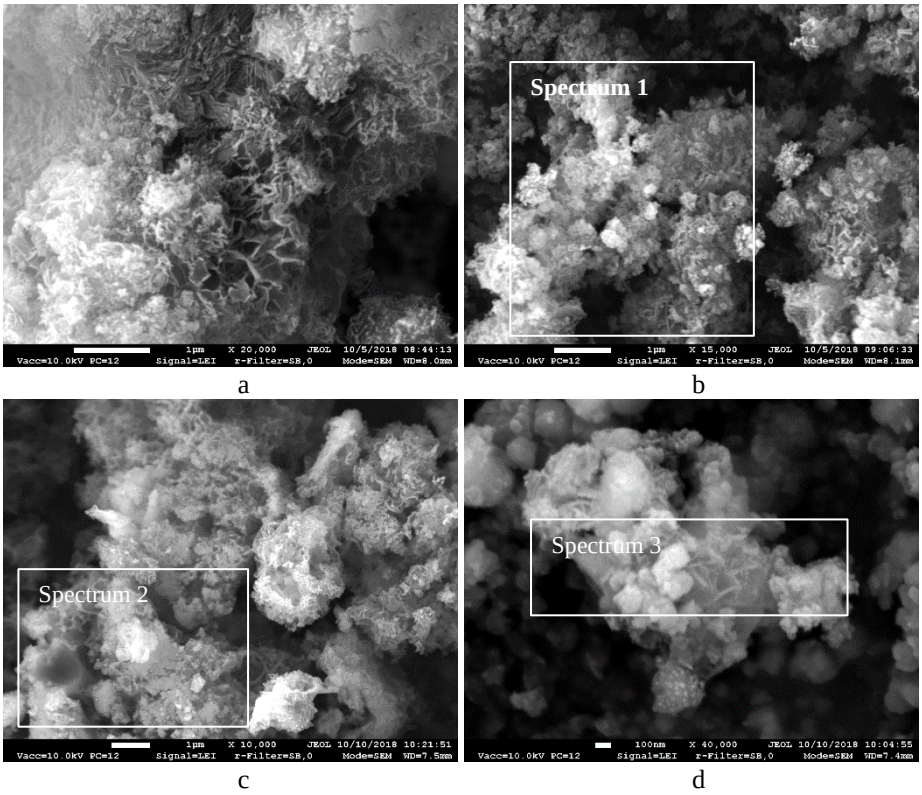

Fig. 3.19. SEM images of A2 adsorbent (a), A2-Cu sample (b), Spectrum 1: Cu – 31.18, Si – 10.78, Ca – 13.69, O – 44.34 mass %, A2-Co sample (c), Spectrum 2: Co – 28.95, Si – 15.84, Ca – 10.66, O – 44.55 mass %, and A2-Cr sample (d), Spectrum 3: Cr – 59.86, Si – 6.33, Ca – 6.34, O – 27.47 mass % samples; magnification: a – 20 000 times, b – 15 000 times, c – 10 000 times, and d – 40 000 times

3.2.2. The structure properties and porosity of A2 adsorbent

It is known that one of the most important parameters of materials is thermal stability, which leads to the successful application [151, 152]. For this reason, in the next part of this work, the thermal stability of A2 adsorbent was investigated In Situ XRD in 25–1000 °C temperature range (Fig. 3.20). The calcination was carried out at a heating rate of 50 °C/min after the equilibration for 5 min at the desired temperature. It was estimated that the dibasic A2 adsorbent is stable up to 400 °C temperature, because the diffraction maximums that are typical to this compound remained unchanged. Meanwhile, at a higher temperature (450 °C), α-C_2SH recrystallized to anhydrous C_2S phases [153]. However, due to the small intensity of its diffraction peaks, the formed compounds could not be identified.

Furthermore, when the calcination temperature was increased to 650 °C, calcium carbonate decomposed, and the peaks of calcium oxide (PDF No. 00-002-1088) were observed in the XRD patterns. It has been determined that at 800–850 °C temperature, the semicrystalline type compounds and C_2S phases recrystallized to

wollastonite (PDF No. 00-066-0271) and β-C_2S (PDF No. 00-033-0302). In the 850–1000 °C temperature range, the diffraction peaks, characteristic to the mentioned compounds, were increased. The present results were in good agreement with the data that have been obtained by the other authors [154].

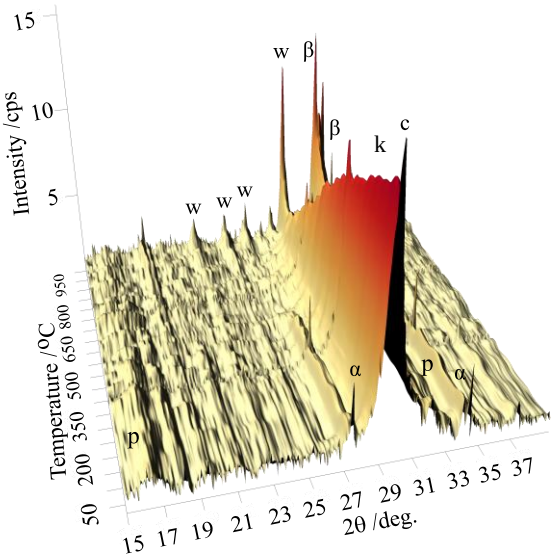

Fig. 3.20. In Situ XRD patterns of the A2 adsorbent, when the temperature of calcination varied in 25–1000 °C range; indexes: α – α-C_2SH, k – $CaCO_3$, c – C-S-H(I), and/or C-S-H(II), w – wollastonite, β – β-C_2S

In order to evaluate the structural transformations and how the physical parameters of the material change, the synthetic sample was calcined in the furnace "Nabertherm LH 15/13" at 750 °C (this temperature was chosen to investigate the porosity of sample at the beginning of wollastonite and β-C_2S formation) and 850 °C (this temperature was chosen to investigate the sample structural changes when wollastonite and β-C_2S started to be form) temperatures for 24 h. It was obtained that after the calcination at 850 °C temperature, wollastonite and β-C_2S were formed (Fig. 3.21 a). The formation of wollastonite and β-C_2S in the A2 adsorbent sample after the calcination was confirmed by the SEM analysis: the plate-shaped crystals of wollastonite and oval crystals characteristic of β-C_2S were observed (Fig. 3.21 b) [155–157]. The XRD and SEM results were verified with FT-IR analysis. Meanwhile, the symmetrical stretching signals at 644 cm^{-1} (Si–O–Si) were observed. It should be noted that the absorption signal at ~707 cm-1, reflecting the symmetrical νs(Si–O–Si) stretching vibrations, a significant shift up to 682 cm^{-1} was noticed. Meanwhile, the adsorption signals at ~908 cm^{-1} and ~987 cm^{-1}, which can be attributed to the symmetrical ν(O–SiO–) stretching signals, were observed [158, 159].

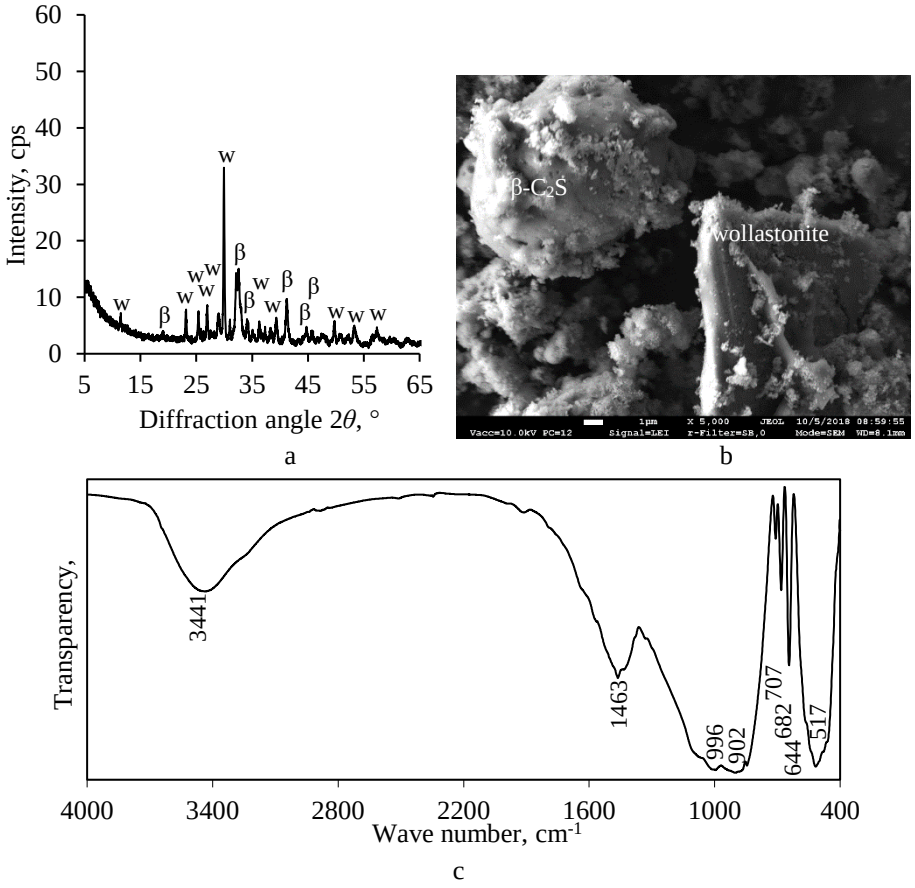

Fig. 3.21. XRD pattern (a), SEM image (magnification of 5000 times) (b), and FT-IR spectrum (c) of A2 adsorbent calcined at 850 °C temperature; indexes: w – wollastonite, β – β-C_2S

It is known that one of the most important parameters of all catalysts is surface area, which leads to a successful application. Thus, in order to determine the specific surface area, the nitrogen gas adsorption, combined with the Brunauer, Emmett, and Teller (BET) equation, was performed.

The nitrogen adsorption-desorption isotherms of adsorbent and calcined adsorbent samples are presented in Fig. 3.22. The adsorption isotherm of synthetic adsorbent can be classified as Type II (does not have plateau at $P/P_0 > 0.7$) or Type IV (the presence of hysteresis loop) (Fig. 3.22 a). This uncertainty occurs due to the presence of macro-pores in the sample that cause the unrestricted multilayer adsorption on the surface. A similar shape of adsorption isotherms is as well presented in other calcium silicate hydrate samples and can be used for the calculations of surface area (by using the BET equation) and the dominant shape of pores [98, 160, 161].

The adsorption and desorption isotherms of adsorbent do not coincide with the P/P_0 range of 0.66–0.95, i.e., the hysteresis loop is formed (Fig. 3.22 a). The hysteresis

loop of adsorbent can be classified as Type H1, which is a characteristic for mesoporous materials, in which spherical particles or well-defined cylindrical-like pore channels are dominant [162]. According to the literature [97], in this type of isotherm, the plateau should be presented; however, due to the presence of pores between parallel plates and/or macro-pores, the plateau is not observed. The existence of macro-pores was confirmed by the SEM micrographs where huge pores can be seen between the particles of adsorbent (Fig. 3.23 a). These results are in good agreement with other authors, whom state that during hydrothermal synthesis of calcium silicate hydrates, cylindrical-like, slit-like, or ink-bottle pores can be presented in the products [162, 163].

The remarkable changes in the shape of adsorption-desorption isotherms of nitrogen on calcined adsorbent (750 °C) were observed (Fig. 3.22 b): the adsorption isotherm corresponds to Type II and does not have the hysteresis loop. Such type of isotherm is present in non-porous or macro-porous materials [161, 164]. The changes can be explained by the sintering of adsorbent particles during the calcination process. This fact was confirmed by the TEM analysis where sintered smooth particles/crystallites were detected (Fig. 3.23 b). It is worth mentioning that this type of isotherms can be used for the calculations of BET surface area; however, the calculations of the shape of dominant pores are meaningless.

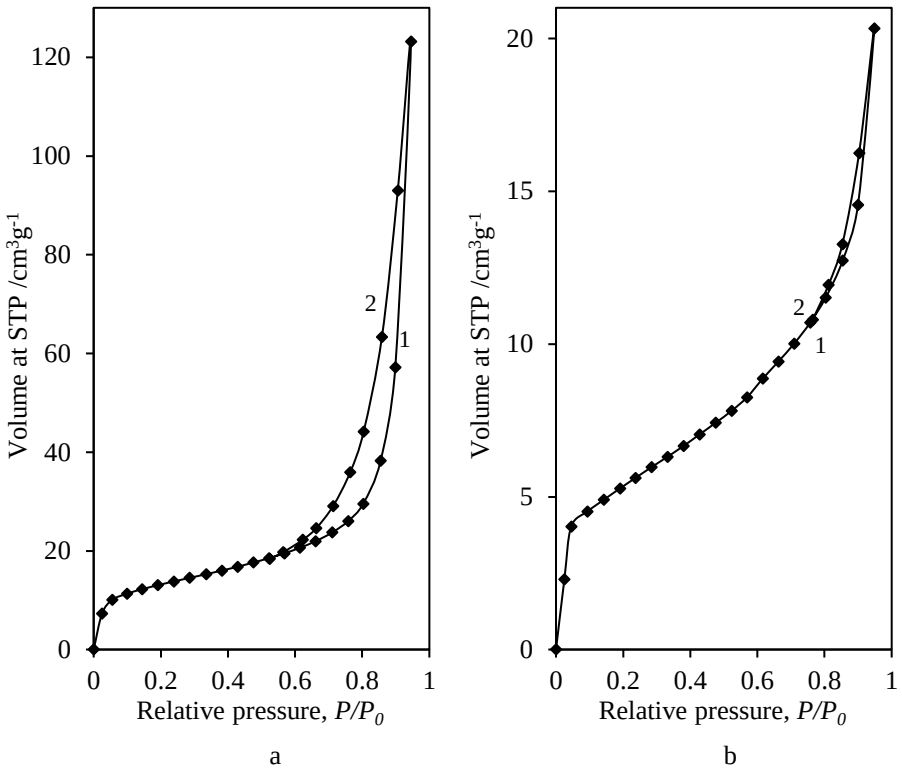

Fig. 3.22. Nitrogen adsorption (1), desorption (2) isotherms of A2 adsorbent (a) and A-750 sample (b)

The presently discussed results were confirmed by the TEM data (Fig. 3.23). The TEM micrograph showed disordered uncertainly shaped crystallites of cylindrical pores crystalline phase C-S-H and parallel plates crystallites of α-C_2SH (Fig. 3.23 a). The analysis of the A2-750 sample (Fig. 3.23 b) showed oval crystals of β-C_2S [157].

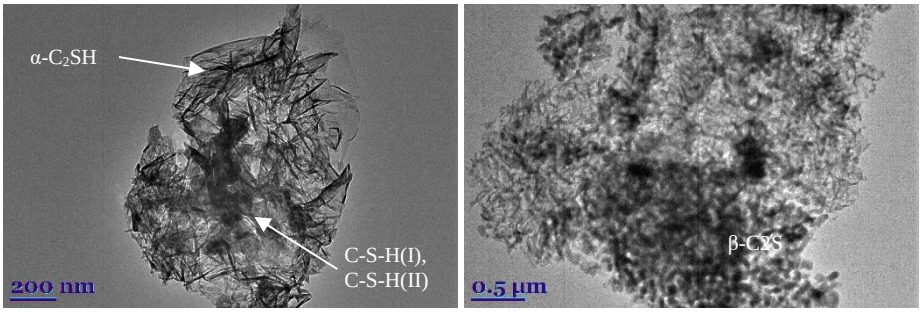

a b

Fig. 3.23. TEM micrographs of A2 adsorbent (a) and A2-750 sample (b)

According to the literature [100, 161], the BET method can be used to calculate the surface area of samples that are characterized by Type II and Type IV adsorption isotherms. The calculations by the mentioned method are valid if a straight line in BET coordination $(1/(X[(P_0/P) - 1])) - (P_0/P)$ is obtained, and the value of C_{BET} constant is higher than 2 (in the ideal case varying from 50 to 150–250) (Fig. 3.24). The calculations revealed that in both cases, the reliability coefficient (R^2) is higher than 0.999, while the values of C_{BET} constant are equal to 233.78 (synthetic adsorbent) and 251.33 (calcined adsorbent) (Table 3.7). Thus, the calculations by the BET equation can be accepted as reliable. It has been determined that the surface area of synthetic and calcined adsorbent are equal to 46.13 m^2/g and 18.70 m^2/g, respectively. According to the literature [60, 165], the surface area of synthetic calcium silicate hydrates is equal to 30–500 m^2/g, while calcium silicates have a lower surface area: wollastonite – 2 m^2/g, kilchoanite – 6 m^2/g, rankinite – 11.7 m^2/g, etc. [166–168].

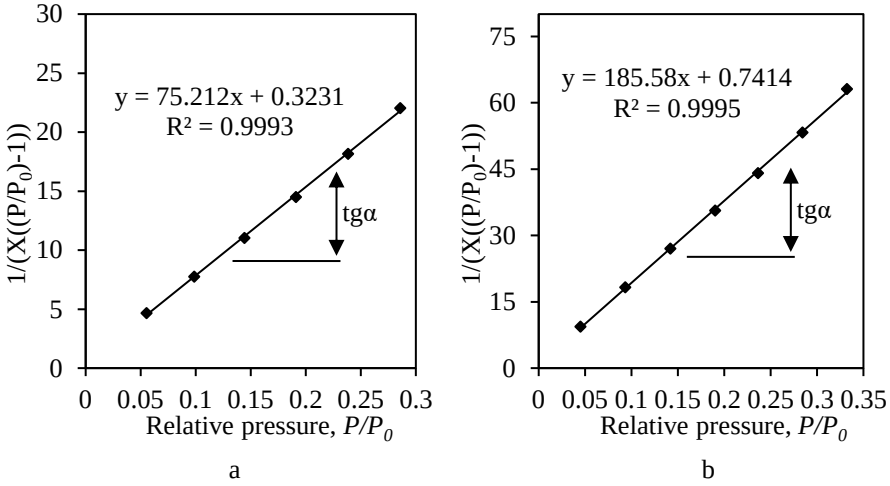

a b

Fig. 3.24. The isotherm of N_2 adsorption at 77 K in the BET plot of A2 adsorbent (a) and A2-750 sample (b)

Table 3.7. Calculated parameters of A2 adsorbent and A2-750 sample by the BET method

Sample	BET equation constants		Capacity of mono layer X_m	S_{BET}, m^2/g	C_{BET} constant	Reliability coefficient, R^2
	Slope $S = tga$	Intercept I				
A2 adsorbent	75.21	0.32	0.013	46.13	233.78	0.9993
A2-750	185.58	0.74	0.005	18.70	251.33	0.9999

The application of adsorbents and later as a catalyst is limited by specific surface area and the total pore volume. In order to determine the cumulative pore volume, the shape of the pores should be known; however, the analysis of adsorption isotherms can be misleading. Thus, in order to confirm the results of the adsorption isotherms analysis and calculate the cumulative pore volume, the corrected Kelvin equation and the scheme developed by Orr et al. were applied. The calculations were performed by using the two most common models, i.e., cylindrical-like pores and slit-like pore models. The model is considered appropriate if the difference between S_{BET} and calculated surface area ($\sum A$) is insignificant (up to 20%). The summarized results of the calculations are given in Table 2. It has been obtained that the difference between S_{BET} and $\sum A$ values is significantly lower when using a cylindrical-like shape model than a parallel plates pore model. These results are in good agreement with the classification of the hysteresis loop as Type H1 (Fig. 3.22 a). Further calculations revealed that the cumulative pore volume ($\sum VP$) of the synthetic adsorbent is equal to 0.207 cm^3/g (Table 3.8).

Table 3.8. The data of ΣA and ΣV_P calculations of A2 adsorbent

Sample	S_{BET}, m^2/g	Results using a cylindrical pore model				Results using a parallel plates pore model			
		ΣA, m^2/g	$\lvert S_{BET} - \Sigma A \rvert$, m^2/g	$\lvert S_{BET} - \Sigma A \rvert$, %	ΣV_P, cm^3/g	ΣA, m^2/g	$\lvert S_{BET} - \Sigma A \rvert$, m^2/g	$\lvert S_{BET} - \Sigma A \rvert$, %	ΣV_P, cm^3/g
A2 ads.	46.13	52.29	6.16	13.34	0.207	35.39	10.74	23.29	0.188

It was calculated that the value of the cumulative pore volume of A2 adsorbent sample depends on the used model and is equal to (V_p) 0.207 (Table 3.8). The differential distributions of volume pore sizes showed that the A2 sample is mesoporous material, because the pores with 3–12 nm diameter are dominant (Fig. 3.25).

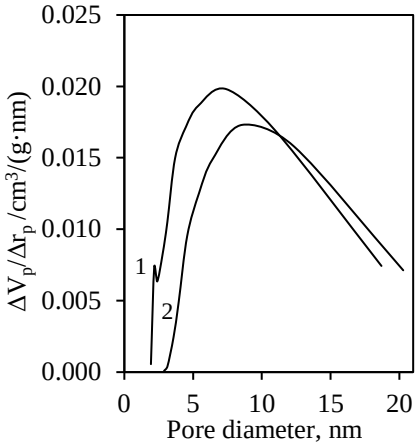

Fig. 3.25. Differential distributions of volume pore sizes of A2 adsorbent; indexes: 1 – values obtained using a cylindrical-like pore model, 2 – values obtained using a slit-like pore model

3.2.3. Texture and microstructure parameters of A2 adsorbent substituted with Cu^{2+} ions

In the next part of this work, the thermal stability of A2 adsorbent substituted with Cu^{2+} ions were proved by In Situ XRD experiment (Fig. 3.26). It has been determined that the investigated sample was stable when the temperature varied in 25–600 °C temperature range (Fig. 3.26). Meanwhile, at a higher temperature, the formation of metal oxide CuO (PDF No. 00-048-1548) and CaO (PDF No. 00-002-1088) were noticed. It should be indicated that the mentioned compounds remained stable up to 1000 °C. Moreover, when the temperature was increased to 700–750 °C and 800–850 °C, the decomposition of calcium carbonate and recrystallization of semicrystalline type compounds to wollastonite and β-C_2S, respectively, was observed.

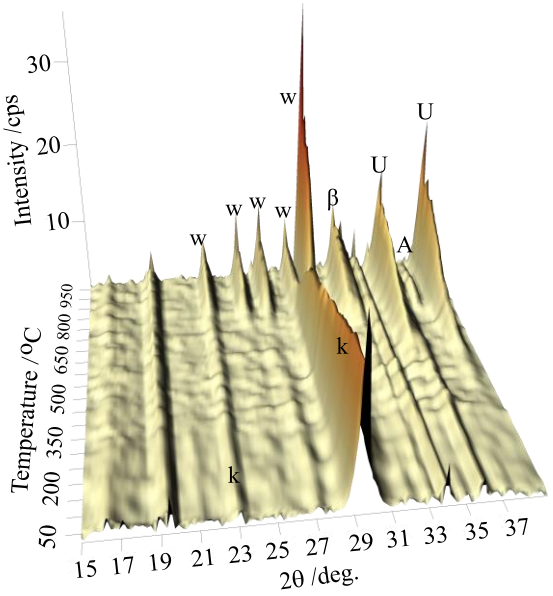

Fig. 3.26. In Situ XRD pattern of A2-Cu-Cu sample; indexes: k – $CaCO_3$, A – CaO, U – CuO, w – wollastonite, β – β-C_2S

These In Situ XRD results were confirmed by the calcination experiment (Fig. 3.27). It was observed that during the calcination at 600 °C, the formation of CaO and CuO starts (Fig. 3.27 a). The proceeding calcination, diffraction XRD patterns show that at 850 °C temperature, wollastonite, β-C_2S and heavy metals containing compounds were observed (Fig. 3.27 b). It should be noted that during the calcination from 600 °C to 850 °C temperature, the CuO intensity of the diffraction peaks increased 3–3.5 times. Meanwhile, the CaO intensity of the diffraction peaks increased 1.57 times.

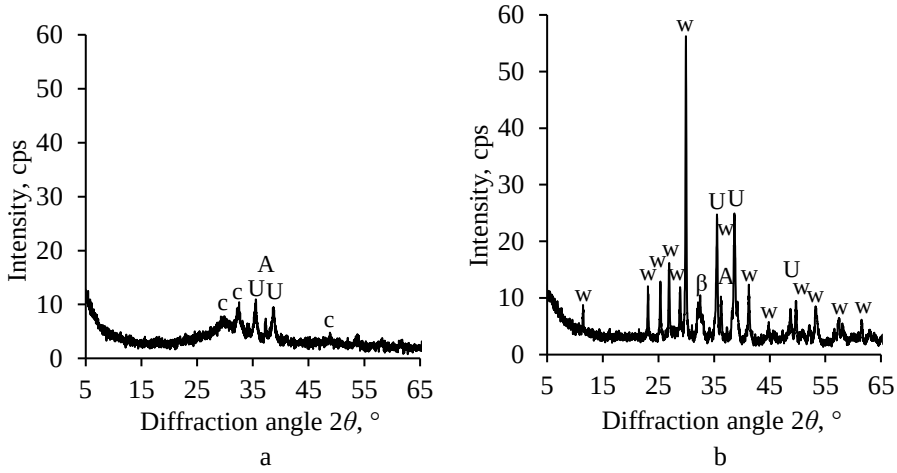

a b

Fig. 3.27. XRD patterns of A2-Cu600 sample (a) and A2-Cu850 sample (b); indexes: c – C-S-H(I) and/or C-S-H(II), A – CaO, U – CuO, w – wollastonite, β – β-C_2S

The previous results were in good agreement with the data of SEM analysis (Fig. 3.28). The SEM micrograph of the A2-Cu600 sample showed that each other thin crystals, characteristic to C-S-H(I) and/or C-S-H(II), still dominated at the adsorbent structure (Fig. 3.28 a). The formations of wollastonite and β-C2S compounds are determined in a sample, calcinated at 850 °C temperature (Fig. 3.28 b). The metal ions incorporation was as well proved by the SEM/EDX analysis: it was calculated that ~20% of Spectrum 1 was concluded with Cu^{2+} ions (Fig. 3.28 b).

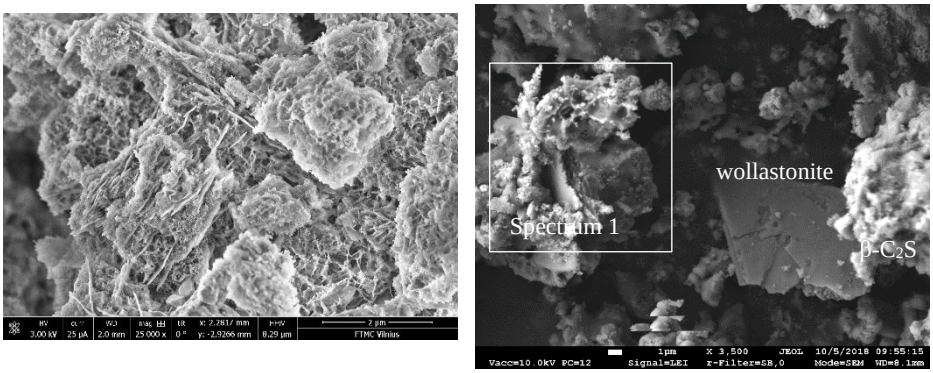

a b

Fig. 3.28. SEM images of A2-Cu600 (a) and A2-Cu850 (b) (Spectrum 1: Cu – 19.43, Si – 20.56, Ca – 35.63, O – 24.37 mass %) samples; magnification: a – 25 000 times, b – 3 500 times

In the previous study, it has been shown that the adsorbent with intercalated copper ions is stable up to 600 °C temperature, while at a higher temperature, CuO and CaO were formed. Thus, the adsorbent after the adsorption of Cu^{2+} ions as well

as after the calcination at 600 °C temperature was characterized by nitrogen adsorption.

It has been found that the intercalation of Cu^{2+} ions influences the shape of nitrogen adsorption-desorption isotherms (Fig. 3.29). The adsorption isotherm of the A-Cu sample is steeper than the synthetic adsorbent, but as in a previous case, it can be classified as Type II or Type IV. Meanwhile, the hysteresis loop became narrower and closed at the lower value of P/P_0 (0.47). The assignment of the hysteresis loop of the A-Cu sample is complicated, because it has similarities to Type H1 and Type H3, i.e., it closes at P/P_0 equal to ~0.5 and is steep. It has been obtained that the calcination of A-Cu sample at 600 °C temperature does not have an influence on the shape of adsorption isotherm; however, the hysteresis loop can be classified as H1.

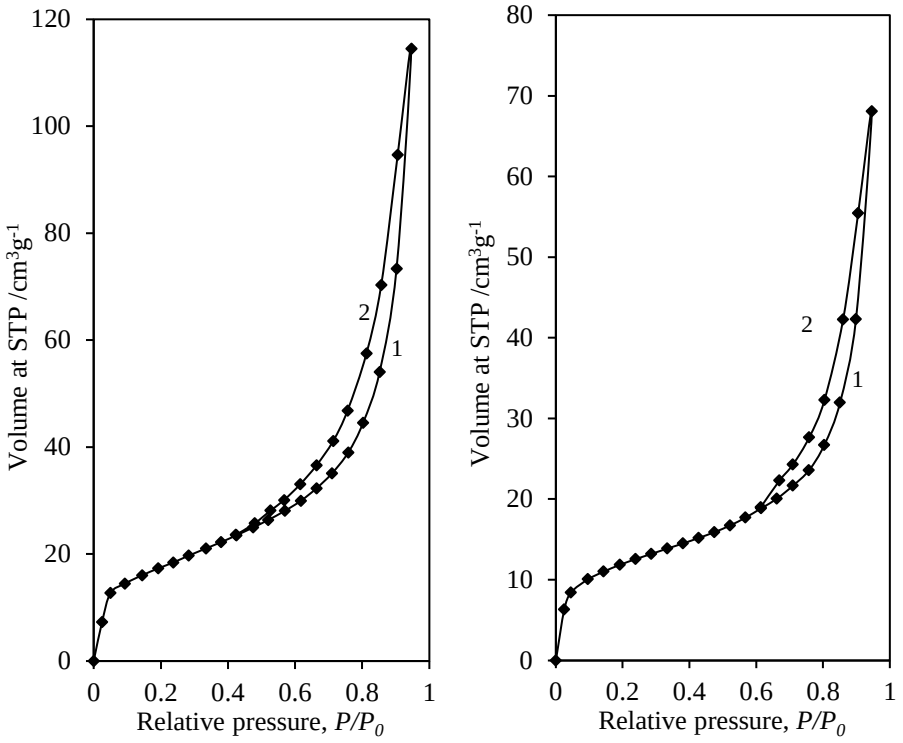

Fig. 3.29. Nitrogen adsorption (1) – desorption (2) isotherms of A2-Cu sample (a) and A2-Cu600 samples (b)

The results of the TEM analysis show that the hysteresis loop of samples can be classified as H1 because similar size oval crystallites are dominant in both samples (Fig. 3.30). It is worth mentioning that in the A-Cu sample, the needle crystallites were observed as well (Fig. 3.30 a); thus, the shape of the hysteresis loop has similarities to Type H3.

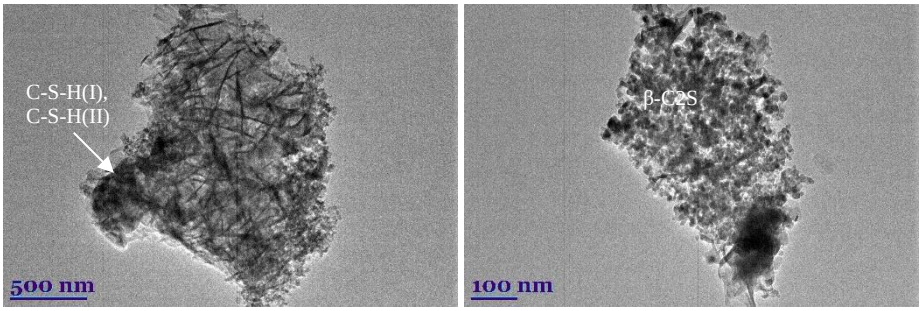

a b

Fig. 3.30. TEM micrographs of A2-Cu sample (a) and A2-Cu600 sample (b)

It has been determined that the calculations of surface area of A2-Cu and A2-Cu600 samples by using the BET equation are reliable, because the values of R^2 (> 0.99) and C_{BET} constant ($50 < C_{BET} < 250$) match the requirements (Table 3.9). The calculations revealed that after the adsorption of Cu^{2+} ions, the specific surface area of the adsorbent increased from 46.13 m^2/g to 63.31 m^2/g. As expected, during the calcination at 600 °C temperature, the latter value decreased to 42.38 m^2/g (Table 3.9).

The calculations of the dominant pore shape showed that the cylindrical-like pore model is more suitable than the parallel plates pore model, because the difference between S_{BET} and $\sum A$ values is significantly lower (Table 3.9). Even by using a cylindrical-like pore model, a high difference (~22%) between S_{BET} and $\sum A$ values was obtained, which can be explained by the fact that the spherical particles of similar size are dominant in the samples. Further calculations have shown that during the adsorption of Cu^{2+} ions on the adsorbent, the total pore volume decreased slightly (from 0.207 cm^3/g to 0.191 cm^3/g), despite the increase of specific surface area (Table 3.10). Finally, due to the particle compaction during the calcination, the value of $\sum VP$ decreased to 0.114 cm^3/g. Thus, the intercalated metal ions into the structure of the adsorbent changed the porosity of both synthetic and calcined samples. Since the adsorbent with intercalated copper ions is stable and during calcination does not lose porosity, it can be applied as a catalyst for the oxidation reactions.

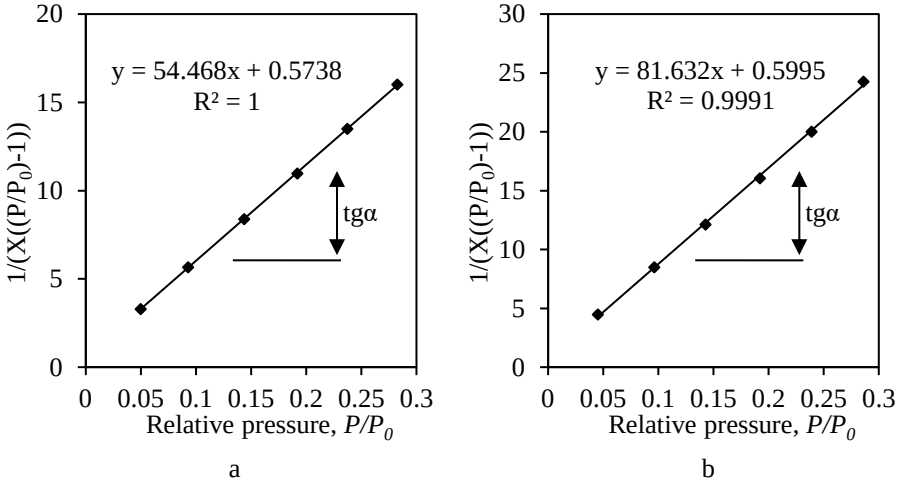

a b

Fig. 3.31. The isotherm of N_2 adsorption at 77 K in the BET plot of A2-Cu sample (a) and A2-Cu600 sample (b)

Table 3.9. Calculated parameters of A2-Cu sample and A2-Cu600 sample of the BET method

Sample	BET equation constants		Capacity of mono layer X_m	S_{BET}, m^2/g	C_{BET} constant	Reliability coefficient, R^2
	Slope $S = tga$	Intercept I				
A2-Cu	54.47	0.57	0.018	63.31	95.93	1
A2-Cu600	81.63	0.59	0.012	42.38	137.16	0.9991

Table 3.10. The data of ΣA and ΣV_P calculations of the A2-Cu sample and A2-Cu600 sample

Sample	S_{BET}, m^2/g	Results using a cylindrical pore model				Results using a parallel plates pore model			
		ΣA, m^2/g	$\lvert S_{BET} - \Sigma A \rvert$, m^2/g	$\lvert S_{BET} - \Sigma A \rvert$, %	ΣV_P, cm^3/g	ΣA, m^2/g	$\lvert S_{BET} - \Sigma A \rvert$, m^2/g	$\lvert S_{BET} - \Sigma A \rvert$, %	ΣV_P, cm^3/g
A2-Cu	63.31	77.22	13.91	21.97	0.191	39.29	24.02	37.94	-
A2-Cu600	42.38	51.89	9.51	22.44	0.114	21.49	20.89	49.29	-

Differential distributions of volume pore sizes showed that A2-Cu and A2-Cu600 samples are mesoporous material, because the pores with 2–10 nm diameter are dominant in both samples (Fig. 3.32).

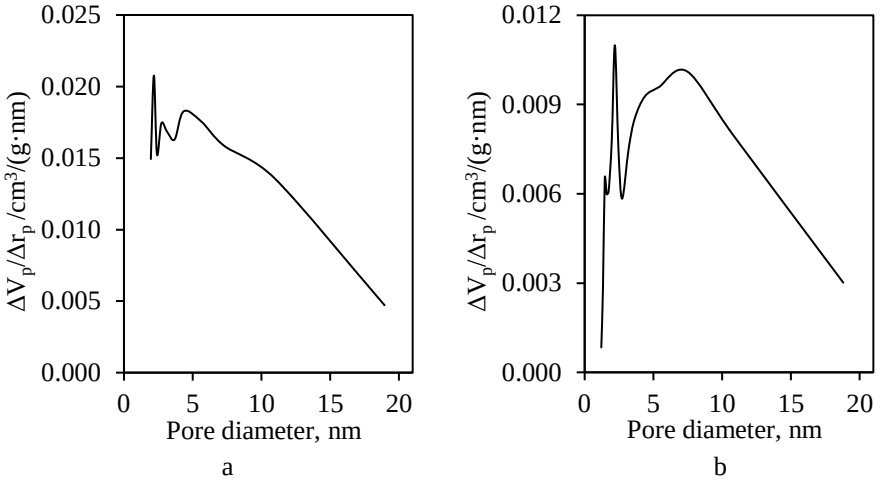

Fig. 3.32. Differential distributions of volume pores sizes of A2-Cu sample (a) and A2-Cu600 sample (b)

3.2.4. Texture and microstructure parameters of A2 adsorbent substituted with Co^{2+} ions

In order to determine the influence of Co^{2+} ions on the thermal stability and structural properties of the A2 adsorbent, an In Situ XRD experiment was performed in the next step of this work (Fig. 3.33). A2 adsorbent with incorporated Co^{2+} ions remained stable in a 25–700 °C temperature range. It should be mentioned that at 700 °C temperature, the formation of Co_3O_4 (PDF No. 00-043-1003) oxide was observed. It was determined that in the primary A2 adsorbent calcination experiment, at 700–750 °C and 800–850 °C temperatures, wollastonite, β-C_2S, and CaO compounds were identified in In Situ XRD patterns (Fig. 3.33).

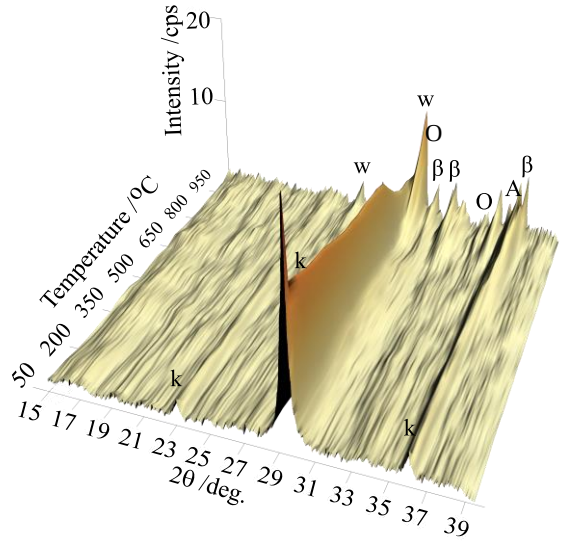

Fig. 3.33. In Situ XRD patterns of A2-Co sample in a 25–1000 °C temperature range; indexes: k – $CaCO_3$, A – CaO, O – Co_3O_4, w – wollastonite, β – β-C_2S

In order to provide In Situ XRD results, the calcination experiment was performed (Fig. 3.34). The XRD patterns show that at 700 °C temperature, the Co_3O_4 started formatting because the diffraction peaks of Co_3O_4 (*d*-spacing 0.285) were identified (Fig. 3.34 a). It has been determined that during the calcination at 850 °C temperature, one more Co_3O_4 diffraction peak (*d*-spacing 0.243) was observed (Fig. 3.34 b). Moreover, in higher temperatures, the calcite diffraction peak was no longer determined, and wollastonite, β–C_2S compounds were observed (Fig. 3.34).

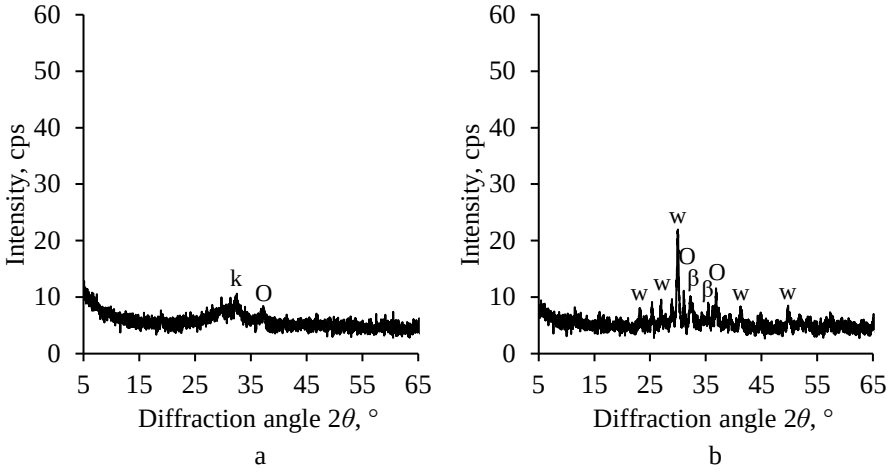

Fig. 3.34. XRD patterns of A2-Co700 sample (a) and A2-Co850 sample (b); indexes: k – $CaCO_3$, O – Co_3O_4, w – wollastonite, β – β-C_2S

Meanwhile, the SEM micrograph of the calcination A2-Co sample showed the sintered structure of products where the crystals of wollastonite and β-C_2S cannot be distinguished (Fig. 3.35). It is worth mentioning that the EDX analysis results have shown that the spectrum 1 consists of Co^{2+} (22.13%) ions (Fig. 3.35 b).

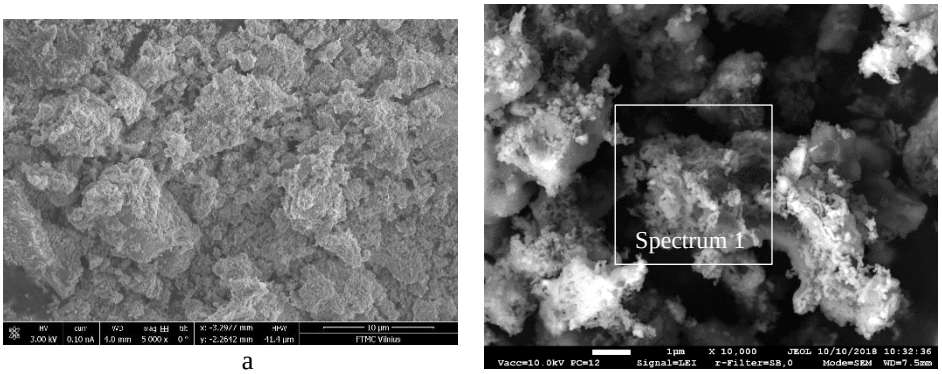

a

b

Fig. 3.35. SEM images of A2-Co700 (a) and A2-Co850 (b) (Spectrum 1: Co – 22.13, Si – 16.43, Ca – 21.91, O – 39.53 mass %); magnification: a – 5 000 times, b – 10 000 times

In the next part of this work, the adsorbent after the adsorption for cobalt ions as well as after calcination (750 °C) was characterized by the N_2 adsorption-desorption experiment. The calcination temperature was chosen based on the formation of cobalt oxide (Co_3O_4). The sample with intercalated Co^{2+} ions was labeled as A2-Co, while the adsorbent with intercalated Co^{2+} ions and after calcination at 750 °C was labeled as A2-Co750.

The nitrogen adsorption-desorption isotherms on A2-Co and A2-Co750 samples are presented in Fig. 3.36. As in a previous case, the adsorption isotherms of both samples can be classified as Type II or Type IV, which shows that in the samples, meso-pores and macro-pores are presented. Meanwhile, the hysteresis loop of the A2-Co sample is an intermediate case between Type H1 and Type H3 (Fig. 3.36 a), while the hysteresis loop of the A2-Co750 sample is typical Type H1 (Fig. 3.36 b).

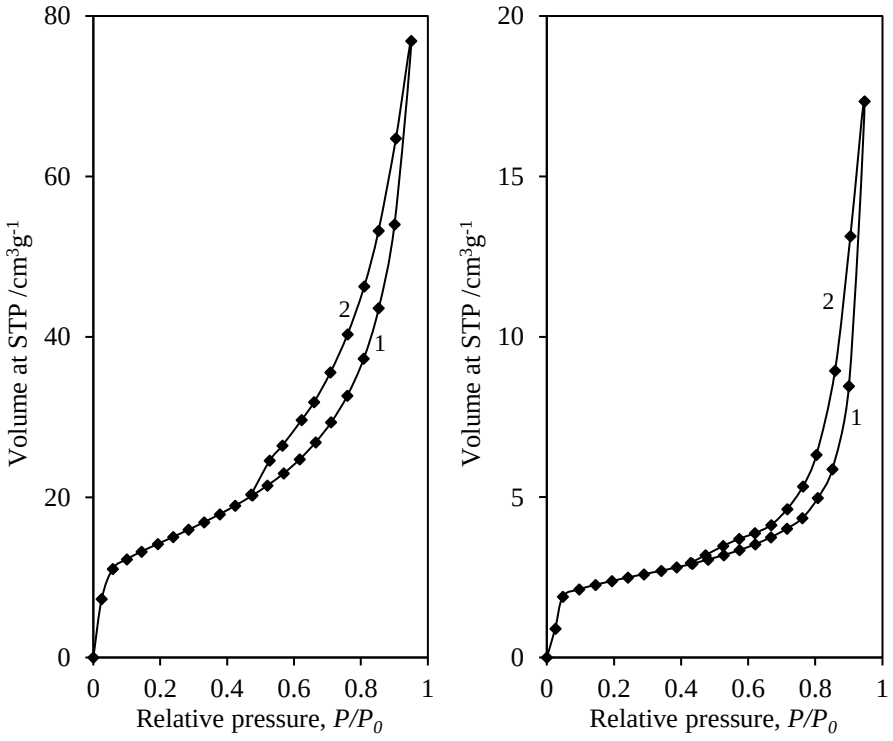

Fig. 3.36. Nitrogen adsorption (1) – desorption (2) isotherms of A2-Co sample (a) and A2-Co750 sample (b)

The analysis of adsorption isotherms and hysteresis loops was confirmed by the TEM data (Fig. 3.37). In TEM micrographs of the A-Co sample, small uncertain shape crystallites were observed, which can lead to the difficult classification of hysteresis loop (Fig. 3.37 a). Meanwhile, in the calcined sample, smooth sintered crystallites were dominant (Fig. 3.37 b, c).

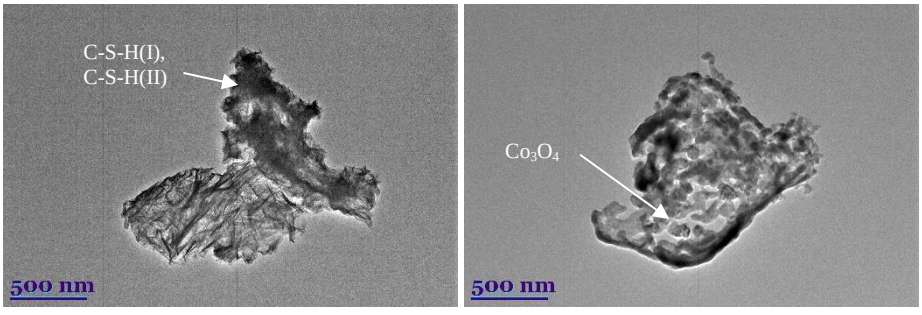

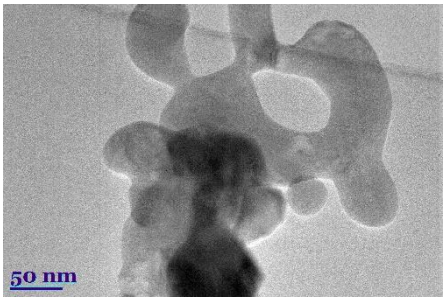

c

Fig. 3.37. TEM micrographs of A2-Co sample (a) and A2-Co750 samples (b, c)

It was observed that the BET equation could be used for the calculations of specific surface area of A2-Co and A2-Co750 samples, because the values of R^2 and C_{BET} meet the requirements (Table 3.11). It is worth mentioning that the A2-Co750 sample showed a high value of C_{BET} constant (319.82). According to the literature, it can be related to the sorption of nitrogen on high energy sites or filling narrow micropores. Since the surface of the A2-Co750 sample is sintered and the micropores are not presented, the high value of the C_{BET} constant can be caused by the sorption of nitrogen. Thus, the calculated specific surface area of the A2-Co750 sample can have some errors.

It was calculated that during the adsorption of cobalt ions, the surface area of the adsorbent slightly increased to 50.06 m^2/g (Table 3.11). Meanwhile, during the calcination at 750 °C, the particles of adsorbent sintered (Fig. 3.37 b, c); thus, the specific surface area of the sample decreased almost 6 times and was equal to 8.53 m^2/g. It is worth mentioning that the pure calcined (750 °C) adsorbent has more than two times higher value of the surface area (18.70 m^2/g) (Table 3.12). Probably, due to the intercalated ions, the sintering temperature of particles decreased; thus, higher particles with the lower porosity were formed.

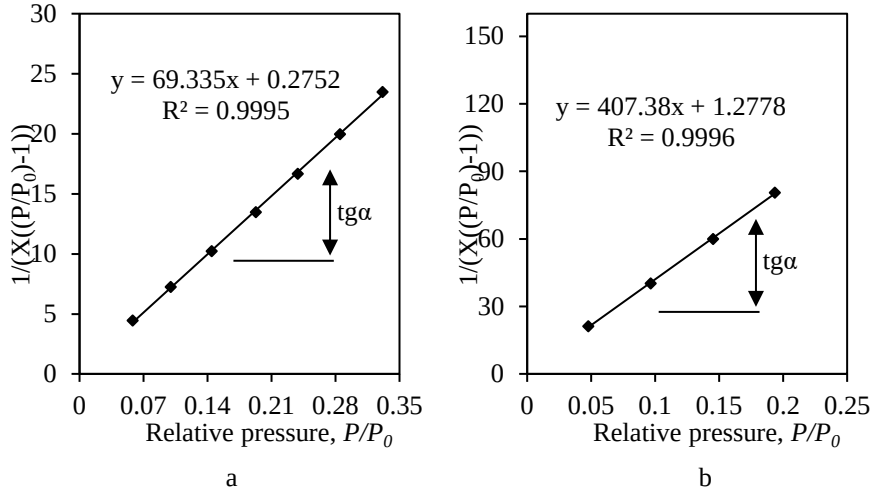

Fig. 3.38. The isotherm of N_2 adsorption at 77 K in the BET plot of A2-Co sample (a) and A2-Co750 sample (b)

Table 3.11. Calculated parameters of A2-Co sample and A2-Co750 sample of a BET method

Sample	BET equation constants		Capacity of monolayer X_m	S_{BET}, m^2/g	C_{BET} constant	Reliability coefficient, R^2
	Slope $S = tga$	Intercept I				
A2-Co	69.34	0.28	0.014	50.06	252.95	0.9995
A2-Co750	407.38	1.28	0.002	8.53	319.82	0.9996

The calculations of the dominant pores shape in A2-Co and A2-Co750 samples, using a parallel plate pore model, have shown high differences between S_{BET} and $\sum A$ values (> 30%); thus, this model is not suitable for the characterization of samples (Table 3.12). Meanwhile, the significantly lower differences between the mentioned values were obtained by using cylindrical-like pores (< 11%), which allows to state that the cylindrical pores are dominant in the samples. It is worth mentioning that the hysteresis loop of the A2-Co750 sample was classified as Type H1, which is in good agreement with the results of calculations (Fig. 3.36 a). Meanwhile, the classification of the hysteresis loop of the A2-Co sample was complicated, because its shape had similarities between Type H1 and Type H3 (Fig. 3.36 b). Probably, the difference occurs due to the irregular shape of crystallites of the A2-Co sample.

Further calculations have shown that during the adsorption of cobalt ions, the value of the cumulative pore volume of the adsorbent decreased from 0.207 cm^3/g to 0.125 cm^3/g (Table 3.12). It is worth mentioning that the intercalation of copper ions did not have a significant influence on the cumulative pore volume of the adsorbent. As expected, the total pore volume of the sample with intercalated cobalt ions decreased by more than 4 times during the calcination. Such decrement can have a negative influence on the activity of the sample, despite the formation of the active compound-cobalt oxide Co_3O_4.

Table 3.12. The data of ΣA and ΣV_P calculations of A2-Co sample and A2-Co750 sample

Sample	S_{BET}, m^2/g	Results using a cylindrical pore model				Results using a parallel plates pore model			
		ΣA, m^2/g	$\lvert S_{BET} - \Sigma A \rvert$, m^2/g	$\lvert S_{BET} - \Sigma A \rvert$, %	ΣV_P, cm^3/g	ΣA, m^2/g	$\lvert S_{BET} - \Sigma A \rvert$, m^2/g	$\lvert S_{BET} - \Sigma A \rvert$, %	ΣV_P, cm^3/g
A2-Co	50.06	54.33	4.27	8.53	0.125	34.62	15.44	30.84	-
A2-Co750	8.53	7.66	0.87	10.20	0.028	4.33	4.20	49.24	-

According to the data in Table 3.12, the value of the cumulative pore volume of the A2-Co sample is equal to 0.125 cm^3/g. This compound could be assigned to

microporous material, because the pores with 2–3 nm diameter are dominant (Fig. 3.39). The results of the A2-Co750 sample of cumulative pore volume are lower and equal to 0.028 cm^3/g (Table 3.10), but this compound is a mesoporous material with dominated pores in 2–15 nm diameter range (Fig. 3.39).

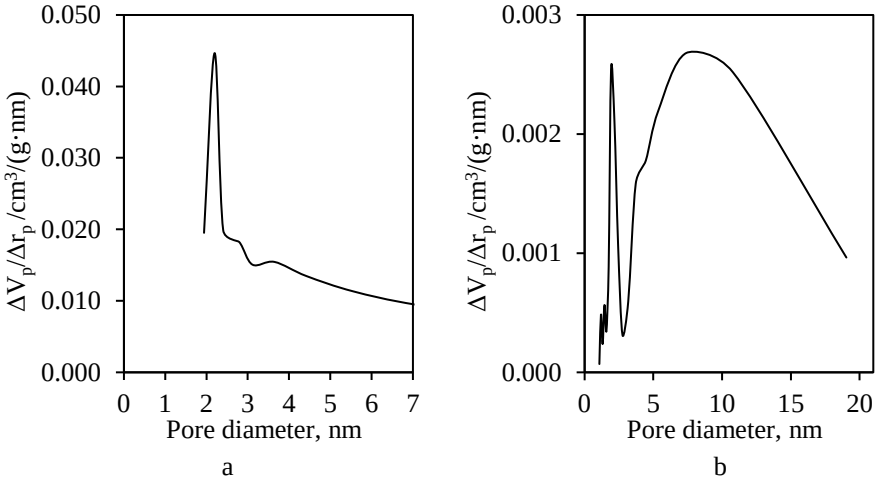

Fig. 3.39. Differential distributions of volume pore sizes of A2-Co sample (a) and A2-Co750 sample (b)

3.2.5. Texture and microstructure parameters of A2 adsorbent substituted with Cr^{3+} ions

The In Situ XRD experiment was performed to investigate A2 adsorbent with incorporated Cr^{3+} ions structural parameters (Fig. 3.40). It was observed that the sample remains stable in 25–550 °C temperature interval. The new compounds, $CaCrO_4$ (PDF No. 00-008-0458) and Cr_2O_3 (PDF No. 00-038-1479), were determined respectably at 550 °C and 850 °C temperatures. As in the results above, in higher temperatures (700–850 °C), the formation of wollastonite, β-C_2S, and CaO compounds were identified in In Situ XRD patterns (Fig. 3.40).

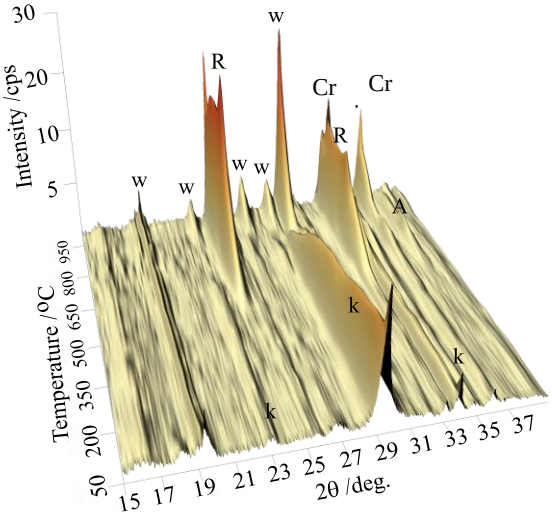

Fig. 3.40. In Situ XRD patterns of A2-Cr sample in a 25–1000 °C temperature range; indexes: k – $CaCO_3$, A – CaO, R – Cr_2O_3, Cr – $CaCrO_4$, w – wollastonite, β – β-C_2S

According to the In Situ XRD results, the calcination of the A2-Cr sample was performed at 550 °C, 750 °C, and 850 °C temperatures (Fig. 3.41). As the XRD pattern shows, at 550 °C temperature (Fig. 3.41 a), the $CaCO_3$ compound was determined. The new compound, $Cr(OH)_3 \cdot 3H_2O$ (PDF No. 00-038-1479), was identified in the A2-Cr550 sample. Typically, this compound is formed in poorly crystalline or amorphous materials [169]. When the temperature increased, this compound was not observed. It should be noted that $CaCrO_4$ starts formatting at this temperature (Fig. 3.41 a). Meanwhile, in the 750 °C temperature, the amount of $CaCrO_4$.incrases, because more diffraction peaks that are attributed to this compound were determined. It could be noted that Cr_2O_3 and wollastonite start to form in this sample at 750 °C temperature (Fig. 3.41 b). The XRD patterns show that at 850 °C temperature, wollastonite, β-C_2S, CaO, and chromium ions containing compounds were observed (Fig. 3.41 c).

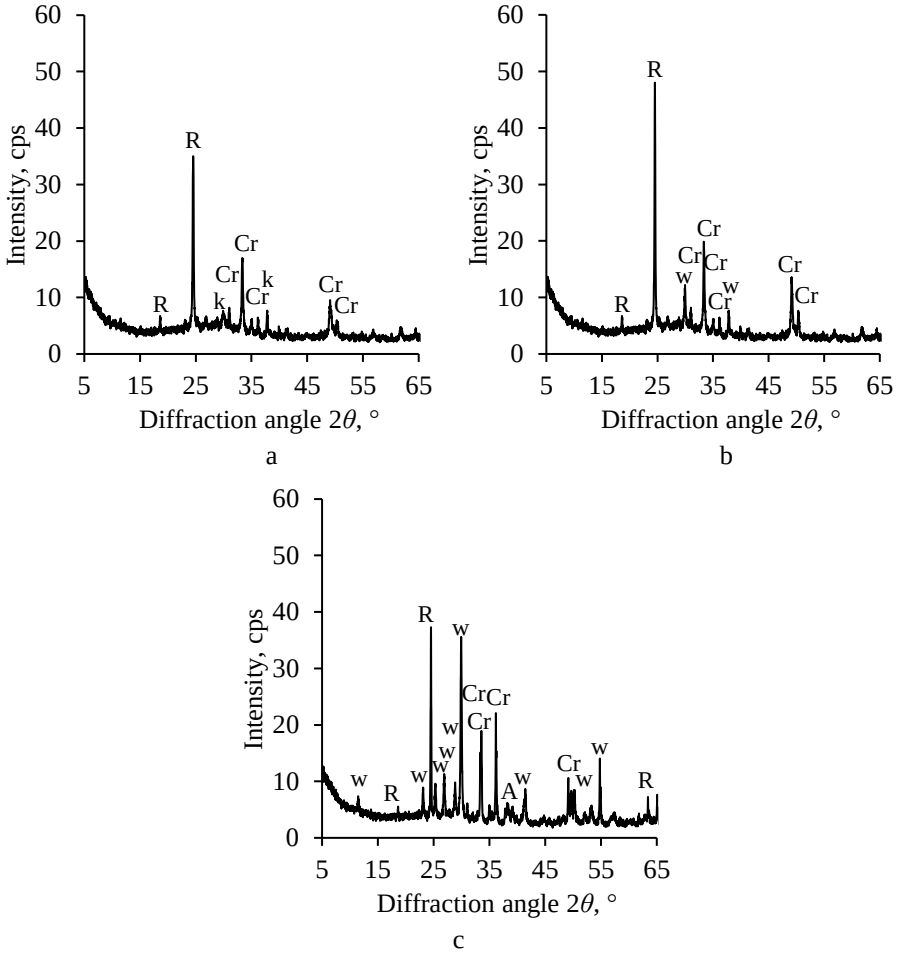

Fig. 3.41. XRD patterns of A2-Cr550 sample (a), A2-Cr750 sample (b), and A2-Cr850 sample (c); indexes: A – CaO, Cr – $CaCrO_4$, R – Cr_2O_3, Cr – $CaCrO_4$, k – $CaCO_3$, w – wollastonite, β – β-C_2S

The SEM analysis results confirm the formation of calcium chromate, because at 550 °C temperature, small crystals, characteristic of $CaCrO_4$, were observed (Fig. 3.42 a). It is worth mentioning that in the A2-Cr sample at 850 °C temperature, the hexagonal crystals of Cr_2O_3 were observed (Fig. 3.24 b). The EDX analysis results showed that the mentioned crystals mainly consist of Cr (73.79%) atoms.

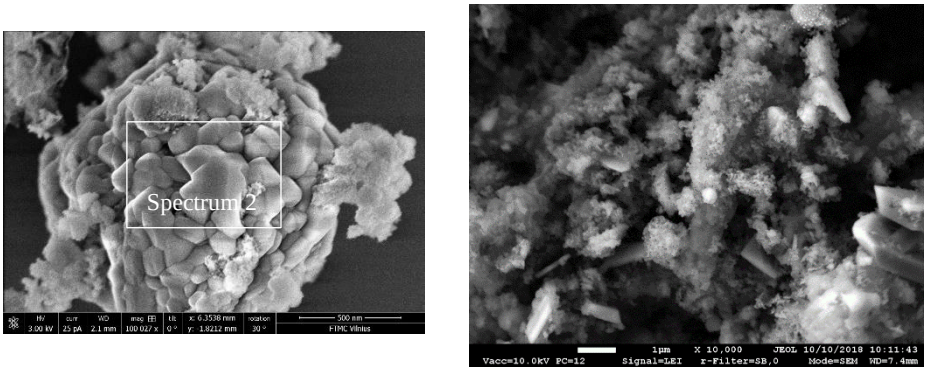

a b

Fig. 3.42. SEM images of A2-Cr550 (a) and A2-Cr850 (b) (Spectrum 1: Cr – 43.89, Si – 13.52, Ca – 13.52, O – 29.08 mass %; Spectrum 2: Cr – 73.79, Si – 1.12, Ca – 1.42, O – 23.67 mass %) samples; magnification: a – 100 027 times, b –10 000 times

In order to determine the structure of compounds porous, the parameters of porosity of adsorbent with intercalated Cr^{3+} ions (labeled as A2-Cr) and its calcination products at 550 °C (labeled as A2-Cr550) were determined. The calcination temperature was chosen based on the formation of calcium chromate ($CaCrO_4$).

As in the previous cases, the adsorption isotherms of both samples (A2-Cr and A2-Cr550) can be classified as Type II (do not have plateau at high P/P_0 values) or Type IV (have hysteresis loop), which shows that meso- and macro-pores are presented in the samples (Fig. 3.43). The hysteresis loop of the A2-Cr sample can be classified as Type H3, since the adsorption isotherm increases evenly with the relative pressure (P/P_0) and the hysteresis loop close at P/P_0 ~0.42. It is worth mentioning that the hysteresis loop of the previously investigated samples showed Type H1 or intermediate case between Type H1 and H3; thus, it can be stated that the intercalated Cr^{3+} ions strongly affect the porosity of adsorbent. Further analysis has shown that the shape of the hysteresis loop of the calcined A2-Cr sample becomes narrower and closed at a higher value of P/P_0 (~0.55). Probably, the shape of the pores of the adsorbent changed during the calcination.

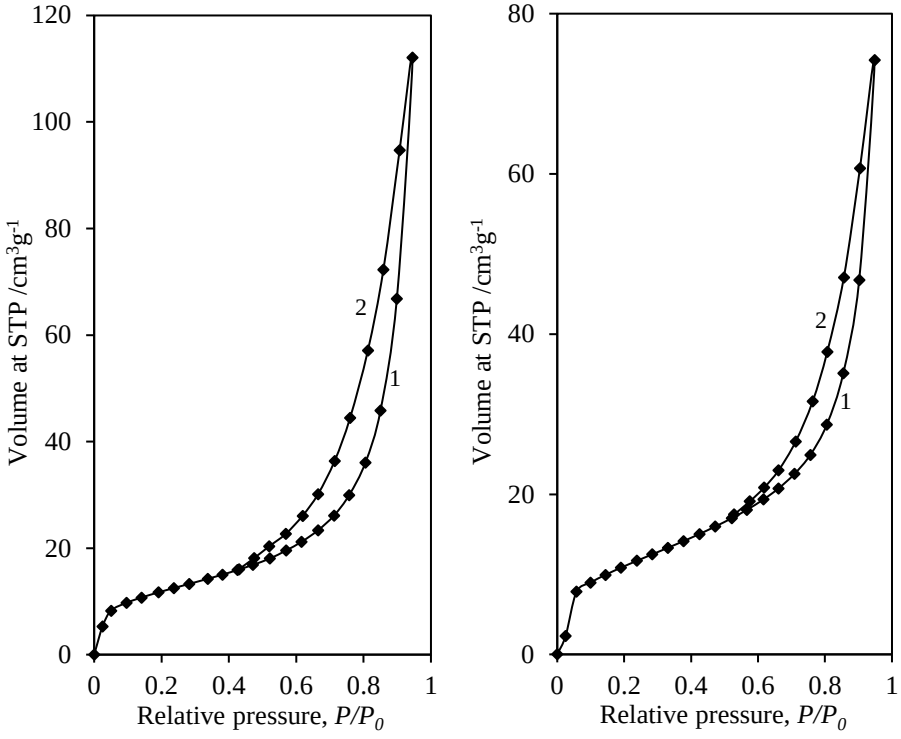

a b

Fig. 3.43. Nitrogen adsorption (1) – desorption (2) isotherms of A2-Cr sample (a) and A2-Cr550 samples (b)

The results of TEM analysis are in good agreement with the classification of hysteresis loops (Fig. 3.44). The sample with intercalated chromium ions mainly consists of irregular plate crystallites (Fig. 3.44 a). Meanwhile, small rounded (< 20 nm) and huge plate-like crystallites are presented in the calcined sample (Fig. 3.44 b); thus, the classification of the hysteresis loop is complicated.

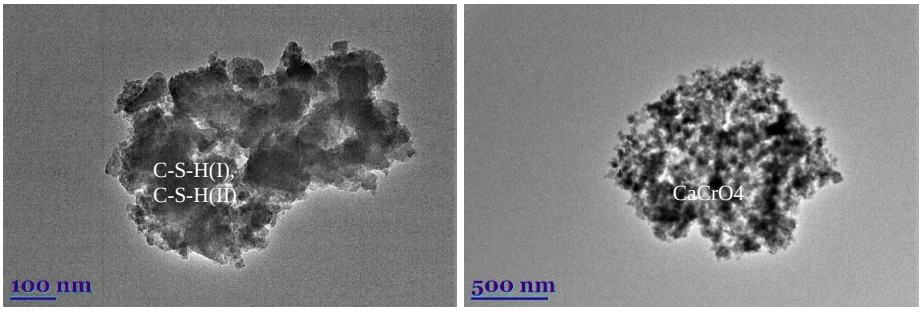

a b

Fig. 3.44. TEM micrographs of A2-Cr sample (a) and A2-Cr550 sample (b)

It has been determined that a stable monolayer of N_2 was adsorbed on the surfaces of A2-Cr and A2-Cr-550 samples, because the value of C_{BET} constant falls in the range of 50–150, and a straight line with $R^2 > 0.999$ was obtained (Table 3.13). It was calculated that during the adsorption of chromium ions on the adsorbent, its specific surface area decreased slightly (Table 3.13). Moreover, the sample with intercalated Cr^{3+} ions after the calcination at 550 °C temperature is characterized by the value of specific surface area, which is important in further application of the material.

The calculations of dominant pore shape confirmed the classification of hysteresis loops (Table 3.14). As expected, slit-like pores between plate-like particles are dominant in the A2-Cr sample, because the difference between S_{BET} and $\sum A$ values was equal only to 3.22% (Table 3.14). Meanwhile, by using cylindrical-like pores, the difference between the mentioned values was equal to more than 50%. The difference results were obtained in the A2-Cr550 sample, because both models showed similar errors (> 30%). This is caused by the different shapes of crystallites (small spherical and plate-like), which are dominant in the sample. Further calculations revealed that the total pore volume of the adsorbent decreased to 0.171 cm^3/g during the adsorption of chromium ions (Table 3.14). The same tendency was observed during the calcination; however, the value of the total pore volume depends on the used model and is approximately equal to 120 cm^3/g.

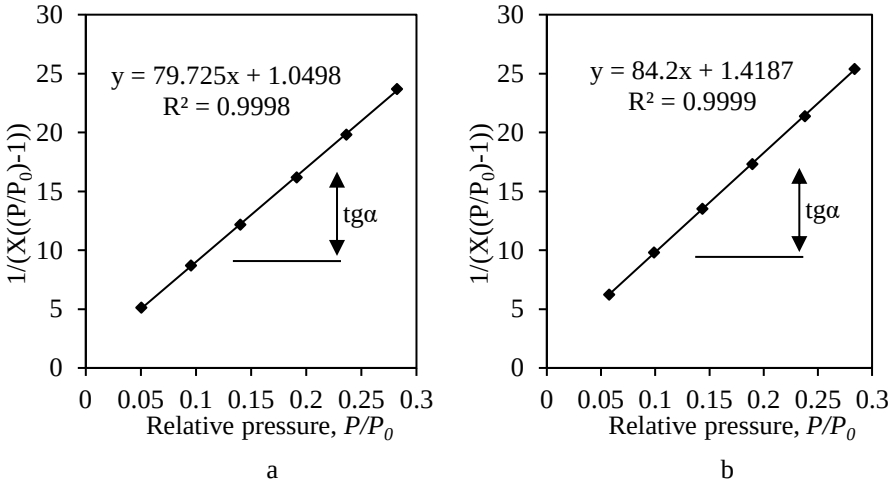

Fig. 3.45. The isotherm of N_2 adsorption at 77 K in the BET plot of A2-Cr sample (a) and A-Cr550 sample (b)

Table 3.13. The calculated parameters of A2-Cr sample and A-Cr550 sample by a BET method

Sample	BET equation constants		Capacity of mono layer X_m	S_{BET}, m^2/g	C_{BET} constant	Reliability coefficient, R^2
	Slope $S = tga$	Intercept I				
A2-Cr	79.72	1.05	0.012	43.14	76.94	0.9998
A2-Cr550	84.20	1.42	0.012	40.70	60.35	0.9999

Table 3.14. The data of ΣA and ΣV_P calculations of A2-Cr sample and A-Cr550 sample

Sample	S_{BET}, m^2/g	Results using a cylindrical pore model				Results using a parallel plates pore model			
		ΣA, m^2/g	$\lvert S_{BET} - \Sigma A \rvert$, m^2/g	$\lvert S_{BET} - \Sigma A \rvert$, %	ΣV_P, cm^3/g	ΣA, m^2/g	$\lvert S_{BET} - \Sigma A \rvert$, m^2/g	$\lvert S_{BET} - \Sigma A \rvert$, %	ΣV_P, cm^3/g
A2-Cr	43.14	67.36	24.22	56.13	-	44.53	1.39	3.22	0.171
A2-Cr550	40.70	54.70	14.00	34.39	0.129	27.79	12.91	31.73	0.109

The differential distributions of volume pore sizes have shown that the mesoporous size particles predominated in the samples, because the pores with 4–10 nm in A2-Cr and 3–7 nm in A2-Cr550 diameters are dominant in both samples (Fig. 3.46).

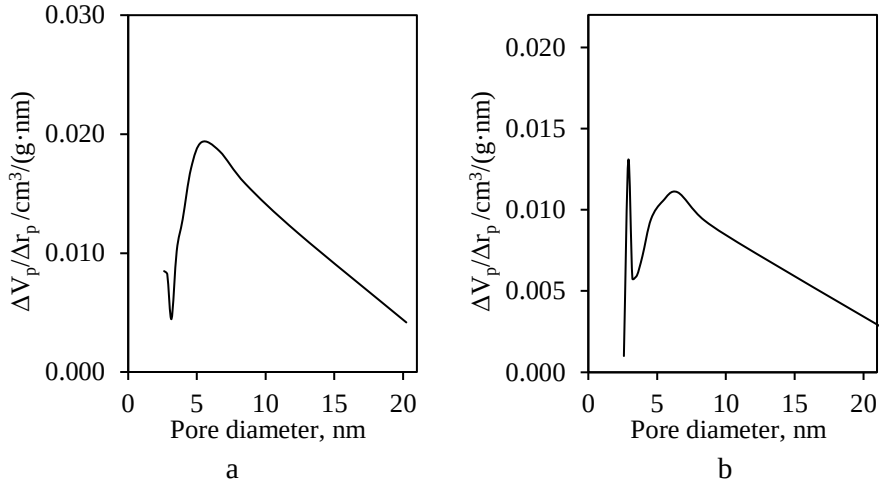

Fig. 3.46. Differential distributions of volume pores sizes of A2-Cr sample (a) and A-Cr550 sample (b)

By summarizing the results, it can be stated that the application of the N_2 adsorption-desorption analysis on the characterization of calcium silicate hydrate with intercalated transitions metal ions is a challenging process. These samples can have different meso- and macro-pores as well as consist of different crystallites with different shape; thus, the obtained isotherms and hysteresis loops usually are the intermediate cases between two types. Despite the mentioned issues, the description of calcium silicate hydrates, using the N_2 adsorption-desorption isotherms, can be considered accurate if the samples are additionally characterized by the SEM and TEM microscopy as well as the calculations of dominant pore shape are performed. It was obtained that the adsorption isotherm of all samples (except calcined adsorbent) can be classified as Type II (do not have plateau at high P/P_0 values) and Type IV (have hysteresis loop). Such intermediate case is characteristic of the materials that have both meso- and macro-pores. The adsorption-desorption isotherms of calcined adsorbent coincide in all P/P_0 range, i.e., do not have a hysteresis loop; thus, the adsorption isotherm can be classified as Type II. This type of isotherm is characteristic of nonporous materials. The analysis of hysteresis loops showed that all samples, except the samples with chromium ions, are characterized by Type H1 or are intermediate between Type H1 and Type H3. The classification of hysteresis loops was confirmed by the calculations of dominant pore shapes according to the cylindrical-like pores and slit-like pore models. The calculations revealed that the cylindrical-like pore model fit the description of samples, because the obtained differences between S_{BET} and ΣA values were significantly lower than using slit-like pore models. During the adsorption of chromium ions, the shape of dominant pores of the adsorbent changed from the cylindrical-like pores to the slit-like pores, because the hysteresis loop can be classified as Type H3, and the slit-like pore model showed a good agreement between S_{BET} and ΣA values. It was determined that the synthetic adsorbent (C/S = 1.5), which mainly consist of semicrystalline type compounds C-S-H(I) and C-S-H(II), is a mesoporous material with high values of the specific surface area (46.13 m^2/g) and the total pore volume (0.207 cm^3/g). The specific surface area of synthetic adsorbent is 2–3 times higher in comparison to the other dibasic calcium silicate hydrates. The specific surface area of the adsorbent increases during the adsorption of Cu^{2+} and Co^{2+} ions and decreases during the adsorption of Cr^{3+} ions. Due to the intercalated metal ions into the structure of the adsorbent, the total pore volume decreased in all investigated cases, despite the increment of surface area. The highest decrement was observed during the adsorption of cobalt ions. During the calcination at 750 °C temperature; the synthetic adsorbent became non-porous material with a specific surface area equal to 18.70 m^2/g. Due to the low calcination temperature, the mentioned value is significantly higher in comparison to the other calcium silicates [170, 171]. The intercalated cobalt ions negatively affect the porosity of adsorbent during the calcination, because the specific surface area and the total pore volume decreased to 8.53 m^2/g and 0.028 cm^3/g, respectively. The adsorbent with intercalated Cr^{3+} and Cu^{2+} ions showed a different tendency because after the calcination, a specific surface area and the total pore volume of both samples was equal to ~43 m^2/g and 0.120 cm^3/g, respectively. For this reason, in the next part of

this work, heavy metals incorporation into the calcium silicate hydrate structure during the hydrothermal synthesis was determined.

3.3. Intercalation of Cu^{2+}, Co^{2+}, Cr^{3+} ions into the synthetic compounds under hydrothermal synthesis conditions

Calcium silicate hydrates form in nature by curing cement, and they can be synthesized in CaO-SiO_2-H_2O mixtures under hydrothermal conditions within the 100–350 °C temperature range [27]. Meanwhile, calcium silicates can be synthesized by calcining calcium silicate hydrates or solid sintering of calcium- and silicon-containing materials [153, 172]. Usually, the preparation of the catalysts supported with the calcium silicates or calcium silicate hydrates involves three steps [162]: (1) synthesis of calcium silicates or calcium silicate hydrates, (2) adsorption of metal ions, (3) calcination at a selected temperature (in order to achieve active metal oxides). In addition, it is possible to incorporate metal ions into the structure of calcium silicates or calcium silicate hydrates during their synthesis. Such compounds with incorporated metal ions can be used as catalysts for ethanol conversion to butadiene, the synthesis of bisphenol F, and the oxidation of ketones and aldehydes [173–175]. Unfortunately, there is a lack of information about the influence of metals on the formation, thermal stability, microstructure, and other properties of such materials. According to the literature, some metal ions, such as sodium or potassium ions, have a positive effect on the reactivity of silicon-containing compounds and promote the formation of calcium silicate hydrates [176].

Meanwhile, aluminum ions affect the stability and morphology of tobermorite because by increasing the aluminum content, the form of crystals changes from plate-like to lath-like and then to needle-like [177]. Different results were obtained by using aluminum oxide for the synthesis of dibasic calcium silicate hydrate α-C_2SH at 200 °C, because this additive retarded the formation of calcium silicate hydrates but stimulated the crystallization of calcium silicate [153]. According to the literature, some cations, such as Al^{3+}, B^{3+}, and Be^{2+}, can change the silicon in the silicon-oxygen tetrahedron, while others (Na^+, K^+, Fe^{2+}, Mn^{2+}, Ti^{2+}, Zr^{2+}, etc.) intercalate outside it. These cations connect silicon-oxygen tetrahedrons to each other. Thus, different cations change the composition, structure, and other properties of calcium silicate hydrates and calcium silicates [178].

For these reasons, the thermal stability, microstructure, and catalytic activity of compounds formed in the CaO-SiO_2-$Me(NO_3)_x$-H_2O system under hydrothermal conditions was examined in detail.

3.3.1. The synthesis of calcium silicate hydrates with incorporated Cr^{3+} ions

The synthesis of dibasic calcium silicate hydrate samples with incorporated Cr^{3+} ions (H-Cr sample) was based on the hydrothermal method. The dry primary mixture of fine-grained $SiO_2 \cdot nH_2O$, and calcium oxide was mixed with $Cr(NO_3)_3 \cdot 9H_2O$ solution (Cr^{3+} ions concentration 10 g/L) to reach a water-to-solid ratio 10 with the C/S molar ratio of 1.5. Based on the previous adsorption studies, the hydrothermal synthesis has been carried out in unstirred suspensions, under saturated steam pressure at 175 °C temperature for 16 hours. After hydrothermal treatment, the obtained

products were filtered off, rinsed with ethanol, dried at 50 °C ± 5 for 24 h, and sieved (< 80 μm).

The data of X-ray diffraction analysis have shown that during hydrothermal treatment in $CaO\text{-}SiO_2\text{-}Cr(NO_3)_3\text{-}H_2O$ mixture, the semicrystalline calcium silicate hydrates C-S-H(I) and/or C-S-H(II) was formed in the products (Fig. 3.47 a). Moreover, due to the carbonization, when the products were dried in the air-conditioned chamber, the traces of calcite were detected in the XRD pattern [179]. It is worth mentioning that chromium ions do not affect the mineral composition of the synthesis products, because at the same synthesis conditions in the pure system ($CaO\text{-}SiO_2\text{-}H_2O$), only C-S-H(I), C-S-H(II), and calcite were formed [180].

The results of atomic absorption spectroscopy showed that after the synthesis, the concentration of Cr^{3+} ions in the liquid medium did not exceed even 0.001% of the primary metal ions concentration. Meanwhile, the results of FIA analysis showed that more than 80% (from the primary concentration) of the NO_3^- anions are present in the liquid medium. It should be noted that the XRD results did not show the formation of compounds containing Cr^{3+} or NO_3^- ions. Thus, it can be stated that all Cr^{3+} ions intercalated into the structure of calcium silicate hydrates or formed amorphous compounds, while NO_3^- anions only partially (~20%) participate in the process.

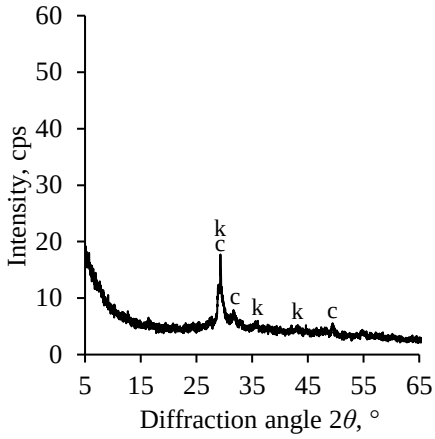

a

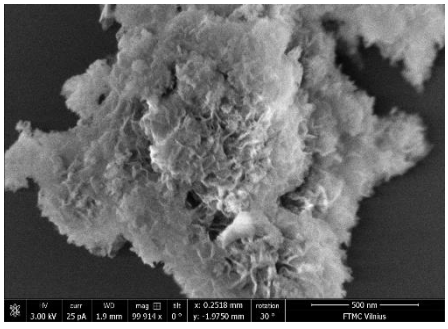

b

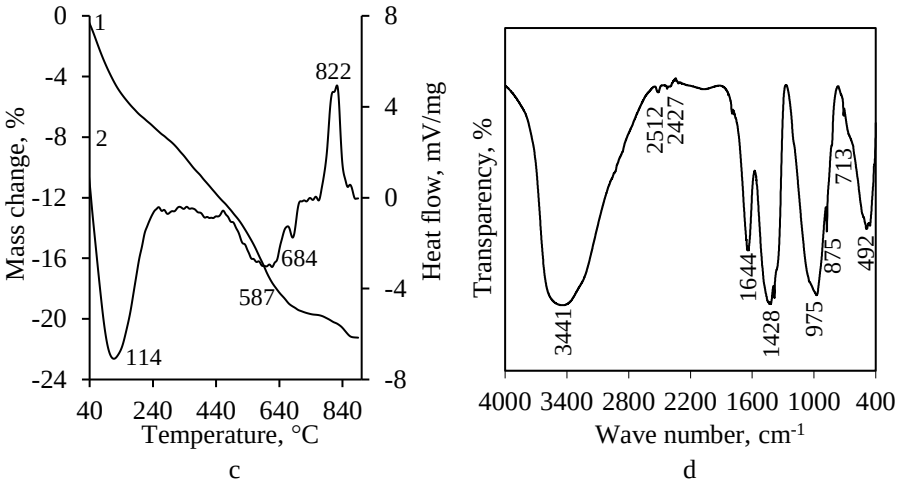

Fig. 3.47. XRD pattern (a), SEM image (magnification 100 000 times) (b), STA curves (curve 1 – TG, curve 2 – DSC) (c), and FT-IR spectrum (d) of H-Cr sample; indexes: k – $CaCO_3$, c – C-S-H(I), and/or C-S-H(II)

The XRD results were confirmed by the SEM micrographs (Fig. 3.47 b), because only thin close-packed particles (called foils or honeycomb) of semicrystalline type compounds were observed [167, 181]. The existence of the mentioned compounds was confirmed by the DSC data: the endothermic effect at 114 °C temperature can be assigned to the removal of adsorption/crystallization water in semicrystalline calcium silicate hydrates, while the exothermic effect at 822 °C temperature is characteristic of the recrystallization process of C-S-H(I) and C-S-H(II) (Fig. 3.47 c, curve 2). Furthermore, the endothermic effects at 587 °C temperature can be assigned to the dehydration or decomposition of a compound, containing Cr^{3+} and/or NO_3^- ions, as well as to the formation of double metal oxides (Fig. 3.47 c, curve 2) [182]. The small thermal effect at 684 °C temperature corresponds to the decomposition of calcium carbonate. The data of TGA showed that less than 0.8% of the mentioned compounds are present in the products (Fig. 3.47 c, curve 1).

The identification of absorption bands in the FT-IR spectrum of the synthesis products is complicated (Fig. 3.47 d). The adsorption bands presented in a 400–700 cm^{-1} frequency range are typical to the semicrystalline C-S-H and compounds that are containing Cr^{3+} ions vibrations [183]. In higher frequency intervals (800–1000 cm^{-1}), the absorption bands can be assigned to the symmetrical ν_s(O–SiO–) vibrations in the C-S-H structure [158]. Furthermore, the adsorption maximums at ~1428 cm^{-1} and ~875 cm^{-1} correspond to $\nu(CO_3^{2-})$ and $\delta(CO_3^{2-})$ or NO_3^- group vibrations [184]. Meanwhile, the adsorption band at 1644 cm^{-1} can be assigned to the vibration of the OH^- bonds in both C-S-H and compounds containing Cr^{3+} ions structure. Finally, the broad band in a 2500–4000 cm^{-1} range reflected the H–O–H bending vibration of the water. It is worth mentioning that the adsorption bands associated with NO_3^- group occur in the same frequency interval as $\nu(CO_3^{2-})$ and OH^- vibrations.

In order to determine the formation of potential catalytic active compounds, the synthesis products were calcined in a high-temperature camera (Fig. 3.48). The results

of In Situ XRD patterns have shown that the synthesis products are stable in a 25–550 °C temperature range (Fig. 3.48). It is worth mentioning that the DSC curve showed an endothermic effect at 114 °C temperatures (Fig. 3.47 c). The difference between the mentioned results can occur due to the dehydration and/or decomposition of the amorphous phase, which cannot be identified in the XRD patterns. By increasing the calcination temperature (> 550 °C), the formation of calcium chromate $CaCrO_4$ (PDF 00-008-0458) and chromium oxide Cr_2O_3 (PDF 00-002-1362) proceeded. It was obtained that the mentioned compounds remained stable up to 1000 °C. These data are in good agreement with the DSC results (Fig. 3.47 c). Moreover, when the calcination temperature was increased to 800–850 °C, the formation of calcium silicates wollastonite was observed.

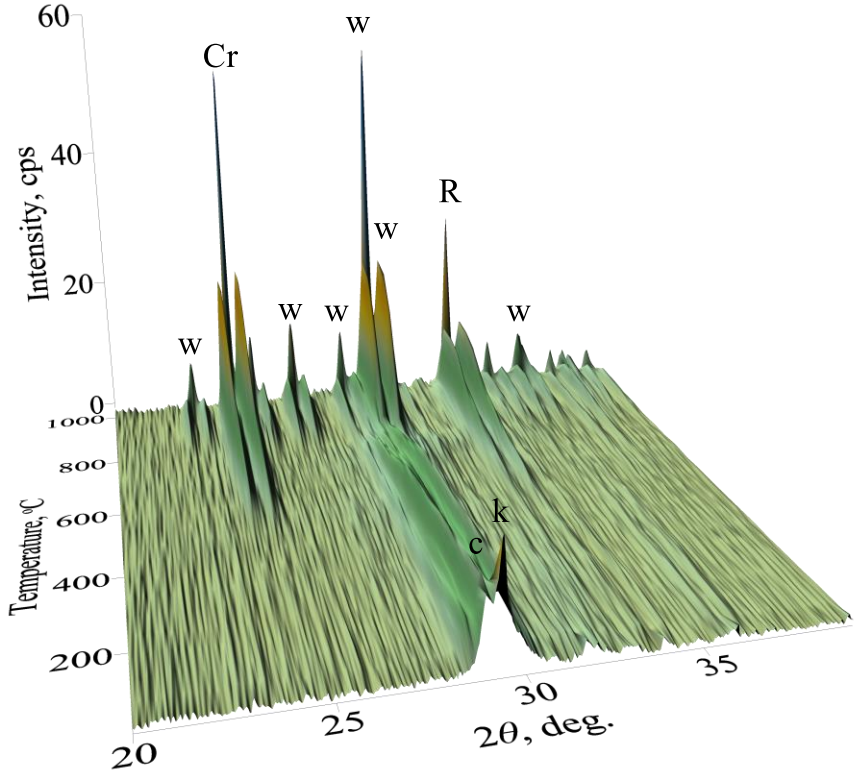

Fig. 3.48. In Situ XRD patterns of the H-Cr sample when the temperature of calcination is 25–1000 °C; indexes: c – C-S-H(I)/C-S-H(II), w – wollastonite, k – $CaCO_3$, Cr – $CaCrO_4$, R – Cr_2O_3

In order to obtain a calcined sample with calcium chromate and a high surface area, a synthetic sample was calcined in the furnace Nabertherm LH 15/13 at 550 °C temperature for 24 h. The calcination temperature was reached within 48 h. It was obtained that after the calcination, only one crystalline compound, i.e., calcium chromate, was formed (Fig. 3.49 a). Moreover, a broad basal reflection in a 25–37° 2θ range can be assigned to the amorphous calcium silicate hydrate. It is worth

mentioning that under these calcination conditions, the traces of calcite remained stable.

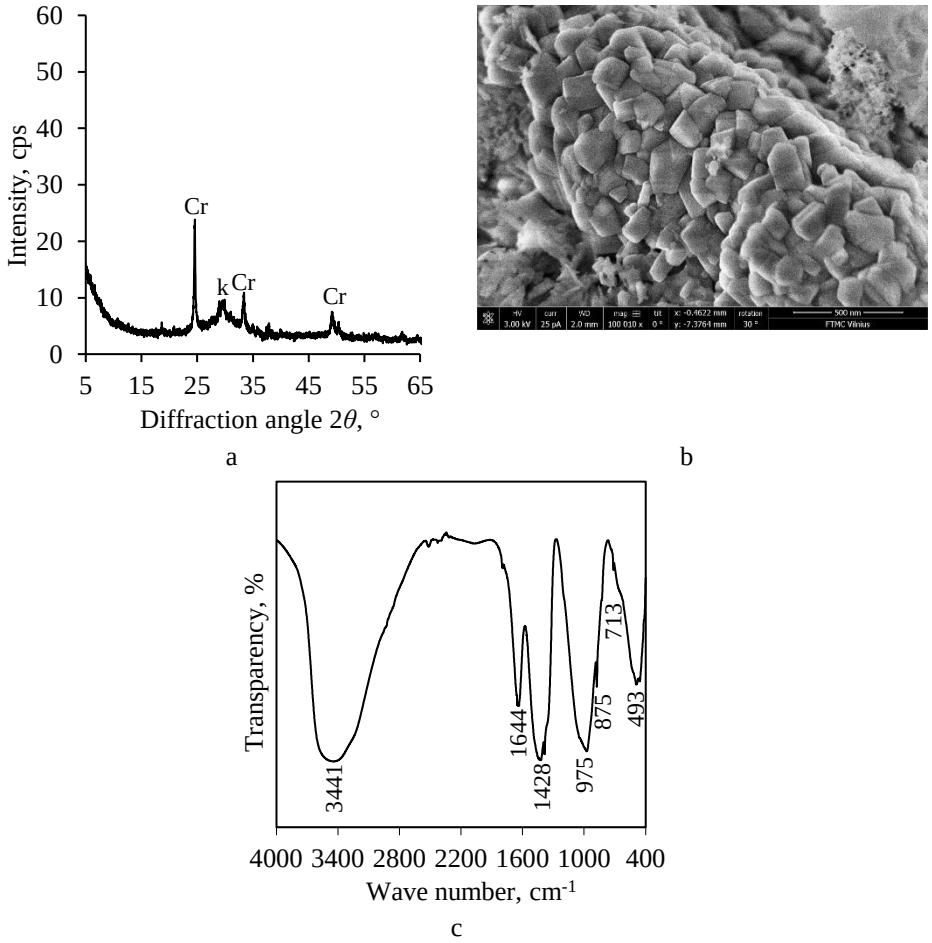

Fig. 3.49. XRD pattern (a), SEM image (magnification 100 000 times) (b), and FT-IR spectrum (c) of H-Cr550 sample; indexes: k – $CaCO_3$, Cr – $CaCrO_4$

The results of SEM analysis confirm the formation of calcium chromate, because small crystals, characteristic of $CaCrO_4$, were observed (Fig. 3.49 b). In addition, in the FT-IR spectrum, the intensive adsorption band at 875 cm^{-1} can be attributed to Cr^{+6}–O bonds vibrations in $CaCrO_4$ [185] (Fig. 3.49 c). It is worth mentioning that at these calcination conditions, the dehydration of semi-crystalline type compounds proceeded partially because the intensive bands, characteristic to OH^- group vibrations in FT-IR spectrum, are visible (Fig. 3.49 c). These results are in good agreement with TGA results, because the mass changes of synthetic product in the 550–900 °C temperature range are equal to 8.66% (Fig. 3.47 c).

3.3.2. H-Cr sample texture and microstructure parameters in the temperature range 25–550 °C

It was determined that during calcination, the shape of dominant pores changed from a mixture of cylindrical-like and slit-like pores to well-defined cylindrical-like pores (Fig. 3.50 a). The changes may have occurred due to the solid sintering reactions and new compounds (with different crystal lattice) formation during the calcination (Fig. 3.48).

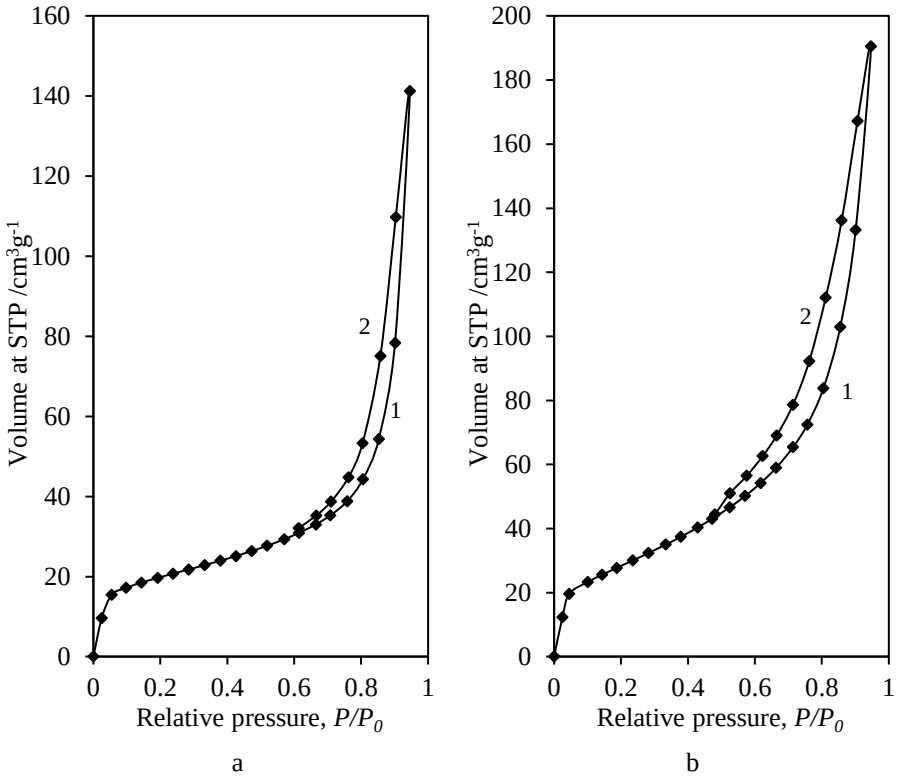

Fig. 3.50. Nitrogen adsorption (1) – desorption (2) isotherms of H-Cr sample (a) and H-Cr550 sample (b)

The presently discussed results were confirmed by the TEM data (Fig. 3.51). The TEM micrograph of the H-Cr sample showed an amorphous mass and needle-like crystallites (Fig. 3.51 a). Presumably, the cylindrical-like pores form in amorphous mass, while slit-like pores form between needle-like crystallites. Meanwhile, in the H-Cr550 sample, amorphous structure compounds (partially dehydrated C-S-H(I) and/or C-S-H(II)) and plate-like crystals of $CaCr_2O_4$ [186] were identified (Fig. 3.51 b).

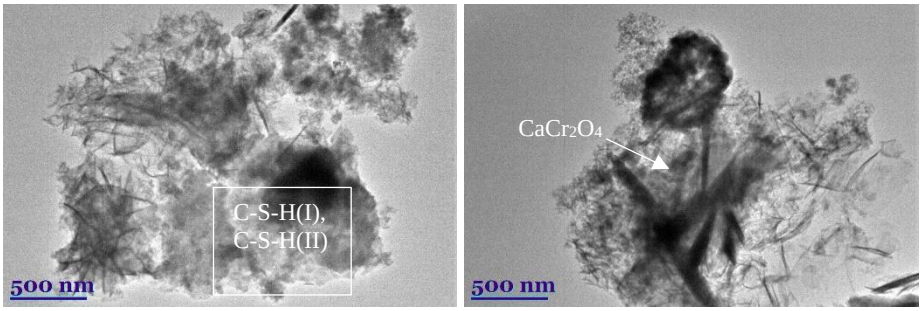

a b

Fig. 3.51. TEM micrographs of H-Cr sample (a) and H-Cr550 sample (b)

The BET method was used to calculate sample surface area (Fig. 3.52, Table 3.15). The calculations revealed that the values of C_{BET} constant of H-Cr sample and H-Cr550 sample are equal to 65.56 and 421.30, respectively. The higher value of the C_{BET} constant of the H-Cr550 sample can be explained by nitrogen adsorption on high-energy surface sites (probably $CaCr_2O_4$ crystals) or the filling of micropores [187]. It was calculated that the H-Cr sample has a relatively large surface area of 104.76 m^2/g (Table 3.15). It was determined that during the calcination at 550 °C temperature, the value of surface area decreased to 68.92 m^2/g (Table 3.15).

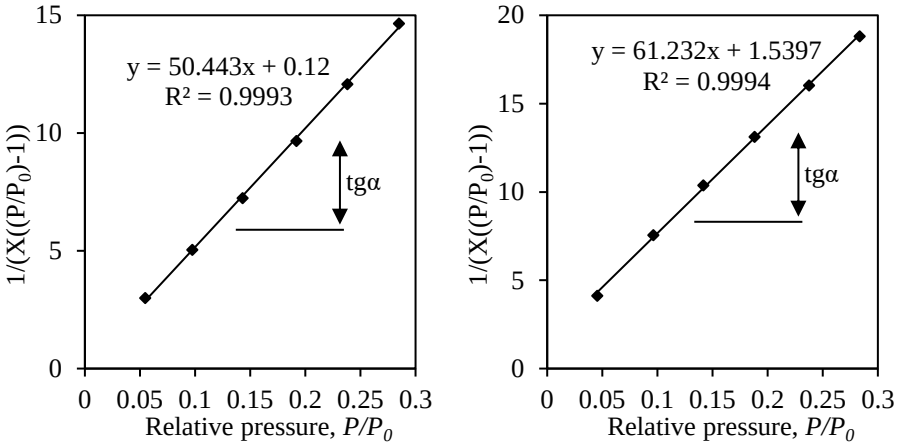

a b

Fig. 3.52. The isotherm of N_2 adsorption at 77 K in the BET plot of H-Cr sample (a) and H-Cr550 sample (b)

Table 3.15. Calculated parameters of H-Cr sample and H-Cr550 sample by a BET method

Sample	BET equation constants		Capacity of mono layer X_m	S_{BET}, m^2/g	C_{BET} constant	Reliability coefficient, R^2
	Slope/ $S = tg\alpha$	Intercept/*I*				
H-Cr	32.70	0.51	0.030	104.76	65.56	0.9950
H-Cr550 sample	50.44	0.12	0.020	68.92	421.30	0.9950

In order to determine the cylindrical-like and slit-like pore models, the corrected Kelvin equation and the scheme developed by Orr et al. were applied. These calculation results confirm the hysteresis loop classification as an intermediate case of H1 and H3 (Fig. 3.50 a). Moreover, it can be stated that both cylindrical-like and slit-like pores were formed in the structure of the H-Cr sample. The further calculations showed that during calcination, the shape of pores changed to well-defined cylindrical, because the difference between S_{BET} and $\sum A$ values was equal only to 7.73% (Table 3.16).

Table 3.16. The data of ΣA and ΣV_P calculations of H-Cr sample and H-Cr550 sample

Sample	S_{BET}, m^2/g	Results using a cylindrical pore model				Results using a parallel plates pore model			
		ΣA, m^2/g	$\lvert S_{BET} - \Sigma A \rvert$, m^2/g	$\lvert S_{BET} - \Sigma A \rvert$, %	ΣV_P, cm^3/g	ΣA, m^2/g	$\lvert S_{BET} - \Sigma A \rvert$, m^2/g	$\lvert S_{BET} - \Sigma A \rvert$, %	ΣV_P, cm^3/g
H-Cr sample	104.76	134.46	29.70	28.35	-	84.46	20.68	19.37	0.278
H-Cr550 sample	68.92	74.25	5.33	7.73	0.232	37.27	31.65	45.92	-

It was calculated that the value of cumulative pore volume of the H-Cr sample depends on the used model and is equal to 0.278 cm^3/g (Table 3.16). The differential distributions of volume pore sizes showed that the H-Cr sample is a mesoporous material, because the pores with 6–10 nm diameter are dominant (Fig. 3.53 a).

It was determined that during the calcination cumulative pore volume of the H-Cr550 sample decreased to 0.232 cm^3/g (Table 3.16). The results of differential distributions of volume pore sizes showed that the H-Cr550 sample is a mesoporous material with the dominant 1–15 nm pores (Fig. 3.53 b).

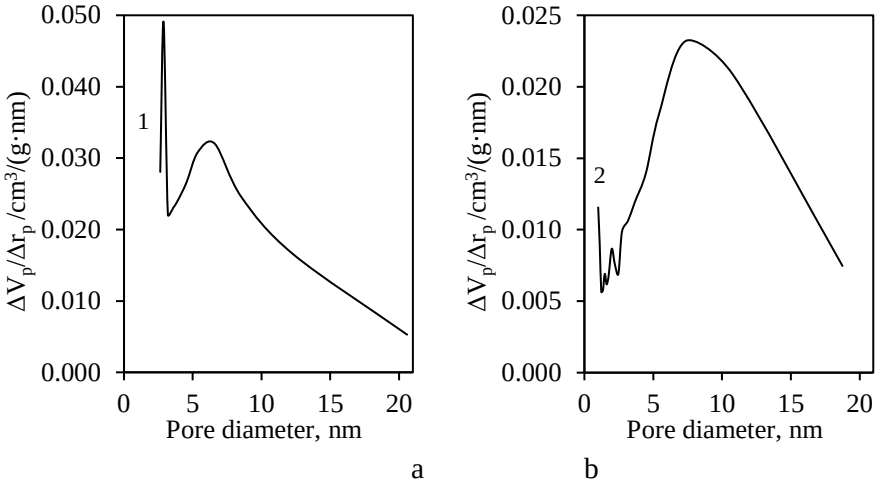

Fig. 3.53. Differential distributions of volume pore sizes of H-Cr sample (a) and H-Cr550 sample (b), where curve 1 values are obtained using a slit-like pore model and curve 2 values are obtained using a cylindrical-like pore model

By summarizing the results, it can be stated that during hydrothermal synthesis in $CaO\text{-}SiO_2\text{-}Cr(NO_3)_3\text{-}H_2O$ system, all Cr^{3+} ions are incorporated into the structure of synthesis products. Meanwhile, during the calcination of synthesis products, the composite of calcium silicates and calcium chromate, which have potential application in the catalysis process, is obtained.

3.3.3. The synthesis of calcium silicate hydrates with incorporated Cu^{2+} ions

In order to investigate copper ions influence on the calcium silicate hydrate structural properties, in the next stage of this work, the hydrothermal synthesis was carried out in $Cu(NO_3)_2 \cdot 3H_2O$ solution (H-Cu sample). The hydrothermal synthesis parameters were analogous to the H-Cr sample synthesis.

The results of XRD analysis have shown that after the hydrothermal treatment in $CaO\text{-}SiO_2\text{-}Cu(NO_3)_2\text{-}3H_2O$ mixture, the CuO was formed in the synthesis product (Fig. 3.54 a). These results are in good agreement with the atomic absorption spectroscopy analysis. After synthesis, in the remaining liquid, the concentration of Cu^{2+} ions did not exceed even 0.001% from the primary metal ions concentration. It should be mentioned that the results of FIA analysis showed that about 56% (from the primary concentration) of the NO^{3-} anions are present in the liquid medium.

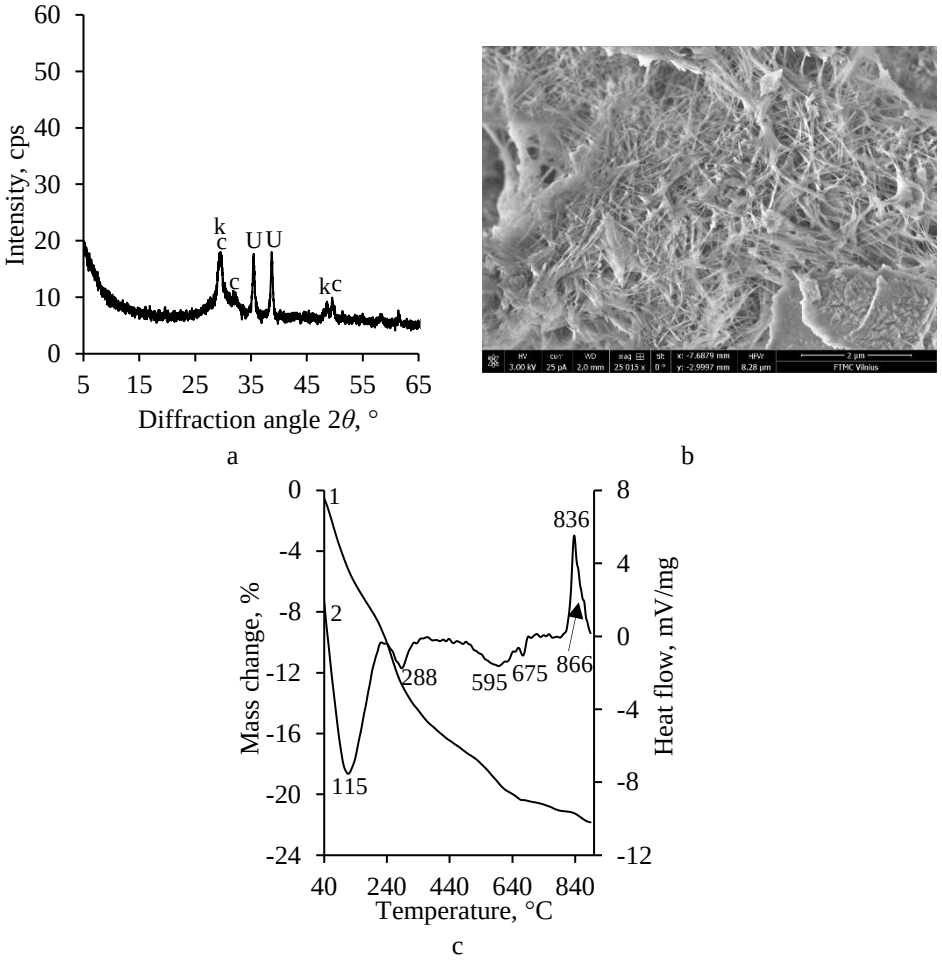

Fig. 3.54. XRD pattern (a), SEM image (magnification 5000 times) (b), STA curves (curve 1 – TG, curve 2 – DSC) (c) of H-Cu sample; indexes: k – $CaCO_3$, U – CuO, c – C-S-H(I), and/or C-S-H(II)

In order to confirm the XRD results, the SEM micrographs were fulfilled (Fig. 3.54 b). It has been determined that clews-like shape or nano rod-like structure particles, which could be identified as CuO nanoparticles, were observed [188, 189]. These data are in good agreement with the DSC data: the endothermic effects at 288 °C and 595 °C temperatures can be assigned to the decomposition or dehydration of NO^{3-} anions and H_2O containing compounds (Fig. 3.54 c, curve 2) [82]. This process could be related to the mass change, because afterwards, about 7.3% mass loss was identified in the TGA curves of the H-Cu sample (Fig. 3.54 c, curve 1). Similarly to the H-Cr sample, the exothermic effect at 836 °C and shoulder at 866 °C temperature are characteristic of the recrystallization process of C-S-H(I) and C-S-H(II); the effect at 114 °C temperature corresponds to the removal of adsorption/crystallization water, and the effect at 675 °C temperature can be assigned to the decomposition of calcium

carbonate. According to the TGA analysis calculation, less than 0.5% of calcium carbonate is intercalated in the products (Fig. 3.54 c, curve 1).

The In Situ XRD patterns of the H-Cu sample after calcination in a high-temperature camera showed that the CuO compound remained stable up to 1000 °C (Fig. 3.55). It should be noted that the C-S-H(I) and/or C-S-H(II) and calcite compounds start recrystallizing around 800–850 °C temperature range, and calcium silicates (wollastonite and β-C2S) start forming (Fig. 3.55). These data are in good agreement with the DSC results (Fig. 3.54 c). Moreover, the intensity of CuO diffraction peaks as well increases at 850–1000 °C temperature, which confirms that a part of the Cu is intercalated into the CSH structure (Fig. 3.55).

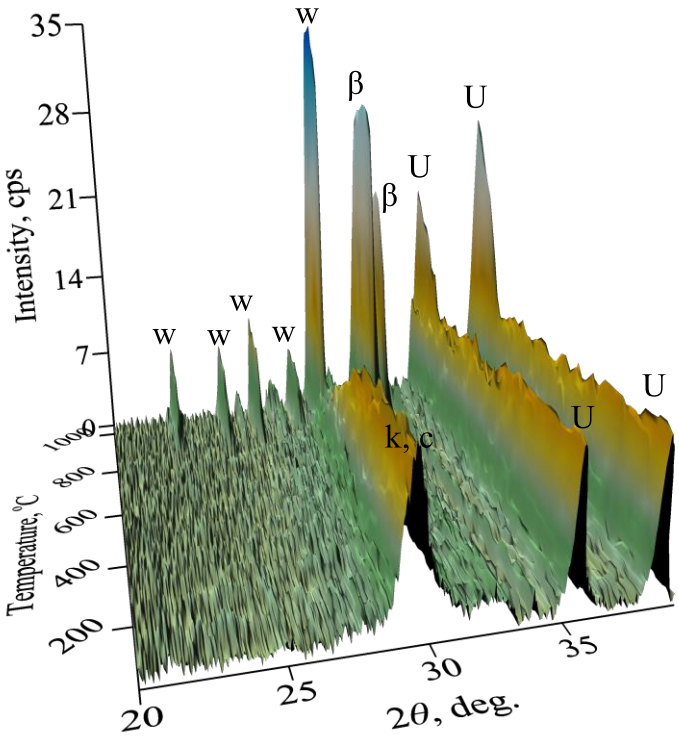

Fig. 3.55. In Situ XRD patterns of H-Cu sample, when the temperature of calcination is 25–1000 °C; indexes: c – C-S-H(I) and/or C-S-H(II), w – wollastonite, k – $CaCO_3$, U – CuO, β – β-C_2S

It was determined that during the calcination at 600 °C for 24 h, when the temperature was reached within 48 h, the CuO intensity of the diffraction peaks remained stable (Fig. 3.56 a). The results of SEM analysis confirm that after the calculations at 600 °C, CuO tends to agglomerate with increasing rod size (Fig. 3.56 b) [189].

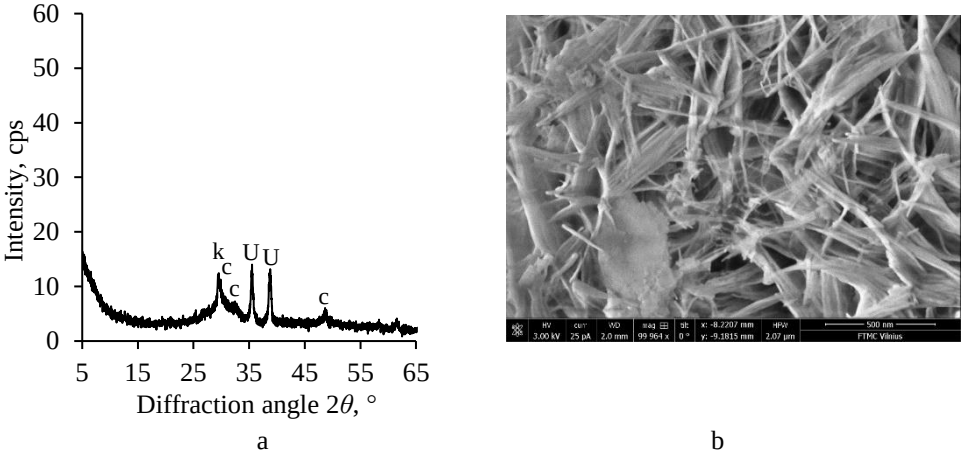

a b

Fig. 3.56. XRD pattern (a), SEM image (magnification 5000 times) (b), and FT-IR spectrum (c) of H-Cu600 sample; indexes: c – C-S-H(I) and/or C-S-H(II), k – $CaCO_3$, U – CuO

3.3.4. H-Cu sample texture and microstructure parameters in the temperature range 25–600 °C

The BET equation calculation was performed in order to determine the structural differences of formed compounds after the hydrothermal synthesis products and calcinated products. The nitrogen adsorption–desorption isotherms of samples show that in H-Cu sample Type IV, the H3 hysteresis loop, which is characteristic of plate-like particles and slit-like pores, is identified (Fig. 3.57 a). Further analysis of the H-Cu600 sample determined that a product can be classified as a Type II isotherm, which means that this compound is nonporous or macroporous material (Fig. 3.57 b).

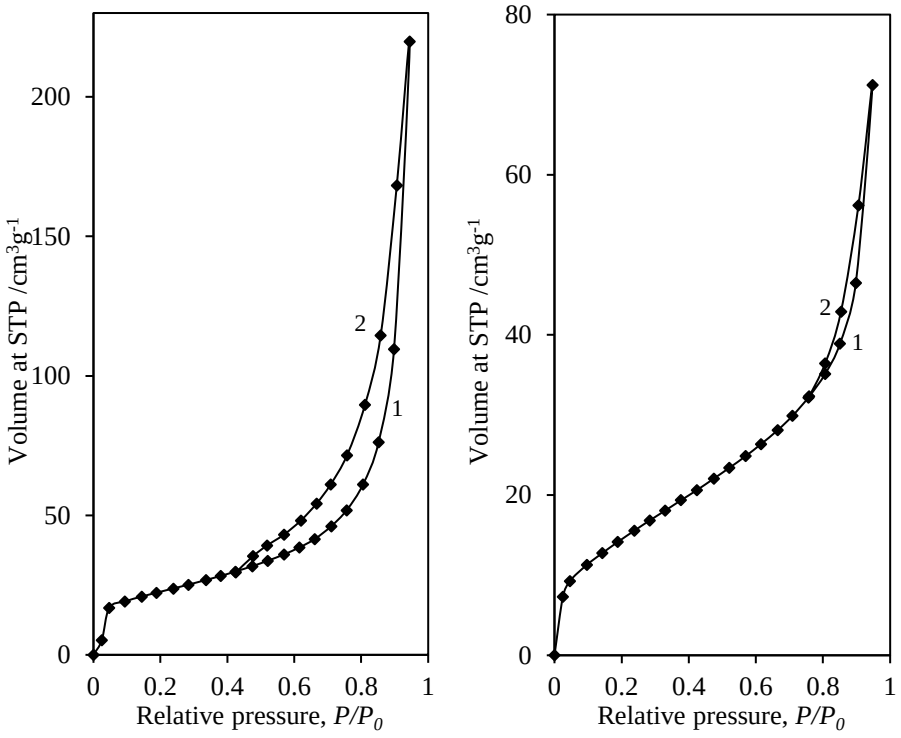

Fig. 3.57. Nitrogen adsorption (1) – desorption (2) isotherms of H-Cu sample (a) and H-Cu600 sample (b)

In order to confirm the adsorption–desorption isotherm results, the TEM micrographs were observed (Fig. 3.58). The rod-like shape particles of CuO and disordered uncertainly shaped crystallites of semi-crystalline phase C-S-H were identified at the H-Cu sample (Fig. 3.58 a). Meanwhile, the amorphous structure compounds (partially dehydrated C-S-H(I) and/or C-S-H(II)) in the H-Cu600 sample were identified (Fig. 3.58 b).

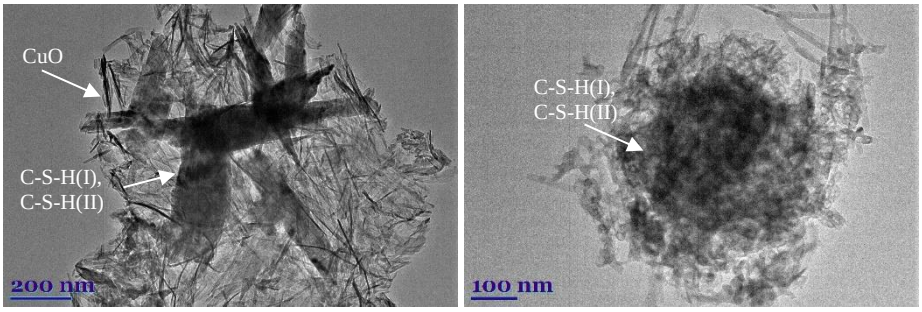

Fig. 3.58. TEM micrographs of H-Cu sample (a) and H-Cu600 sample (b)

As the isotherm of N_2 adsorption in the BET plot shows, the H-Cu and H-Cu600 samples were covered with a stable single-molecular layer of gas, because both sample coefficients R^2 are more than 0.99 (Fig. 3.59). The calculations show that the C_{BET} constant of the H-Cu600 sample (40.77) decreased 4 times, compared to the H-Cu sample (163.00) (Table 3.17). It should be noted that despite C_{BET} constant differences, the surface area S_{BET} of H-Cu and H-Cu600 sample decreased from 80.24 m^2/g to 55.51 m^2/g (Table 3.17).

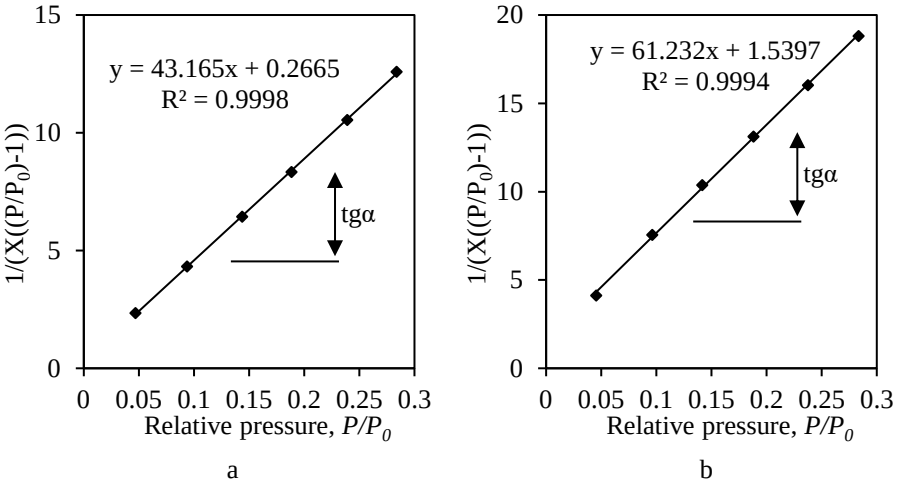

Fig. 3.59. The isotherm of N_2 adsorption at 77 K in the BET plot of H-Cu sample (a) and H-Cu600 sample (b)

Table 3.17. Calculated parameters of H-Cu sample and H-Cu600 sample by a BET method

Sample	BET equation constants		Capacity of mono layer X_m	S_{BET}, m^2/g	C_{BET} constant	Reliability coefficient, R^2
	Slope/ $S = tg\alpha$	Intercept/*I*				
H-Cu	43.17	0.27	0.023	80.24	163.00	0.9998
H-Cu600	61.23	1.54	0.016	55.51	40.77	0.9994

The calculation shows that the difference between S_{BET} and $\sum A$ values was equal only to 5.47%, and the value of the cumulative pore volume of the H-Cu sample is equal to 0.341 cm^3/g (Table 3.18). The differential distributions of volume pore sizes showed that H-Cu sample is a mesoporous material, because the pores with 7–15 nm diameter are dominant (Fig. 3.60 a).

Table 3.18. The data of ΣA and ΣV_P calculations of the H-Cu sample

Sample	S_{BET}, m^2/g	Results using a cylindrical pore model				Results using a parallel plates pore model			
		ΣA, m^2/g	$\lvert S_{BET} - \Sigma A \rvert$, m^2/g	$\lvert S_{BET} - \Sigma A \rvert$, %	ΣV_P, cm^3/g	ΣA, m^2/g	$\lvert S_{BET} - \Sigma A \rvert$, m^2/g	$\lvert S_{BET} - \Sigma A \rvert$, %	ΣV_P, cm^3/g
H-Cu	80.24	115.17	34.93	43.53	-	75.85	4.39	5.47	0.341

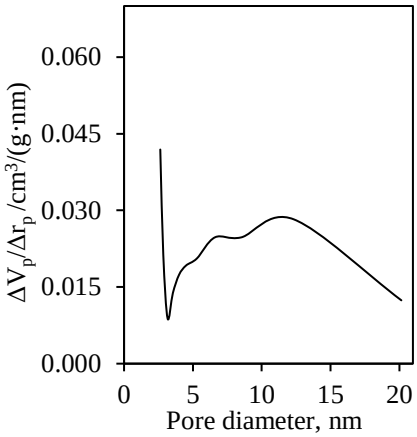

Fig. 3.60. Differential distributions of volume pore sizes of H-Cu where the curve value was obtained using a slit-like pore model

3.3.5. The synthesis of calcium silicate hydrates with incorporated Co^{2+} ions

In order to determine the influence of cobalt ions on the calcium silicate hydrate structural properties, the hydrothermal synthesis (analogous to H-Cr sample synthesis) was carried out in $Co(NO_3)_2 \cdot 6H_2O$ solution (H-Co sample).

According to the XRD analysis, after the hydrothermal treatment in $CaO\text{-}SiO_2\text{-}Co(NO_3)_2 \cdot 6H_2O$ mixture, the $CaCO_3$ and C-S-H(I) and/or C-S-H(II) were formed in the synthesis product (Fig. 3.61 a). The AAS results showed that after synthesis, the concentration of Co^{2+} ions in the liquid medium did not exceed even 0.001% of the primary cobalt ions concentration. It was determined that FIA analysis results showed that more than 57% (from the primary concentration) of the NO_3^- anions are detected in the liquid medium. It should be noted that the XRD results did not show the formation of compounds, containing Co^{2+} or NO_3^- ions.

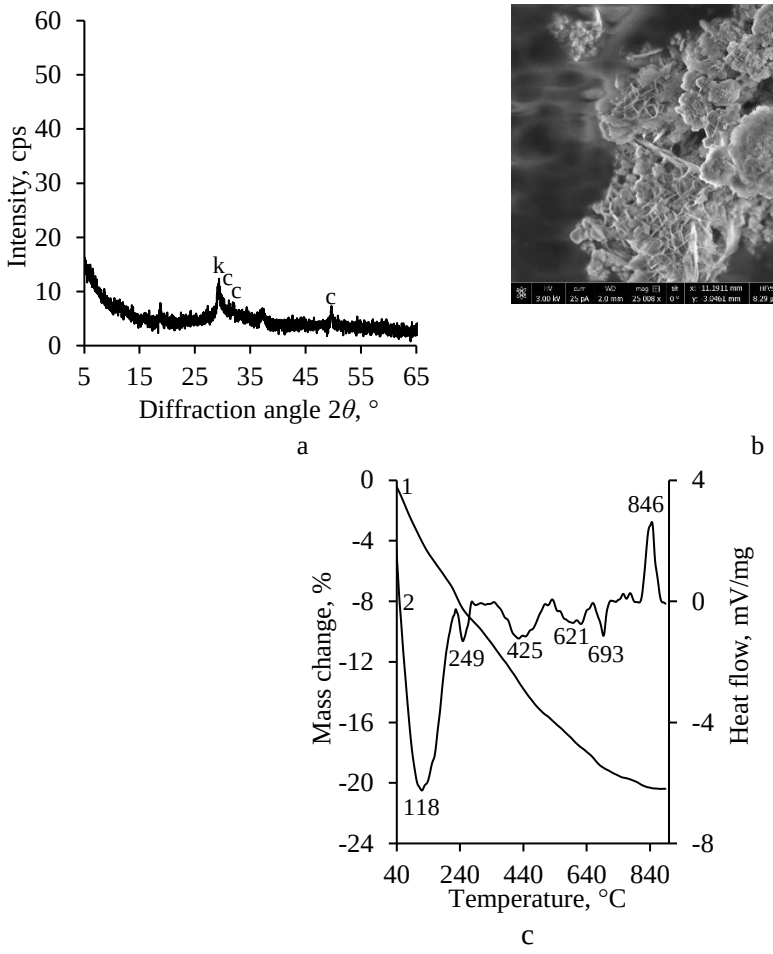

Fig. 3.61. XRD pattern (a), SEM image (magnification 25 000 times) (b), STA curves (curve 1 – TG, curve 2 – DSC) (c) of H-Co sample; indexes: k – $CaCO_3$, c – C-S-H(I), and/or C-S-H(II)

Meanwhile, the H-Co sample SEM micrographs show that thin close-packed particles (called foils or honeycomb) were formed in the synthesis products (Fig. 3.61 b). According to the DSC data, the endothermic effect at 118 °C temperature can be assigned to the removal of adsorption/crystallization water from C-S-H(I) and/or C-S-H(II) structure (Fig. 3.61 c, curve 2). It should be noted that the thermal effects at 249 °C, 425 °C, and 621 °C temperatures can be assigned to the decomposition or dehydration of Co^{2+} and/or NO^{3-} ions containing compounds (Fig. 3.61 c, curve 2). The data of TGA showed that 9.72% mass change in the mentioned temperature range is presented in the products (Fig. 3.61 c, curve 1). The endothermic effect at 693 °C temperature can be assigned to the decomposition of calcium carbonate. It was determined that the thermal effects at 846 °C temperature are characteristic of the recrystallization process of C-S-H(II) (Fig. 3.61 c, curve 2).

In order to investigate the thermal stability of the H-Co sample, the In Situ XRD experiment was examined (Fig. 3.62). It should be noticed that the H-Co sample was stable when the temperature varied in 25–550 °C interval. It was determined that at higher temperatures, the CoO compounds start to form (Fig. 3.62). According to In Situ XRD data, when the temperature was increased to 700–750 °C and 800–850 °C, the decomposition of calcium carbonate and recrystallization of semicrystalline type compounds to wollastonite and β-C_2S, respectively, was observed to form (Fig. 3.62). It should be indicated that the mentioned compounds remained stable up to 1000 °C.

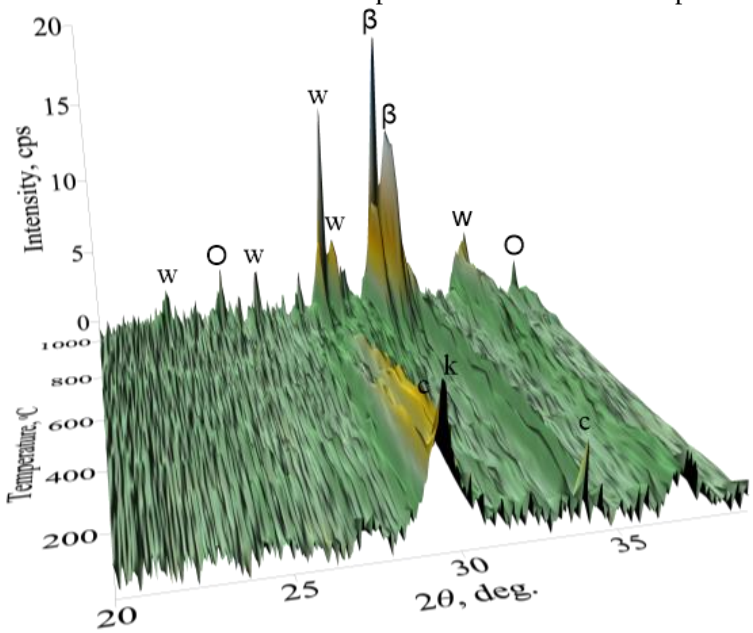

Fig. 3.62. In Situ XRD patterns of H-Co sample when the temperature of calcination is 25–1000 °C; indexes: k – $CaCO_3$, O – CoO, c – C-S-H(I) and/or C-S-H(II), w – wollastonite, β – β-C_2S

In order to improve In Situ XRD results, the calcination experiment was performed at 550 °C temperature (Fig. 3.63 a). It was determined that only $CaCO_3$ was observed in the XRD pattern. Furthermore, the SEM micrograph of the H-Co sample showed the sintered structure of products where the crystals of wollastonite, CoO, or β-C_2S cannot be distinguished (Fig. 3.63 b).

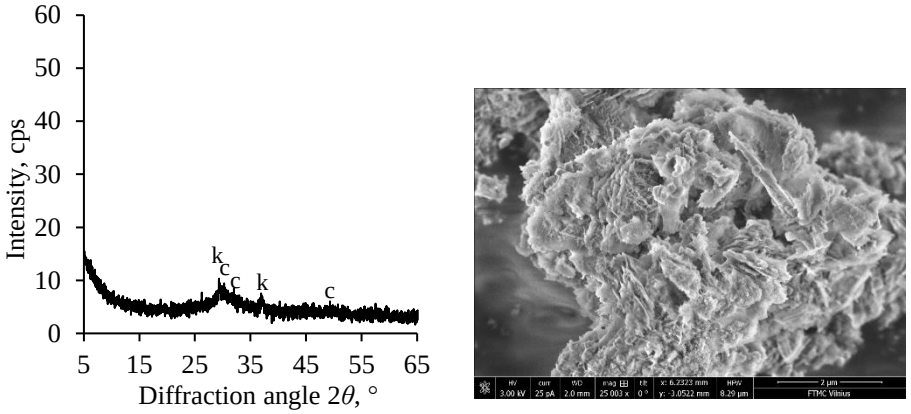

a b

Fig. 3.63. XRD pattern (a), SEM image (magnification 100 000 times) (b) of H-Co550 sample; indexes: k – $CaCO_3$

3.3.6. H-Co sample texture and microstructure parameters in 25–550 °C temperature range

There were compared N_2 adsorption/desorption isotherms of samples after the hydrothermal synthesis and calcination at 550 °C temperature (Fig. 3.64). It was determined that the adsorption/desorption isotherm of the H-Co sample showed that it matches with the Type IV, H3 hysteresis loop (Fig. 3.64 a). Meanwhile, the H-Co550 sample matches the Type IV, H3 hysteresis loop (Fig. 3.64 b).

These results were confirmed by the TEM data (Fig. 3.65). The uncertainly shaped crystallite of C-S-H was identified at the H-Co sample (Fig. 3.65 a). According to the TEM micrograph results, the nanoparticles of amorphous states compounds can be identified in H-Co550 as well (Fig. 3.65 b).

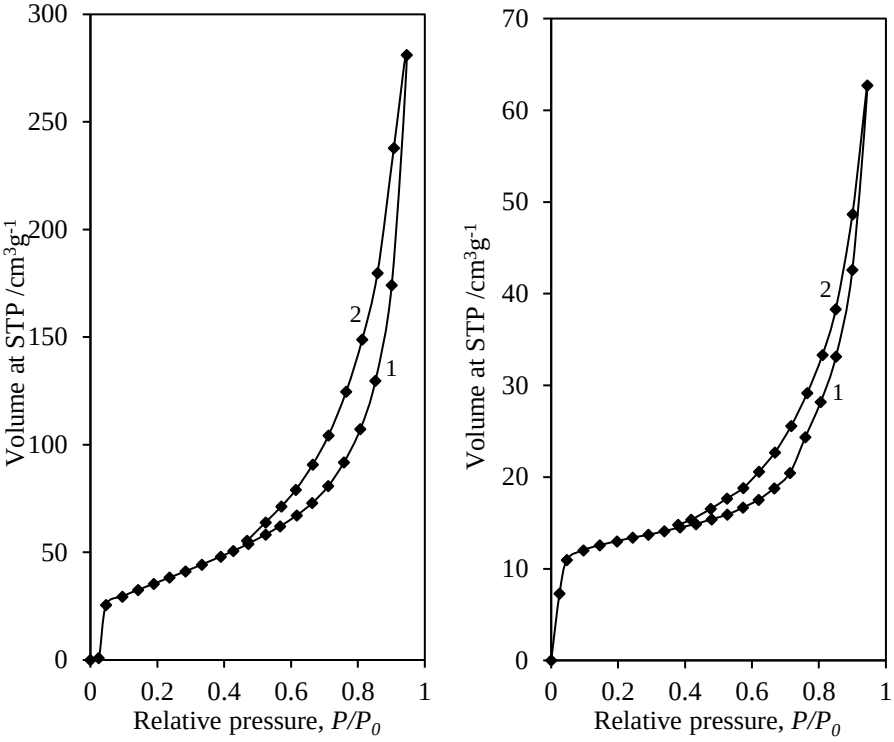

a b

Fig. 3.64. Nitrogen adsorption (1) – desorption (2) isotherms of H-Co sample (a) and H-Co550 sample (b)

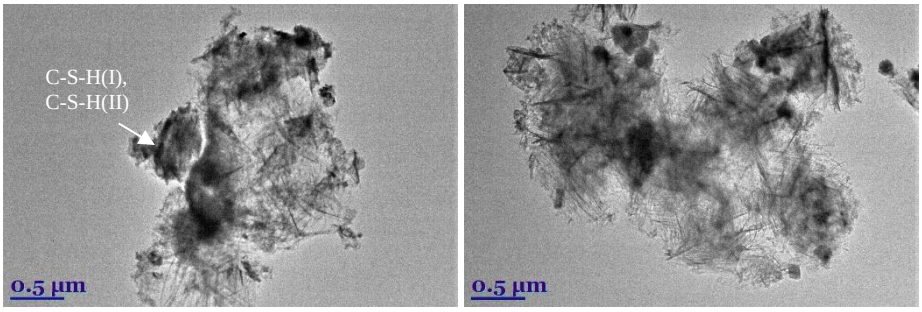

a b

Fig. 3.65. TEM micrographs of H-Co sample (a) and H-Co550 sample (b)

It was determined that a stable single-molecular layer of adsorbed N2 is formed on the H-Co and H-Co550 sample surface (Fig. 3.66). It could be mentioned that the C_{BET} constant of H-Co and H-Co550 samples is equal to 25.99 and 73.51, respectively (Table 3.19). According to the calculation, the surface area S_{BET} was equal to 132.23 m^2/g of the H-Co sample and 47.34 m^2/g of the H-Co550 samples (Table 3.19). It was determined that only slit-like pores were formed in the structure of the H-Co

sample (Table 3.10), because the difference between S_{BET} and ∑A values was equal to 13.23%.

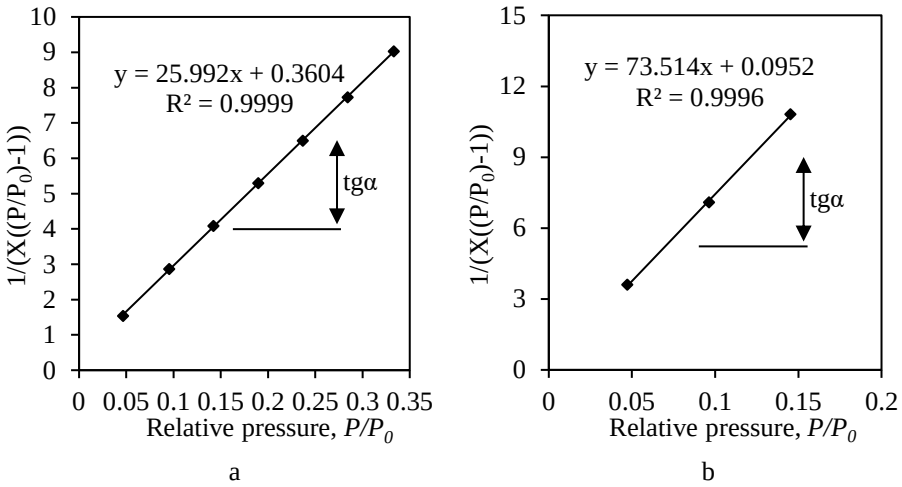

Fig. 3.66. The isotherm of N_2 adsorption at 77 K in the BET plot of H-Co sample (a) and H-Co550 sample (b)

Table 3.19. Calculated parameters of H-Co sample and H-Co550 sample by a BET method

Sample	BET equation constants		Capacity of mono layer X_m	S_{BET}, m^2/g	C_{BET} constant	Reliability coefficient, R^2
	Slope/ S = tgα	Intercept/*I*				
H-Co	25.99	0.36	0.038	132.23	73.12	0.9999
H-Co550	73.51	0.10	0.014	47.34	773.13	0.9996

It was calculated that the value of the cumulative pore volume of the H-Cr sample depends on the used model and is equal to 0.419 cm^3/g (Table 3.20). Differential distributions of volume pore sizes showed that the H-Co sample is mesoporous material because the pores with 2–5 nm in diameter are dominant (Fig. 3.67 a).

Table 3.20. The data of ΣA and ΣV_P calculations of H-Co sample and H-Co550 sample

Sample	S_{BET}, m^2/g	Results using a cylindrical pore model				Results using a parallel plates pore model			
		ΣA, m^2/g	$\lvert S_{BET} - \Sigma A \rvert$, m^2/g	$\lvert S_{BET} - \Sigma A \rvert$, %	ΣV_P, cm^3/g	ΣA, m^2/g	$\lvert S_{BET} - \Sigma A \rvert$, m^2/g	$\lvert S_{BET} - \Sigma A \rvert$, %	ΣV_P, cm^3/g
H-Co	132.23	180.63	48.40	36.60	-	114.73	17.50	13.23	0.419
H-Co550	47.34	31.32	16.02	33.84	0.096	20.14	27.20	57.46	0.086

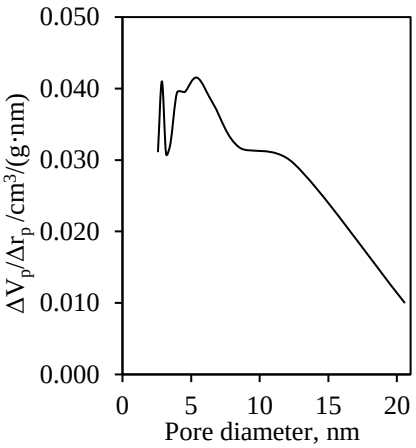

Fig. 3.67. Differential distributions of volume pore sizes of H-Co sample; curve 1 values are obtained using a cylindrical-like pore model and curve 2 values are obtained using a slit-like pore model

3.4. Application of poorly-ordered and well-ordered structure synthesized calcium silicate hydrates compounds in propanol oxidation reactions

The catalytic activity of synthesized and calcined samples was measured during the complete oxidation of propanol in the air stream. The main product of complete oxidation is carbon dioxide; thus, the main parameter of catalyst performance is the decrease in the concentration of the volatile organic compound in relation to CO_2 accumulation. As the initial concentration of propanol slightly varied, all the measured concentration values were normalized and are presented per one gram of catalyst and per one gram of propanol in the ingoing stream. The decrease of propanol concentration is presented as conversion expressed in percentage units, whereas the selectivity of the catalysts was evaluated by the amounts of intermediates found in the outgoing flow. The experiments were performed within the temperature range of 150–300 °C with the step of temperature increasing by around 25 °C per hour.

It has been determined that at the beginning of the experiments (150 °C), by using synthetic and calcined H-Cr samples, the concentration of propanol in the outgoing stream decreased by 56.5% and 51.8% of the initial amount, respectively (Fig. 3.68). However, the further analysis has shown the absence of CO_2 in the outgoing stream, which indicates that propanol was adsorbed by samples, but it was not oxidized. The higher adsorption of propanol by the synthetic sample can be explained by its higher surface area (104.76 m^2/g) than that of the calcined sample (68.92 m^2/g) (Table 3.15).

Propanol oxidation starts at 175 °C temperature, because the CO_2 concentration increases in the outgoing stream. At this temperature, the differences between synthetic and calcined samples appear. The synthetic sample showed higher catalytic activity than the calcined one because a sharper increase in CO_2 concentration was observed (Fig. 3.68). The conversion and CO_2 accumulation curves coincide well, which indicates that with the increase in temperature, the process switches from adsorption to catalytic oxidation.

By comparing the aforementioned curves, it can be stated that the synthetic sample reached 95% conversion at around 240 °C temperature, which is a good result compared to the bulk, supported, and mixed catalysts [190–192]. This indicates that semicrystalline calcium silicate hydrates with intercalated chromium ions are able to exchange oxygen during the heterogeneous oxidation process. It should be noted that chlorinated organics, as well as esters, are less destructible than alcohols. It was determined that the calcined sample struggled with catalytic oxidation as the formation of carbon dioxide was much slower; the conversion of 95% was reached only at temperatures higher than 290 °C temperature (Fig. 3.68). It can be concluded that the formation of calcium chromate has a negative effect on the propanol oxidation reactions; thus, the synthetic sample should be used at lower temperatures than 500 °C temperature (in order to avoid the formation of calcium chromate). Similar results are presented in literature, specifically, that copper dichromate did not show high catalytic activity [192]. Evidently, both samples had a high adsorptive affinity for propanol, as the influence of adsorption on the overall process was observed at temperatures as high as 275 °C. As the temperature was increased in the catalyst bed, sharp increases in CO_2 concentration and sudden spikes in temperature due to the exothermal effect of the oxidation reaction were observed.

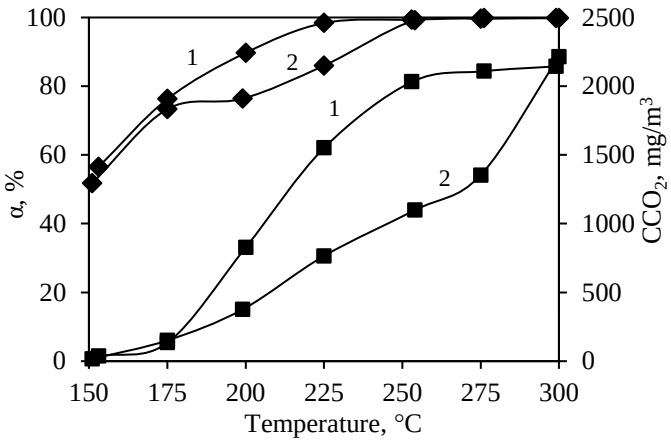

Fig. 3.68. Conversion temperature degree (♦) and accumulated CO_2 concentration (■) during the catalytic oxidation of propanol in synthetic H-Cr (1) and calcined H-Cr550 (2) samples

The different results were observed in the catalytic activity experiments of H-Cu and H-Co samples. The analysis of conversion and accumulated CO_2 concentration on H-Cu dates (Fig. 3.69 a, curve 1 ♦) showed that in 150–175 °C temperature range, the concentration of propanol in the outgoing stream started increasing and was from 50.51% to 10.38% of the initial amount. The same tendency was observed during the experiments with the calcinated H-Cu sample (Fig. 3.69 a, curve 2 ♦). In the 150–200 °C temperature range, the concentration of propanol in the outgoing stream increased as well from 74.08% to 92.21% of the initial amount. The conversion of 94.61% and 92.21% in H-Cu and H-Cu600 samples were reached only at temperatures higher than 290 °C (Fig. 3.69 a). Meanwhile, on the H-Co catalyst, at the 150 °C, the concentration of propanol in the outgoing stream was negligible (Fig. 3.69 b, curve 1 ♦). It reached the conversion of 96% at 275 °C. The catalytic oxidation of propanol on the H-Co550 started when 200 °C of temperature was reached (Fig. 3.69 b, curve 2). Up to the point, when the adsorption influence was observed in the range of 150–200 °C, with the increase of temperature, the propanol concentration increased as well from 56.59% to 84.54%, indicating that the desorption took over. As in the previous samples, it reached conversion of 94.50% at 275 °C temperature.

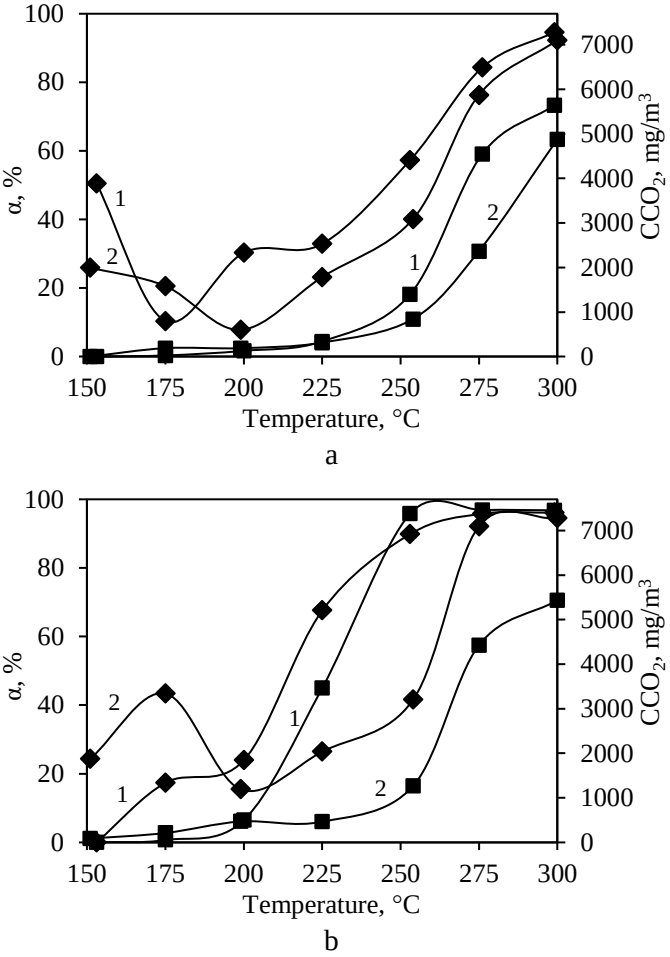

Fig. 3.69. Conversion temperature degree (♦) and accumulated CO_2 concentration (■) during the catalytic oxidation of propanol in synthetic (1) and calcined (2) H-Cu (a) and H-Co (b) samples

The CO probe and GC/MS monitoring of the outgoing gas stream during the experiments with calcinated and non-calcinated H-Cr, H-Cu, H-Co samples have shown the appearance of incomplete catalytic oxidation product intermediates. Usually, carbon monoxide forms at the beginning of the catalytic oxidation reactions, and it is oxidized to CO_2 faster by increasing the temperature. In this case, the formation of CO could be used for the determination of catalytic activity. The initial formation of CO could be observed at lower temperatures only for the synthetic sample, where it reached the maximum value of 161 mg/m^3 at 200 °C temperature and started decreasing afterward (Fig. 3.70). Meanwhile, the calcined sample reached the maximum concentration of CO (48 mg/m^3) at a temperature higher than 25 °C, i.e., at 225 °C temperature, and it was more than three times lower in comparison to the synthetic sample. CO formation curves (Fig. 3.70) showed that the slower

formation of carbon monoxide during the oxidation on the calcined sample is caused by the lower overall activity of catalyst but not due to its higher selectivity.

Both samples have shown similar results for the formation of the second intermediate compound propanal, where they yielded similar amounts of this aldehyde, i.e., 175 mg/m^3 for the synthesized sample and 180 mg/m^3 for the calcined sample (Fig. 3.70). The formation of propanal takes place up until catalytic oxidation takes over the adsorption, and the maximum values are reached at 175 °C temperature for the synthesized sample and 200 °C temperature for the calcined sample. Although aldehydes are harder to oxidize than alcohols, because of the relatively smaller concentration of propanal in the stream, its concentration still decreases fast as the temperature in the catalyst bed increases, and it can no longer be detected at 250 °C temperature. Propanal forms as a result of the interaction between propanol and the surface of the catalyst, which means that the dehydrogenation of propanol takes place. Therefore, it is evident that the largest amount of propanal forms when the adsorption process is the strongest and it is as well attributed to the apparent decrease in the propanol concentration, before the start of the catalytic oxidation reactions.

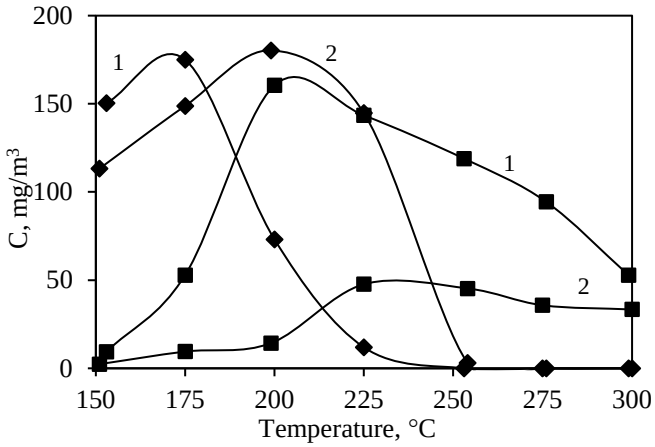

Fig. 3.70. Changes in the concentrations of pentanal (♦) and CO (■) formed during the propanol catalytic oxidation in synthetic (1) and calcined (2) samples

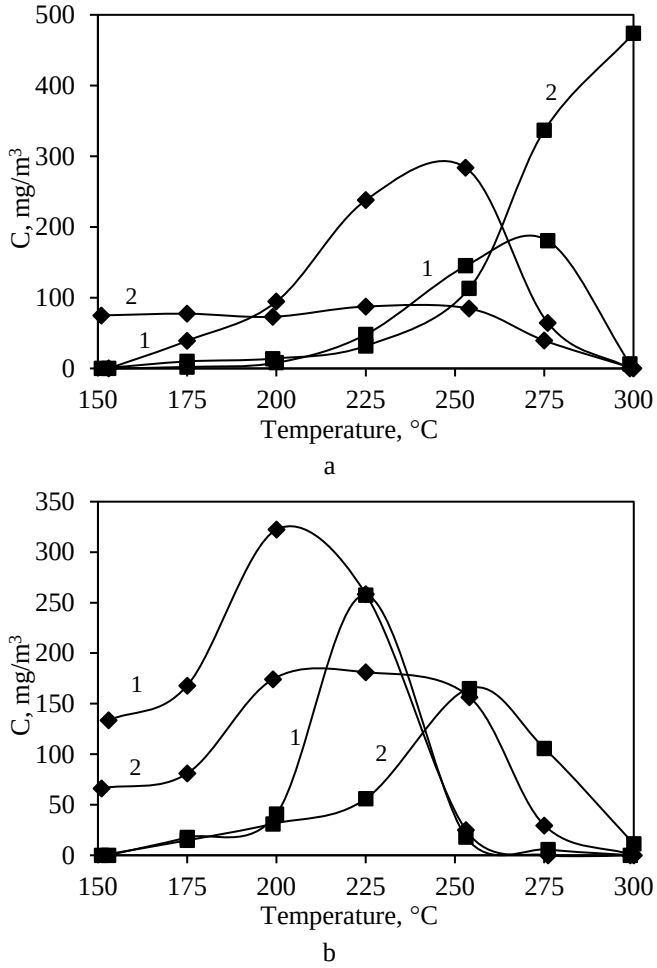

Fig. 3.71. Changes in the concentrations of pentanal (♦) and CO (■) formed during the propanol catalytic oxidation on the synthetic (1) and calcined (2) H-Cu (a) and H-Co (b) samples

3.5. Technological recommendations for the poorly-ordered and well-ordered structure calcium silicate hydrates compounds synthesis, adsorption, or thermal activation

Fig. 3.72 is a recommended schematic diagram for the preparation of samples of synthesis of poorly-ordered and well-ordered structure calcium silicate hydrates, combining hydrothermal synthesis, adsorption, or thermal activation methods. Amorphous $SiO_2 \cdot nH_2O$ and $CaCO_3$ are stored in raw material hoppers (1), (2). The calcium carbonate is fed from the hopper (2) to a kiln (3), which is incinerated at 550 °C for 1 h, and the CO_2 that was formed during the decomposition is removed. After combustion, it enters the mill (4). The prepared calcium oxide is fed to a sieve (5), from which the crushed material is further fed to a weight dispenser (6), and the required amount is obtained to acquire a C/S molar ratio of 1.5 (7). The ground raw

material is stored in a hopper (8). Then, the ground material is fed to a weighted dispenser (6), which weighs the required amount, according to the C/S ratio. Both the amorphous silica and the calcium oxide are weighted and added into the mixer (12), where they are mixed. The method of the synthesis method is chosen: I is hydrothermal synthesis of well-ordered structure calcium silicate hydrates compounds, II is hydrothermal synthesis of poorly-ordered structure calcium silicate hydrates compounds with embedded heavy metal ions. In case I, the required amount of distilled water (10% of dry matter) is added to the mixer (12) via the volumetric dispenser (9). In case of II, from the raw material hopper (10), depending on which metal ion insertion will be performed ($Cu(NO_3)_2 \cdot 3H_2O$, $Co(NO_3)_2 \cdot 6H_2O$, $Cr(NO_3)_3 \cdot 9H_2O$ granules), the weighing device (6) weighs the required amount of nitrate salt of heavy metals (concentration 10 g Me^{x+}/L). The required amount of granules was weighted and added into a batch propeller mixer (11), then was added the required amount of water to achieve the desired concentration of metal ions and dissolve the raw material by stirring until completely dissolved. Using the volumetric dispenser (9), the required amount of 10 g Me^{x+}/L solution (10% of dry matter) was added to the mixer (12). The mixed feedstocks are pumped (13) into a saturated water vapor autoclave (14) where they are hydrothermally treated at 175 °C for 16 hours. After the hydrothermal synthesis, the product is pumped (13) into the intermediate tank (15). From the intermediate tank via a pump (13), the synthesis product is fed to a drum vacuum filter (16), in which the excess solution remaining after the synthesis is removed. The product is fed from the drum vacuum filter (16) to the spray dryer (17). The calcium hydrosilicate granules of the well-ordered structure that were obtained in the process I are further fed to a batch adsorber (21), to which a metal ion $Cu(NO_3)_2 \cdot 3H_2O$, $Co(NO_3)_2 \cdot 6H_2O$, $Cr(NO_3)_3 \cdot 9H_2O$ granules, the required amount of nitrate salt are fed. Moreover, the required amount of distilled water (concentration 1 g Me^{x+}/l) is added to the adsorber (21) via the volume dispenser (9). The adsorption time at 25 °C is 15 minutes. After the adsorption process, the excess water is removed from the drum vacuum filter (16), which is returned to the production by a pump (13). The calcium hydrosilicates of poorly-ordered structure that were obtained in this process and in process II are fed to the furnace (22) with interfering heavy metal ions and kept there at the appropriate temperature, according to the intended method of the catalyst production.

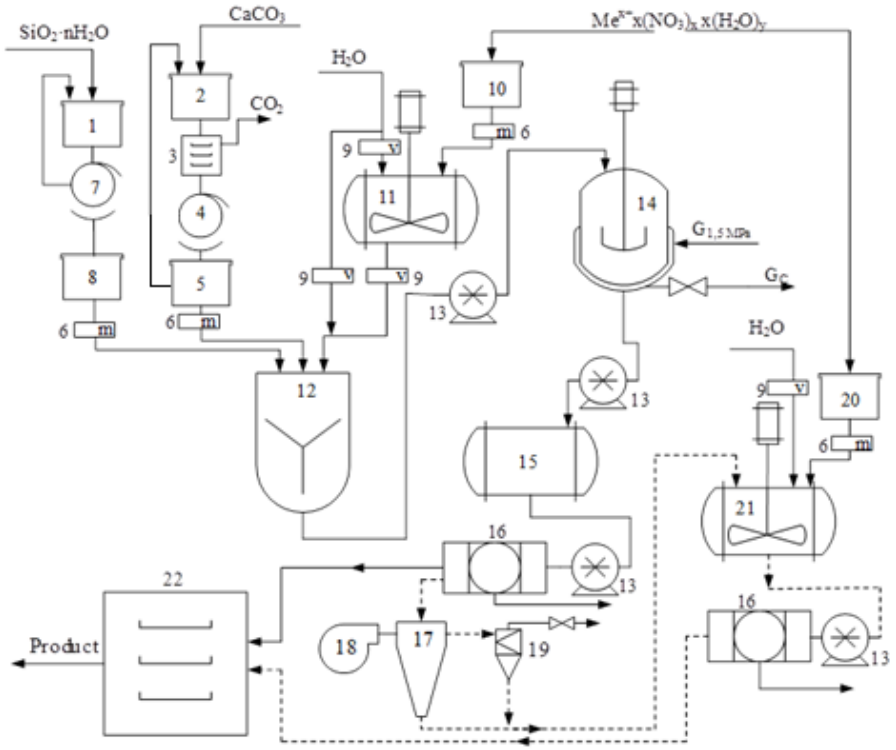

Fig. 3.72. The principal scheme of synthesis of poorly-ordered and well-ordered structure calcium silicate hydrates (CaO/SiO_2 = 1.5) samples with specific properties under periodic operation in production, which includes hydrothermal synthesis, adsorption, or thermal activation; indexes: 1, 2, 8 – hoppers, 3, 22 – furnaces, 4, 7 – mills, 5 – sieve, 6 – weight dispensers, 9 – volume dispensers, 10, 21 – tanks, 11 – propeller mixer, 12 – mixer, 13 – pumps, 14 – autoclave, 15 – tank, 16 – drum vacuum filter, 17 – spray dryer, 18 – fan, 19 – cyclone, 21 – adsorber

4. CONCLUSIONS

1. It was observed that the adsorption capacity of synthesized poorly-ordered and well-ordered structure calcium silicate hydrates (CaO/SiO_2 = 1.5) samples as well as the intercalation of heavy metal ions in their structure depends on the chemical nature of the used adsorbates. Extremely high uptake (up to 100%) of Cu^{2+}, Co^{2+}, and Cr^{3+} ions was observed in 0.25 g/L and 1 g/L concentration solutions. It has been found that that majority of metal ions (> 80%) participated in the ion-exchange reaction, while the remaining part was bound by the weaker physical interaction forces.
2. It was estimated that the pseudo-second-order model fits well with the heavy metals ions adsorption mechanism description, because the calculated $q_{e(cal)}$ values were close to the experimental $q_{e(exp)}$ ones. The Cu^{2+}, Co^{2+}, and Cr^{3+} ions adsorption rate (k_2) depends on the initial metal ions concentration. It has been determined that the adsorption reactions are not reversible in a neutral liquid medium, because after the desorption experiment, Cu^{2+} and Cr^{3+} ions concentration in the solution did not exceed ~0.01%; meanwhile, Co^{2+} ion did not exceed ~0.008%. According to the kinetic calculations, it was proved that the synthesized poorly-ordered and well-ordered structure calcium silicate hydrates samples acts as a chemisorbents.
3. It has been determined that the synthesized poorly-ordered and well-ordered structure calcium silicate hydrates (CaO/SiO_2 = 1.5) samples are stable in the lowest concentration solutions ($\leq$ 0.25 g Me^{x+}/L); however, when the concentration of Cu^{2+}, Co^{2+}, and Cr^{3+} ions was increased to 1 g/L, the structure of the compounds was partially disrupted. After the adsorption in 10 g/L solutions, the crystal structure of adsorbents samples was fully destroyed, and amorphous phases and/or gerhardtite $Cu_2(NO_3)(OH)_3$ were formed.
4. It was observed that the poorly-ordered calcium silicate hydrates (CaO/SiO_2 = 1.5) samples substituted with Cu^{2+}, Co^{2+}, and Cr^{3+} ions were stable up to 550–600 °C temperature, while at the higher temperature, the formation of CuO, Co_3O_4, and Cr_2O_3 proceeded. The calcined samples are mesoporous materials, whose specific surface area (S_{BET}) is in the range from 61.23 m^2/g to 73.51 m^2/g. It was obtained that the cylindrical and parallel plates pores are presented in the structure of synthetic and calcinated samples.
5. It was observed that Cu^{2+}, Co^{2+}, and Cr^{3+} ions (1 g Me^{x+}/L) from the liquid solution can be incorporated into the poorly-ordered structure of calcium silicate hydrates (CaO/SiO_2 = 1.5) under hydrothermal treatment conditions (175 °C, 16 h) and do not affect the mineral composition of products, despite copper ions. Meanwhile, the value of specific surface area (S_{BET}) of products significantly decreased, and seeks 43.17, 25.99, and 32.70 m^2/g in chromium, copper, and cobalt nitrate solutions, respectively. For this reason, the thermal behavior of synthetic compounds substituted with heavy metals ions is similar, compared with adsorbents substituted with metal ions.
6. It has been determined that during complete oxidation of propanol in the air stream at temperatures lower than 175 °C, synthesized and calcined poorly-

ordered calcium silicate hydrates samples act as adsorbents, while at the higher temperatures (more than 500 °C), catalytic oxidation proceeds. It was determined that the synthetic sample with incorporated Cr^{3+} ions reached 95% conversion at around 240 °C, while the calcined sample reached this value only at temperatures higher than 290 °C. Moreover, the formation of calcium chromate has a negative effect on the propanol oxidation reactions. Therefore, the synthetic sample should be used at temperatures lower than 500 °C.

7. The principal scheme of synthesis of poorly-ordered and well-ordered structure calcium silicate hydrates (CaO/SiO_2 = 1.5) samples with specific properties under periodic operation in production, which includes hydrothermal synthesis, adsorption, or thermal activation techniques that were offered.

5. SANTRAUKA

5.1 ĮVADAS

Pasak įvairių literatūrinių šaltinių, žmonija šiomis dienomis susiduria su daugiau nei 15 aplinkosaugos problemų, tokių kaip oro, vandens ir dirvožemio tarša, visuotinis atšilimas, sveikatos problemos ir kt. Vienas iš pagrindinių pasaulio oro taršos veiksnių yra lakieji organiniai junginiai (LOJ) – alkenai, alkanai, esteriai, alkoholiai ir kt. Pagrindiniai šių junginių šaltiniai yra chemijos ir naftos pramonė, farmacijos gamyklos, taip pat buitinės nuotekos, iš kurių susidaro įvairių LOJ. Yra daug LOJ neutralizavimo technologijų: biologinis skaidymas, adsorbcija, ozonavimas, terminis apdorojimas ar oksidacija. Katalizinė oksidacija yra vienas iš labiausiai paplitusių būdų pašalinti šiems junginiams, paverčiant juos į CO_2 ir H_2O žemoje temperatūroje (200–500 °C). Įprasti katalizatoriai gaminami iš platinos, paladžio ar aukso junginių, kurie yra brangūs, todėl katalizatorių gamybai mokslininkai ieško naujų alternatyvių metalų iš pereinamosios metalų grupės.

Kalcio hidrosilikatai (KHS) pasižymi būdinga pluoštine kristaline forma ir dideliu stabilumu aukštoje temperatūroje, dėl to šie junginiai yra gaminami pramoniniu būdu kaip pagrindinės šilumą izoliuojančios medžiagos, statybinių medžiagų ar dirbtinės medienos sudedamosios dalys. Be to, dėl didelio adsorbcijos pajėgumo KHS yra reikšmingi daugelyje sričių, tokių kaip vaistų tiekimo, kaulinio audinio inžinerijos, sunkiųjų metalų jonų adsorbcijos ir kiti procesai. Žinoma, kad dvibaziai kalcio hidrosilikatai pasižymi geromis daugelio metalų jonų adsorbcijos savybėmis. Dėl šios priežasties moksliniuose tyrimuose mezoporiai kalcio silikatai (xCaO·ySiO$_2$) arba kalcio hidrosilikatai (xCaO·ySiO$_2$·zH$_2$O) sulaukia didelio susidomėjimo kaip didelę adsorbcinę gebą turintys adsorbentai ir perspektyvi katalizatorių atraminė konstrukcija. Šie junginiai ne tik pasižymi minėtomis savybėmis, bet ir yra chemiškai stabilūs, taip pat gali išsklaidyti metalų jonų daleles ant savo paviršiaus. Be to, KS ir KHS leidžia išlaikyti unikalias metalo jonų savybes ir skatina katalizinį aktyvumą.

Kalcio hidrosilikatai yra aptinkami gamtoje arba formuojasi kaip portlandcemenčio hidratacijos produktas, taip pat gali būti susintetinti CaO-SiO$_2$-H$_2$O mišiniuose hidroterminėmis sąlygomis, esant 100–350 °C temperatūrai. O štai kalcio silikatai gali būti susintetinami degant kalcio hidrosilikatus arba skystai ir kietai sukepinant kalcio ir silicio turinčias medžiagas. Paprastai katalizatorių, kurių atraminiai karkasai yra KS arba KHS, paruošimas apima tris etapus: (1) KHS ar KS sintezė; (2) metalo jonų adsorbcija; (3) išdegimas pasirinktoje temperatūroje (siekiant gauti aktyviųjų metalų oksidų). Be to, į KHS ar KS struktūrą metalo jonus galima įterpti ir jų sintezės metu. Tokie junginiai su įterptais metalo jonais gali būti naudojami kaip katalizatoriai etanoliui paversti butadienu, bisfenolio F sintezei ir ketonų ar aldehidų oksidavimui. Deja, trūksta informacijos apie metalų įtaką tokių medžiagų susidarymui, terminiam stabilumui, mikrostruktūrai ir kitoms savybėms.

Remiantis literatūra, kai kurie metalo jonai, tokie kaip natrio ar kalio, teigiamai veikia kristalinio silicio turinčių junginių reaktyvumą, ardydami jų paviršių ir skatina KHS susidarymą. Skirtingi rezultatai buvo gauti naudojant aliuminio oksidą dvibazio

KHS – α-C_2SH sintezei 200 °C temperatūroje, nes šis priedas sulėtino KHS susidarymą, bet paskatino KS kristalizaciją. Katijonai, tokie kaip Al^{3+}, B^{3+} ir Be^{2+}, gali pakeisti silicį silicio ir deguonies tetraedre, o kiti, tokie kaip Na^{+}, K^{+}, Fe^{2+}, Mn^{2+}, Ti^{2+}, Zr^{2+} ir kt. įsiterpia už jo ribų. Šie katijonai jungia silicio ir deguonies tetraedrus. Taigi skirtingi katijonai keičia KHS ir KS susidarymą, terminį stabilumą, mikrostruktūrą ir kitas savybes.

Dėl šių priežasčių buvo nuodugniai ištirtas vario, kobalto ir chromo metalų jonų įterpimas į kalcio hidrosilikatų struktūrą adsorbcijos arba hidroterminės sintezės būdu ir jų mineralinės sudėties stabilumas (arba pokyčiai). Tačiau ištyrus KHS adsorbcijos gebą sunkiųjų metalų jonams, nustatyta sintetinių ir išdegtų produktų mikrostruktūra ir katalizinis aktyvumas.

Darbo tikslas: nustatyti netvarkingos ir tvarkingos struktūros susintetintų kalcio hidrosilikatų ($CaO/SiO_2 = 1,5$) bandinių adsorbcijos kinetinius parametrus Cu^{2+}, Co^{2+} ir Cr^{3+} jonams, jų terminį stabilumą bei katalizinį aktyvumą.

Darbo uždaviniai

1. Nustatyti netvarkingos ir tvarkingos struktūros susintetintų kalcio hidrosilikatų ($CaO/SiO_2 = 1,5$) bandinių adsorbcijos gebą Cu^{2+}, Co^{2+} ir Cr^{3+} jonams ir šiuos procesus apibūdinti taikant adsorbcijos kinetinius modelius.
2. Ištirti sintetinių adsorbentų bandinių su įsiterpusiais Cu^{2+}, Co^{2+} ir Cr^{3+} jonais terminį stabilumą 25–1000 °C temperatūros intervale oro aplinkoje.
3. Įvertinti hidroterminės sintezės metu įterptų Cu^{2+}, Co^{2+} ir Cr^{3+} jonų įtaką kalcio hidrosilikatų ($CaO/SiO_2 = 1,5$) bandinių mineralinei sudėčiai ir struktūros stabilumui.
4. Ištirti geriausių sintetinių ir degtų kalcio hidrosilikatų panaudojimo galimybes adsorbentų / katalizatorių gamyboje ir parengti technologines rekomendacijas pramonei.

Disertacijos ginamieji teiginiai

1. Susintetinti netvarkingos ir tvarkingos struktūros kalcio hidrosilikatų ($CaO/SiO_2 = 1,5$) bandiniai pasižymi didele sunkiųjų metalų jonų adsorbcijos geba (25–100 mg/g).
2. Gryni ir su įsiterpusiais Cu^{2+}, Co^{2+} ir Cr^{3+} jonais kalcio hidrosilikatų ($CaO/SiO_2 = 1,5$) bandiniai yra mezoporės medžiagos, kurios turi didelį paviršiaus plotą (>68 m^2/g).

Mokslinio darbo naujumas

1. Įrodyta, kad hidroterminio apdorojimo sąlygomis į netvarkingos struktūros kalcio hidrosilikatų ($CaO/SiO_2 = 1,5$) bandinius gali būti įterptas skirtingas kiekis (25–100 mg/g) Cu^{2+}, Co^{2+} ir Cr^{3+} jonų.
2. Susintetinti, kontroliuojamo specifinio paviršiaus chemosorbentų bandiniai su įsiterpusiais Cu^{2+}, Co^{2+} ir Cr^{3+} jonais yra stabilūs iki 550–750 °C temperatūros, o aukštesnėje temperatūroje vyksta CuO, Co_3O_4 ir Cr_2O_3 susidarymas.

Praktinė vertė

Susintetinti netvarkingos ir tvarkingos struktūros kalcio hidrosilikatų (CaO/SiO_2 = 1,5) bandiniai gali būti naudojami kaip chemosorbentai Cu^{2+}, Co^{2+} ir Cr^{3+} jonų šalinimui adsorbcijos procesuose. Hidroterminio apdorojimo sąlygomis sunkiųjų metalų jonai iš skystosios terpės terpiasi į netvarkingos struktūros kalcio hidrosilikatų bandinių struktūrą. Susintetinti ir degti bandiniai su įsiterpusiais Cu^{2+}, Co^{2+} ir Cr^{3+} metalų jonais gali būti naudojami kaip katalizatoriai propanolio oksidacijos reakcijoms, nes žemesnėje nei 175 °C temperatūroje junginiai veikia kaip adsorbentai, o aukštesnėje temperatūroje vyksta katalizinė oksidacija.

Darbo aprobavimas ir publikavimas

Disertacinio darbo tema paskelbtos 4 mokslinės publikacijos: 3 straipsniai recenzuojamuose mokslo leidiniuose *Web of Science* duomenų bazėje, indeksuotuose leidiniuose su cituojamumo rodikliu (JCR SCIE) ir 1 leidinyje, įtrauktame į *Web of Science* duomenų bazę, leidiniuose, indeksuotuose be cituojamumo rodiklio (JCR SCIE). Darbo rezultatai pristatyti 5 tarptautinėse mokslinėse konferencijose.

Darbo apimtis

Disertaciją sudaro įvadas, literatūrinių duomenų analizė, eksperimentinė dalis, tyrimų rezultatai bei jų aptarimas, išvados, 191 literatūros šaltinio sąrašas, mokslinių publikacijų sąrašas. Pagrindinė medžiaga išdėstyta 164 puslapiuose, įskaitant 20 lentelių ir 72 paveikslus.

Autorės ir bendraautorių mokslinis indėlis

Autorė susintetino ir aprašė visus disertacijoje aprašytus dvibazius kalcio hidrosilikatus. Taip pat ji ištyrė susintetintų junginių adsorbcines, terminio aktyvinimo bei katalizines savybes, atliko kinetinius ir BET skaičiavimus. Kęstutis Baltakys konsultavo apie kalcio silikatų susidarymo galimybes hidroterminės sintezės metu, eksperimento eigą ir rankraščių rengimą. Tadas Dambrauskas patarė junginių terminio aktyvinimo savybių ir adsorbcijos kinetikos skaičiavimo klausimais. Dėl technologinių rekomendacijų padėjo apsispręsti Anatolijus Eisinas kartu su Kęstučiu Baltakiu. Andrius Jaskūnas negailėjo patarimų adsorbcijos ir katalitinių procesų klausimais.

5.2 EKSPERIMENTINĖ DALIS

Naudotos medžiagos

1) Kalcio oksidas, gautas degant $Ca(OH)_2$ (1 h; 550 °C), maltas 30 s 600 aps/min greičiu vibraciniame diskiniame *Pulverisette 9* malūne ir persijotas per sietą. Savitasis paviršius $S_{pav.}$ = 2071 m^2/kg; $CaO_{laisvas}$ = 98,7 %.

2) Amorfinis silicio dioksidas – $SiO_2 \cdot nH_2O$, maltas 2,5 min 850 aps/min greičiu vibraciniame diskiniame *Pulverisette 9* malūne. $S_{pav.}$ = 1291 m^2/kg; kaitmenys – 5,19 %.

3) Vario nitrato tirpalai (c = 0,25; 1; 10 g Cu^{2+}/l), pagaminti distiliuotame vandenyje ištirpinus $Cu(NO_3)_2 \cdot 3H_2O$ granules, grynumas 99 %.

4) Kobalto nitrato tirpalai (c = 0,25; 1; 10 g Co^{2+}/l), pagaminti distiliuotame vandenyje ištirpinus $Co(NO_3)_2 \cdot 6H_2O$ granules, grynumas 99 %.

5) Chromo nitrato tirpalai (c = 0,25; 1; 10 g Cr^{3+}/l), pagaminti distiliuotame vandenyje ištirpinus $Cr(NO_3)_3 \cdot 9H_2O$ granules, grynumas 99 %.

6) Kalcio nitrato tirpalas (c = 1 g Ca^{2+}/l), pagamintas distiliuotame vandenyje ištirpinus $Ca(NO_3)_2 \cdot 4H_2O$ granules, grynumas 99 %.

4) Kiti gryni cheminiai reagentai: druskos rūgštis (1:1), acetonas, distiliuotas vanduo.

Hidroterminė adsorbentų A1 ir A2 sintezė

Kaip pradinės medžiagos buvo naudojamas smulkiai sumaltas $SiO_2 \cdot nH_2O$ ir CaO. Pradinių mišinių sudėtis atitiko molinį santykį C/S = 1,5. Homogenizuoti pradiniai mišiniai (45 min, 49 aps/min greičiu) užpilti distiliuotu vandeniu, kad suspensijoje vandens ir kietųjų medžiagų santykis V/K būtų lygus 10. Sintezė vykdyta suspensijoje nemaišant, 25 ml talpos PTFE induose, sudėtuose į autoklavą, kai sočiųjų vandens garų temperatūra 175 °C, o izoterminio išlaikymo trukmė – 24 h (A1 adsorbentas) ir 16 h (A2 adsorbentas). Sočiųjų vandens garų temperatūra buvo pasiekta per 2 h. Sintezės produktai praplauti acetonu, kad mažiau karbonizuotųsi, džiovinti 50 °C ± 5 temperatūroje 24 h ir persijoti per sietą, kurio akučių skersmuo 80 μm.

Nustatyta, kad *hidroterminės adsorbento A1 sintezės* metu, po 24 h izoterminio išlaikymo, susidaro dvibazis kalcio silikatas – α-C_2SH (PDF Nr. 04-009-6343) ir pusiau kristaliniai KSH tipo junginiai CSH (I)/CSH (II) (PDF Nr. 00-033-0306 ir PDF00-034-0002) (1 pav., a). Ištirta, kad junginyje taip pat susidaro ir mažo intensyvumo kalcio karbonato difrakcinės smailės (PDF Nr. 04-012-0489). Rentgeno spindulių difrakcijos analizės (RSDA) duomenys buvo patvirtinti vienalaikės terminės analizės (STA) rezultatais (1 pav., b). DSK kreivėje pirmasis endoterminis efektas (50–200 °C) gali būti priskirtas kristalizacinio vandens praradimui. O štai 400–500 °C temperatūros intervale stebimas α-C_2SH skilimas. Nustatyta, kad netenkama ~5,26 % sintezės produkto masės (1 pav., b, 1 kr.). Remiantis šiais duomenimis, buvo apskaičiuota, kad α-C_2SH susidarė ~55,5 %. O štai kalcio karbonato skilimui galima priskirti endoterminį efektą, esantį ~679 °C temperatūroje. Be to, buvo nustatyti du egzoterminiai efektai, esantys ~852 ir ~872 °C temperatūroje, kurie būdingi C-S-H (I)/C-S-H (II) persikristalizavimui į volastonitą (1 pav., 2 kr.).

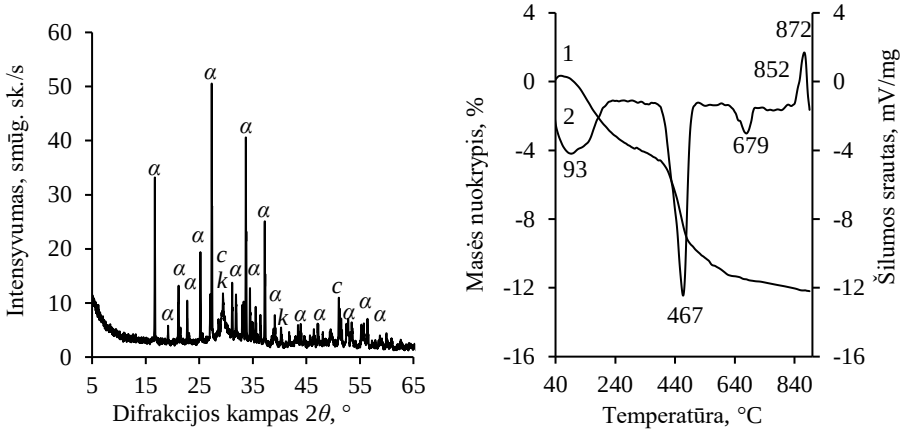

a b

1 pav. Adsorbento A1 RSDA (a) ir VTA (b, TGA (1 kr.) bei DSK (2 kr.)) kreivės. Čia: α – α-C_2SH; *k* – $CaCO_3$; *c* – C-S-H(I)/C-S-H(II)

Hidroterminės adsorbento A2 sintezės metu nustatyta, kad po 16 h izoterminio išlaikymo sintezės produkte dominavo pusiau kristaliniai C-S-H (I)/C-S-H (II) (2 pav., a). Taip pat RSDA kreivėje buvo nustatyti dvibazio kalcio silikato – α-C_2SH pėdsakai (2 pav., a). Šie rezultatai buvo patvirtinti ir VTA. Nustatyta, kad po hidroterminio apdorojimo DSK kreivėje endoterminis efektas, esantis 116 °C temperatūroje, gali būti priskirtas kristalizacinio vandens praradimui pusiau kristaliniuose C-S-H tipo junginiuose (2 pav., b, 2 kr.). O štai esant aukštesnei temperatūrai (400–500 °C) pastebėta α-C_2SH dehidratacija (2 pav., b, 2 kr.). Be to, buvo pastebėti du egzoterminiai efektai ~804 ir ~868 °C temperatūroje, atspindintys C-S-H (I)/C-S-H (II) persikristalinimą į kalcio silikatus (2 pav., b, 2 kr.). Verta paminėti, kad endoterminis efektas, kuris gali būti priskirtas kalcio karbonato skilimui, buvo pastebėtas 666 °C temperatūroje. Remiantis TGA duomenimis, minėto junginio susidarė mažiau nei 3 % (2 pav., b, 1 kr.).

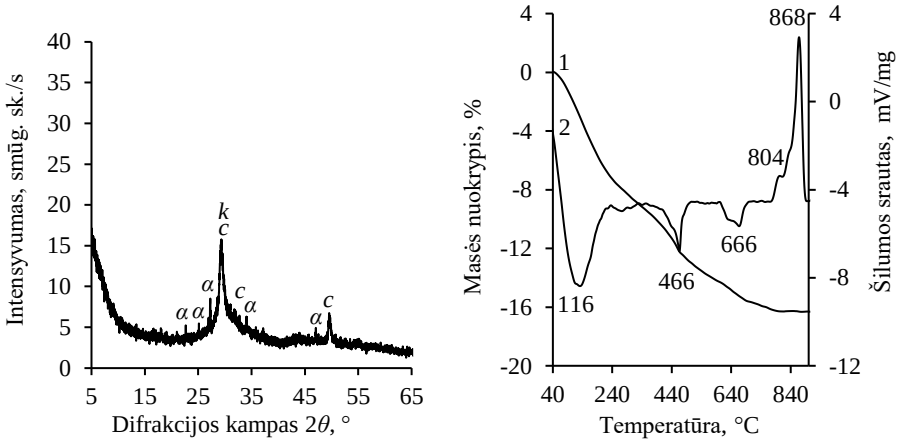

a b

2 pav. Adsorbento A2 RSDA (a) ir VTA (b, TGA (1 kr.) bei DSK (2 kr.)) kreivės.
Čia: α – α-C_2SH; *k* – $CaCO_3$; *c* – C-S-H(I)/C-S-H(II)

Sunkiųjų metalų (Cu^{2+}, Co^{2+}, Cr^{3+}) jonų adsorbcijos procesai vykdyti termostatuojamame adsorberyje (*Grant SUB 14*), į 500 ml $Me(NO_3)_x \cdot yH_2O$ tirpalą (Me^{x+} koncentracija 0,25; 1; 10 g/l) įberta 5,0 g susintetinto adsorbento (A1 arba A2); adsorbcijos trukmė 25 °C temperatūroje – 30 min. Adsorbuotų jonų kiekis nustatytas dviem būdais: apskaičiuojant pagal tirpalo koncentracijos mažėjimą laike (po: 0,5; 1; 3; 5; 10; 15 ir 30 min) ir analizuojant prisotintus adsorbentus A1 ir A2. Darbe visi cheminės analizės matavimai atlikti 3 kartus, o cheminė sudėtis ir metalų jonų koncentracijos pateiktos masės procentais.

Sunkiųjų metalų (Cu^{2+}, Co^{2+}, Cr^{3+}) jonų desorbcijos procesai vykdyti į 500 ml distiliuoto vandens įbėrus 5,0 g adsorbento (A1 arba A2) su įterptais sunkiaisiais metalais; desorbcijos trukmė 25 °C temperatūroje – 30 min. Desorbuotų jonų kiekis nustatytas ištyrus skystąją terpę, nustatant desorbuotų jonų koncentraciją.

Tirpalų *p*H vertės buvo išmatuotos *p*H-metru – *Hanna instruments* (*Hi 9321, microprocessor pH meter*) su stiklo elektrodu, kurio *p*H matavimo ribos nuo 1 iki 14,00. Tikslumas ±0,01.

Me^{x+} jonų koncentracija tiriamuose tirpaluose nustatyta atominės absorbcinės spektrinės analizės (AAS) būdu, *Perkin Elmen Analyst 4000* firmos spektrometru.

Nitratų anijonų koncentracija buvo nustatyta naudojant srauto įpurškimo analizatorių *FIAlyzer-100*. *FIAlyzer-100* sistema: *FIAlyzer-100,* integruotas FIA LOB kolektorius, USB4000 UV/VIS spektrometras, HL2000-LL matoma volframo lempa.

Sunkiųjų metalų jonų adsorbcijos kinetiniai parametrai apskaičiuoti taikant klasikinius adsorbcijos modelius. Skaičiavimai atlikti pagal pseudopirmojo laipsnio ir pseudoantrojo laipsnio lygtis.

Rentgenodifrakcinė analizė (RSDA) atlikta *Bruker AXS D8 Advance* difraktometru. Naudota: spinduliuotė – CuK_α, filtras – Ni, detektoriaus judėjimo žingsnis 0,02°, intensyvumo matavimo trukmė žingsnyje – 0,5 s, anodo įtampa U_a = 40 kV, srovės stipris I = 40 mA. Rentgenodifrakcinės analizės matavimų tikslumas 2θ = 0,001°.

Terminis stabilumas nustatytas taip:

1) aukštatemperatūrėje krosnyje *Nabertherm Model L5/11*, išlaikant bandinius 550, 600 ir 750 °C temperatūroje 24 h. Degimo temperatūra buvo pasiekta per 48 h.

2) Vienalaikės terminės analizės (VTA) tyrimai atlikti LINSEIS PT1000 terminiu analizatoriumi. DSK–TGA parametrai: temperatūros didinimo greitis – 15 °C/min, temperatūros intervalas – 30–1000 °C, etalonas – tuščias Pt tiglis, atmosfera krosnyje – oras. Matavimų tikslumas ±3 °C.

3) Aukštatemperatūrėje krosnyje *MTC-hightemp* (*Bruker AXS*). Parametrai: temperatūros didinimo greitis – 50 °C/min, pusiausvyros temperatūros nusistovėjimo trukmė – 2 min, temperatūros intervalas – 25–1200 °C, atmosfera krosnyje – oras. Pasirinktų temperatūrų aplinkoje atlikta RSDA analizė (detektoriaus judėjimo žingsnis 0,02°, intensyvumo matavimo trukmė žingsnyje – 1 s).

FT–IR spektrinė analizė atlikta spektrometru *Perkin Elmer FT-IR System*. Analizei naudota vakuuminėje presavimo formoje supresuota tabletė (1 mg medžiagos sumaišyta su 200 mg KBr). Tirta infraraudonojo spektro pagrindiniame diapazone nuo 4000 cm^{-1} iki 400 cm^{-1}.

Skenuojamoji elektroninė mikroskopija (SEM) atlikta naudojant prietaisą JEOL JSM-7600F. Greitinimo įtampa (ETH) – 10 kV, darbinis atstumas tarp bandinio ir paskutinio elektrooptinio lęšio briaunos (WD) – 8,6 mm, detektorius – SE.

Peršviečiamoji elektroninė mikroskopija (TEM) atlikta naudojant prietaisą *Tecnai G2F20 X-TWIN* su *Schottky-type* elektronų šaltiniu. Greitinimo įtampa (ETH) – 200 kV, detektorius – HAADFD.

Savitojo paviršiaus ploto nustatymas taikant BET metodą. Bandinių savitojo paviršiaus plotas nustatytas Brunauerio, Emmeto ir Tellerio (BET) metodu. Matavimai atlikti spektrometru *Kelvin 1042 Sorptometer* (*Costech Instruments*) naudojant azoto adsorbcijos izotermę 77 K temperatūroje.

Katalizinis aktyvumas nustatytas naudojant *Nabertherm LH 15/13* krosnies viduje sumontuotą kvarcinį reaktorių, kuriame yra ritės pašildytuvas. Katalizinė oksidacija buvo atlikta pastoviu 370 ml/min oro srautu, kuris buvo prisotintas 475–640 ppm lakiųjų organinių junginių. Propanolio koncentracija dujų sraute buvo nustatyta naudojant *Perkin Elmer Clarus 500 GC/MS* sistemą, aprūpintą COL-ELITE 5MS universalia kapiliarine kolonėle.

Laisvojo CaO kiekis buvo nustatytas remiantis Europos standartu *Building lime – Part 2: Test Methods. LST EN 459-2:2010*.

5.3 REZULTATAI IR JŲ APTARIMAS

5.3.1 Sintetinio adsorbento A1 sunkiųjų metalų adsorbcijos

Norint nustatyti adsorbento A1 adsorbcijos gebą sunkiesiems metalams, adsorbcijos eksperimentas buvo atliktas $Co(NO_3)_2 \cdot 6H_2O$ tirpale, kuriame pradinė Co^{2+} jonų koncentracija buvo 0,25 g Co^{2+}/l. Nustatyta, kad adsorbcijos procesas intensyviausiai vyksta pradžioje, nes po 30 s reakcijos į adsorbento A1 struktūrą įsiterpia apie 50 % kobalto jonų. Ilginant sąveikos trukmę iki 5 min, į adsorbento A1 struktūrą įsiterpusių Co^{2+} jonų kiekis buvo lygus 24,68 mg Co^{2+}/g. Ištirta, kad ilgesnis

sąveikos laikas neturėjo įtakos Co^{2+} jonų įsisavinimui, nes po 30 min reakcijos absorbuotų jonų kiekis išliko beveik toks pat ir buvo lygus 24,73 mg Co^{2+}/g.

Nustačius adsorbento A1 gebą adsorbuoti sunkiuosius metalų jonus 0,25 g/l koncentracijoje, nuspręsta Co^{2+} jonų koncentraciją padidinti iki 1 g/l. Ištirta, kad didesnė Co^{2+} jonų koncentracija teigiamai paveikė adsorbcijos procesą (3 pav., a), nes po 30 s adsorbcijos adsorbentas A1 adsorbavo 90 % pradinių Co^{2+} jonų. Eksperimento trukmę prailginus iki 10 min, buvo pasiekta adsorbcijos pusiausvyra, o adsorbuotų jonų kiekis buvo lygus 99,61 mg Co^{2+}/1g A1 adsorbento (3 pav., a). Verta paminėti, kad dėl Ca^{2+} jonų desorbcijos iš adsorbento, skystos terpės *p*H vertė padidėjo nuo 4,91 iki 10,97.

Siekiant nustatyti didžiausią adsorbento A1 adsorbcinį pajėgumą Co^{2+} jonams, $Co(NO_3)_2 \cdot 6H_2O$ tirpalo koncentracija buvo padidinta iki 10 g/l. Nustatyta, kad sorbcijos geba po 30 min adsorbcijos buvo lygi 288 mg Co^{2+}/g (3 pav., b). Tačiau žema pradinio $Co(NO_3)_2 \cdot 6H_2O$ tirpalo *p*H vertė turėjo neigiamą įtaką adsorbento A1 struktūros stabilumui, ir ~50 % Ca^{2+} jonų per tą patį laiką pateko iš adsorbento A1 į skystąją terpę.

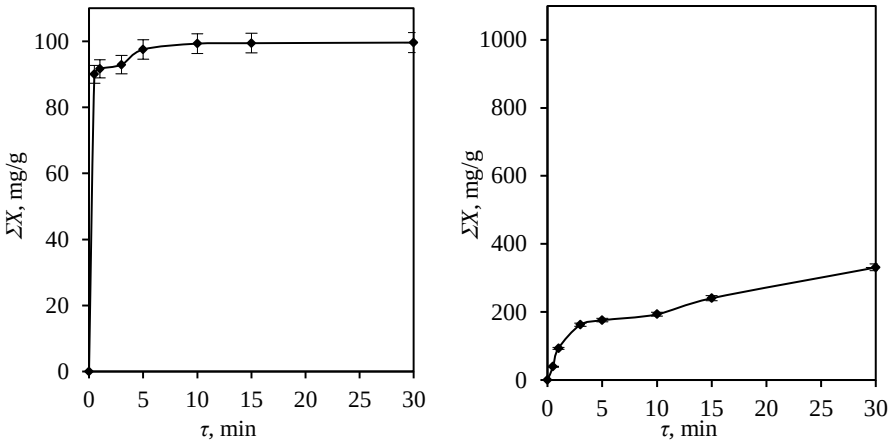

3 pav. Co^{2+} jonų adsorbcijos adsorbentu A1 integralinės kinetinės kreivės, kai pradiniame tirpale Co^{2+} jonų koncentracija yra 1 g/l (a) ir 10 g/l (b)

Panaši tendencija buvo stebima ir Cu^{2+} bei Cr^{3+} jonų adsorbcijos metu. Nustatyta, kad vykdant adsorbciją 0,25 g/l koncentracijos tirpaluose, jau po 30 s visi Cu^{2+} ir Cr^{3+} jonai įsiterpė į adsorbento A1 struktūrą. Padidinus sunkiųjų metalų jonų koncentraciją iki 1 g Me^{x+}/l, adsorbcija adsorbentu A1 vyksta lėčiau, nes per 30 s Cu^{2+} jonų adsorbcijos įsisavinimas siekia ~73 % (72,91 mg/g). O štai minėto junginio adsorbuotų Cr^{3+} jonų kiekis buvo didesnis ir lygus 86 % (86,14 mg/g). Pailginus eksperimento trukmę iki 3 min, Cr^{3+} jonų įsisavinimas pasiekė 100 %. O štai Cu^{2+} jonų įsisavinimas pasiekė 100 % tik po 30 min.

Nustatyta, kad 10 g/l Cu^{2+} jonų adsorbcijos pradžioje (30 s) minėtų jonų adsorbuotas kiekis greitai padidėjo iki 228,2 mg/g, o po 30 min jis buvo lygus 615,54 mg/g. Cr^{3+} jonų adsorbcijos atveju adsorbcijos geba buvo ~2,5 karto mažesnė, o adsorbuotų jonų kiekis lygus 241,42 mg Cr^{3+}/g. Adsorbcijos metu abiem atvejais iš

adsorbento į skystą terpę išsiskyrė daugiau nei 50 % Ca^{2+} jonų, o tai parodo, kad didelės sunkiųjų metalų jonų koncentracijos tirpaluose adsorbentas A1 tampa nestabilus. Dėl šios priežasties tolesniame tyrimų etape tyrimai buvo atliekami su 1 Me^{x+} mg/l koncentracijos $Co(NO_3)_2 \cdot 6H_2O$, $Cu(NO_3)_2 \cdot 3H_2O$ ir $Cr(NO_3)_3 \cdot 9H_2O$ tirpalais.

5.3.2 Sintetinio adsorbento A2 sunkiųjų metalų adsorbcijos ypatumai ir struktūros savybės

Panaudojus sintetinį adsorbentą Cu^{2+}, Co^{2+} ir Cr^{3+} jonų adsorbcijai iš nitratų druskų tirpalų, kuriuose pradinė Me^{x+} jonų koncentracija yra lygi 1 g/l, nustatyta, kad procesas intensyviausiai vyksta per pirmąją reakcijos minutę, nes jau po 30 s į adsorbento A2 kristalinę gardelę įsiterpia visi pradiniame tirpale esantys Cr^{3+} (100 mg Cr^{3+}/g) jonai. Panašus procesas nustatytas ir Cu^{2+} jonų adsorbcijos metu, nes per pirmąsias 30 s adsorbuotų metalo jonų kiekis buvo 92,0 mg Cu^{2+}/g, o po 1 min adsorbcijos procesas buvo pasibaigęs (1 lentelė). Palyginimui, Co^{2+} jonų adsorbcija adsorbentu A2 buvo lėtesnė, po 30 s buvo adsorbuota tik 62 % (62,50 mg Co^{2+}/g) minėtų jonų. Ilginant sąveikos trukmę, kobalto jonų koncentracija tirpale mažėja ir po 15 min į adsorbento A2 struktūrą įsiterpia 100 % tirpale esančių Co^{2+} jonų (100 mg Co^{2+}/g) (1 lentelė).

1 lentelė. Adsorbentu A2 adsorbuotų Me^{x+} jonų kiekis, kai pradiniame tirpale Me^{x+} jonų koncentracija yra 1 g/l

Adsorbuoti Me^{x+} jonai	τ, min / adsorbuotų Me^{x+} jonų kiekis, mg/g						
	0,5	1	3	5	10	15	30
Cr^{3+}	100	100	100	100	100	100	100
Cu^{2+}	99,20	100	100	100	100	100	100
Co^{2+}	62,50	74,55	79,90	85,46	99,69	100	100

Naudojant pseudopirmojo ir pseudoantrojo laipsnio lygtis buvo aprašyti sunkiųjų metalų jonų adsorbcijos į adsorbentą A2 kinetiniai parametrai. Dėl greito Cu^{2+} ir Cr^{3+} jonų įsiskverbimo į adsorbentą A2 adsorbcijos duomenys negalėjo būti naudojami minėtiems parametrams apskaičiuoti. Apskaičiuota, kad pseudopirmojo laipsnio lygties tiesinė priklausomybė rodo, jog vykstantys Co^{2+} jonų ir adsorbento A2 adsorbcijos procesai neaprašomi pseudopirmojo laipsnio modeliu. Taip teigti leidžia tiesinis regresinių kreivių tinkamumas eksperimentiniams duomenims, nes determinacijos koeficiento R^2 vertė nėra artima vienetui, o apskaičiuota q_{eaps} koncentracija skiriasi nuo nustatytos pusiausvirosios koncentracijos reikšmių q_{enust} (2 lentelė). Todėl galima teigti, kad pseudopirmojo laipsnio modelis nėra tinkamas adsorbento A2 adsorbcijos procesams aprašyti. Nustatyta, kad pseudoantrojo laipsnio modelis tinkamai aprašo Co^{2+} ir adsorbento A2 adsorbcijos mechanizmą, nes eksperimentinėmis sąlygomis apskaičiuoto R^2 koeficiento vertė yra lygi $R^2 = 0{,}99$. Apskaičiuota, kad kobalto jonų adsorbcijos reakcijos greičio konstanta k_2 yra lygi 0,015 g/mg·min, o q_{eaps} Co^{2+} jonų kiekis pusiausvyros sąlygomis yra artimas q_{enust} Co^{2+} jonų kiekiui (2 lentelė).

2 lentelė. Pseudopirmojo laipsnio ir pseudoantrojo laipsnio Co^{2+} jonų adsorbcijos kinetiniai parametrai

Pseudopirmojo laipsnio lygties adsorbcijos kinetiniai parametrai			
R^2	q_{enust}, mg/g	q_{eapsk}, mg/g	k_1, (g/(mg·min))
0,80	99,30	50,11	0,331
Pseudoantrojo laipsnio lygties adsorbcijos kinetiniai parametrai			
R^2	q_{enust}, mg/g	q_{eapsk}, mg/g	k_2, (g/(mg·min))
0,99	99,30	98,23	0,015

Norint nustatyti, ar sunkiųjų metalų įsiterpimas į adsorbento A2 struktūrą daro įtaką jo struktūros pokyčiams, po adsorbcijos proceso adsorbentas A2 buvo apibūdintas RSDA (4 pav.). Rentgeno spindulių difrakcijos analizės duomenys parodė, kad adsorbcijos eksperimentų metu adsorbento A2 struktūroje vyko karbonizacija, nes buvo nustatytos intensyvios difrakcijos smailės, būdingos kalcio karbonatui (4 pav.). Pažymėtina, kad minėtų smailių intensyvumas buvo ~2 kartus didesnis adsorbento A2 su įsiterpusiais Cu^{2+} jonais (toliau žymima: A2-Cu) (4 pav., 1 kreivė) bandinyje ir adsorbento A2 su įsiterpusiais Co^{2+} jonais (toliau žymima: A2-Co) (4 pav., 2 kreivė) bandinyje, lyginant juos su adsorbentu A2 su įsiterpusiais Cr^{3+} jonais (toliau žymima: A2-Cr) (4 pav., 3 kreivė) bandiniu. Taip pat visuose tirtuose bandiniuose buvo nustatytas platus pusiau kristalinės struktūros junginių bazinis atspindys (25–37°). Verta paminėti, kad α-C_2SH būdingos difrakcijos smailės RSDA kreivėje nebuvo pastebėtos. Nustatyta, kad adsorbcijos metu A2-Cr bandinyje susidarė chromo hidroksido hidratas ($Cr(OH)_3 \cdot 3H_2O$, (PDF Nr. 00-016-0817) (4 pav., 3 kreivė).

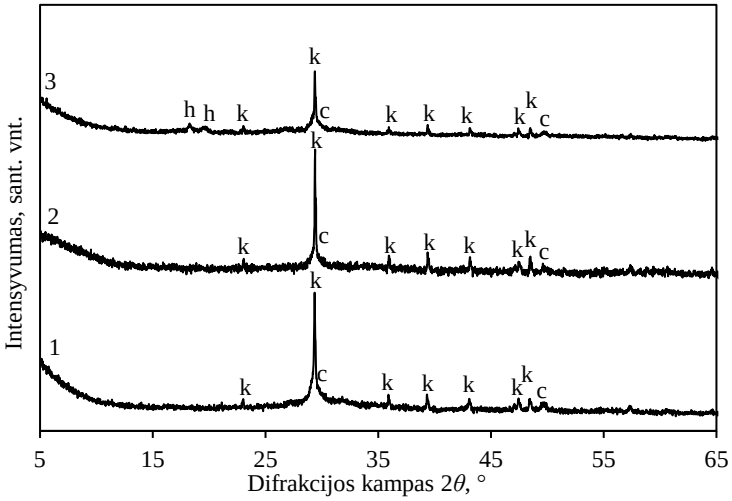

4 pav. A2-Cu (1 kreivė), A2-Co (2 kreivė) ir A2-Cr (3 kreivė) bandinių RSDA kreivės. Čia: *k* – $CaCO_3$; *h* – $Cr(OH)_3 \cdot 3H_2O$

Norint nustatyti adsorbento A2 terminį stabilumą buvo atlikta RSD analizė 25–1000 °C temperatūros intervale (5 pav.). Apskaičiuota, kad dvibazis adsorbentas A2 yra stabilus iki 400 °C temperatūros, nes šiam junginiui būdingi difrakcijos maksimumai (*d* – 0,304; 0,279; 0,182 nm) nepasikeitė. O štai, esant aukštesnei

temperatūrai (450 °C), α-C_2SH persikristalizavo į bevandenes C_2S fazes, tačiau dėl mažo difrakcijos smailių intensyvumo susidariusių junginių nustatyti neįmanoma (5 pav.). Nustatyta, kad degimo temperatūrai didėjant iki 650 °C kalcio karbonatas skyla ir RSDA kreivėse identifikuojamos kalcio oksido smailės (PDF Nr. 00-002-1088). Nustatyta, kad esant 800–850 °C temperatūrai pusiau kristalinio tipo ir C_2S fazės junginiai persikristalizuoja į volastonitą (PDF Nr. 00-066-0271) ir β-C_2S (PDF Nr. 00-033-0302). Keliant temperatūrą iki 1000 °C intensyvėja minėtiems junginiams būdingos difrakcijos smailės (5 pav.).

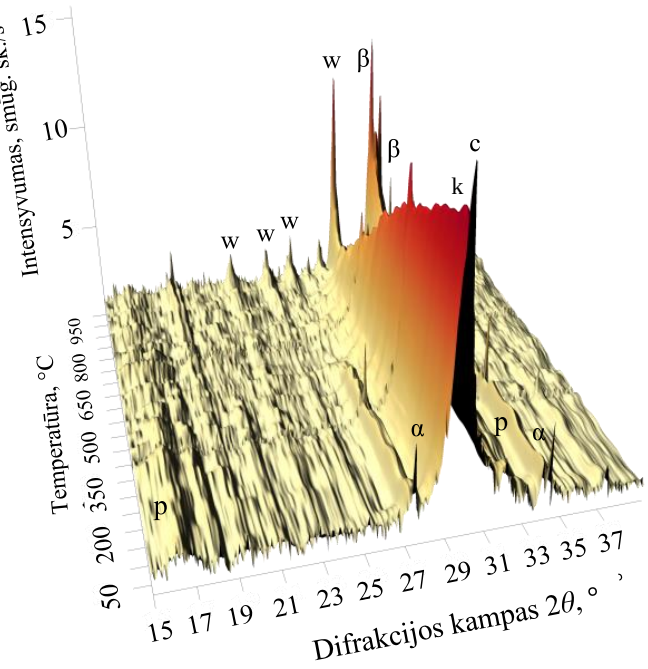

5 pav. Adsorbento A2 RSDA kreivės 25–1000 °C temperatūros intervale. Čia: α – α-C_2SH;
k – $CaCO_3$; c – C-S-H(I)/C-S-H(II); w – volastonitas; β – β-C_2S

Medžiagos sandara yra viena pagrindinių charakteristikų, lemiančių jos taikymo sritis ir eksploatacines savybes. Kitame tyrimų etape buvo nustatyta adsorbento A2 bandinių paviršiaus mikrostruktūra, savitasis paviršiaus plotas, vyraujantis porų dydis ir jų pasiskirstymas pagal spindulius, kristalų dydis ir forma. Adsorbentas A2 buvo išdegtas 750 °C temperatūroje (ši temperatūra buvo pasirinkta, norint ištirti bandinio poringumą prieš pradedant formuotis volastonitui ir β-C_2S; (toliau žymima A2-750) 24 h. Atlikus adsorbento A2 ir A2-750 bandinių savitojo paviršiaus ploto tyrimą BET metodu nustatyta, kad adsorbento A2 adsorbcijos izotermės (6 pav., a) gali būti priskiriamos IV histerezės kilpų tipui. Išanalizuota, kad esant dideliam santykiniam slėgiui P/P_0 (>0,7), rodančiam visišką porų užpildymą, adsorbento A2 bandinių izotermė atitinka plyšinio tipo poras. O štai izotermių analizė parodė, kad SA histerezės kilpa atitinka H1 ir (arba) H3 tipą (6 pav., a). H1 histerezės

kilpa būdinga mezoporinėms medžiagoms, kurios susideda iš sferinių dalelių arba turi aiškiai apibrėžtus cilindrinių porų kanalus. Paprastai medžiagos su H1 histerezės kilpa turi sujungtas panašaus dydžio poras. O štai H3 histerezės kilpą sudaro medžiagos, susidedančios iš plyšius primenančių porų. Šio tipo histerezės kilpa neturi ribojančios adsorbcijos esant dideliam P/P_0 ir užsidaro P/P_0 0,4–0,45 diapazone. Taigi gali būti, kad adsorbente A2 susidaro ir į cilindrus, ir į plyšius panašios poros (6 pav., a). Kitokia tendencija buvo pastebėta adsorbento A2, išdegto 750 °C temperatūroje (6 pav., b), bandinyje. A2-750 bandinio adsorbcijos izotermė atitinka II tipą, nes izotermėje nėra histerezės kilpos. Įdomu tai, kad II tipo izotermė būna neporingose ar makroporinėse medžiagose (6 pav., b).

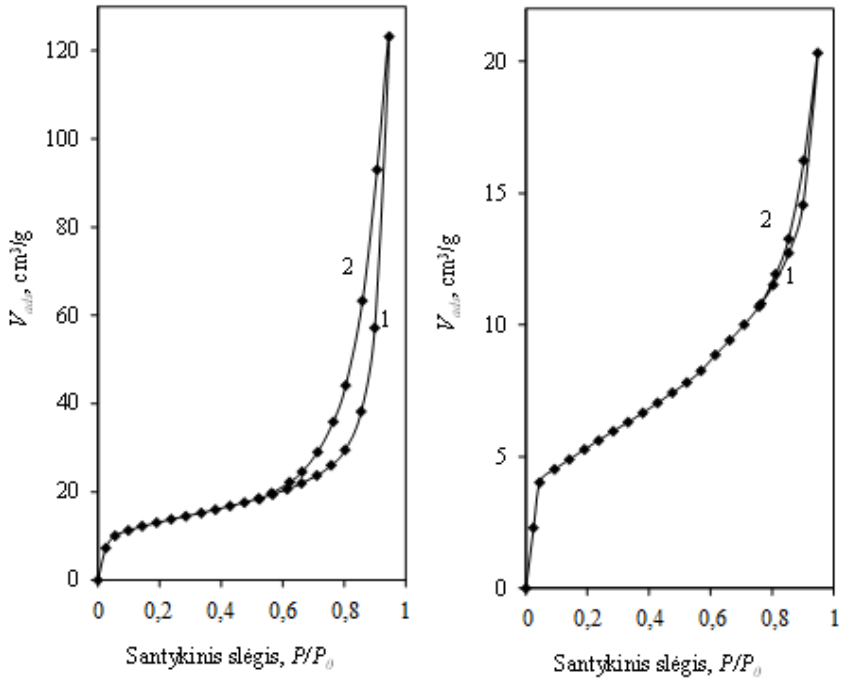

a b

6 pav. Azoto adsorbento A2 (a) ir A2-750 (b) bandinių adsorbcijos (1) ir desorbcijos (2) izotermės

Norint patikrinti, kuris porų modelis geriau aprašo adsorbento A2 savitojo paviršiaus plotą bei vyraujančių porų formas, atlikti skaičiavimai taikant du modelius: cilindrinių porų ir porų tarp lygiagrečiųjų plokštumų. Taikant šiuos modelius apskaičiuojamas suminis porų tūris ir porų pasiskirstymas pagal spindulius panaudojant koreliuotą Kelvino lygtį ir C. Orr bei J. M. Dalla Valle skaičiavimų metodiką. Taikytas modelis galioja tol, kol skirtumas tarp S_{BET} ir $\sum A$ nėra reikšmingas (iki 20 %).

Pradiniai skaičiavimai yra analogiški ir tinka abiem modeliams, t. y. naudojant išmatuotą adsorbuoto azoto tūrio kiekį, esant skirtingiems santykiniams slėgiams, iš Kelvino ir Halsey lygčių apskaičiuojamas porų Kelvino spindulys ir adsorbuoto N_2

sluoksnio storis. Šios vertės naudojamos tolimesniems skaičiavimams, taikant skirtingus porų modelius. Savitojo paviršiaus BET skaičiavimai parodė, kad adsorbento A2 ir A2-750 bandinių C_{BET} konstantos reikšmės yra atitinkamai lygios 233,78 ir 251,33 (3 lentelė). Apskaičiuota, kad adsorbento A2 paviršiaus plotas yra gana didelis – 46,13 m^2/g (3 lentelė). Verta paminėti, kad sintetinių kalcio hidrosilikatų S_{BET} vertė paprastai svyruoja nuo 30 iki 500 m^2/g. Nustatyta, kad išdegus adsorbentą A2 750 °C temperatūroje, paviršiaus ploto vertė sumažėjo iki 18,70 m^2/g (3 lentelė). Nors paviršiaus ploto vertė sumažėjo, ji yra 1,5–9 kartus didesnė nei kitų kalcio silikatų: volastonito – 2 m^2/g, kilchoanito – 6 m^2/g, rankinito – 11,7 m^2/g ir kt. [167, 168].

3 lentelė. Adsorbento A2 ir A2-750 bandinių savitojo paviršiaus ploto S_{BET} parametrai

Bandinys	BET tiesės lygties konstantos		Įkrovos mono-sluoksnio talpa, X_m, g	Savitasis paviršiaus plotas, S_{BET}, m^2/g	Kons-tanta, C_{BET}	Reikšmingumo koeficientas, R^2
	Tiesės polinkio kampas, $S = tg\alpha$	Ordinačių ašyje atkertamos atkarpos ilgis, I				
Adsorben-tas A2	75,21	0,32	0,013	46,13	233,78	0,9993
A2-750	185,58	0,74	0,005	18,70	251,33	0,9999

Adsorbento A2 struktūroje dominuojančių porų formų skaičiavimai parodė gana didelį S_{BET} ir ∑A verčių skirtumą (4 lentelė). Šie rezultatai patvirtina histerezės kilpos klasifikaciją kaip tarpinį H1 ir H3 atvejį (9 pav., a). Be to, galima teigti, kad adsorbento A2 struktūroje susidarė tiek cilindrinės formos, tiek lygiagrečiųjų plokštumų formos poros.

4 lentelė. Adsorbento A2 suminio paviršiaus ploto skaičiavimo rezultatai taikant skirtingų formų porų modelius

Bandinys	S_{BET} /m^2g^{-1}	Skaičiavimo rezultatai taikant cilindrinių formų porų modelį				Skaičiavimo rezultatai taikant lygiagrečiųjų plokštumų formų porų modelį			
		ΣA, m^2g^{-1}	$\lvert S_{BET} - \Sigma A\rvert$, m^2g^{-1}	$\lvert S_{BET} - \Sigma A\rvert$, %	ΣV_P, $\times 10^3$ cm^3g^{-1}	ΣA, m^2g^{-1}	$\lvert S_{BET} - \Sigma A\rvert$, m^2g^{-1}	$\lvert S_{BET} - \Sigma A\rvert$, %	ΣV_P, $\times 10^3$ cm^3g^{-1}
Adsorbentas A2	46,13	52,29	6,16	13,34	0,207	35,39	10,74	23,29	0,188

Apskaičiuota, kad adsorbento A2 bandinio kaupiamojo porų tūrio vertė priklauso nuo taikomo modelio ir yra lygi (V_p) 0,207 (4 lentelė). Skirtingo tūrio porų dydžių pasiskirstymai parodė, kad adsorbentas A2 yra mezoporė medžiaga, nes bandinyje dominuoja 3–12 nm skersmens poros.

Siekiant nustatyti Cu^{2+}, Co^{2+} ir Cr^{3+} jonų įtaką adsorbento A2 terminiam stabilumui, buvo išanalizuoti RSDA duomenys, gauti bandinius apdorojus 25–1000 °C temperatūros intervale. Nustatyta, kad A2-Cu bandinys išlieka stabilus 25–600 °C temperatūroje (7 pav.). O štai esant aukštesnei temperatūrai buvo pastebėtas CuO (PDF Nr. 00-048-1548) susidarymas. Būtina pažymėti, kad minėti junginiai

išliko stabilūs iki 1000 °C. Tačiau adsorbentas A2 su įterptais Co^{2+} jonais išlieka stabilus esant 25–700 °C temperatūrai. Ištirta, kad 700 °C temperatūroje susidaro Co_3O_4 (PDF Nr. 00-043-1003), kuris išlieka stabilus iki 1000 °C. Nagrinėjant A2-Cr RSDA kreives pastebėta, kad bandinys išlieka stabilus esant 25–550 °C temperatūrai. Ištirta, kad nauji junginiai, $CaCrO_4$ (PDF Nr. 00-008-0458) ir Cr_2O_3 (PDF Nr. 00-038-1479), atitinkamai susidaro esant 550 °C ir 850 °C temperatūrai. Nustatyta, kad didėjant temperatūrai, visuose tirtuose bandiniuose esant ~650 °C temperatūrai skyla kalcio karbonatas, o pusiau kristalinio tipo junginiai persikristalizuoja į volastonitą (700–750 °C temperatūroje) ir β-C_2S (800–850 °C temperatūroje) bei susidaro CaO (PDF Nr. 00-002-1088).

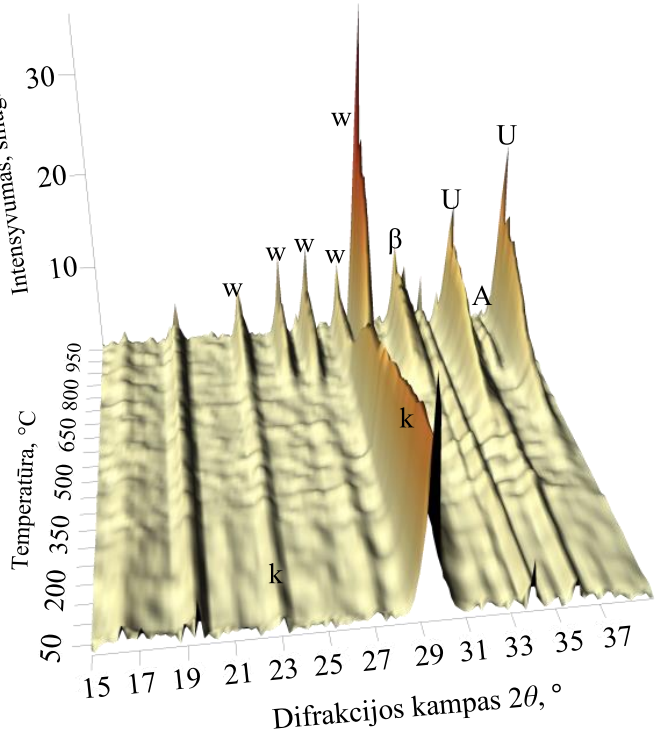

7 pav. A2-Cu RSDA kreivės 25–1000 °C temperatūros intervale. Čia: *k* – $CaCO_3$; *U* – CuO; *A* – CaO; *w* – volastonitas; β – β-C_2S

Remiantis RSD analizės 25–1000 °C temperatūros intervale duomenimis, buvo pasirinkta adsorbento A2 bandinių su įsiterpusiais metalų jonais paviršiaus mikrostruktūros ir savitojo paviršiaus ploto tyrimus tęsti su bandiniais, apdorotais:

- adsorbento A2 su įsiterpusiais Cu^{2+} jonais, išdegtais 600 °C temperatūroje (toliau žymima: A2-Cu600);
- adsorbento A2 su įsiterpusiais Co^{2+} jonais, išdegtais 750 °C temperatūroje (toliau žymima: A2-Co750);
- adsorbento A2 su įsiterpusiais Cr^{3+} jonais, išdegtais 550 °C temperatūroje (toliau žymima: A2-Cu550).

Nustatyta, kad A2-Cu, A2-Cu600 ir A2-Co750 bandinių N_2 adsorbcijos/ desorbcijos izotermės atitinka IV tipo H1 histerezės kilpas, kurios priskiriamos gerai apibrėžtoms, į cilindrus panašioms mezoporinėms medžiagoms. O štai A2-Co, A2-Cr ir A2-Cr550 bandinių adsorbcijos/desorbcijos izotermes galima priskirti IV tipo H1 ir H3 histerezės kilpoms; tai rodo, kad junginiai gali būti sudaryti iš plokštelę ir plyšius primenančių mezoporių medžiagų.

Atlikus skaičiavimus pagal BET metodą ir Kelvino lygtį bei Orr schemą, buvo nustatyta, kad ant visų tirtų bandinių paviršiaus susidaro stabilus N_2 vienmolekulinis dujų sluoksnis (5 lentelė). Nustatyta, kad A2-Co bandinio C_{BET} konstanta yra beveik lygi pradiniam adsorbento A2 junginiui, o A2-Co750 pasižymi didžiausia C_{BET} konstanta iš visų tirtų junginių (5 lentelė). Būtina pažymėti, kad A2-Co750 bandinio paviršiaus ploto skaičiavimo rezultatas rodo, kad po degimo bandinio S_{BET} sumažėjo beveik 6 kartus iki 8,53 m^2/g lyginant su nedegtu bandiniu A2-Co (50,05 8,53 m^2/g) (5 lentelė). O štai bandiniai su įsiterpusiais Cu ir Cr jonais pasižymi 2–2,5 karto mažesnėmis C_{BET} konstantomis, lyginant su pradiniu adsorbento A2 bandiniu, tačiau paviršiaus plotas S_{BET} išliko artimas adsorbento A2 bandiniui.

5 lentelė. Adsorbento A2 su įsiterpusiais Me^{x+} jonais bandinių savitojo paviršiaus ploto S_{BET} parametrai

Bandinys	BET tiesės lygties konstantos		Įkrovos monosluoksnio talpa, X_m, g	Savitasis paviršiaus plotas, S_{BET}, m^2/g	Konstanta C_{BET}	Reikšmingumo koeficientas, R^2
	Tiesės polinkio kampas, $S = tg\alpha$	Ordinačių ašyje atkertamos atkarpos ilgis, I				
A2-Cu	54,47	0,57	0,018	63,31	95,93	1,00
A2-Cu600	81,63	0,59	0,012	42,38	137,16	0,9991
A2-Co	69,34	0,28	0,01	50,06	252,95	0,9995
A2-Co750	407,38	3,24	0,002	8,53	319,82	0,9969
A2-Cr	79,72	1,05	0,012	43,14	76,94	0,9998
A2-Cr550	84,20	1,42	0,012	40,70	60,35	0,9999

Adsorbcijos / desorbcijos izotermių tyrimus papildo ir S_{BET}, ir ∑A verčių skirtumų skaičiavimai (6 lentelė). Nustatyta, kad A2-Cu ir A2-Cu600 bandinio struktūroje susidarė cilindrinės formos poros, nes skirtumas tarp S_{BET} ir ∑A verčių atitinkamai lygus 21,97 % ir 22,44 % (6 lentelė). Tačiau A2-Co bandinio adsorbcijos / desorbcijos izotermė negali būti siejama su H3 histerezės kilpa (11 pav.), nes lygiagrečiųjų plokštumų formos porų modelio S_{BET} ir ∑A verčių skirtumas yra žymiai didesnis nei leistinos ribos (30,84 %). Apskaičiuoti duomenys rodo, kad A2-Co ir A2-Co750 bandinių struktūroje susidarė tik cilindrinę formą primenančios poros, o A2-Cr bandinyje – lygiagrečiųjų plokštumų formos poros (6 lentelė). Nustatyta, kad A2-Cr550 bandinio negalima priskirti jokiam porų modeliui (6 lentelė).

6 lentelė. Adsorbento A2 su įsiterpusiais Me^{x+} jonais bandinių suminio paviršiaus ploto skaičiavimo rezultatai taikant skirtingų formų porų modelius

Bandinys	S_{BET}, m^2g^{-1}	Skaičiavimo rezultatai taikant cilindrinių formų porų modelį				Skaičiavimo rezultatai taikant lygiagrečiųjų plokštumų formų porų modelį			
		ΣA, m^2g^{-1}	$\lvert S_{BET} - \Sigma A\rvert$, m^2g^{-1}	$\lvert S_{BET} - \Sigma A\rvert$, %	ΣV_P, $\times10^3$ cm^3g^{-1}	ΣA, m^2g^{-1}	$\lvert S_{BET} - \Sigma A\rvert$, m^2g^{-1}	$\lvert S_{BET} - \Sigma A\rvert$, %	ΣV_P, $\times10^3$ cm^3g^{-1}
A2-Cu	63,31	77,22	13,91	21,97	0,191	39,29	24,02	37,94	–
A2-Cu600	42,38	51,89	9,51	22,44	0,114	21,49	20,89	49,29	–
A2-Co	50,06	54,33	4,27	8,53	0,125	34,62	15,44	30,84	–
A2-Co750	8,53	7,66	0,87	10,20	0,028	4,33	4,20	49,24	–
A2-Cr	43,14	67,36	24,22	56,13	–	44,53	1,39	3,22	0,171
A2-Cr550	40,70	54,70	14,00	34,39	0,129	27,79	12,91	31,73	0,109

Nustatyta, kad visi nagrinėti bandiniai, išskyrus A2-Co, yra mezoporės medžiagos, nes jose dominuoja 2–15 nm skersmens poros. O štai A2-Co yra mikroporė medžiaga, nes joje dominuoja 2–3 nm skersmens poros.

5.3.3 Skirtingos struktūros kalcio hidrosilikatų sintezė su įterptais Cu^{2+} Co^{2+} ir Cr^{3+} jonais

Remiantis ankstesniais adsorbcijos tyrimais, tolimesniuose tyrimuose buvo nuspręsta tirtus sunkiuosius metalus įterpti hidroterminės sintezės metu. Hidroterminė sintezė atlikta sumaišius $SiO_2 \cdot nH_2O$ ir CaO (C/S = 1,5) mišinį su $Cu(NO_3)_2 \cdot 3H_2O$, $Co(NO_3)_2 \cdot 6H_2O$ ar $Cr(NO_3)_3 \cdot 9H_2O$ tirpalu (Me^{x+} jonų koncentracija 10 g/l), kai tirpalo ir kietosios medžiagos santykis lygus 10. RSDA duomenys parodė, kad po hidroterminės sintezės CaO-SiO_2-$Cr(NO_3)$-$3H_2O$ (8 pav., a) ar CaO-SiO_2-$Co(NO_3)_2 \cdot 6H_2O$ (8 pav., b) produktuose susidarė pusiau kristaliniai kalcio hidrosilikatai CSH (I) ir/arba CSH (II). Be to, dėl karbonizacijos, kai produktai buvo džiovinami oro kondicionavimo kameroje, RSDA rentgenogramose buvo identifikuota kalcito pėdsakų. Verta paminėti, kad chromo ir kobalto jonai neturi įtakos sintezės produktų mineralinei sudėčiai, nes tomis pačiomis grynos sistemos (CaO-SiO_2-H_2O) sintezės sąlygomis susiformavo tik CSH (I), CSH (II) ir kalcitas (8 pav., a, b), o RSDA rezultatai neparodė junginių, kuriuose yra Cr^{3+} Co^{2+} arba NO^{3-} jonų, susidarymo. Tačiau po hidroterminio apdorojimo CaO-SiO_2-$Cu(NO_3)_2$-$3H_2O$ mišinyje RSDA rezultatai parodė, kad sintezės produkte be CSH (I) ir/arba CSH (II) ir kalcito, susidarė CuO (8 pav., c). AAS rezultatai parodė, kad po sintezės Me^{x+} jonų koncentracija skystose terpėse neviršija net 0,001 % nuo pirminės chromo, kobalto ar vario jonų koncentracijos.

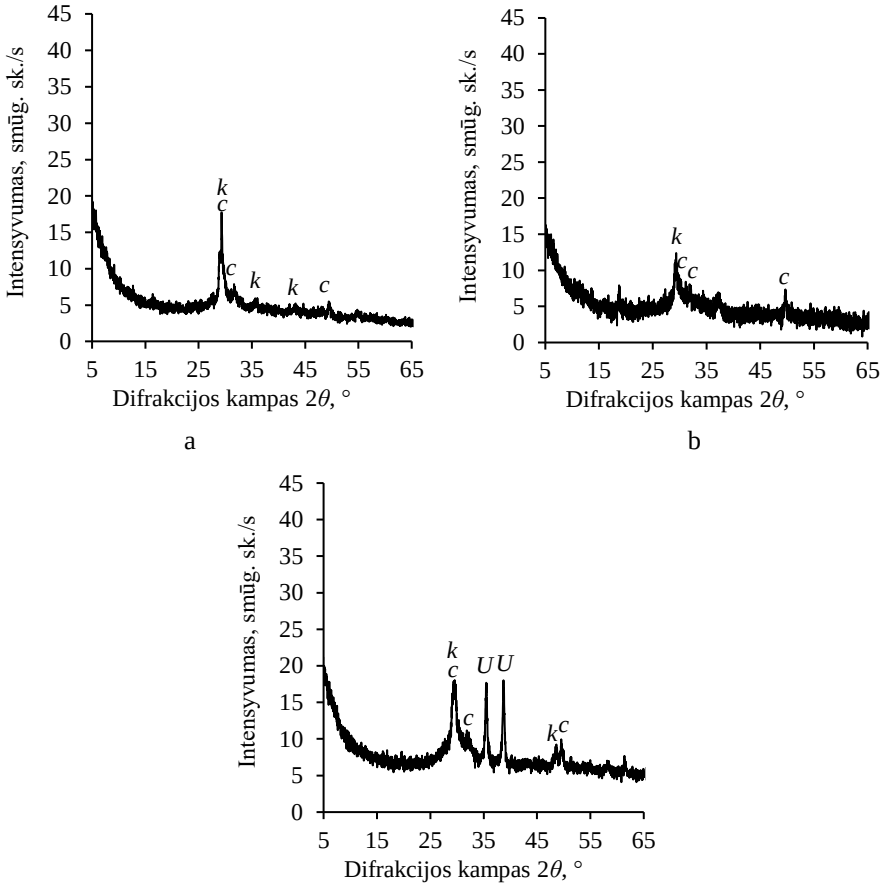

8 pav. H-Cr (a), H-Co (b) ir H-Cu (c) bandinių RSDA kreivės. Čia: *k* – $CaCO_3$; *c* – C-S-H(I)/C-S-H(II); *U* – CuO

Siekiant nustatyti susidariusių junginių terminį stabilumą ir jų katalitinį aktyvumą, sintezės produktai buvo išdegti aukštos temperatūros kameroje. RSDA rezultatai, gauti bandinius apdorojus 25–1000 °C temperatūros intervale, parodė, kad H-Cr (9 pav.) ir H-Co (10 pav., b) bandiniai išlieka stabilūs 25–550 °C temperatūros diapazone, o H-Cu bandinys – iki 600 °C temperatūros (10 pav., a). Padidinus degimo temperatūrą (>550 °C), H-Cr bandinyje pradeda formuotis kalcio chromatas $CaCrO_4$ (PDF Nr. 00-008-0458) ir chromo oksidas Cr_2O_3 (PDF Nr. 00-002-1362) (9 pav.), o H-Co bandinyje – CoO. Be to, minėti junginiai išlieka stabilūs iki 1000 °C temperatūros. Tačiau H-Cu bandinio RSDA junginys išliko stabilus 25–800 °C temperatūros intervale, o temperatūrai didėjant iki 1000 °C šiam junginiui būdingas difrakcinių smailių intensyvumas didėjo. Būtina paminėti, kad visuose bandiniuose 800–850 °C temperatūros intervale C-S-H (I), C-S-H (II) ir kalcito junginiai ima persikristalizuoti ir pradeda formuotis kalcio silikatai volastonitas bei β-C_2S.

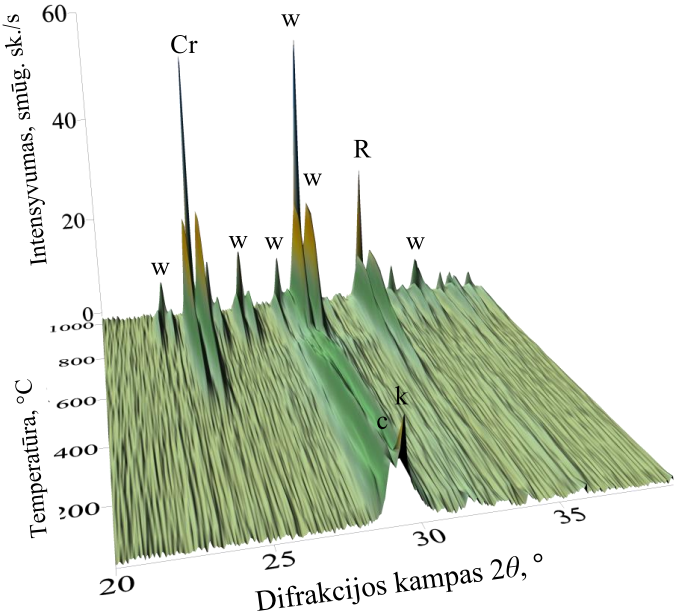

9 pav. H-Cr RSDA kreivės 25–1000 °C temperatūros intervale. Čia: *k* – $CaCO_3$; *c* – C-S-H(I)/C-S-H(II); *R* – Cr_2O_3; *Cr* – $CaCrO_4$; *w* – volastonitas; *β* – *β*-C_2S

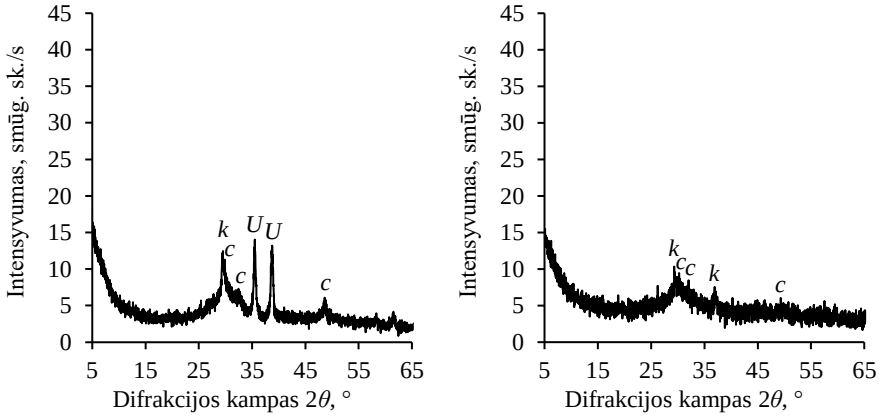

10 pav. H-Cu600 (a) ir H-Co550 (b) bandinių RSDA kreivės.
Čia: *k* – $CaCO_3$; *U* – CuO

Siekiant nustatyti susidariusių junginių struktūrinius skirtumus po hidroterminės sintezės ir degimo, buvo atlikti produktų pagal BET metodą ir Kelvino lygtį bei Orr schemą skaičiavimai. Remiantis RSDA rezultatais, gautais bandinius apdorojus 25–1000 °C temperatūros intervale, H-Cr, H-Co bandiniai buvo išdegti 550 °C, o H-Cu 600 °C temperatūroje 24 h, kai temperatūra buvo pasiekta per 48 h (atitinkamai bandiniai toliau žymimi: H-Cr550, H-Cu600 ir H-Co550). Nustatyta, kad H-Cr bandinio struktūroje degimo metu dominuojančių porų forma pasikeitė iš

lygiagrečiųjų plokštumų formos porų į aiškiai apibrėžtas cilindrinės formos poras, nes H-Cr550 bandinyje skirtumas tarp S_{BET} ir ∑A verčių buvo tik 7,73 % (7 lentelė). Tokia pati situacija stebima ir su H-Cu bandiniu (7 lentelė). Nustatyta, kad H-Co bandinio kaupiamojo porų tūrio vertė priklauso nuo taikomo modelio ir yra lygi 0,419 cm^3/g (7 lentelė). Apskaičiuota, kad H-Co550 bandiniui negalima priskirti porų struktūros modelio, nes skirtumas tarp S_{BET} ir ∑A verčių abiem atvejais viršija numatytas ribas (7 lentelė).

7 lentelė. Hidroterminės sintezės metu įterptų Me^{x+} jonų bandinių suminio paviršiaus ploto skaičiavimo rezultatai taikant skirtingų formų porų modelius

Bandinys	S_{BET}, m^2g^{-1}	Skaičiavimo rezultatai taikant cilindrinių formų porų modelį				Skaičiavimo rezultatai taikant lygiagrečiųjų plokštumų formų porų modelį			
		ΣA, m^2g^{-1}	$\lvert S_{BET} - \Sigma A\rvert$, m^2g^{-1}	$\lvert S_{BET} - \Sigma A\rvert$, %	ΣV_P, $\times 10^3$ cm^3g^{-1}	ΣA, m^2g^{-1}	$\lvert S_{BET} - \Sigma A\rvert$, m^2g^{-1}	$\lvert S_{BET} - \Sigma A\rvert$, %	ΣV_P, $\times 10^3$ cm^3g^{-1}
H-Cr	104,76	134,46	29,70	28,35	–	84,46	20,68	19,37	0,278
H-Cr550	68,92	74,25	5,33	7,73	0,232	37,27	31,65	45,92	–
H-Cu	80,24	115,17	34,93	43,53	–	75,85	4,39	5,47	0,341
H-Cu600	55,51	66,53	11,02	19,85	0,124	34,48	21,03	37,89	0,105
H-Co	132,23	180,63	48,40	36,60	–	114,73	17,50	13,23	0,419
H-Co550	47,34	31,32	16,02	33,84	0,096	20,14	27,20	57,46	0,086

Nustatyta, kad H-Cu bandinio azoto adsorbcijos–desorbcijos izotermėje identifikuojama IV tipo H3 histerezės kilpa, būdinga į plokšteles panašioms dalelėms ir į plyšius panašioms poroms. Šiuos rezultatus papildė porų tūrio skaičiavimas, kuris rodo, kad skirtumas tarp H-Cu bandinio S_{BET} ir ∑A verčių buvo lygus tik 5,47 %, o kaupiamojo porų tūrio vertė lygi 0,341 cm^3/g (7 lentelė). Nustatyta, kad H-Cu600 gali būti priskiriamas II tipo izotermei, o tai reiškia, kad šis junginys yra neporinė arba makroporė medžiaga.

Bandinių paviršiaus ploto skaičiavimai parodė, kad H-Cr ir H-Cr550 bandinių C_{BET} konstantų vertės atitinkamai lygios 65,56 ir 421,30 (8 lentelė). Didelę H-Cr550 bandinio C_{BET} konstantos vertę galima paaiškinti azoto adsorbcija energetiškai aktyviose bandinio vietose (tikėtina, ant $CaCr_2O_4$ kristalų) arba mikroporų užpildymu. Apskaičiuota, kad H-Cr bandinys pasižymi dideliu paviršiaus plotu – 104,76 m^2/g (8 lentelė). Tačiau išdegto bandinio paviršiaus ploto vertė sumažėjo iki 68,92 m^2/g (8 lentelė).

Išnagrinėti H-Cu600 bandinio skaičiavimai rodo, kad šio junginio C_{BET} konstanta (40,77) sumažėja 4 kartus, lyginant su H-Cu bandiniu (163,00) (8 lentelė). Reikėtų pažymėti, kad, nepaisant didelio C_{BET} konstantų skirtumo, H-Cu ir H-Cu600 bandinių paviršiaus plotas S_{BET} sumažėjo tik nuo 80,24 m^2/g iki 55,51 m^2/g (8 lentelė).

O štai H-Co ir išdegto H-Co550 bandinių C_{BET} konstantos skaičiavimuose gaunami priešingi rezultatai. Išdegto bandinio C_{BET} konstantos padidėja daugiau nei 10 kartų lyginant su neišdegtu bandiniu, tačiau skaičiavimai atliekami įvertinus tik tris izotermės taškus (8 lentelė). Nustatyta, kad H-Co bandinio struktūroje susidarė tik į plyšius panašios poros (8 lentelė), nes skirtumas tarp S_{BET} ir ∑A verčių buvo lygus 13,23 %.

8 lentelė. Hidroterminės sintezės metu įterptų Me^{x+} jonų bandinių savitojo paviršiaus ploto S_{BET} parametrai

Bandinys	BET tiesės lygties konstantos		Įkrovos monosluoksnio talpa, X_m, g	Savitasis paviršiaus plotas, S_{BET}, m^2/g	Konstanta C_{BET}	Reikšmingumo koeficientas, R^2
	Tiesės polinkio kampas, $S = tg\alpha$	Ordinačių ašyje atkertamos atkarpos ilgis, I				
H-Cr	32,70	0,51	0,030	104,76	65,56	0,9950
H-Cr550	50,44	0,12	0,020	68,92	421,3	0,9950
H-Cu	43,17	0,27	0,023	80,24	163,00	0,9998
H-Cu600	61,23	1,54	0,016	55,51	40,77	0,9994
H-Co	25,99	0,36	0,038	132,23	73,12	0,9999
H-Co550	73,51	0,10	0,014	47,34	773,13	0,9996

5.3.4 Katalizatoriaus aktyvumas oksidacijos reakcijose

Katalizinis sintetinių ir degtų bandinių aktyvumas buvo išmatuotas visiškai oksiduojant propanolį oro sraute. Pagrindinis visiškos oksidacijos produktas yra anglies dioksidas; taigi pagrindinis katalizatoriaus veikimo parametras yra lakiųjų organinių junginių koncentracijos sumažėjimas, lyginant su CO_2 koncentracijos padidėjimu. Nustatyta, kad eksperimento pradžioje (150 °C), naudojant H-Cr ir H-Cr550 bandinius, propanolio koncentracija išeinančiame sraute sumažėjo atitinkamai iki 56,5 % ir 51,8 % (11 pav.). Tačiau tolesnė analizė parodė, kad išeinančiame sraute nėra CO_2, o tai rodo, kad propanolis buvo adsorbuotas bandiniuose, bet nebuvo oksiduotas. Didesnę propanolio adsorbciją sintetiniame bandinyje galima paaiškinti didesniu jo paviršiaus plotu (104,76 m^2/g) nei degto bandinio (68,92 m^2/g) (8 lentelė).

Didinant temperatūrą, propanolio oksidacija intensyvėja, nes išeinančiame sraute didėja CO_2 koncentracija. Nustatyta, kad H-Cr bandinys pasiekė 95 % konversiją esant maždaug 240 °C temperatūrai, Tai rodo, kad pusiau kristaliniai kalcio hidrosilikatai su įsiterpusiais chromo jonais gali keisti deguonį heterogeniško oksidacijos proceso metu. O štai H-Cr550 bandinys pasižymi prastesnėmis katalizinės oksidacijos savybėmis, nes anglies dioksidas susidarė daug lėčiau – 95 % konversija buvo pasiekta tik esant aukštesnei nei 290 °C temperatūrai (11 pav.). Galima daryti išvadą, kad kalcio chromato susidarymas neigiamai veikia propanolio oksidacijos reakcijas, todėl sintetinis bandinys turėtų būti naudojamas žemesnėje nei 500 °C temperatūroje (siekiant išvengti kalcio chromato susidarymo).

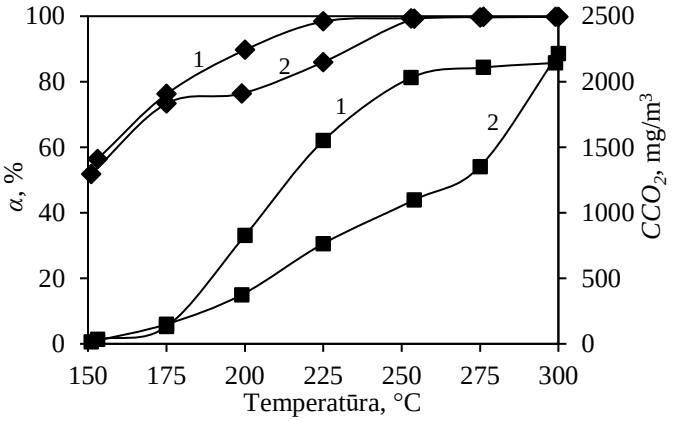

11 pav. Konversijos laipsnis (♦) ir susikaupusi CO_2 koncentracija (■) katalizinės propanolio oksidacijos metu H-Cr (1) ir H-Cr550 (2) bandiniuose

5.4 Tikslinės paskirties junginių sintezės periodinio veikimo gamyboje technologinės rekomendacijos

12 paveiksle pateikta rekomendacinė netvarkingos ir tvarkingos struktūros kalcio hidrosilikatų bandinių paruošimo principinė schema, jungianti hidroterminės sintezės, adsorbcijos ar terminio aktyvavimo metodus. Amorfinis $SiO_2 \cdot nH_2O$ bei $CaCO_3$ laikomi žaliavų bunkeriuose (1), (2). Iš bunkerio (2) kalcio karbonatas tiekiamas į krosnį (3), kurioje yra degamas 550 °C temperatūroje 1 h ir pašalinamas skilimo metu susidaręs CO_2. Po degimo jis patenka į malūną (4). Paruoštas kalcio oksidas tiekiamas į sijotuvą (5), iš kurio susmulkinta medžiaga toliau tiekiama ant svorinio dozatoriaus (6) ir pasveriamas reikiamas kiekis, norint gauti *C/S* molinį santykį 1,5. Amorfinis silicio dioksidas iš žaliavų bunkerio (1) tiekiamas į malūną (7). Sumalta žaliava sandėliuojama bunkeryje (8). Vėliau sumalta medžiaga tiekiama į svorinį dozatorių (6), pasveriantį reikiamą kiekį pagal *C/S* santykį. Pasverti tiek amorfinis silicio dioksidas, tiek ir kalcio oksidas patenka į maišytuvą (12), kuriame yra sumaišomi tarpusavyje. Pasirenkamas sintezės metodo būdas: I – hidroterminė tvarkingos struktūros kalcio hidrosilikatų junginių sintezė; II – hidroterminė netvarkingos struktūros kalcio hidrosilikatų junginių sintezė su įterptais sunkiaisiais metalų jonais. I atveju tūriniu dozatoriumi (9) į maišytuvą (12) įpilamas reikiamas kiekis distiliuoto vandens (10 % nuo sausų medžiagų). II atveju iš žaliavų bunkerio (10), pagal tai, koks metalų jono įterpimas bus vykdomas ($Cu(NO_3)_2 \cdot 3H_2O$, $Co(NO_3)_2 \cdot 6H_2O$, $Cr(NO_3)_3 \cdot 9H_2O$ granulės), svoriniu dozatoriumi (6) pasveriamas reikiamas kiekis sunkiųjų metalų nitratų druskos (koncentracija 10 g Me^{x+}/l). Pasvertas reikiamas granulių kiekis tiekiamas į periodinio veikimo propelerinį maišytuvą (11), pripilamas reikimas kiekis vandens norimai metalų jonų koncentracijai pasiekti ir žaliava tirpinama maišant, kol visiškai ištirpsta. Tūriniu dozatoriumi (9) į maišytuvą (12) įpilamas reikiamas kiekis 10 g Me^{x+}/l koncentracijos tirpalo (10 % nuo sausų medžiagų). Sumaišytos pradinės žaliavos siurbliu (13) tiekiamos į sočiųjų vandens garų autoklavą (14), ten 175 °C temperatūroje

hidrotermiškai apdorojamos 16 h. Po hidroterminės sintezės produktas siurbliu (13) tiekiamas į tarpinį rezervuarą (15). Iš tarpinio rezervuaro siurbliu (13) sintezės produktas tiekiamas į būgninį vakuuminį filtrą (16), kuriame yra pašalinamas po sintezės likęs perteklinis tirpalo kiekis. Iš būgninio vakuuminio filtro (16) produktas tiekiamas į purkštuvinę džiovyklą (17). I proceso metu gautos tvarkingos struktūros kalcio hidrosilikatų granulės toliau tiekiamos į periodinio veikimo adsorberį (21), į kurį svoriniu dozatoriumi (6) iš žaliavų bunkerio (20), pagal tai, koks metalų jono įterpimas bus vykdomas ($Cu(NO_3)_2 \cdot 3H_2O$, $Co(NO_3)_2 \cdot 6H_2O$, $Cr(NO_3)_3 \cdot 9H_2O$ granulės), paduodamas reikiamas kiekis nitratų druskos. Taip pat tūriniu dozatoriumi (9) į adsorberį (21) įpilamas reikiamas kiekis distiliuoto vandens (koncentracija 1 g Me^{x+}/l). Adsorbcijos trukmė 25 °C temperatūroje yra 15 min. Po adsorbcijos proceso būgniniame vakuuminiame filtre (16) pašalinamas perteklinis vanduo, kuris siurbliu (13) yra grąžinamas atgal į gamybą. Šio ir II proceso metu gauti netvarkingos struktūros kalcio hidrosilikatai su įsiterpusiais sunkiųjų metalų jonais tiekiami į krosnį (22) ir ten išlaikomi atitinkamoje temperatūroje pagal numatytą katalizatorių gamybos būdą.

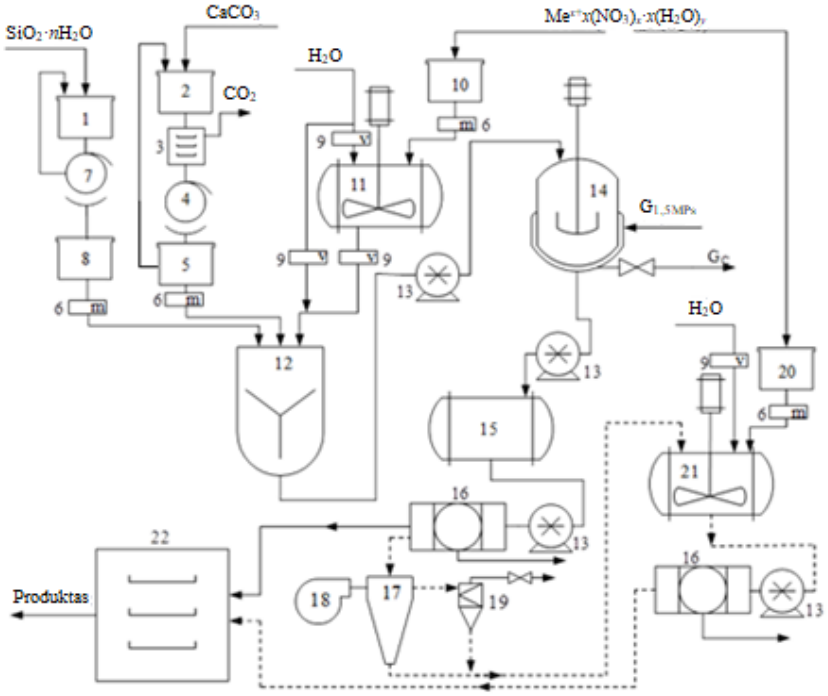

12 pav. Netvarkingos ir tvarkingos struktūros kalcio hidrosilikatų bandinių paruošimo principinė schema, sujungianti hidroterminės sintezės, adsorbcijos ir terminio aktyvinimo metodus. Čia: 1, 2, 8 – bunkeriai; 3, 22 – krosnys; 4, 7 – malūnai; 5 – sijotuvas; 6 – svoriniai dozatoriai; 9 – tūriniai dozatoriai; 10, 20 – talpyklos; 11 – propelerinis maišytuvas;12 – maišytuvas; 13 – siurbliai; 14 – autoklavas; 15 – tarpinis rezervuaras; 16 – būgninis vakuuminis filtras; 17 – purkštuvinė džiovykla; 18 – ventiliatorius; 19 – ciklonas; 21 – adsorberis

5.6 IŠVADOS

1. Nustatyta, kad netvarkingos ir tvarkingos struktūros susintetintų kalcio hidrosilikatų (CaO/SiO_2 = 1,5) bandinių adsorbcijos geba bei sunkiųjų metalų jonų įsiterpimas į jų struktūrą priklauso nuo naudojamų adsorbatų cheminės prigimties. Ištirta, kad 0,25 g/l ir 1 g/l koncentracijos tirpaluose Cu^{2+}, Co^{2+} ir Cr^{3+} adsorbcijos geba yra labai didelė ir gali siekti 100 %. Nustatyta, kad daugelis metalo jonų (>80 %) dalyvavo jonų mainų reakcijoje, o likusi jų dalis prisijungiama silpnesnėmis fizikinės sąveikos jėgomis.

2. Ištirta, kad pseudoantrojo laipsnio modelis tinkamai aprašo sunkiųjų metalų jonų adsorbcijos mechanizmą, nes apskaičiuotos q_{eapsk} reikšmės buvo artimos eksperimentinėms q_{enust} reikšmėms. Nustatyta, kad Cu^{2+}, Co^{2+} ir Cr^{3+} jonų adsorbcijos greitis (k_2) priklauso nuo pradinės sunkiųjų metalų jonų koncentracijos, o neutralioje skystoje terpėje adsorbcija nėra grįžtama, nes po desorbcijos eksperimento Cu^{2+} ir Cr^{3+} jonų koncentracija tirpale neviršija ~0,01 %, palyginimui Co^{2+} jonų – ~0,008 %. Kinetiniais skaičiavimais įrodyta, kad netvarkingos ir tvarkingos struktūros kalcio hidrosilikatų (CaO/SiO_2 = 1,5) bandiniai veikia kaip chemosorbentai.

3. Nustatyta, kad netvarkingos ir tvarkingos struktūros kalcio hidrosilikatų (CaO/SiO_2 = 1,5) bandiniai yra stabilūs mažos koncentracijos tirpaluose (≤ 0,25 g Me^{x+}/l), tačiau padidinus Cu^{2+}, Co^{2+} ir Cr^{3+} jonų koncentraciją iki 1 g/l, buvo identifikuoti minėtų junginių struktūros patvarumo pokyčiai. O štai po adsorbcijos 10 g/l tirpaluose adsorbentų kristalų struktūra buvo visiškai suardyta ir susidarė amorfinės būsenos junginiai ir/arba gerhardtitas – $Cu_2(NO_3)(OH)_3$.

4. Nustatyta, kad netvarkingos struktūros kalcio hidrosilikatų (CaO/SiO_2 = 1,5) bandiniai su įsiterpusiais Cu^{2+}, Co^{2+} ir Cr^{3+} jonais buvo stabilūs iki 550–600 °C temperatūros, o aukštesnėje temperatūroje atitinkamai susidarė CuO, Co_3O_4 ir Cr_2O_3. Degti bandiniai yra mezoporės medžiagos, kurių savitasis paviršiaus plotas (S_{BET}) kinta atitinkamai nuo 61,23 m^2/g iki 73,51 m^2/g. Ištirta, kad sintetinių ir degtų bandinių struktūroje vyrauja cilindrinės formos ir lygiagrečiųjų plokštumų formos poros.

5. Ištirta, kad hidroterminio apdorojimo sąlygomis (175 °C, 16 h) sunkiųjų metalų (1 g/l) jonai iš skystosios terpės įsiterpia į netvarkingos struktūros kalcio hidrosilikatų (CaO/SiO_2 = 1,5) bandinių struktūrą ir neturi įtakos sintezės produktų mineralinei sudėčiai, išskyrus vario jonus. Be to, bandinių savitojo paviršiaus ploto (S_{BET}) vertė žymiai sumažėjo ir buvo lygi 43,17; 25,99 ir 32,70 m^2/g atitinkamai chromo, vario ir kobalto nitrato tirpaluose. Pažymėtina, kad hidroterminės sintezės metu susintetintų junginių su įsiterpusiais sunkiųjų metalų jonais terminis stabilumas yra panašus, lyginant su adsorbentais, į kuriuos įsiterpę metalų jonai.

6. Nustatyta, kad visiškai oksiduojant propanolį oro sraute žemesnėje nei 175 °C temperatūroje, susintetinti ir degti netvarkingos struktūros kalcio hidrosilikatų

bandiniai veikia kaip adsorbentai, o aukštesnėje temperatūroje (daugiau nei 500 °C) vyksta katalizinė oksidacija. Susintetintas bandinys su įterptais chromo jonais pasiekė 95 % konversiją 240 °C temperatūroje, o degtas bandinys minėtą vertę pasiekė tik aukštesnėje nei 290 °C temperatūroje. Kalcio chromato susidarymas neigiamai veikia propanolio oksidacijos reakcijas. Todėl susintetintas bandinys turėtų būti naudojamas žemesnėje nei 500 °C temperatūroje.

7. Pasiūlyta principinė netvarkingos ir tvarkingos struktūros kalcio hidrosilikatų (CaO/SiO_2 = 1,5) bandinių sintezės periodinio veikimo gamyboje schema, sujungianti hidroterminės sintezės, adsorbcijos ir terminio aktyvinimo metodus.

REFERENCES

1. Ulucak R, Khan SU. Does information and communication technology affect CO2 mitigation under the pathway of sustainable development during the mode of globalization?. Sustainable Dev. 2020;28:857-67
2. Canoluk C, Gursoy SS. Chemical modification of rose leaf with polypyrrole for the removal of Pb (II) and Cd (II) from aqueous solution. 2017;54:782-90
3. Anonymous The United Nations world water development report. 2017;2018
4. Wadhawan S, Jain A, Nayyar J, Mehta SK. Role of nanomaterials as adsorbents in heavy metal ion removal from waste water: A review. 2020;33:101038; doi: https://doi.org/10.1016/j.jwpe.2019.101038.
5. Gupta K, Joshi P, Gusain R, Khatri OP. Recent advances in adsorptive removal of heavy metal and metalloid ions by metal oxide-based nanomaterials. Coord Chem Rev. 2021;445:214100; doi: https://doi.org/10.1016/j.ccr.2021.214100.
6. Seiyaboh EI, Izah SC. Impacts of soil pollution on air quality under Nigerian setting. 2019;3:45-53
7. Afroze S, Sen TK. A review on heavy metal ions and dye adsorption from water by agricultural solid waste adsorbents. 2018;229:1-50
8. Cheok CY, Mohd Adzahan N, Abdul Rahman R, Zainal Abedin NH, Hussain N, Sulaiman R, Chong GH. Current trends of tropical fruit waste utilization. Crit Rev Food Sci Nutr. 2018;58:335-61
9. Huang S, Xiao L, Zhang Y, Wang L, Tang L. Interactive effects of natural and anthropogenic factors on heterogenetic accumulations of heavy metals in surface soils through geodetector analysis. Sci Total Environ. 2021;789:147937; doi: https://doi.org/10.1016/j.scitotenv.2021.147937.
10. Tomczyk A, Sokołowska Z, Boguta P. Biomass type effect on biochar surface characteristic and adsorption capacity relative to silver and copper. 2020;278:118168; doi: https://doi.org/10.1016/j.fuel.2020.118168.
11. Meng J, Feng X, Dai Z, Liu X, Wu J, Xu J. Adsorption characteristics of Cu (II) from aqueous solution onto biochar derived from swine manure. 2014;21:7035-46
12. Hubicki Z, Kołodyńska D. Selective removal of heavy metal ions from waters and waste waters using ion exchange methods. 2012;7:193-240
13. Montes de Oca-Palma R, Solache-Ríos M, Jiménez-Reyes M, García-Sánchez JJ, Almazán-Sánchez PT. Adsorption of cobalt by using inorganic components of sediment samples from water bodies. 2021;36:524-31; doi: https://doi.org/10.1016/j.ijsrc.2020.11.003.
14. Rzetala MA. Cobalt and Vanadium in bottom sediments of anthropogenic lakes in the Silesian Upland (Southern Poland). 2016;1:169-76
15. Dehghani MH, Yetilmezsoy K, Salari M, Heidarinejad Z, Yousefi M, Sillanpää M. Adsorptive removal of cobalt (II) from aqueous solutions using multi-walled carbon nanotubes and γ-alumina as novel adsorbents: Modelling and optimization based on response surface methodology and artificial neural network. 2020;299:112154
16. Tang Y, Liao X, Zhang X, Peng G, Gao J, Chen L. Enhanced adsorption of hexavalent chromium and the microbial effect on quartz sand modified with Al-

layered double hydroxides. Sci Total Environ. 2021;762:143094; doi: https://doi.org/10.1016/j.scitotenv.2020.143094.
17. Karnjanakom S, Maneechakr P. Adsorption behaviors and capacities of Cr(VI) onto environmentally activated carbon modified by cationic (HDTMA and DDAB) surfactants. J Mol Struct. 2019;1186:80-90; doi: https://doi.org/10.1016/j.molstruc.2019.03.022.
18. Anonymous Dėl Lietuvos higienos normos HN 60:2004 "Pavojingų cheminių medžiagų didžiausios leidžiamos koncentracijos dirvožemyje" patvirtinimo
19. Giaccio L, Cicchella D, De Vivo B, Lombardi G, De Rosa M. Does heavy metals pollution affects semen quality in men? A case of study in the metropolitan area of Naples (Italy). 2012;112:218-25
20. Zhao J, Zhu Y, Wu J, Zheng J, Zhao X, Lu B, Chen F. Chitosan-coated mesoporous microspheres of calcium silicate hydrate: environmentally friendly synthesis and application as a highly efficient adsorbent for heavy metal ions. J Colloid Interface Sci. 2014;418:208-15
21. Hegazi HA. Removal of heavy metals from wastewater using agricultural and industrial wastes as adsorbents. 2013;9:276-82
22. Mahmoud AM, Ibrahim FA, Shaban SA, Youssef NA. Adsorption of heavy metal ion from aqueous solution by nickel oxide nano catalyst prepared by different methods. 2015;24:27-35
23. Ali A, Saeed K. Phenol removal from aqueous medium using chemically modified banana peels as low-cost adsorbent. 2016;57:11242-54
24. Khandegar V, Saroha AK. Electrocoagulation for the treatment of textile industry effluent – A review. 2013;128:949-63
25. Ihsanullah, Abbas A, Al-Amer AM, Laoui T, Al-Marri MJ, Nasser MS, Khraisheh M, Atieh MA. Heavy metal removal from aqueous solution by advanced carbon nanotubes: Critical review of adsorption applications. 2016;157:141-61
26. Lothenbach B, Scrivener K, Hooton RD. Supplementary cementitious materials. Cem Concr Res. 2011;41:1244-56
27. Richardson IG. The calcium silicate hydrates. 2008;38:137-58
28. Qomi MA, Krakowiak KJ, Bauchy M, Stewart KL, Shahsavari R, Jagannathan D, Brommer DB, Baronnet A, Buehler MJ, Yip S. Combinatorial molecular optimization of cement hydrates. 2014;5:1-10
29. Wang S, Peng X, Tao Z, Tang L, Zeng L. Influence of drying conditions on the contact-hardening behaviours of calcium silicate hydrate powder. Constr Build Mater. 2017;136:465-73
30. Liu Y, Jia H, Zhang G, Sun Z, Pan Y, Zheng S. Synthesis and humidity control performances of natural opoka based porous calcium silicate hydrate. 2019;30:2733-41
31. Biagioni C, Merlino S, Bonaccorsi E. The tobermorite supergroup: a new nomenclature. 2015;79:485-95
32. Bonaccorsi E, Merlino S, Taylor H. The crystal structure of jennite, Ca9Si6O18 (OH) 6· 8H2O. Cem Concr Res. 2004;34:1481-8
33. Bonaccorsi E, Merlino S, Kampf AR. The crystal structure of tobermorite 14 Å (plombierite), a C–S–H phase. J Am Ceram Soc. 2005;88:505-12

34. L'Hôpital E, Lothenbach B, Kulik DA, Scrivener K. Influence of calcium to silica ratio on aluminium uptake in calcium silicate hydrate. Cem Concr Res. 2016;85:111-21; doi: https://doi.org/10.1016/j.cemconres.2016.01.014.
35. Zou J, Guo C, Jiang Y, Wei C, Li F. Structure, morphology and mechanism research on synthesizing xonotlite fiber from acid-extracting residues of coal fly ash and carbide slag. Mater Chem Phys. 2016;172:121-8; doi: https://doi.org/10.1016/j.matchemphys.2016.01.050.
36. Tan W, Zhu G, Liu Y, Zhang Z, Liu L. Effects and mechanism research of the crystalline state for the semi-crystalline calcium silicate. Cem Concr Res. 2015;72:69-75; doi: https://doi.org/10.1016/j.cemconres.2015.02.020.
37. Frost RL, Mahendran M, Pologanathan K, Xi Y. Raman spectroscopic study of the mineral xonotlite Ca6Si6O17 (OH) 2—A component of plaster boards. Mater Res Bull. 2012;47:3644-9
38. He S, Zhao C, Yao P, Yang S. Chemical modification of silica gel with multidentate ligands for heavy metals removal. 2016;57:1722-32
39. Konuklu Y, Ersoy O. Fabrication and characterization of form-stable phase change material/xonotlite microcomposites. Solar Energy Mater Solar Cells. 2017;168:130-5; doi: https://doi.org/10.1016/j.solmat.2017.04.019.
40. Martusevičius M., Kaminskas R., Mituzas J. Rišamųjų medžiagų cheminė technologija. Kaunas: Technologija. 2002
41. Pei LZ, Yang LJ, Yang Y, Fan CG, Yin WY, Chen J, Zhang QF. A green and facile route to synthesize calcium silicate nanowires. Mater Charact. 2010;61:1281-5
42. Bernstein S, Fehr KT. The formation of 1.13 nm tobermorite under hydrothermal conditions: 1. The influence of quartz grain size within the system CaO–SiO2–D2O. 2012;58:84-91; doi: https://doi.org/10.1016/j.pcrysgrow.2012.02.006.
43. Galvánková L, Bartoníčková E, Opravil T, Tkacz J, Ptáček P. The influence of starting materials solubility on tobermorite structure formation under the hydrothermal conditions. 2018;379:012001
44. Huang X, Jiang D, Tan S. Novel hydrothermal synthesis method for tobermorite fibers and investigation on their thermal stability. Mater Res Bull. 2002;37:1885-92; doi: https://doi.org/10.1016/S0025-5408(02)00854-1.
45. Li J, Zhang W, Garbev K, Beuchle G, Monteiro PJM. Influences of cross-linking and Al incorporation on the intrinsic mechanical properties of tobermorite. Cem Concr Res. 2020;136:106170; doi: https://doi.org/10.1016/j.cemconres.2020.106170.
46. Yazıcı H, Yiğiter H, Karabulut AŞ, Baradan B. Utilization of fly ash and ground granulated blast furnace slag as an alternative silica source in reactive powder concrete. 2008;87:2401-7; doi: https://doi.org/10.1016/j.fuel.2008.03.005.
47. Hu C, Ruan Y, Yao S, Wang F, He Y, Gao Y. Insight into the evolution of the elastic properties of calcium-silicate-hydrate (C-S-H) gel. 2019;104:103342; doi: https://doi.org/10.1016/j.cemconcomp.2019.103342.
48. Black L, Garbev K, Stemmermann P, Hallam KR, Allen GC. X-ray photoelectron study of oxygen bonding in crystalline C–S–H phases. 2004;31:337-46

49. Eisinas A, Baltakys K, Siauciunas R. The effect of gyrolite additive on the hydration properties of Portland cement. Cem Concr Res. 2012;42:27-38
50. Baltakys K, Eisinas A, Barauskas I, Prichockiene E, Zaleckas E. Removal of Zn (II), Cu (II) and Cd (II) from aqueous solution using gyrolite. J Sci Ind Res. 2012;71:566
51. Levinskas R, Baltušnikas A, Lukošiūtė I, Baltakys K, Kalpokaitė-Dičkuvienė R, Grybėnas A. Modification of structure of synthetic gyrolite. 2013;17:495-500
52. Kriskova L, Pontikes Y, Zhang F, Cizer Ö, Jones PT, Van Balen K, Blanpain B. Influence of mechanical and chemical activation on the hydraulic properties of gamma dicalcium silicate. Cem Concr Res. 2014;55:59-68
53. Criado YA, Alonso M, Abanades JC. Enhancement of a CaO/Ca (OH) 2 based material for thermochemical energy storage. 2016;135:800-9
54. Gou Z, Chang J. Synthesis and in vitro bioactivity of dicalcium silicate powders. 2004;24:93-9
55. Siauciunas R, Stankeviciute M, Gendvilas R, Baltakys K. Heat release during the hydration of calcinated α-C 2 SH and its mixture with killalaite. 2017;127:163-71
56. Chen H, Yuan X, Xiong T, Jiang L, Wang H, Wu Z. Biochar Facilitated Hydroxyapatite/Calcium Silicate Hydrate for Remediation of Heavy Metals Contaminated Soils. 2020;231:1-16
57. Youssef AMA. PAINTS INDUSTRY. 2019
58. Nurhadi B, Roos YH. Influence of anti-caking agent on the water sorption isotherm and flow-ability properties of vacuum dried honey powder. J Food Eng. 2017;210:76-82; doi: https://doi.org/10.1016/j.jfoodeng.2017.04.020.
59. Manjunatha M, Seth D, Balaji, K. V. G. D. Role of engineered fibers on fresh and mechanical properties of concrete prepared with GGBS and PVC waste powder – An experimental study. 2021; doi: https://doi.org/10.1016/j.matpr.2021.01.605.
60. Morales-Flórez V, Findling N, Brunet F. Changes on the nanostructure of cementitius calcium silicate hydrates (C–S–H) induced by aqueous carbonation. J Mater Sci. 2012;47:764-71
61. Stemmermann P, Schweike U, Garbev K, Beuchle G, Möller H. Celitement–a sustainable prospect for the cement industry. 2010;8:52-66
62. Baltakys K, Dambrauskas T, Siauciunas R, Eisinas A. FORMAREA [alpha]-C^ sub 2^ S HIDRATAT ÎN AMESTECURI CU CaO/SiO^ sub 2^= 1, 75 PRIN TRATAMENT HIDROTERMAL LA 200° C/FORMATION OF [alpha]-C^ sub 2^ S HYDRATE IN THE MIXTURES WITH CaO/SiO^ sub 2^= 1.75 BY HYDROTHERMAL TREATMENT AT 200° C. 2014;44:109
63. Siauciunas R, Gendvilas R, Mikaliunaite J, Urbonas L. Heat flow and strength properties of perspective hydraulic binder material. 2015;121:57-65
64. Gendvilas R, Siauciunas R, Baltakys K. Quantitative thermal analysis of α-C2SH as a precursor for low-energy cements. 2015;121:155-62
65. Siauciunas R, Baltakys K, Gendvilas R, Prichockiene E. Synthesis of low-energy cement based on α-C2SH. 2015;28:241-50
66. Dashkevich RY, Aleksandrov AV. Resonance character of polymorphic transformations for the phase transition α′ L→ β-Ca 2 SiO 4. 2007;48:404-6

67. Dutta N, Chatterjee A. Hydrothermal synthesis of dicalcium silicate based cement. 2017;216:012027
68. Wang Q, Li F, Shen X, Shi W, Li X, Guo Y, Xiong S, Zhu Q. Relation between reactivity and electronic structure for α′ L-, β-and γ-dicalcium silicate: A first-principles study. Cem Concr Res. 2014;57:28-32
69. Shaheen F, Pradhan B. Influence of sulfate ion and associated cation type on steel reinforcement corrosion in concrete powder aqueous solution in the presence of chloride ions. Cem Concr Res. 2017;91:73-86; doi: https://doi.org/10.1016/j.cemconres.2016.10.008.
70. Garcia-Lodeiro I, Palomo A, Fernández-Jiménez A, Macphee DE. Compatibility studies between N-A-S-H and C-A-S-H gels. Study in the ternary diagram Na2O–CaO–Al2O3–SiO2–H2O. Cem Concr Res. 2011;41:923-31; doi: https://doi.org/10.1016/j.cemconres.2011.05.006.
71. Różycka A, Pichór W. Effect of perlite waste addition on the properties of autoclaved aerated concrete. Constr Build Mater. 2016;120:65-71
72. Haha MB, Lothenbach B, Le Saout G, Winnefeld F. Influence of slag chemistry on the hydration of alkali-activated blast-furnace slag — Part II: Effect of Al2O3. Cem Concr Res. 2012;42:74-83; doi: https://doi.org/10.1016/j.cemconres.2011.08.005.
73. Wang S, Peng X, Tang L, Zeng L, Lan C. Influence of inorganic admixtures on the 11Å-tobermorite formation prepared from steel slags: XRD and FTIR analysis. Constr Build Mater. 2014;60:42-7; doi: https://doi.org/10.1016/j.conbuildmat.2014.03.002.
74. Bernard E, Lothenbach B, Le Goff F, Pochard I, Dauzères A. Effect of magnesium on calcium silicate hydrate (C-S-H). Cem Concr Res. 2017;97:61-72; doi: https://doi.org/10.1016/j.cemconres.2017.03.012.
75. Baltakys K, Siauciunas R. Influence of gypsum additive on the gyrolite formation process. Cem Concr Res. 2010;40:376-83
76. Tian H, Stephan D, Lothenbach B, Lehmann C. Influence of foreign ions on calcium silicate hydrate under hydrothermal conditions: A review. Constr Build Mater. 2021;301:124071; doi: https://doi.org/10.1016/j.conbuildmat.2021.124071.
77. Mostafa NY, Shaltout AA, Omar H, Abo-El-Enein SA. Hydrothermal synthesis and characterization of aluminium and sulfate substituted 1.1nm tobermorites. J Alloys Compounds. 2009;467:332-7; doi: https://doi.org/10.1016/j.jallcom.2007.11.130.
78. Baltakys K, Eisinas A, Baltakys M, Siauciunas R. Incorporation of insoluble heavy metal oxide in structure of Z phase during hydrothermal treatment. 2014;113:466-71
79. Liu F, Wang X, Cao J. Effect of Na on xonotlite crystals in hydrothermal synthesis. 2013;20:88-93
80. Wang S, Peng X, Tang L, Zeng L, Lan C. Influence of inorganic admixtures on the 11 Å-tobermorite formation prepared from steel slags: XRD and FTIR analysis. Constr Build Mater. 2014;60:42-7
81. L'Hôpital E, Lothenbach B, Scrivener K, Kulik DA. Alkali uptake in calcium alumina silicate hydrate (CASH). Cem Concr Res. 2016;85:122-36

82. Matsui K, Kikuma J, Tsunashima M, Ishikawa T, Matsuno S, Ogawa A, Sato M. In situ time-resolved X-ray diffraction of tobermorite formation in autoclaved aerated concrete: Influence of silica source reactivity and Al addition. Cem Concr Res. 2011;41:510-9
83. Mostafa NY, Kishar EA, Abo-El-Enein SA. FTIR study and cation exchange capacity of Fe3+- and Mg2+-substituted calcium silicate hydrates. J Alloys Compounds. 2009;473:538-42; doi: https://doi.org/10.1016/j.jallcom.2008.06.029.
84. Haastrup S, Yu D, Yue Y. Impact of minor iron content on crystal structure and properties of porous calcium silicates during synthesis. Mater Chem Phys. 2018;205:180-5
85. Qian G, Sun DD, Tay JH, Lai Z, Xu G. Autoclave properties of kirschsteinite-based steel slag. Cem Concr Res. 2002;32:1377-82
86. Luke K. Phase studies of pozzolanic stabilized calcium silicate hydrates at 180 C. Cem Concr Res. 2004;34:1725-32
87. Colston SL, Barnes P, Jupe AC, Jacques SD, Hall C, Livesey P, Dransfield J, Meller N, Maitland GC. An in situ synchrotron energy-dispersive diffraction study of the hydration of oilwell cement systems under high temperature/autoclave conditions up to 130 C. Cem Concr Res. 2005;35:2223-32
88. Garbev K, Gasharova B, Beuchle G, Kreisz S, Stemmermann P. First Observation of α-Ca2 [SiO3 (OH)](OH)–Ca6 [Si2O7][SiO4](OH) 2 Phase Transformation upon Thermal Treatment in Air. J Am Ceram Soc. 2008;91:263-71
89. Palmisani J, Nørgaard AW, Kofoed-Sørensen V, Clausen PA, de Gennaro G, Wolkoff P. Formation of ozone-initiated VOCs and secondary organic aerosol following application of a carpet deodorizer. Atmos Environ. 2020;222:117149
90. Nematollahi N, Kolev SD, Steinemann A. Volatile chemical emissions from 134 common consumer products. 2019;12:1259-65
91. Salam OEA, Reiad NA, ElShafei MM. A study of the removal characteristics of heavy metals from wastewater by low-cost adsorbents. 2011;2:297-303
92. Thommes M, Cychosz KA. Physical adsorption characterization of nanoporous materials: progress and challenges. 2014;20:233-50
93. Romaškevič. T. Sorbentų chemija. 2012
94. Valatka. E. Cheminių reakcijų inžinerija. 2012
95. Pourhakkak P, Taghizadeh A, Taghizadeh M, Ghaedi M, Haghdoust S. Chapter 1 - Fundamentals of adsorption technology. 2021;33:1-70; doi: https://doi.org/10.1016/B978-0-12-818805-7.00001-1.
96. Wang J, Guo X. Adsorption isotherm models: Classification, physical meaning, application and solving method. 2020;258:127279; doi: https://doi.org/10.1016/j.chemosphere.2020.127279.
97. Lapham DP, Lapham JL. BET surface area measurement of commercial magnesium stearate by krypton adsorption in preference to nitrogen adsorption. 2019;568:118522
98. Thommes M, Kaneko K, Neimark AV, Olivier JP, Rodriguez-Reinoso F, Rouquerol J, Sing KS. Physisorption of gases, with special reference to the evaluation of surface area and pore size distribution (IUPAC Technical Report). 2015;87:1051-69

99. Cychosz KA, Guillet-Nicolas R, García-Martínez J, Thommes M. Recent advances in the textural characterization of hierarchically structured nanoporous materials. Chem Soc Rev. 2017;46:389-414
100. Naderi M. Surface Area: Brunauer–Emmett–Teller (BET). In: Anonymous Progress in filtration and separation. : Elsevier; 2015. pp. 585-608.
101. Inglezakis VJ, Poulopoulos SG, Kazemian H. Insights into the S-shaped sorption isotherms and their dimensionless forms. 2018;272:166-76; doi: https://doi.org/10.1016/j.micromeso.2018.06.026.
102. Verbraeken MC, Brandani S. A priori predictions of type I and type V isotherms by the rigid adsorbent lattice fluid. 2019:1-12
103. Fabus MS, Peggs S. No title. 2019
104. Schreiber A, Reinhardt S, Findenegg GH. The lower closure point of the adsorption hysteresis loop of fluids in mesoporous silica materials. 2002;144:177-84; doi: https://doi.org/10.1016/S0167-2991(02)80132-X.
105. Azizian S. Kinetic models of sorption: a theoretical analysis. 2004;276:47-52
106. Simonin J. On the comparison of pseudo-first order and pseudo-second order rate laws in the modeling of adsorption kinetics. Chem Eng J. 2016;300:254-63
107. Lin J, Wang L. Comparison between linear and non-linear forms of pseudo-first-order and pseudo-second-order adsorption kinetic models for the removal of methylene blue by activated carbon. 2009;3:320-4
108. Ho YS, McKay G. Pseudo-second order model for sorption processes. 1999;34:451-65
109. Inyinbor AA, Adekola FA, Olatunji GA. Kinetics, isotherms and thermodynamic modeling of liquid phase adsorption of Rhodamine B dye onto Raphia hookerie fruit epicarp. 2016;15:14-27
110. You Y, Kalebaila KK, Brock SL, Oupicky D. Temperature-controlled uptake and release in PNIPAM-modified porous silica nanoparticles. 2008;20:3354-9
111. Sotomayor FJ, Cychosz KA, Thommes M. Characterization of micro/mesoporous materials by physisorption: concepts and case studies. 2018;3:34-50
112. Okano K, Miyamaru S, Kitao A, Takano H, Aketo T, Toda M, Honda K, Ohtake H. Amorphous calcium silicate hydrates and their possible mechanism for recovering phosphate from wastewater. 2015;144:63-9
113. Bertron A, Escadeillas G, Duchesne J. Cement pastes alteration by liquid manure organic acids: chemical and mineralogical characterization. Cem Concr Res. 2004;34:1823-35
114. Al-Wakeel EI, El-Korashy SA, El-Hemaly SA, Rizk MA. Divalent ion uptake of heavy metal cations by (aluminum alkali metals)–substituted synthetic 1.1 nm-tobermorites. J Mater Sci. 2001;36:2405-15
115. Chen S, Cheng C, Li C, Chai P, Chang Y. Reduction of chromate from electroplating wastewater from pH 1 to 2 using fluidized zero valent iron process. 2007;142:362-7
116. Miretzky P, Cirelli AF. Cr(VI) and Cr(III) removal from aqueous solution by raw and modified lignocellulosic materials: A review. 2010;180:1-19

117. Badruddoza AZM, Shawon ZBZ, Tay WJD, Hidajat K, Uddin MS. Fe3O4/cyclodextrin polymer nanocomposites for selective heavy metals removal from industrial wastewater. 2013;91:322-32
118. Heidari A, Younesi H, Mehraban Z. Removal of Ni(II), Cd(II), and Pb(II) from a ternary aqueous solution by amino functionalized mesoporous and nano mesoporous silica. 2009;153:70-9
119. Sen Gupta S, Bhattacharyya KG. Kinetics of adsorption of metal ions on inorganic materials: A review. 2011;162:39-58
120. Algarra M, Jiménez MV, Rodríguez-Castellón E, Jiménez-López A, Jiménez-Jiménez J. Heavy metals removal from electroplating wastewater by aminopropyl-Si MCM-41. 2005;59:779-86
121. Garbev K, Gasharova B, Stemmermann P. A Modular Concept of Crystal Structure Applied to the Thermal Transformation of α-C 2 SH. J Am Ceram Soc. 2014;97:2286-97
122. Garbev K, Black L, Beuchle G, Stemmermann P. Inorganic polymers in cement based materials. 2002;1:19-30
123. Kasperaviciute V, Baltakys K, Siauciunas R. The sorption properties of gyrolite for copper ions. 2008;52:95-101
124. Bankauskaite A, Eisinas A, Baltakys K, Zadaviciute S. A study on the intercalation of heavy metal ions in a wastewater by synthetic layered inorganic adsorbents. 2015;56:1576-86
125. Zadaviciute S, Baltakys K, Eisinas A, Bankauskaite A. Simultaneous adsorption at 25° C and the peculiarities of gyrolite substituted with heavy metals. 2017;127:335-43
126. Pradhan N, Rene E, Lens P, Dipasquale L, D'Ippolito G, Fontana A, Panico A, Esposito G. Adsorption behaviour of lactic acid on granular activated carbon and anionic resins: thermodynamics, isotherms and kinetic studies. 2017;10:665
127. Ho YS, Wase DJ, Forster CF. Batch nickel removal from aqueous solution by sphagnum moss peat. Water Res. 1995;29:1327-32
128. Ho YS, Wase DJ, Forster CF. Kinetic studies of competitive heavy metal adsorption by sphagnum moss peat. Environ Technol. 1996;17:71-7
129. Mehrbod M, Martinelli M, Martino AG, Cronauer DC, Jeremy Kropf A, Marshall CL, Jacobs G. Fischer-Tropsch synthesis: Direct cobalt nitrate reduction of promoted Co/TiO2 catalysts. 2019;245:488-504; doi: https://doi.org/10.1016/j.fuel.2019.02.083.
130. Zhang L, Dong L, Yu W, Liu L, Deng Y, Liu B, Wan H, Gao F, Sun K, Dong L. Effect of cobalt precursors on the dispersion, reduction, and CO oxidation of CoOx/γ-Al2O3 catalysts calcined in N2. J Colloid Interface Sci. 2011;355:464-71; doi: https://doi.org/10.1016/j.jcis.2010.11.076.
131. Bankauskaite A, Baltakys K, Eisinas A, Zadaviciute S. Study on adsorption of heavy metal ions in wastewater by synthetic layered inorganic adsorbents. 2014;26
132. Siauciunas R, Baltakys K, Gendvilas R, Eisinas A. The influence of Cd-impure gyrolite on the hydration of composite binder material based on α-C2S hydrate. 2014;118:857-63

133. Guo X, Shi H. Microstructure and heavy metal adsorption mechanisms of hydrothermally synthesized Al-substituted tobermorite. Mater Struct. 2017;50:245
134. Shaw S, Henderson CMB, Komanschek BU. Dehydration/recrystallization mechanisms, energetics, and kinetics of hydrated calcium silicate minerals: an in situ TGA/DSC and synchrotron radiation SAXS/WAXS study. 2000;167:141-59
135. Gong J, Liu T, Wang X, Hu X, Zhang L. Efficient removal of heavy metal ions from aqueous systems with the assembly of anisotropic layered double hydroxide nanocrystals@ carbon nanosphere. Environ Sci Technol. 2011;45:6181-7
136. Pereira DC, Faria, Dalva Lúcia A de, Constantino VR. CuII hydroxy salts: characterization of layered compounds by vibrational spectroscopy. 2006;17:1651-7
137. Simonin J. On the comparison of pseudo-first order and pseudo-second order rate laws in the modeling of adsorption kinetics. Chem Eng J. 2016;300:254-63
138. Wang Z, Tan K, Cai J, Hou S, Wang Y, Jiang P, Liang M. Silica oxide encapsulated natural zeolite for high efficiency removal of low concentration heavy metals in water. Colloids Surf Physicochem Eng Aspects. 2019;561:388-94
139. Chen Q, Hills CD, Yuan M, Liu H, Tyrer M. Characterization of carbonated tricalcium silicate and its sorption capacity for heavy metals: A micron-scale composite adsorbent of active silicate gel and calcite. J Hazard Mater. 2008;153:775-83
140. Ogata F, Ueta E, Kawasaki N. Characteristics of a novel adsorbent Fe–Mg-type hydrotalcite and its adsorption capability of As(III) and Cr(VI) from aqueous solution. 2018;59:56-63
141. Link T, Bellmann F, Ludwig HM, Haha MB. Reactivity and phase composition of Ca2SiO4 binders made by annealing of alpha-dicalcium silicate hydrate. Cem Concr Res. 2015;67:131-7
142. Vargas AMM, Cazetta AL, Kunita MH, Silva TL, Almeida VC. Adsorption of methylene blue on activated carbon produced from flamboyant pods (Delonix regia): Study of adsorption isotherms and kinetic models. 2011;168:722-30
143. Crini G, Peindy HN, Gimbert F, Robert C. Removal of CI Basic Green 4 (Malachite Green) from aqueous solutions by adsorption using cyclodextrin-based adsorbent: Kinetic and equilibrium studies. 2007;53:97-110
144. Zhuang X, Wan Y, Feng C, Shen Y, Zhao D. Highly efficient adsorption of bulky dye molecules in wastewater on ordered mesoporous carbons. 2009;21:706-16
145. Southam DC, Lewis TW, McFarlane AJ, Johnston JH. Amorphous calcium silicate as a chemisorbent for phosphate. 2004;4:355-8
146. Southam DC, Lewis TW, McFarlane AJ, Borrmann T, Johnston JH. Calcium–phosphorus interactions at a nano-structured silicate surface. J Colloid Interface Sci. 2008;319:489-97
147. Niuniavaite D, Baltakys K, Dambrauskas T. The Adsorption Kinetic Parameters of Co2 Ions by α-C2SH. 2018;8:10
148. Baltakys K, Dambrauskas T, Eisinas A, Siauciunas R. α-C2SH synthesis in the mixtures with CaO/SiO2= 1.5 and application as a precursor for binder material. Sci Iranica. 2016;23:2800-10
149. Diamond S. The microstructure of cement paste in concrete. 1986:122-47

150. Franus W, Panek R, Wdowin M. SEM investigation of microstructures in hydration products of portland cement. 2015:105-12
151. Becker O, Varley RJ, Simon GP. Thermal stability and water uptake of high performance epoxy layered silicate nanocomposites. 2004;40:187-95
152. Gallucci E, Zhang X, Scrivener KL. Effect of temperature on the microstructure of calcium silicate hydrate (C-S-H). 2013;53:185-95
153. Dambrauskas T, Baltakys K, Eisinas A. Formation and thermal stability of calcium silicate hydrate substituted with Al3 ions in the mixtures with CaO/SiO2= 1.5. 2018;131:501-12
154. Garbev K, Gasharova B, Beuchle G, Kreisz S, Stemmermann P. First Observation of α-Ca2 [SiO3 (OH)](OH)–Ca6 [Si2O7][SiO4](OH) 2 Phase Transformation upon Thermal Treatment in Air. J Am Ceram Soc. 2008;91:263-71
155. Liu X, Ding C. Plasma-sprayed wollastonite 2M/ZrO2 composite coating. 2003;172:270-8
156. Xue H, Wang G, Hu M, Chen B. Modification of wollastonite by acid treatment and alkali-induced redeposition for use as papermaking filler. 2015;276:193-9
157. Nour WMN, Mostafa AA, Ibrahim DM. Recycled wastes as precursor for synthesizing wollastonite. 2008;34:101-5
158. He Y, Zhao X, Lu L, Struble LJ, Hu S. Effect of C/S ratio on morphology and structure of hydrothermally synthesized calcium silicate hydrate. 2011;26:770-3
159. Yu P, Kirkpatrick RJ, Poe B, McMillan PF, Cong X. Structure of calcium silicate hydrate (C-S-H): Near-, mid-, and far-infrared spectroscopy. J Am Ceram Soc. 1999;82:742-8
160. Sun Z, Huang D, Duan X, Hong W, Liang J. Functionalized nanoflower-like hydroxyl magnesium silicate for effective adsorption of aflatoxin B1. 2020;387:121792
161. Rouquerol J, Rouquerol F, Llewellyn P, Maurin G, Sing KS. Adsorption by powders and porous solids: principles, methodology and applications. : Academic press; 2013.
162. Liu L, Liu S, Peng H, Yang Z, Zhao L, Tang A. Surface charge of mesoporous calcium silicate and its adsorption characteristics for heavy metal ions. 2020;99:106072
163. Zhang Y, Liu C, Liu Z, Liu G, Yang L. Modelling of diffusion behavior of ions in low-density and high-density calcium silicate hydrate. 2017;155:965-80
164. Lowell S, Shields JE, Thomas MA, Thommes M. Characterization of porous solids and powders: surface area, pore size and density. : Springer Science & Business Media; 2012.
165. Roosz C, Gaboreau S, Grangeon S, Prêt D, Montouillout V, Maubec N, Ory S, Blanc P, Vieillard P, Henocq P. Distribution of water in synthetic calcium silicate hydrates. 2016;32:6794-805
166. Zdujić M, Lukić I, Kesić Ž, Janković-Častvan I, Marković S, Jovalekić Č, Skala D. Synthesis of CaOSiO2 compounds and their testing as heterogeneous catalysts for transesterification of sunflower oil. 2019;30:1141-50

167. Dambrauskas T, Baltakys K, Eisinas A, Kitrys S. The specific surface area and porosity of synthetic and calcined α-C2SH, kilchoanite and hydroxyledgrewite. 2019;355:504-13
168. Yang Y, Liu W, Hu Y, Sun J, Tong X, Li Q, Zhou Z. Novel low cost Li4SiO4-based sorbent with naturally occurring wollastonite as Si-source for cyclic CO2 capture. 2019;374:328-37
169. Tang Y, Michel FM, Zhang L, Harrington R, Parise JB, Reeder RJ. Structural properties of the Cr (III)− Fe (III)(Oxy) hydroxide compositional series: insights for a nanomaterial “solid solution”. 2010;22:3589-98
170. Ungarish M, Aharoni C. Kinetics of chemisorption. Deducing kinetic laws from experimental data. 1981;77:975-85
171. Ho YS, McKay G. A Comparison of Chemisorption Kinetic Models Applied to Pollutant Removal on Various Sorbents. 1998;76:332-40
172. Novembre D, Pace C, Gimeno D. Synthesis and characterization of wollastonite-2 M by using a diatomite precursor. 2018;82:95-110
173. Shimizu K, Kanno S, Kon K, Hakim Siddiki, S. M. A., Tanaka H, Sakata Y. N-alkylation of ammonia and amines with alcohols catalyzed by Ni-loaded CaSiO3. 2014;232:134-8
174. Xia X, Xu Y, Chen Y, Liu Y, Lu Y. The distinct catalytic behaviours of calcium silicate hydrate for the high selectivity of 2, 2′-isomer in reaction of phenol with formaldehyde. 2019;118:15-8
175. Segawa A, Nakashima A, Nojima R, Yoshida N, Okamoto M. Acetaldehyde Production from Ethanol by Eco-Friendly Non-Chromium Catalysts Consisting of Copper and Calcium Silicate. Ind Eng Chem Res. 2018;57:11852-7
176. Zhu G, Li H, Wang X, Li S, Hou X, Wu W, Tang Q. Synthesis of calcium silicate hydrate in highly alkaline system. J Am Ceram Soc. 2016;99:2778-85
177. Qu X, Zhao Z, Zhao X. Microstructure and characterization of aluminum-incorporated calcium silicate hydrates (Câ€“Sâ€“H) under hydrothermal conditions. 2018;8:28198-208
178. El-Korashy SA. Characterization of Cation Exchange and Cesium Selectivity of Synthetic Beta-Dicalcium Silicate Hydrate. 2002;46:515-22
179. Meng Y, Ling T, Mo KH, Tian W. Enhancement of high temperature performance of cement blocks via CO2 curing. 2019;671:827-37
180. Niuniavaite D, Baltakys K, Dambrauskas T, Eisinas A. Cu 2 , Co 2 and Cr 3 adsorption by synthetic dibasic calcium silicate hydrates and their thermal stability in a 25–1000° C temperature range. 2019;138:2241-9
181. Franus W, Panek R, Wdowin M. SEM investigation of microstructures in hydration products of portland cement. 2015:105-12
182. Berei E, Ştefănescu O, Muntean C, Ţăranu B, Ştefănescu M. Study on the formation of CoCr 2 O 4/SiO 2 nanocomposite obtained from Co (II) carboxylate and ammonium dichromate. 2019;138:1863-70
183. Chang SK, Seong IW. Characterization of Cr/silica ethylene polymerization catalyst by TPO/TPR and FT—IR. 1992;73:249-63
184. Shao C, Chen M. In situ FT-IR studies on the CO2 hydrogenation over the SiO2-supported RhM (M=Cr, Mo, W) complex catalysts. 2001;166:331-5

185. El-Sheikh SM, Rabah MA. Optical properties of calcium chromate 1D-nanorods synthesized at low temperature from secondary resources. 2014;37:235-40
186. Veksha A, Moo JGS, Krikstolaityte V, Oh W, Udayanga WDC, Giannis A, Lisak G. Synthesis of CaCr2O4/carbon nanoplatelets from non-condensable pyrolysis gas of plastics for oxygen reduction reaction and charge storage. 2019;849:113368
187. Anokhin AS, Chernova ES, Strelnikova SS, Andrianov NT, Ashmarin AA, Zheleznyi MV. Influence of additives of aluminum, magnesium and calcium on synthesis and sintering of lanthanum chromite. 2014;5:323-9
188. Sahooli M, Sabbaghi S, Saboori R. Synthesis and characterization of mono sized CuO nanoparticles. Mater Lett. 2012;81:169-72
189. Phiwdang K, Suphankij S, Mekprasart W, Pecharapa W. Synthesis of CuO nanoparticles by precipitation method using different precursors. 2013;34:740-5
190. Rotter H, Landau MV, Carrera M, Goldfarb D, Herskowitz M. High surface area chromia aerogel efficient catalyst and catalyst support for ethylacetate combustion. 2004;47:111-26
191. Kang M, Lee C. Methylene chloride oxidation on oxidative carbon-supported chromium oxide catalyst. 2004;266:163-72
192. Hosseini SA, Niaei A, Salari D, Alvarez-Galvan MC, Fierro J. Study of correlation between activity and structural properties of Cu-(Cr, Mn and Co) 2 nano mixed oxides in VOC combustion. Ceram Int. 2014;40:6157-63

CURRICULUM VITAE

Name, surname: Domantė Davidovičienė
E-mail: domante.n@gmail.com

Education

2012–2016
Bachelor's degree in Applied Chemistry, Kaunas University of Technology, Kaunas, Lithuania
2016–2018
Master's degree in Chemical Engineering, Kaunas University of Technology, Kaunas, Lithuania
2018–2022
PhD in Chemical Engineering, Kaunas University of Technology, Kaunas, Lithuania

Work experience

2016–2019
Science researcher at NANDO
2019
Junior researcher in the project "Synthesis and application of $Me_xO_yCa_zSi_q$ nanostructures in energy efficient technologies"
2020
Junior researcher in the project "Synthesis and application of calcium silicate with interfering metal ions in the production of alternative cements"
2020–2021
New product specialist at BOOK Laboratory

LIST OF SCIENTIFIC PUBLICATIONS

Articles published in journals indexed in the Clarivate Analytics Web of Science with Impact Factor

1. Niuniavaite, Domante; Baltakys, Kestutis; Dambrauskas, Tadas; Eisinas, Anatolijus; Rubinaite, Dovile; Jaskunas, Andrius. Microstructure, thermal stability, and catalytic activity of compounds formed in $CaO\text{-}SiO_2\text{-}Cr(NO_3)_3\text{-}H_2O$ system // Nanomaterials. ISSN 2079-4991. 2020, vol. 10, iss. 7, p. 1-16.
2. Niuniavaite, Domante; Baltakys, Kestutis; Dambrauskas, Tadas; Eisinas, Anatolijus. Cu^{2+}, Co^{2+} and Cr^{3+} adsorption by synthetic dibasic calcium silicate hydrates and their thermal stability in a 25–1000 °C temperature range // Journal of Thermal Analysis and Calorimetry. ISSN 1388-6150. 2019, Vol. 138, p. 2241-2249.
3. Niuniavaite, Domante; Baltakys, Kestutis; Dambrauskas, Tadas. The adsorption kinetic parameters of Cu^{2+} and Cr^{3+} ions by $\alpha\text{-}C_2SH$ // Desalination and water treatment. ISSN 1944-3994. 2020, vol. 185, p. 175-184. D

Publications in other international databases

1. Niuniavaite, Domante; Baltakys, Kestutis; Dambrauskas, Tadas. The adsorption kinetic parameters of Co^{2+} ions by $\alpha\text{-}C_2SH$ // Buildings. ISSN 2075-5309. 2018, vol. 8, p. 1-9.

Articles published in the conference proceedings

1. Niuniavaite, Domante; Baltakys, Kestutis; Dambrauskas, Tadas. The influence of copper ions on the formation, thermal stability and porosity of dibasic calcium silicate hydrates: poster // 6th Central and Eastern European conference on thermal analysis and calorimetry (CEEC-TAC6) and 15th Mediterranean conference on calorimetry and thermal analysis (Medicta2021), 20-24 July 2021, Split, Croatia: book of abstracts / A. Rotaru, M. Erceg (eds), ISBN 9786061178612, p. 105.
2. Knabikaite, Inga; Baltakys, Kestutis; Eisinas, Anatolijus; Dambrauskas, Tadas; Niuniavaite, Domante. The influence of chromium and aluminium ions on the calcium silicate hydrates formation: poster // Advanced materials and technologies: book of abstracts of 21st international conference - school, 19-23 August 2019, Palanga, Lithuania. Kaunas: Kaunas University of Technology. ISSN 1822-7759. 2019, p. 137.
3. Niuniavaite, Domante; Baltakys, Kestutis; Dambrauskas, Tadas. Texture properties and thermal stability of compounds formed in $CaO\text{-}SiO_2\text{-}Cu(NO_3)_2/Co(NO_3)_2/Cr(NO_3)_3\text{-}H_2O$ system: poster // 5th Central and Eastern European conference on thermal analysis and calorimetry (CEEC-TAC5) and 14th Mediterranean conference on calorimetry and thermal analysis (Medicta2019), 27-30 August 2019, Roma, Italy: book of abstracts. Rostock: Academica Greifswald, 2019, ISBN 9783940237590, p. 294.
4. Baltakys, Kęstutis; Eisinas, Anatolijus; Dambrauskas, Tadas; Niūniavaitė, Domantė; Knabikaitė, Inga. The synthesis of multifunctional MexOyCazSiq nano sized adsorbents/catalysts // Technorama 2019: from vision to innovation!

2019 m. gegužės 9 d.: innovation catalogue. Kaunas: KTU. 2019, project no. 74, p. 27
5. Niuniavaite, Domante; Dambrauskas, Tadas; Baltakys, Kestutis. The influence of granite dust additive on the properties of cement mortar: poster // Open readings 2019: 62nd international conference for students of physics and natural sciences, March 19-22, Vilnius, Lithuania: abstract book. Vilnius: Vilnius University, 2019, ISBN 9786090701379. p. 96.

ACKNOWLEDGMENTS

I would like to acknowledge the enthusiastic and encouraging supervision of Professor **Kestutis Baltakys** who has provided invaluable counseling on the thesis and shown confidence in me.

I owe a special thanks to lecturer T. Dambrauskas and Assoc. Prof. Dr. A. Eisinas for their support, professional comments, and valuable remarks. I am grateful to all my friends and colleagues from the Department of Silicate Technology for their support and friendship. They all contributed to the success of this project in very different ways.

I would like to thank the Research Council of Lithuania and Kaunas University of Technology for providing the funding as well as giving me the opportunity to attend conferences.

Finally, I would like to thank my family, who through my childhood and studies has always encouraged and supported me in any direction it took me.

Appendix 1. Adsorbent A2 texture and specific surface area

No.	Relative pressure, P/P_0	N_2 volume adsorbed on the V_{ad} (ncm^3/g)	Kelvin radius of the pores, r_K (Å)	Thickness of N_2 layer, t (Å)	True pore radius (Å)	Average Kelvin radius of the pores, r_K (Å)	Average true pore radius, r_p (Å)	Change, Δt (Å)	Change, ΔV ad (ncm^3/g)	Change of evaporated liquid adsorbate volume, ΔV_L ($\times 10^3$ cm^3/g)	ΔtΣA ($\times 10^3$ cm3/g)	True volume of the pores, V p ($\times 10^3$ cm3/g)	Surface of pore walls, A (m2/g)	Total surface, ΣA (m^2/g)
Calculations using between parallel plates pore model														
1	0.9457	123.193	171.0	15.84	202.7	134.09	163.05	2.73	30.18	46.48	0.00	56.52	6.93	0.17
2	0.9064	93.0107	97.10	13.11	123.3	79.98	104.44	1.77	29.69	45.72	0.03	59.62	11.42	11.59
3	0.8591	63.3229	62.87	11.35	85.56	53.38	74.79	1.28	19.20	29.56	1.48	37.26	9.96	21.55
4	0.8045	44.1277	43.89	10.06	64.02	39.70	59.15	0.69	8.24	12.69	1.48	14.50	4.90	26.45
5	0.7643	35.8896	35.52	9.38	54.27	31.89	49.97	0.69	6.83	10.52	1.82	10.79	4.32	30.77
6	0.7135	29.0591	28.27	8.69	45.66	25.75	42.58	0.55	4.51	6.95	1.70	5.87	2.76	33.53
7	0.6629	24.5476	23.22	8.14	39.50	21.70	37.60	0.37	2.32	3.58	1.25	1.87	0.99	34.52
8	0.6230	22.2252	20.17	7.77	35.71	18.43	33.49	0.48	2.53	3.89	1.65	1.08	0.65	35.17
9	0.5642	19.7001	16.68	7.29	31.26	15.74	30.04	0.28	1.33	2.05	1.00	0.09	0.06	35.23
10	0.5246	18.3668	14.80	7.01	28.81	13.77	27.44	0.34	1.63	2.51	1.20	0.21	0.16	35.39
11	0.4726	16.7339	12.74	6.66	26.07									

Calculations using a cylindrical pore model														
1	0.9457	123.1934	171.09	15.84	186.93	134.09	148.57	2.73	30.18	46.48	0.00	57.06	7.68	0.17
2	0.9064	93.0107	97.10	13.11	110.21	79.98	92.21	1.77	29.69	45.72	0.03	60.73	13.17	13.34
3	0.8591	63.3229	62.87	11.35	74.21	53.38	64.08	1.28	19.20	29.56	1.71	40.14	12.53	25.87
4	0.8045	44.1277	43.89	10.06	53.95	39.70	49.42	0.69	8.24	12.69	1.77	16.91	6.84	32.72
5	0.7643	35.8896	35.52	9.38	44.89	31.89	40.93	0.69	6.83	10.52	2.25	13.63	6.66	39.37
6	0.7135	29.0591	28.27	8.69	36.97	25.75	34.16	0.55	4.51	6.95	2.17	8.40	4.92	44.29
7	0.6629	24.5476	23.22	8.14	31.36	21.70	29.65	0.37	2.32	3.58	1.65	3.60	2.43	46.72
8	0.6230	22.2252	20.17	7.77	27.94	18.43	25.96	0.48	2.53	3.89	2.23	3.29	2.54	49.26
9	0.5642	19.7001	16.68	7.29	23.97	15.74	22.89	0.28	1.33	2.05	1.40	1.37	1.20	50.46
10	0.5246	18.3668	14.80	7.01	21.81	13.77	20.60	0.34	1.63	2.51	1.72	1.77	1.72	52.18
11	0.4726	16.7339	12.74	6.66	19.40	11.95	18.47	0.29	1.01	1.55	1.50	0.10	0.11	52.29
12	0.4250	15.7287	11.16	6.38	17.53									

Appendix 2. A2-750 texture and specific surface area

No.	Relative pressure, P/P_0	N_2 volume adsorbed on the V_{ad} (ncm^3/g)	Kelvin radius of the pores, r_K (Å)	Thickness of N_2 layer, t (Å)	True pore radius (Å)	Average Kelvin radius of the pores, r_K (Å)	Average true pore radius, r_p (Å)	Change, Δt (Å)	Change, ΔV ad (ncm^3/g)	Change of evaporated liquid adsorbate volume, ΔV_L ($\times 10^3$ cm^3/g)	$\Delta t \Sigma A$ ($\times 10^3$ cm3/g)	True volume of the pores, V p ($\times 10^3$ cm3/g)	Surface of pore walls, A (m2/g)	Total surface, ΣA (m^2/g)
Calculations using between parallel plates pore model														
1	0.94853	20.3239	180.65	16.13	212.91	137.30	166.40	3.16	4.08	6.29	0.00	7.62	0.92	0.17
2	0.90339	16.2415	93.96	12.97	119.90	77.13	101.29	1.78	2.98	4.58	0.03	5.94	1.17	1.34
3	0.85357	13.2652	60.30	11.19	82.67	53.10	74.51	0.97	1.33	2.05	0.13	2.51	0.67	2.02
4	0.81227	11.934	45.91	10.22	66.35	40.78	60.39	0.83	1.14	1.75	0.17	2.10	0.70	2.71
5	0.76509	10.7966	35.65	9.39	54.44	32.09	50.20	0.67	0.89	1.38	0.18	1.58	0.63	3.34
6	0.71553	9.9029	28.52	8.72	45.95	26.05	42.95	0.53	0.79	1.22	0.18	1.42	0.66	4.00
7	0.66717	9.1124	23.59	8.18	39.95	21.76	37.68	0.45	0.45	0.69	0.18	0.58	0.31	4.31
8	0.61952	8.6621	19.94	7.74	35.41	18.53	33.62	0.38	0.53	0.81	0.17	0.87	0.52	4.83
9	0.57262	8.1351	17.12	7.35	31.83	15.96	30.32	0.35	0.49	0.75	0.17	0.79	0.52	5.35
10	0.52469	7.6457	14.80	7.01	28.81	13.84	27.53	0.32	0.50	0.77	0.17	0.85	0.62	5.97
11	0.47649	7.1471	12.88	6.69	26.25	11.91	24.94	0.35	0.52	0.80	0.21	0.80	0.64	6.61

12	0.41825	6.626	10.95	6.34	23.62	10.39	22.84	0.22	0.35	0.54	0.15	0.54	0.48	7.09
13	0.37858	6.2726	9.83	6.11	22.05	9.26	21.24	0.24	0.38	0.59	0.17	0.56	0.53	7.62
14	0.33353	5.8891	8.69	5.87	20.43	8.16	19.65	0.25	0.37	0.57	0.19	0.47	0.48	8.10
15	0.28639	5.516	7.63	5.62	18.87	7.15	18.14	0.25	0.33	0.51	0.20	0.26	0.29	8.39
16	0.23884	5.1875	6.67	5.37	17.41	6.22	16.71	0.25	0.37	0.57	0.21	0.41	0.49	8.88
17	0.19162	4.8159	5.78	5.12	16.02	5.36	15.33	0.26	0.39	0.59	0.23	0.36	0.47	9.35
18	0.14438	4.4309	4.93	4.86	14.65	4.51	13.94	0.29	0.39	0.60	0.27	0.17	0.25	9.59
19	0.09719	4.0401	4.10	4.57	13.23	3.64	12.41	0.36	0.47	0.72	0.35	0.08	0.13	9.73
20	0.05029	3.5714	3.19	4.20	11.60									
Calculations using a cylindrical pore model														
1	0.94853	20.3239	180.65	16.13	196.78	137.30	151.85	3.16	4.08	6.29	0.00	7.69	1.01	0.17
2	0.90339	16.2415	93.96	12.97	106.93	77.13	89.21	1.78	2.98	4.58	0.03	6.09	1.37	1.54
3	0.85357	13.2652	60.30	11.19	71.48	53.10	63.81	0.97	1.33	2.05	0.15	2.74	0.86	2.40
4	0.81227	11.934	45.91	10.22	56.13	40.78	50.59	0.83	1.14	1.75	0.20	2.39	0.95	3.34
5	0.76509	10.7966	35.65	9.39	45.04	32.09	41.14	0.67	0.89	1.38	0.23	1.89	0.92	4.26
6	0.71553	9.9029	28.52	8.72	37.24	26.05	34.50	0.53	0.79	1.22	0.23	1.74	1.01	5.27

7	0.66717	9.1124	23.59	8.18	31.77	21.76	29.72	0.45	0.45	0.69	0.23	0.86	0.58	5.84
8	0.61952	8.6621	19.94	7.74	27.68	18.53	26.08	0.38	0.53	0.81	0.22	1.16	0.89	6.74
9	0.57262	8.1351	17.12	7.35	24.48	15.96	23.14	0.35	0.49	0.75	0.23	1.09	0.94	7.68
10	0.52469	7.6457	14.80	7.01	21.81	13.84	20.69	0.32	0.50	0.77	0.24	1.17	1.13	8.81
11	0.47649	7.1471	12.88	6.69	19.57	11.91	18.43	0.35	0.52	0.80	0.31	1.18	1.28	10.09
12	0.41825	6.626	10.95	6.34	17.29	10.39	16.61	0.22	0.35	0.54	0.23	0.81	0.98	11.07
13	0.37858	6.2726	9.83	6.11	15.94	9.26	15.25	0.24	0.38	0.59	0.27	0.87	1.14	12.20
14	0.33353	5.8891	8.69	5.87	14.56	8.16	13.91	0.25	0.37	0.57	0.30	0.79	1.13	13.34
15	0.28639	5.516	7.63	5.62	13.25	7.15	12.64	0.25	0.33	0.51	0.33	0.55	0.86	14.20
16	0.23884	5.1875	6.67	5.37	12.04	6.22	11.47	0.25	0.37	0.57	0.36	0.74	1.29	15.49
17	0.19162	4.8159	5.78	5.12	10.90	5.36	10.34	0.26	0.39	0.59	0.41	0.69	1.34	16.83
18	0.14438	4.4309	4.93	4.86	9.79	4.51	9.23	0.29	0.39	0.60	0.49	0.46	1.00	17.82
19	0.09719	4.0401	4.10	4.57	8.66	3.64	8.03	0.36	0.47	0.72	0.65	0.36	0.89	18.72
20	0.05029	3.5714	3.19	4.20	7.39									

Appendix 3. H-Cr texture and specific surface area

No.	Relative pressure, P/P_0	N_2 volume adsorbed on the V_{ad} (ncm^3/g)	Kelvin radius of the pores, r_K (Å)	Thickness of N_2 layer, t (Å)	True pore radius (Å)	Average Kelvin radius of the pores, r_K (Å)	Average true pore radius, r_p (Å)	Change, Δt (Å)	Change, ΔV ad (ncm^3/g)	Change of evaporated liquid adsorbate volume, ΔV_L ($\times 10^3$ cm^3/g)	$\Delta t \Sigma A$ ($\times 10^3$ cm3/g)	True volume of the pores, V p ($\times 10^3$ cm3/g)	Surface of pore walls, A (m2/g)	Total surface, ΣA (m^2/g)
Calculations using between parallel plates pore model														
1	0.95	190.5081	173.93	15.93	205.78	135.55	164.59	2.81	23.33	35.92	0.00	43.62	5.30	0.17
2	0.91	167.1814	97.17	13.12	123.40	80.02	104.49	1.77	31.06	47.84	0.03	62.38	11.94	12.11
3	0.86	136.1194	62.88	11.35	85.58	54.27	75.82	1.15	24.04	37.02	1.39	47.83	12.62	24.73
4	0.81	112.0824	45.66	10.20	66.06	40.41	59.95	0.85	19.84	30.56	2.11	39.09	13.04	37.77
5	0.76	92.2393	35.15	9.35	53.85	31.71	49.75	0.65	13.67	21.06	2.47	25.28	10.16	47.93
6	0.71	78.5648	28.27	8.69	45.66	25.82	42.67	0.53	9.58	14.75	2.56	15.91	7.46	55.39
7	0.66	68.9852	23.37	8.16	39.69	21.78	37.71	0.39	6.40	9.86	2.15	9.61	5.10	60.48
8	0.62	62.5832	20.19	7.77	35.72	18.73	33.87	0.39	6.15	9.48	2.38	8.52	5.03	65.51
9	0.58	56.4302	17.27	7.38	32.02	16.06	30.44	0.36	5.47	8.42	2.38	6.96	4.57	70.08
10	0.53	50.9606	14.84	7.01	28.87	13.94	27.67	0.30	6.53	10.05	2.07	11.73	8.48	78.56
11	0.48	44.4335	13.04	6.72	26.48	12.07	25.16	0.35	5.90	9.08	2.76	7.43	5.90	84.46

12	0.42	38.5345	11.10	6.37	23.83									
Calculations using a cylindrical pore model														
1	0.9466	190.5081	173.93	15.93	189.85	135.55	150.07	2.81	23.33	35.92	0.00	44.03	5.87	0.17
2	0.9064	167.1814	97.17	13.12	110.28	80.02	92.26	1.77	31.06	47.84	0.03	63.54	13.77	13.94
3	0.8591	136.1194	62.88	11.35	74.23	54.27	65.04	1.15	24.04	37.02	1.60	50.87	15.64	29.59
4	0.8113	112.0824	45.66	10.20	55.86	40.41	50.18	0.85	19.84	30.56	2.52	43.24	17.23	46.82
5	0.7622	92.2393	35.15	9.35	44.50	31.71	40.73	0.65	13.67	21.06	3.07	29.68	14.57	61.40
6	0.7134	78.5648	28.27	8.69	36.97	25.82	34.25	0.53	9.58	14.75	3.28	20.18	11.78	73.18
7	0.6647	68.9852	23.37	8.16	31.53	21.78	29.74	0.39	6.40	9.86	2.85	13.08	8.79	81.97
8	0.6232	62.5832	20.19	7.77	27.96	18.73	26.30	0.39	6.15	9.48	3.23	12.32	9.37	91.34
9	0.5753	56.4302	17.27	7.38	24.64	16.06	23.25	0.36	5.47	8.42	3.31	10.71	9.21	100.56
10	0.5256	50.9606	14.84	7.01	21.86	13.94	20.81	0.30	6.53	10.05	2.97	15.77	15.15	115.71
11	0.4810	44.4335	13.04	6.72	19.76	12.07	18.61	0.35	5.90	9.08	4.07	11.93	12.82	128.53
12	0.4232	38.5345	11.10	6.37	17.47	10.56	16.81	0.22	2.18	3.36	2.77	1.48	1.76	130.29
13	0.3854	36.3551	10.01	6.15	16.16	9.28	15.27	0.32	3.07	4.72	4.13	1.60	2.09	132.38
14	0.3270	33.2882	8.54	5.83	14.37	8.12	13.85	0.20	1.87	2.87	2.62	0.73	1.05	133.44

15	0.2894	31.4217	7.70	5.63	13.33	7.14	12.62	0.29	2.63	4.05	3.87	0.57	0.90	134.33
16	0.2339	28.7934	6.57	5.34	11.92	6.20	11.44	0.21	1.82	2.80	2.78	0.07	0.13	134.46
17	0.1948	26.9724	5.84	5.14	10.97									

Appendix 4. H-Cr550 texture and specific surface area

No.	Relative pressure, P/P_0	N_2 volume adsorbed on the V_{ad} (ncm^3/g)	Kelvin radius of the pores, r_K (Å)	Thickness of N_2 layer, t (Å)	True pore radius (Å)	Average Kelvin radius of the pores, r_K (Å)	Average true pore radius, r_p (Å)	Change, Δt (Å)	Change, ΔV ad (ncm^3/g)	Change of evaporated liquid adsorbate volume, ΔV_L ($\times 10^3$ cm^3/g)	ΔtΣA ($\times 10^3$ cm3/g)	True volume of the pores, V p ($\times 10^3$ cm3/g)	Surface of pore walls, A (m2/g)	Total surface, ΣA (m^2/g)
Calculations using between parallel plates pore model														
1	0.95	141.2279	171.77	15.86	203.50	133.24	162.11	2.86	31.53	48.56	0.00	59.08	7.29	0.17
2	0.90	109.6953	94.71	13.01	120.72	78.50	102.82	1.70	34.68	53.40	0.03	69.87	13.59	13.76
3	0.86	75.0192	62.29	11.31	84.91	53.11	74.49	1.24	21.74	33.48	1.71	42.17	11.32	25.08
4	0.80	53.2764	43.94	10.07	64.07	39.60	59.02	0.71	8.48	13.06	1.78	14.14	4.79	29.87
5	0.76	44.7967	35.26	9.36	53.98	31.58	49.60	0.70	6.11	9.41	2.10	8.19	3.30	33.18
6	0.71	38.6837	27.90	8.65	45.21	25.70	42.52	0.48	3.49	5.37	1.60	3.59	1.69	34.86
7	0.67	35.1953	23.49	8.17	39.83	21.51	37.36	0.49	3.10	4.77	1.70	2.37	1.27	36.13
8	0.61	32.1	19.53	7.68	34.90	18.37	33.43	0.32	1.86	2.86	1.14	1.05	0.63	36.76
9	0.57	30.2449	17.22	7.37	31.95	16.10	30.50	0.34	1.67	2.57	1.23	0.20	0.13	36.89
10	0.53	28.5768	14.97	7.03	29.04	13.99	27.74	0.32	1.60	2.47	1.18	0.20	0.14	37.03
11	0.48	26.9748	13.02	6.71	26.44	12.03	25.10	0.36	1.81	2.79	1.32	0.30	0.24	37.27

12	0.42	25.1648	11.05	6.35	23.76									
Calculations using a cylindrical pore model														
1	0.9459	141.2279	171.77	15.86	187.63	133.24	147.68	2.86	31.53	48.56	0.00	59.65	8.08	0.17
2	0.9041	109.6953	94.71	13.01	107.72	78.50	90.66	1.70	34.68	53.40	0.03	71.19	15.70	15.87
3	0.8579	75.0192	62.29	11.31	73.60	53.11	63.80	1.24	21.74	33.48	1.97	45.47	14.25	30.13
4	0.8047	53.2764	43.94	10.07	54.00	39.60	49.31	0.71	8.48	13.06	2.14	16.93	6.86	36.99
5	0.7628	44.7967	35.26	9.36	44.62	31.58	40.59	0.70	6.11	9.41	2.60	11.26	5.55	42.54
6	0.7103	38.6837	27.90	8.65	36.56	25.70	34.11	0.48	3.49	5.37	2.05	5.85	3.43	45.97
7	0.6660	35.1953	23.49	8.17	31.66	21.51	29.44	0.49	3.10	4.77	2.24	4.73	3.21	49.18
8	0.6133	32.1000	19.53	7.68	27.21	18.37	25.90	0.32	1.86	2.86	1.55	2.59	2.00	51.18
9	0.5744	30.2449	17.22	7.37	24.59	16.10	23.30	0.34	1.67	2.57	1.72	1.79	1.53	52.71
10	0.5286	28.5768	14.97	7.03	22.01	13.99	20.87	0.32	1.60	2.47	1.69	1.73	1.65	54.37
11	0.4803	26.9748	13.02	6.71	19.73	12.03	18.56	0.36	1.81	2.79	1.94	2.01	2.17	56.54
12	0.4214	25.1648	11.05	6.35	17.40	10.48	16.72	0.23	1.06	1.64	1.28	0.92	1.10	57.63
13	0.3815	24.0999	9.91	6.13	16.04	9.34	15.35	0.24	1.11	1.72	1.40	0.85	1.11	58.74
14	0.3369	22.9852	8.77	5.89	14.66	8.24	14.00	0.25	1.15	1.77	1.46	0.91	1.30	60.04

15	0.2899	21.8335	7.71	5.64	13.35	7.22	12.74	0.25	1.11	1.71	1.49	0.70	1.10	61.14
16	0.2425	20.7218	6.74	5.39	12.13	6.29	11.55	0.25	1.12	1.72	1.53	0.65	1.12	62.26
17	0.1951	19.6031	5.84	5.14	10.98	5.42	10.43	0.26	1.23	1.89	1.62	0.99	1.91	64.17
18	0.1480	18.3741	5.00	4.88	9.87	4.58	9.31	0.29	1.40	2.16	1.84	1.29	2.78	66.94
19	0.1010	16.9738	4.16	4.59	8.75	3.72	8.14	0.35	1.92	2.96	2.34	2.97	7.30	74.25
20	0.0547	15.0534	3.29	4.24	7.53									

UDK 661.842(043.3)

SL 344. 2022-*-*, * leidyb. apsk. l. Tiražas 14 egz. Užsakymas *
Išleido Kauno technologijos universitetas, K. Donelaičio g. 73, 44249 Kaunas
Spausdino leidyklos „Technologija“ spaustuvė, Studentų g. 54, 51424 Kaunas